Time-dependent Dalitz-Plot Analysis of the Charmless Decay $B^0 \to K^0_S \pi^+ \pi^-$ at *BABAR*
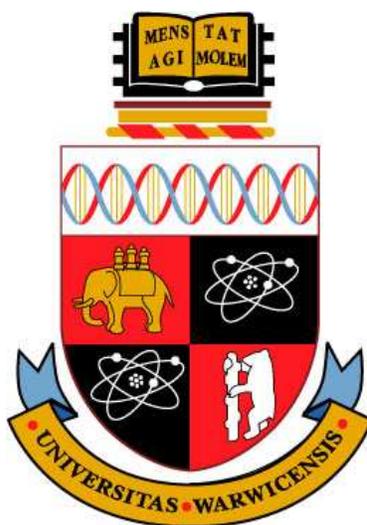
Jelena Ilić

Submitted to the University of Warwick for the

degree of Doctor of Philosophy

University of Warwick

Department of Physics

20th February 2009

Горану

Abstract

A time-dependent amplitude analysis of $B^0 \to K_S^0 \pi^+ \pi^-$ decays is performed in order to extract the CP violation parameters of $f_0(980)K_S^0$ and $\rho^0(770)K_S^0$ and direct CP asymmetries of $K^{*+}(892)\pi^-$. The results are obtained from the final $BABAR$ data sample of $(465 \pm 5)10^6$ $B\overline{B}$ decays, collected with the $BABAR$ detector at the PEP-II asymmetric-energy B factory at SLAC. The time dependent CP asymmetry for $f_0(980)K_S^0$ and $\rho^0(770)K_S^0$ are measured to be $\mathcal{S}(f_0(980)K_S^0) = -0.97 \pm 0.09 \pm 0.01 \pm 0.01$, and $\mathcal{S}(\rho^0(770)K_S^0) = 0.67 \pm 0.20 \pm 0.06 \pm 0.04$, respectively. In decays to $K^{*+}(892)\pi^-$ the direct CP asymmetry is found to be $\mathcal{A}_{CP}(K^{*\pm}(892)\pi^{\mp}) = -0.18 \pm 0.10 \pm 0.04 \pm 0.00$. The relative phases between $B^0 \to K^{*+}(892)\pi^-$ and $\overline{B}^0 \to K^{*-}(892)\pi^+$, relevant for the extraction of the unitarity triangle angle γ, is measured to be $\Delta\phi(K^*(892)\pi) = (34.9 \pm 23.1 \pm 7.5 \pm 4.7)^\circ$, where uncertainties are statistical, systematic and model-dependent, respectively. Fit fractions, direct CP asymmetries and the relative phases of different other resonant modes have also been measured. A new method for extracting longitudinal shower development information from longitudinally unsegmented calorimeters is also presented. This method has been implemented as a part of the $BABAR$ final particle identification algorithm. A significant improvement in low momenta muon identification at $BABAR$ is obtained.

Acknowledgements

Firstly I would like to thank the Particle Physics Group at the University of Warwick and especially to Professor Paul Harrison for giving me the opportunity to study in Warwick and for providing the funding for my Ph.D.

My two supervisors: Tim Gershon and Paul Harrison for all their support, advice and encouragement.

Many thanks to Tom Latham from whom I learnt most of the things I know now about analyses of B meson decays and whose knowledge of C++ and the professional style of writing C++ software influenced me to become a better programmer myself.

Special thanks to Pablo del Amo Sánchez, he was always ready to help and to listen about my problems.

To Gagan Mohanty, for his enthusiasm which made a publication of our work on the longitudinal shower development possible.

Also, to John Back, Ben Morgan John Thornby and Eugenia Puccio, they have always made me feel as a part of the group and made the time I spent at Warwick University enjoyable.

Finally, I would like to thank the examiners, Yorck Ramachers and Jonas Rademacker, for being ready to read a thesis with such short notice.

Declaration

I declare that the work in this thesis was carried out in accordance with the Regulations of the University of Warwick. No part of the thesis has been submitted for any other academic award at this or any other university.

The data used in this analysis were recorded by the *BABAR* detector run by the *BABAR* Collaboration. The author contributed to the running of the detector through the taking of detector shifts and working on the problem of the longitudinal shower development in longitudinally unsegmented calorimeters. The presented analysis is performed on the final *BABAR* data sample. An analysis of the same decay channel, but on a smaller $B\overline{B}$ data sample, in which the author was actively involved, was performed earlier. The event reconstruction described in Chapter 3 makes use of code developed by the Collaboration, with the packages used for 3-body B meson decay event selection (`QnBUser` and `CharmlessFitter`) written by Fergus Wilson and Thomas Latham, respectively. The software used for the likelihood Dalitz-plot fit (`Laura++`) was first developed by Paul Harrison and John Back, and further extended by Thomas Latham, Pablo del Amo Sánchez and the author. For example, the author derived and implemented the formulae for the treatment of the tag side interference effects, added a number of the probability density function lineshapes and the new polar coordinate parametrisation of the isobar coefficients.

The work on the analysis described in this document (Chapters 4 and 5) was carried out solely by the author. A new method for extracting longitudinal shower development information (Chapter A) was developed by the author in collaboration with Gagan Mohanty and David Brown.

SIGNED: .... DATE: ....

Contents

List of Tables

List of Figures

xvii

Introduction

There are at least three discrete transformations of general interest in particle physics:

- parity P (reflecting the space coordinates: $\vec{x}$ into $-\vec{x}$),

- microscopic time reversal T (changing the time coordinate t into $-t$),

- charge conjugation C (replacing a particle by its antiparticle).

Originally it was assumed that all three represent symmetries of nature, since they were known to be conserved in the strong and electromagnetic processes. The first one to lose its "true symmetry" status was parity. In 1957 it was found that P is violated in weak processes [1, 2, 3]. The discovery led to the conclusion that, on the microscopic level, nature distinguishes between left and right. Soon it was realised that the idea of mirror image symmetry of the microspace can be saved as long as the combined CP transformation is conserved: if nature is CP-invariant, then for every process, there exists an appropriate mirror image symmetrical process in which particles are replaced by antiparticles, and all characteristics of both processes have to be equal.

In 1964, experimenting on decays of neutral K mesons, Christenson, Cronin, Fitch and Turlay [4] observed the decay $K_L^0 \rightarrow \pi^+\pi^-$, which if CP were conserved, would be forbidden. This came as a complete surprise. Since the idea of CP violation was not easy to accept, a lot of scepticism regarding the measurements was shown [5, 6]. But the results proved to be correct and the fact

that nature distinguishes between matter and antimater and left and right was accepted.

In the years that followed, many attempts were made in order to build a theoretical framework for CP violation, and give an explanation for its existence. Today, we have the Standard Model which describes the CP violation by the Kobayashi-Maskawa mechanism [7, 8], but does not explain the origin of the CP violation, except that it is connected to the unknown coupling of the fermions to the Higgs field. Also, almost any model of new physics, such as supersymmetry, introduces more CP violating sources in order to generate large CP asymmetries [9] needed for Sakharov's explanation of baryon number asymmetry [10], i.e. the situation that today's Universe is predominantly populated by particles with a very small fraction of antiparticles[1].

Therefore, searches for CP violation in different systems are very important for particle physics in the sense that they may help to give the answer to the fundamental question of the evolution of the Universe.

Charmless three-body B meson decays, such as $B^0 \rightarrow K_S^0 \pi^+ \pi^-$, provide a deep insight into the nature of the CP violating processes. A rich resonance structure and small branching fractions make them difficult to analyse, but nevertheless the information that can be extracted from these analyses makes it worth the effort. Thanks to the involvement of second-order weak interactions, such as mixing and loop diagrams, they are among the most sensitive low energy probes for the new physics effects. The large phase space of three-body B meson decays provides a possibility to measure interference between different resonant processes with more accuracy, and consequently the possibility to extract directly any phase differences involved. This provides additional sensitivity to CP violation effects. Finally, experimental studies of charmless three-body B meson decays address an old, unsolved question related to

---

[1]In 1967, Soviet physicist Andrei Sakharov proposed a set of 3 necessary conditions that have to be met in order to dynamically create the baryon asymmetry of the Universe: baryon number violation; C and CP symmetry violation; interactions out of thermal equilibrium.

hadronic effects: "How to deal with nonperturbative quantum chromodynamic effects?".

In the thesis that follows details and results of the analysis of charmless decays of a neutral B meson into the $K^0_S \pi^+ \pi^-$ final state, performed using the final $BABAR$ data sample, are presented.

Chapter 1

Theory

This chapter introduces the physics of CP violation starting with the Standard Model formalism, after which the three scenarios for CP violation are presented in more detail, followed by the time evolution of neutral B meson states and general remarks about three-body decay kinematics.

1.1 CP violation in Standard Model

The part of the Standard Model (SM) Lagrangian which describes the flavour-changing quark transitions, has the following form [11]:

$$L_{int} = -\frac{g}{\sqrt{2}}(\jmath^\mu W_\mu^+ + \jmath^{\dagger\mu} W_\mu^-).$$ (1.1)

Here, $\jmath^\mu$ is a V-A (vector-axial vector) charged weak current operator that couples to the W boson, $W_\mu^\pm$ denotes the charged vector boson fields, and g is the weak coupling constant. The V-A operator $\jmath^\mu$ can be written in the flavour basis as:

$$\jmath^\mu = \sum_{i,j} \bar{u}_i \gamma^\mu \frac{1}{2}(1 - \gamma^5)d_j,$$ (1.2)

where, $\bar{u}_i$ and d_j are quark fields, γ^μ are Dirac matrices, γ^5 is their product and the indices i and j run over the three quark generations. Since the states that propagate in space and time are mass eigenstates, it is useful to rewrite the

above equation in the mass basis. Denoting the basis transformation matrix with $\mathcal{U}$:

$$
\begin{aligned}
u_m &= \mathcal{U}^u_{mn} u'_n, \quad d_m = \mathcal{U}^d_{mn} d'_n. \\
V_{ij} &\equiv \mathcal{U}^{u\dagger}_{mi} \mathcal{U}^d_{mj},
\end{aligned}
\tag{1.3}
$$

then Eq. (1.2) becomes:

$$
\mathcal{J}^\mu = \sum_{i,j} \bar{u}_i' \gamma^\mu \frac{1}{2} (1 - \gamma^5) V_{ij} d'_j,
\tag{1.4}
$$

where the complex coefficients V_{ij} that appear as a result of changing basis are the elements of the CKM matrix named after Cabibbo, Kobayashi and Maskawa [7, 8]. From Eq. (1.2) and Eq. (1.4) it can be seen that the amplitudes for processes in which a W^- boson is radiated ($d_j \to W^- u_i$ and $\bar{u}_i \to W^- \bar{d}_j$) are proportional to V_{ij}, while the amplitudes for processes in which a W^+ is radiated ($u_i \to W^+ d_j$ and $\bar{d}_j \to W^+ \bar{u}_i$) are proportional to the V_{ij}^* coefficient. In the above equation the CKM matrix appeared as a result of changing basis. Historically, this matrix was introduced to account for the experimentally observed fact, that the weak interaction, unlike strong and electromagnetic, does not conserve quark flavour. In other words, the CKM matrix was introduced to describe the situation that there is no unique set of quark eigenstates of weak interaction. Each up-type quark couples to a mixture of down-type quarks. Therefore, the CKM matrix can be understood as a rotation from the down-type quark states as seen by the strong interaction (d, s and b) to a set of new down-type quark states as seen by the weak interaction (d', s' and b'):

$$
\begin{pmatrix} d' \\ s' \\ b' \end{pmatrix} = \begin{pmatrix} V_{ud} & V_{us} & V_{ub} \\ V_{cd} & V_{cs} & V_{cb} \\ V_{td} & V_{ts} & V_{tb} \end{pmatrix} \begin{pmatrix} d \\ s \\ b \end{pmatrix}
\tag{1.5}
$$

The Standard Model does not predict values of the CKM matrix elements. They are, like fermion masses, fundamental input parameters. The only information about CKM matrix elements that the Standard Model provides are

that they are related to the fermion masses, since both have the same origin: the unknown coupling of the fermions to the Higgs field, and unitarity relations. This Higgs-fermion interaction is usually called the Yukawa interaction. The form of the quark-Higgs Yukawa interaction terms in the SM Lagrangian is the following:

$$\mathcal{L}_{\text{Y}} = -Y_{ij}^u \bar{q}_{L,i} \phi u_{R,j} - Y_{ij}^d \bar{q}_{L,i} \phi d_{R,j}. \tag{1.6}$$

Here, $Y^{u,d}$ are 3×3 complex matrices, the indices i and j label the generations, and ϕ is the Higgs field. The form of Yukawa interaction terms is constrained by $SU(2)_L$ gauge invariance, but this condition does not require the terms to be diagonal in quark flavour. However, to determine the quark masses the Yukawa terms have to be diagonalised. The basis in which this is accomplished is the mass basis. As already shown in Eq. (1.3), the change from flavour to mass basis involves the CKM matrix. Therefore, the fermion masses and CKM matrix parameters are closely related. Together, they account for 13 of the total 18 SM parameters (nine fermion masses, four CKM matrix elements, three $SU(3)_C \times SU(2)_L \times U(1)_Y$ gauge coupling constants, Higgs mass and vacuum expectation value of the Higgs scalar field).

The fact that the CKM matrix consists of four free parameters, three mixing angles and one CP violating phase, can be derived from its unitarity and the requirement that any phase has to be non-trivial (redefinition of the fields cannot lead to the phase being zero). These may be parametrized in a variety of ways, and perhaps the most useful parametrization is the one developed by Wolfenstein [12], based on an empirical observation:

$$|V_{us}|^3 \approx |V_{cb}|^{3/2} \approx |V_{ub}|, \tag{1.7}$$

unitarity and measured values of the CKM matrix elements. The Wolfenstein representation emphasises the hierarchy in the quark couplings and expresses matrix elements in terms of powers of $\lambda \equiv |V_{us}| \approx 0.22$ [13]. Choosing a phase convention in which: V_{ud}, V_{us}, V_{cd}, V_{ts}, and V_{tb} are approximately real,

Wolfenstein found:

$$V_{\text{CKM}} = \begin{pmatrix} 1 - \frac{1}{2}\lambda^2 & \lambda & \lambda^3 A \left(\rho - i\eta\right) \\ -\lambda & 1 - \frac{1}{2}\lambda^2 & \lambda^2 A \\ \lambda^3 A \left(1 - \rho - i\eta\right) & -\lambda^2 A & 1 \end{pmatrix} + \mathcal{O}\left(\lambda^4\right)$$

$$\sim \begin{pmatrix} 1 & \lambda & \lambda^3 e^{-i\gamma} \\ -\lambda & 1 & \lambda^2 \\ \lambda^3 e^{-i\beta} & -\lambda^2 & 1 \end{pmatrix}. \tag{1.8}$$

where the value of the parameter A is $\approx \frac{4}{5}$, $\rho \approx 0.15$ and $\eta \approx 0.35$ [14], and η is the only parameter responsible for the CP violation.

The unitarity condition $(V^\dagger_{\text{CKM}} V_{\text{CKM}} = I)$ leads to 9 relations between the elements of the CKM matrix. For decays of B mesons, the following equation, which describes $b \to d$ quark transition, is of particular interest:

$$V^*_{ud}V_{ub} + V^*_{cd}V_{cb} + V^*_{td}V_{tb} = 0. \tag{1.9}$$

Since the V_{ij} are complex numbers, it is possible to interpret the above equation as a triangle in the complex plane. This triangle is usually called the Unitarity Triangle and is shown in Figure 1.1. To construct this particular Unitarity Triangle Eq. (1.9) is rescaled by a factor $\frac{1}{|V_{cd}V^*_{cb}|}$. Often, instead of using Wolfenstein's η and ρ coordinates, $\bar{\eta}$ and $\bar{\rho}$ coordinates are used. These are related to η and ρ according to:

$$\bar{\rho} = \rho(1 - \lambda^2/2), \qquad \bar{\eta} = \eta(1 - \lambda^2/2). \tag{1.10}$$

Many analyses have been performed to measure the magnitudes of the CKM matrix elements. A high precision value of $|V_{ud}|$ is obtained from superallowed $0^+ \to 0^+$ nuclear, neutron and pion β decays. To determine a value of $|V_{us}|$ leptonic and semileptonic decays of K^0 and K^+, as well as semileptonic decays of hyperons were used, while the extraction of $|V_{cd}|$ and $|V_{cs}|$ has been done by analysing semileptonic D meson decays and dimuon production in deep inelastic scattering of neutrinos on nucleons. Precise measurements of other

8

$$\alpha = \arg\left(-\frac{V_{td}V_{tb}^*}{V_{ud}V_{ub}^*}\right)$$

$$\beta = \arg\left(-\frac{V_{cd}V_{cb}^*}{V_{td}V_{tb}^*}\right) \quad (1.11)$$

$$\gamma = \arg\left(-\frac{V_{ud}V_{ub}^*}{V_{cd}V_{cb}^*}\right)$$
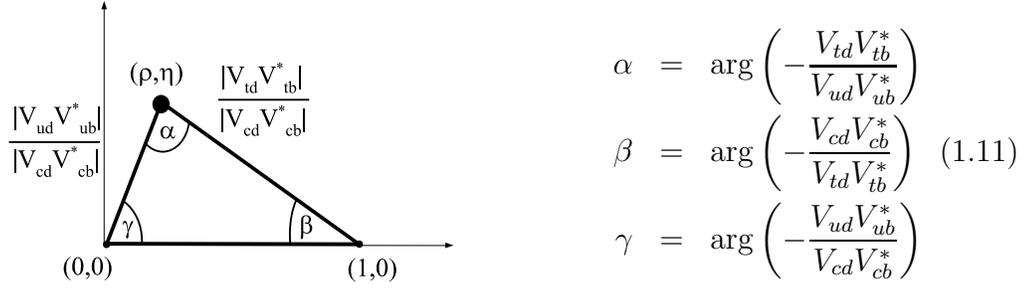
Figure 1.1: *Representation of the triangle formed from Eq. (1.9) divided by $V_{cd}V_{cb}^*$. The definitions of the angles of the triangle in terms of the CKM matrix elements are given on the right.*

CKM matrix elements became possible with the *BABAR* and Belle experiments. Results for $|V_{cb}|$ and $|V_{ub}|$ mainly come from semileptonic B decays to charm and charmless final states, respectively, while values of couplings between d, s and b quarks and the t quark were measured in processes with dominant flavour changing neutral current component. Figure 1.2 shows the current experimental constraints on the sides and angles of the unitarity triangle [15]. It can be seen that all constraints overlap nicely around the apex of the unitarity triangle.

1.1.1   CP violation in decay

One of the simplest ways to study CP violation is to compare the decay rates: $\Gamma(P \to f)$ and $\Gamma(\bar{P} \to \bar{f})$, where P is a pseudoscalar meson and f and $\bar{f}$ are CP-conjugate final states. If we define the action of the CP operator on the states $|P\rangle$ and $|f\rangle$ as:

$$CP|P\rangle = e^{2i\theta(P)}|\bar{P}\rangle$$
$$CP|f\rangle = e^{2i\theta(f)}|\bar{f}\rangle, \quad (1.12)$$

where 2θ is an arbitrary phase, and **assume CP conservation** in $P \to f$ decay, the amplitude $A(P \to f)$ for that decay can be written as:

Figure 1.2: *Experimental constraints on the sides and angles of the unitarity triangle, by the CKMfitter group [15], updated with the results available in summer 2008.*

$$A \approx \langle f|H|P \rangle = \langle f|(CP)^\dagger (CP) H (CP)^\dagger (CP)|P \rangle$$

$$= \langle \bar{f}|H|\bar{P} \rangle e^{2i(\theta(P)-\theta(f))}$$

$$= \bar{A} e^{2i(\theta(P)-\theta(f))}. \tag{1.13}$$

Here, $\bar{A}$ is the amplitude for the CP conjugate process and H is a Hamiltonian which commutes with the CP operator because of the assumed CP symmetry of the decay. Therefore, when CP is conserved:

$$\left| \frac{\bar{A}}{A} \right| = 1, \tag{1.14}$$

while a situation where:

$$\left| \frac{\bar{A}}{A} \right| \neq 1, \tag{1.15}$$

implies *CP violation in decay*. In that case, the rates $\Gamma(P \to f)$ and $\Gamma(\bar{P} \to \bar{f})$ will be different, which then can be expressed as an asymmetry:

$$\mathcal{A}_{CP} = \frac{\Gamma(P \to f) - \Gamma(\bar{P} \to \bar{f})}{\Gamma(P \to f) + \Gamma(\bar{P} \to \bar{f})}. \tag{1.16}$$

To have an observable direct CP asymmetry more then one amplitude has to contribute to a given decay process. The reason for that comes from the fact that in the Standard Model, CP-conjugate amplitudes differ from the original amplitude at most by a phase factor. In the simplest case of two amplitudes that contribute to a given final state:

$$A = \langle f|H|P \rangle = \sum_{i=1}^{2} a_i e^{i(\delta_i + \phi_i)}$$

$$\bar{A} = \langle \bar{f}|H|\bar{P} \rangle = e^{2i(\theta(P)-\theta(f))} \sum_{i=1}^{2} a_i e^{i(\delta_i - \phi_i)}, \tag{1.17}$$

where δ_i is a CP conserving (strong) phase, and ϕ_i is a CP violating (weak) phase, the asymmetry becomes:

$$\mathcal{A}_{CP} = \frac{|A|^2 - |\bar{A}|^2}{|A|^2 + |\bar{A}|^2} = \frac{2|a_1||a_2| \sin(\delta_1 - \delta_2) \sin(\phi_1 - \phi_2)}{|a_1|^2| + |a_2|^2 + 2|a_1||a_2| \cos(\delta_1 - \delta_2) \cos(\phi_1 - \phi_2)}. \tag{1.18}$$

From here it can be seen that $\mathcal{A}_{CP}$ will have a non-zero value only if the weak phases, as well as the strong phases, from the two processes that contribute to the final state are different. Examples showing the interaction of the strong and weak phases leading to appearance of CP asymmetry are shown in Figure 1.3.
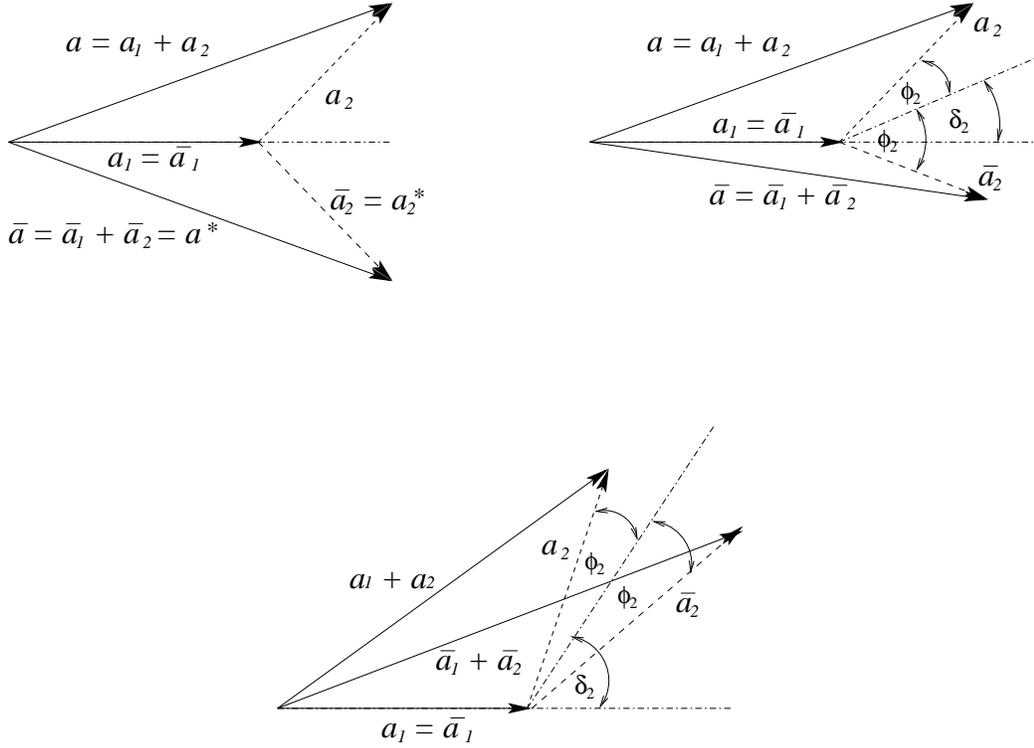
Figure 1.3: *Examples of direct CP violation. In the first case (top left) there is a relative weak phase between amplitudes a_1 and a_2, but no relative strong phase. Therefore, the CP conjugate amplitude $\bar{a} = \bar{a}_1 + \bar{a}_2 = a^*$, and there is no CP asymmetry. In the other two cases (top right and bottom), both, relative weak and strong phases are present, giving a CP asymmetry ($\bar{a} \neq a^*$).*

1.1.2   CP violation in mixing

The spontaneous oscillation of a neutral meson into its antiparticle, often called mixing, has been observed in neutral kaons [1], B_d and B_s [16, 17] mesons
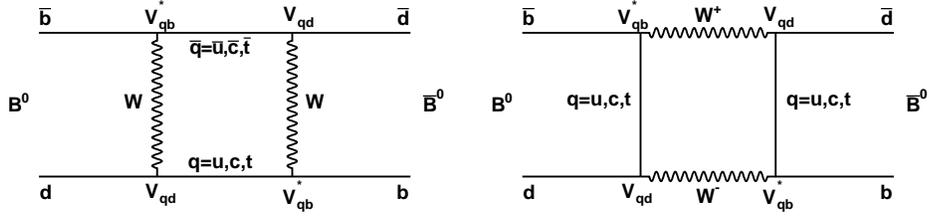
Figure 1.4: *Box diagrams showing mixing between B^0 and $\bar{B}^0$ mesons.*

and recently was seen in D mesons [18, 19]. Mixing does not necessarily imply CP violation, but provides interfering amplitudes that can produce CP violation. The Feynman diagrams of mixing in the B^0 meson system are shown in Figure 1.4. The particle which propagates in the loop has to be one of the quarks with absolute charge 2/3, and therefore one of the up-type quarks. Looking at the relevant CKM matrix elements it can be seen that any choice of an up-quark gives a coupling of order of λ^6. On the other side, the mixing process also includes emission and absorption of W bosons, so each vertex is weighted by a ratio of quark and W boson masses, and therefore the t quark loop dominates. The corresponding CKM factors are then V_{td} and V_{tb}, and the CP violating phase (using the Wolfenstein parametrization) enters the mixing amplitude via V_{td}:

$$(V_{td}V_{tb}^*)^2 \approx e^{-i2\beta}. \tag{1.19}$$

So, an oscillating B^0 compared to a non oscillating B^0 picks up an extra -2β phase, often called the mixing phase. This phase can be measured if both flavours decay to the same state. The standard formalism of mixing [20] is based on a time-dependent perturbation theory analysis of a two-state system, $|P^0\rangle$ and $|\bar{P}^0\rangle$, together with the continuum of states $|f\rangle$ into which the particles P^0 and $\bar{P}^0$ can decay. Any state in the space of $|P^0\rangle$, $|\bar{P}^0\rangle$ and $|f\rangle$ can be written as:

$$|\widetilde{\Psi}(t)\rangle = a(t)|P^0\rangle + b(t)|\bar{P}^0\rangle + \sum_f c_f(t)|f\rangle, \tag{1.20}$$

13

and the Schrödinger equation for this system as:

$$i\frac{d}{dt}|\widetilde{\Psi}(t)\rangle = \boldsymbol{H}\,|\widetilde{\Psi}(t)\rangle. \tag{1.21}$$

Here, $\boldsymbol{H}$ is an infinite-dimensional Hermitian matrix in the Hilbert space of the analysed system. To solve Eq. (1.21) is a difficult task, mainly because of insufficient knowledge of strong interaction dynamics. But, if we assume that the initial state is a linear combination of P^0 and $\bar{P}^0$ alone:

$$|\Psi(0)\rangle = a(0)|P^0\rangle + b(0)|\bar{P}^0\rangle, \tag{1.22}$$

and restrict ourselves to times that are much larger than a typical strong interaction scale (Weisskopf-Wigner approximation), the Schrödinger equation becomes:

$$\mathcal{H}\begin{pmatrix} a(t) \\ b(t) \end{pmatrix} = \begin{pmatrix} H_{11} & H_{12} \\ H_{21} & H_{22} \end{pmatrix}\begin{pmatrix} a(t) \\ b(t) \end{pmatrix} = i\frac{\partial}{\partial t}\begin{pmatrix} a(t) \\ b(t) \end{pmatrix}. \tag{1.23}$$

The new effective Hamiltonian matrix $\mathcal{H}$ is not hermitian, since we are only considering a projection onto the subspace of P^0 and $\bar{P}^0$.

Under the CP transformation the effective Hamiltonian $\mathcal{H}$ transforms in the following way:

$$
\begin{aligned}
H_{12} \equiv \langle P^0|\mathcal{H}|\bar{P}^0\rangle & \xrightarrow{\mathcal{CP}} & \langle P^0|(\mathcal{CP})^\dagger\,(\mathcal{CP})\,\mathcal{H}\,(\mathcal{CP})^\dagger\,(\mathcal{CP})|\bar{P}^0\rangle \\
& = & \langle\bar{P}^0|e^{-2i\theta(P)}\,\mathcal{H}_{\mathrm{cp}}\,e^{-2i\theta(P)}|P^0\rangle \\
& = & e^{-4i\theta(P)}\,\langle\bar{P}^0|\mathcal{H}_{\mathrm{cp}}|P^0\rangle \\
H_{11} \equiv \langle P^0|\mathcal{H}|P^0\rangle & \xrightarrow{\mathcal{CP}} & \langle P^0|(\mathcal{CP})^\dagger\,(\mathcal{CP})\,\mathcal{H}\,(\mathcal{CP})^\dagger\,(\mathcal{CP})|P^0\rangle \\
& = & \langle\bar{P}^0|\mathcal{H}_{\mathrm{cp}}|\bar{P}^0\rangle,
\end{aligned}
$$

$$(1.24)$$
$$(1.25)$$

where:

$$\mathcal{H}_{\mathrm{cp}} \equiv (\mathcal{CP})\,\mathcal{H}\,(\mathcal{CP})^\dagger. \tag{1.26}$$

Therefore CP is conserved if: $\mathcal{H} = \mathcal{H}_{\mathrm{cp}}$, i.e.:

$$|H_{12}| = |H_{21}| \quad \text{and} \quad H_{11} = H_{22}. \tag{1.27}$$

As a result, all CP violating observables occurring in $P^0 - \bar{P}^0$ mixing must be functions of:

$$\frac{|H_{12}| - |H_{21}|}{|H_{12}| + |H_{21}|}. \tag{1.28}$$

In the mass basis, the above calculation becomes simpler because $\mathcal{H}$ is diagonal. If we denote the eigenvectors of $\mathcal{H}$ as:

$$|P_H\rangle = p|P^0\rangle - q|\bar{P}^0\rangle$$
$$|P_L\rangle = p|P^0\rangle + q|\bar{P}^0\rangle \tag{1.29}$$

after some calculation it can be found that:

$$\frac{|H_{12}| - |H_{21}|}{|H_{12}| + |H_{21}|} = \frac{\left|\frac{p}{q}\right| - \left|\frac{q}{p}\right|}{\left|\frac{p}{q}\right| + \left|\frac{q}{p}\right|}. \tag{1.30}$$

Therefore, *CP violation in mixing* occurs if:

$$\left|\frac{p}{q}\right| \neq 1, \tag{1.31}$$

or in other words, if the physical states, which propagate in space and time are not composed of equal amounts of particle and antiparticle states.

1.1.3 Mixing-induced *CP* violation

As shown before (Section 1.1.1) for a *CP* violating effect to manifest itself in the asymmetry of the decay rates we need interfering amplitudes.

When P^0 and $\bar{P}^0$ mesons decay to the same final *CP* eigenstate (f_{CP}), *CP* violation can occur if there is an interference between different amplitudes, which can happen with or without mixing between the neutral P meson states. In other words, *CP* violation can arise as a consequence of the interference between decays: $P^0 \to f_{CP}$ and $P^0 \to \bar{P}^0 \to f_{CP}$. This type of *CP* violation is known as *mixing induced CP violation* and is the one foreseen by Bigi, Carter, Sanda and others [21] to be of primary importance in the decays of neutral B mesons.

1.2   Neutral B meson

1.2.1   Time evolution of neutral B mesons

To find how the neutral B^0 and $\bar{B}^0$ mesons evolve in time and space [22] we can start by expressing the physical states of the neutral B meson in terms of the mass eigenstates (Eq. (1.29)):

$$
\begin{aligned}
|B^0\rangle &= \frac{1}{2p}(|B_L\rangle + |B_H\rangle) \\
|\bar{B}^0\rangle &= \frac{1}{2q}(|B_L\rangle - |B_H\rangle).
\end{aligned}
\tag{1.32}
$$

The $|B_L\rangle$ and $|B_H\rangle$ are stationary states of the effective Hamiltonian $\mathcal{H}$ (Section 1.1.2). It is common to break $\mathcal{H}$ into its hermitian and anti-hermitian parts: $\mathcal{H} = \boldsymbol{M} - (i/2)\boldsymbol{\Gamma}$, where both $\boldsymbol{M}$ and $\boldsymbol{\Gamma}$ are hermitian matrices, usually known as the mass and decay matrix respectively. The eigenvalues corresponding to $|B_L\rangle$ and $|B_H\rangle$ then can be written as:

$$
\lambda_H = M_H - \frac{i}{2}\Gamma_H, \qquad \lambda_L = M_L - \frac{i}{2}\Gamma_L.
\tag{1.33}
$$

Using the above results, the time-dependence of the physical neutral B meson states is:

$$
\begin{aligned}
|B^0(t)\rangle &= e^{-iMt-\Gamma t/2}(\cos(\Delta Mt/2)|B^0(0)\rangle + i\frac{q}{p}\sin(\Delta Mt/2)|\bar{B}^0(0)\rangle) \\
|\bar{B}^0(t)\rangle &= e^{-iMt-\Gamma t/2}(i\frac{q}{p}\sin(\Delta Mt/2)|B^0(0)\rangle + \cos(\Delta Mt/2)|\bar{B}^0(0)\rangle),
\end{aligned}
\tag{1.34}
$$

where $|B^0(0)\rangle$ and $|\bar{B}^0(0)\rangle$ are flavour eigenstates, $\Delta M = M_H - M_L$, $M = (M_H + M_L)/2$ and $\Gamma = (\Gamma_H + \Gamma_L)/2$. The lifetime difference between the two neutral B_d mesons is very small, $\Delta\Gamma/\Gamma = O(10^{-2})$ [23], therefore $\Gamma \approx \Gamma_H \approx \Gamma_L$ (the $\Delta\Gamma = 0$ approximation is used to obtain the above equation), and a unit system of $c = 1$, where c is the velocity of light in the vacuum, is assumed. The previous result can be used to determine the time evolution of a $B^0\bar{B}^0$ pair produced from the decay of the $\Upsilon(4S)$ resonance. A $B\bar{B}$ pair produced

in a $\Upsilon(4S)$ decay behaves as a single entangled object. Before one of the B mesons decays there will be exactly one B^0 and one $\bar{B}^0$ present, even though they will evolve in phase according to Schrödingers equation.

In the $\Upsilon(4S)$ frame, if one of the B mesons is produced at an angle θ with respect to the beam (z) and with azimuth angle ϕ, the other B meson will be produced at an angle $\pi - \theta$ with respect to the beam axis and have an azimuthal angle of $\phi - \pi$. Thus, the time-evolution of the two B meson state in the $\Upsilon(4S)$ rest frame is given by the asymmetric term:

$$S(t_f, t_b, \phi, \theta) = \frac{1}{\sqrt{2}}[B^0(t_f, \theta, \phi)\bar{B}^0(t_b, \pi - \theta, \phi + \pi)-$$

$$\bar{B}^0(t_f, \theta, \phi)B^0(t_b, \pi - \theta, \phi + \pi)]\sin(\theta), \qquad (1.35)$$

where t_f and t_b are the proper times of the forward and backward B mesons respectively. Substituting Eq. (1.34) we get:

$$S(t_f, t_b, \phi, \theta) = \frac{1}{\sqrt{2}}e^{(-\Gamma/2+iM)(t_f+t_b)}[\cos(\Delta M(t_f - t_b)/2)(B_f^0\bar{B}_b^0 - \bar{B}_f^0 B_b^0)-$$

$$i\sin(\Delta M(t_f - t_b)/2)(\frac{p}{q}B_f^0\bar{B}_b^0 - \frac{q}{p}\bar{B}_f^0 B_b^0)]\sin(\theta). \qquad (1.36)$$

Therefore, when both physical states are present, $t_f = t_b$, so we have exactly one B^0 and one $\bar{B}^0$. After one of them decays the other B meson evolves independently by means of mixing.

1.2.2 Decay rate

To calculate the production rate for the two B meson system we need to rewrite equation Eq. (1.36) in terms of decay amplitudes. If one of the B mesons decays to a final state f_1 at a time t_1 and the other decays to the final state f_2 at time t_2, the total amplitude will be:

$$A(t_1, t_2) = m(t_1, t_2)\frac{1}{\sqrt{2}}e^{(-\Gamma/2+iM)(t_1+t_2)}[\cos(\Delta M(t_f - t_b)/2)(A_1\bar{A}_2 - \bar{A}_1 A_2)-$$

$$i\sin(\Delta M(t_1 - t_2)/2)(\frac{p}{q}A_1\bar{A}_2 - \frac{q}{p}\bar{A}_1 A_2)]\sin(\theta), \qquad (1.37)$$

17

where A_i is the amplitude for a B^0 state to decay to the final state f_i, $\bar{A}_i$ is the amplitude for a $\bar{B}^0$ state to decay to the same final state f_i and:

$$
m(t_1, t_2) = \begin{cases} +1, & t_1 = t_f, \ t_2 = t_b \\ -1, & t_1 = t_b, \ t_2 = t_f \end{cases}
$$

The modulus squared of this amplitude, integrated over all possible angles θ gives the production rate for the two B meson states to produce the final states f_1 and f_2. If we are interested in one particular final state (f_{signal}), we will need to determine the flavour of the neutral B meson decaying into that state, which is not a simple task since the oscillating nature of neutral B mesons means that their flavour changes over time. But at the BABAR experiment, $B^0 \bar{B}^0$ pairs produced from the decay of the $\Upsilon(4S)$ resonance are entangled, so when one of the B mesons (tagged B) decays in such a state from which the flavour of the meson can be identified, the flavour of the other meson can be inferred to be opposite at that exact same instant.

So, if we denote the moments when one of the B mesons decays into a flavour-dependent state (which, for example, indicates that the flavour of that meson is B^0) and the other into the signal state, as t_{tag} and t respectively, the amplitude of $B^0 \to f_{\text{tag}}$ as A_{tag} and amplitude of $B^0 \to f_{\text{signal}}$ as A, after some lengthy calculation we can write the expression for production rate as following:

$$
\Gamma(t_{\text{tag}}, t) \approx C e^{-\Gamma(t_{\text{tag}} - t)} |A_{\text{tag}}|^2 [(|A|^2 + |\bar{A}|^2) q_{\text{tag}} -
$$
$$
q_{\text{tag}} (|A|^2 - |\bar{A}|^2) \cos(\Delta M (t_{\text{tag}} - t)) +
$$
$$
q_{\text{tag}} 2 Im[\bar{A} A^* e^{-i\phi_{mix}}] \sin(\Delta M(t_{\text{tag}} - t))], \quad (1.38)
$$

where C is an overall normalisation constant and q_{tag} is the flavour of the B meson decaying into a flavour-specific state:

$$
q_{\text{tag}} = \begin{cases} +1, & \text{tagged } B \text{ is } B^0 \\ -1, & \text{tagged } B \text{ is } \bar{B}^0, \end{cases}
$$

The *CP* asymmetry previously defined in Section 1.1.1, in the case of neutral *B* decays can be rewritten as:

$$\mathcal{A}_{cp}\left(\Delta t\right) = \frac{\Gamma\left(B_{\text{tag}=B^0}\left(\Delta t\right) \to f_{\text{signal}}\right) - \Gamma\left(B_{\text{tag}=\bar{B}^0}\left(\Delta t\right) \to f_{\text{signal}}\right)}{\Gamma\left(B_{\text{tag}=B^0}\left(\Delta t\right) \to f_{\text{signal}}\right) + \Gamma\left(B_{\text{tag}=\bar{B}^0}\left(\Delta t\right) \to f_{\text{signal}}\right)}, \quad (1.39)$$

where Δt is the time between decays of tagged *B* and signal *B* mesons. After substituting Eq. (1.38) it becomes:

$$\mathcal{A}_{cp}\left(\Delta t\right) = \mathcal{S}\sin\left(\Delta m_d \Delta t\right) - \mathcal{C}\cos\left(\Delta m_d \Delta t\right), \quad (1.40)$$

where:

$$\mathcal{S} = \frac{2\text{Im}\lambda}{1 + |\lambda|^2}, \quad \mathcal{C} = \frac{1 - |\lambda|^2}{1 + |\lambda|^2}, \quad \lambda = e^{-i\phi_{\text{mix}}}\frac{\bar{A}}{A}. \quad (1.41)$$

Recalling the definitions of direct and mixing-induced *CP* violation it can be concluded that the coefficient $\mathcal{S}$ is different from zero when there is mixing-induced *CP* violation, while $\mathcal{C} \neq 0$ indicates direct *CP* violation ($|\bar{A}| \neq |A|$). If there is only one SM contribution to the amplitudes A and $\bar{A}$, the expectations are that $\mathcal{S} = -\eta_{CP}\sin\left(2\beta\right)$ and $\mathcal{C} = 0$, where η_{CP} is the *CP* eigenvalue of the final state f_{CP}. Deviations from that imply the existence of unaccounted amplitudes that, depending on the characteristics of the mode, could originate from theoretical uncertainties in the Standard Model contributions, or possible physics beyond the Standard Model.

In order to compare the experimentally measured time-dependent symmetries among themselves and with the theoretical predictions, it is common, instead of the mixing angle 2β, to use the effective mixing angle $2\beta_{\text{eff}}$ [14], defined as:

$$\mathcal{S} = -\eta_{CP}\sqrt{1 - \mathcal{C}^2}\sin 2\beta_{\text{eff}}. \quad (1.42)$$

1.2.3 Loop and Tree diagrams

In the Standard Model the decays of a meson containing a heavy quark usually proceed via charged-current interactions (since flavour changing neutral currents are forbidden at the tree level) and therefore direct coupling between, for example, the b quark and the s or d quark is not possible. The decay amplitudes can be generally divided into two classes, called tree and penguin (or loop) type, examples of which are shown in Figure 1.5. In the penguin
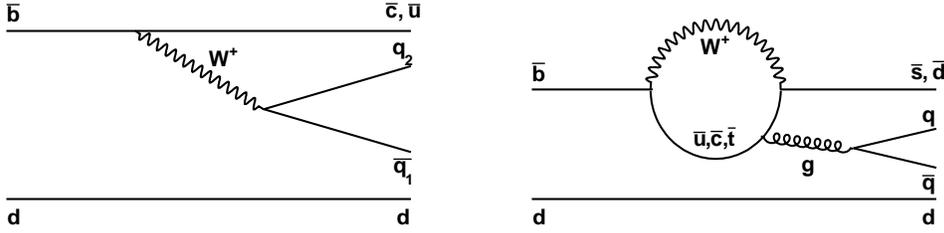
Figure 1.5: *Examples of tree (left) and penguin (right) diagrams. In this particular case of the tree diagram quark q_1 is a d or s quark, while q_2 is a u or c quark. The penguin diagram is of "gluonic" type. If instead of a gluon a photon or Z^0 boson is emitted from the loop the diagram is referred to as an "electromagnetic" and "electroweak" penguin respectively.*

process a quark emits and then reabsorbs a W boson, changing flavour twice, and $b \to s(d)$ coupling is accomplished indirectly via $b \to t(u,c) \to s(d)$ transition. Since the b quark has no kinematically-allowed CKM-favoured decay (Eq. (1.8)), the relative importance of the penguin decays in B meson physics is great. The main contributor to the SM $b \to s$ penguin loop is the t quark. For this conclusion one would just has to look at the magnitudes of the CKM matrix elements involved in the process. A similar conclusion cannot easily be made for a $b \to d$ penguin transition, since all possible SM scenarios ($b \to t \to d$, $b \to c \to d$ and $b \to u \to d$) are of order $\mathcal{O}(\lambda^3)$. But, the penguin process includes emission and absorption of a W boson, so each vertex has to be weighted by a ratio of quark and W mass, which makes the t quark domi-

nant. The SM penguin loops involve heavy particles (t, W; $m_t = 174.2 \pm 3.3$ GeV and $m_W = 80.403 \pm 0.029$ GeV [23]), therefore rates for penguin processes are very sensitive to non-SM extensions with heavy charged Higgs or supersymmetric particles [24] (see Figure 1.6). Because of that measurements of loop processes are the most sensitive low energy probes for such extensions to the Standard Model.
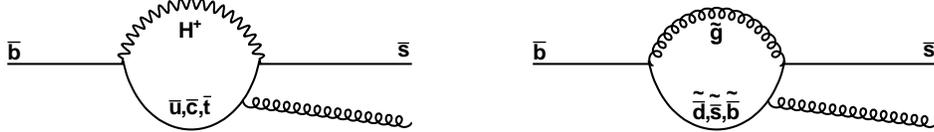
Figure 1.6: *Diagrams demonstrating the potential for new physics sensitivity in $b \rightarrow s$ penguin diagrams. On the left, a charged Higgs, predicted by, for example, the* Minimal Super-symmetrical Model, *enters the loop possibly carrying a complex coupling constant. On the right, the loop formed by a gluino and (anti)squarks is shown.*

1.3 $B^0 \rightarrow K_S^0 \pi^+ \pi^-$ and Unitarity Triangle angles

1.3.1 $\sin 2\beta$ from $B \rightarrow K\pi\pi$ modes

The "golden channel" for the measurement of the Unitarity Triangle angle β is $B^0 \rightarrow J/\psi K_S$ decay (see Figure 1.7). Theoretically and experimentally it is very clean [25]. Since the top quark dominates the loop, the CKM factors in both tree and penguin amplitudes carry approximately the same phases, and the time-dependent asymmetry has a simple form: $\mathcal{A}_{CP}(\Delta t) = \sin 2\beta \sin (\Delta m_d \Delta t)$.

21

The $B \to K\pi\pi$ modes are penguin dominated $b \to s\bar{q}q$ transitions, where q is a u or d quark. The involved CKM matrix elements have the same phases as those in the golden mode, and should therefore exhibit, to a good approximation, the same time-dependent asymmetries. Any significant differences could be a result of non-SM physics appearing in the process (see Figure 1.6). Figure 1.8 shows the measured values of $\sin 2\beta_{\text{eff}}$ from penguin dominated modes compared to the golden mode. It can be seen that the penguin modes tend to
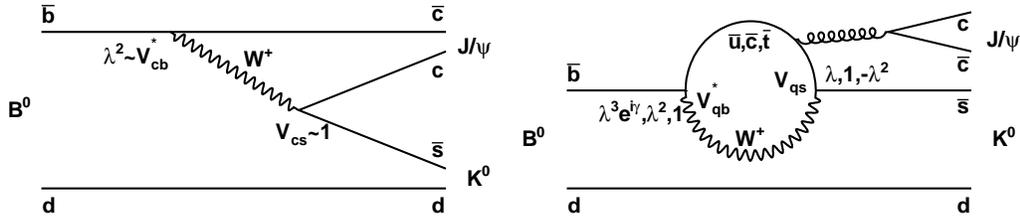
Figure 1.7: *Feynman diagrams for the amplitudes contributing to the $B^0 \to J/\psi K_S^0$ decay.*

lie on the left of the value for the golden channel. The statistical significance of the trend is hard to determine, since the corrections are mode-dependent. However, a naïve average is less than 3σ away from the charmonium value, and there is currently no convincing evidence for new physics effects in these transitions. Also, the most recent results of a number of Dalitz plot analyses shifted the charmless values toward the golden mode measurement, so the differences are becoming less evident. The final state $K_S^0\pi^+\pi^-$ allows measurements of $\sin 2\beta_{\text{eff}}$ in the channels $B^0 \to f_0(980)K_S^0$ and $B^0 \to \rho^0(770)K_S^0$. Such measurements have been performed previously on smaller data samples by isolating each resonant mode (quasi-two-body approach). A Dalitz analysis of a larger sample can improve the quasi-two-body measurements, by properly accounting for interferences between resonances. Also, quasi-two-body analyses are sensitive only to the interference of the state with its oscillated counterpart, which allows a measurement of $\sin 2\beta_{\text{eff}}$, but not the angle β_{eff} itself. On the other hand Dalitz analyses can exploit the interference of other

22

sin(2β^eff) ≡ sin(2φ₁^eff)

$$\sin(2\beta^{\text{eff}}) \equiv \sin(2\phi_1^{\text{eff}})$$

HFAG
ICHEP 2008
PRELIMINARY

		value
b→ccs	World Average	0.67 ± 0.02
φ K⁰	BaBar	$0.21 \pm 0.26 \pm 0.11$
	Belle	$0.50 \pm 0.21 \pm 0.06$
η′ K⁰	BaBar	$0.58 \pm 0.08 \pm 0.02$
	Belle	$0.64 \pm 0.10 \pm 0.04$
K_S K_S K_S	BaBar	$0.71 \pm 0.24 \pm 0.04$
	Belle	$0.30 \pm 0.32 \pm 0.08$
π⁰ K⁰	BaBar	$0.55 \pm 0.20 \pm 0.03$
	Belle	$0.67 \pm 0.31 \pm 0.08$
ρ⁰ K_S	BaBar	$0.61^{+0.22}_{-0.24} \pm 0.09 \pm 0.08$
ω K_S	BaBar	$0.55^{+0.26}_{-0.29} \pm 0.02$
	Belle	$0.11 \pm 0.46 \pm 0.07$
f₀ K⁰	BaBar	$0.25 \pm 0.26 \pm 0.10$
	Belle	$0.18 \pm 0.23 \pm 0.11$
π⁰ π⁰ K_S	BaBar	$-0.72 \pm 0.71 \pm 0.08$
	Belle	$-0.43 \pm 0.49 \pm 0.09$
K⁺ K⁻ K⁰	BaBar	$0.76 \pm 0.11 ^{+0.07}_{-0.04}$
	Belle	$0.68 \pm 0.15 \pm 0.03 ^{+0.21}_{-0.13}$
b→qqs	Naïve average	0.57 ± 0.04

-2   -1   0   1   2

Figure 1.8: $\sin 2\beta_{\text{eff}}$ (the notation ϕ_1 is also used to designate the Unitarity Triangle angle β, notably by the $\mathcal{B}$elle Collaboration) from penguin modes compared to the golden mode. The comparison is made by the Heavy Flavour Averaging Group [26] after the 2008 Summer conferences.

resonances with the oscillation amplitude, which enables the determination of β_{eff} itself, and the ambiguity resulting from the sine is removed.

1.3.2 Constraints on γ from $B \to K\pi\pi$ modes

Recently published papers [27, 28] pointed out the possibility of using Dalitz plot analyses of $B \to K\pi\pi$ decays to extract the angle γ, the most poorly determined angle of the unitarity triangle, $\gamma = \left(70^{+27}_{-29}\right)^{\circ}$ [15].

The currently favoured methods for γ measurement are based on the interference between the colour-allowed $B^- \to D^0 K^-$ and the colour-suppressed $B^- \to \overline{D}^0 K^-$ decay modes. In these decays only tree amplitudes are present, which makes them theoretically very clean, but the small relative magnitude of the two amplitudes ($0.046 \lesssim r_B \lesssim 0.126$) [14] reduces the sensitivity to γ.
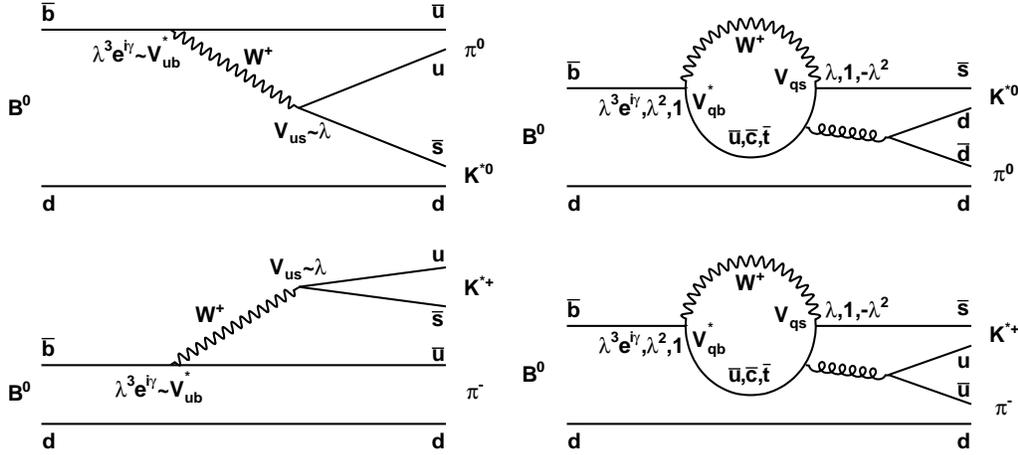
Figure 1.9: *Diagrams contributing to the amplitudes for $B^0 \to K^{*0}\pi^0$ (top) and $B^0 \to K^{*+}\pi^-$ (bottom), with the tree diagrams on the left, and the penguin diagrams on the right. The tree diagram for $B^0 \to K^{*+}\pi^-$ is an external emission tree, while the $B^0 \to K^{*0}\pi^0$ is an internal emission tree.*

The new method proposed by Ciuchini, Pierini and Silvestrini [27] and Gronau, Pirjol, Soni and Zupan [28] is based on the possibility of the Dalitz plot technique to extract relative phases. That, combined with isospin symmetry of the $B \to K\pi\pi$ decays allows determination of the UT angle γ. Feynman diagrams for $B^0 \to K^{*+}\pi^-$ and $B^0 \to K^{*0}\pi^0$ decays are shown in Figure 1.9, and using

isospin symmetry amplitudes for these processes can be written as:

$$A\left(K^{*+}\pi^-\right) = \tilde{P} + \tilde{E}_e \tag{1.43}$$

$$A\left(K^{*0}\pi^0\right) = \frac{-1}{\sqrt{2}}\tilde{P} + \frac{1}{\sqrt{2}}\tilde{E}_i, \tag{1.44}$$

where $\tilde{P}$ is the penguin amplitude, while $\tilde{E}_i$ and $\tilde{E}_e$ are internal and external emission tree amplitudes. With the help of the unitarity triangle relation $V_{tb}^*V_{ts} + V_{cb}^*V_{cs} + V_{ub}^*V_{us} = 0$, the penguin amplitude can be separated into CKM-favoured (P; t quark loop) and CKM-suppressed (P^{GIM}; u and c quark loops) parts, and the above equations can be rewritten as:

$$A\left(K^{*+}\pi^-\right) = V_{tb}^*V_{ts}P - V_{ub}^*V_{us}\left(E_e - P^{\text{GIM}}\right) \tag{1.45}$$

$$\sqrt{2}A\left(K^{*0}\pi^0\right) = -V_{tb}^*V_{ts}P - V_{ub}^*V_{us}\left(E_i + P^{\text{GIM}}\right). \tag{1.46}$$

Since the amplitude for the CP-conjugate $\overline{B}^0$ process is obtained by complex-conjugating the CP-odd phases (i.e. the CKM factors), when combined with the above relations the penguin terms cancel and the following can be written:

$$
\begin{aligned}
A^0 &= A\left(K^{*+}\pi^-\right) + \sqrt{2}A\left(K^{*0}\pi^0\right) \\
&= -V_{ub}^*V_{us}\left(E_e + E_i\right) \tag{1.47} \\
\bar{A}^0 &= A\left(K^{*-}\pi^+\right) + \sqrt{2}A\left(\overline{K}^{*0}\pi^0\right) \\
&= -V_{ub}V_{us}^*\left(E_e + E_i\right), \tag{1.48}
\end{aligned}
$$

from where the ratio of amplitudes A^0 and $\bar{A}^0$ can be calculated:

$$
\begin{aligned}
R^0 &= \frac{\bar{A}^0}{A^0} = \frac{V_{ub}V_{us}^*}{V_{ub}^*V_{us}} = e^{-i2\gamma} \\
\gamma &= -\frac{1}{2}\arg R^0. \tag{1.49}
\end{aligned}
$$

Therefore, to measure the CKM angle γ one has to measure the relative phase between amplitudes A^0 an $\bar{A}^0$. In quasi-two-body approaches, only the magnitudes of the amplitudes of processes in A^0 and $\bar{A}^0$ can be measured. But, the

Dalitz plot approach allows not only the measurement of relative magnitudes, but also of relative phases.

In Figure 1.10 a graphical representation of Eq. (1.47) and Eq. (1.48) is shown. From there one can see that the value of the UT angle γ can be extracted if angles ϕ, $\bar{\phi}$ and $\Delta\phi$ are known. Angles ϕ and $\bar{\phi}$ can be determined from the three-body decay of $B^0 \to K^+\pi^0\pi^-$ as relative phases between A_{+-} and A^{00} amplitudes and $\bar{A}_{+-}$ and $\bar{A}^{00}$, respectively, where A_{ij} denotes amplitudes of $B^0 \to K^{*i}\pi^j$ processes. The angle $\Delta\phi$ can be measured in a Dalitz plot analysis of $B^0 \to K_S^0\pi^+\pi^-$ decay, considering the decay chain $B^0 \to K^{*+}(\to K^0\pi^+)\pi^-$ and the CP conjugate $\bar{B}^0 \to K^{*-}(\to \bar{K}^0\pi^-)\pi^+$. These two decay channels do not overlap in the Dalitz plot, but they both interfere with the decays $B(\bar{B}) \to \rho^0(\to \pi^+\pi^-)K_S$ and with other resonances contributing to the same Dalitz plot, from which the phase between the $K^{*+}\pi^-$ and $K^{*-}\pi^+$ resonances can be calculated.
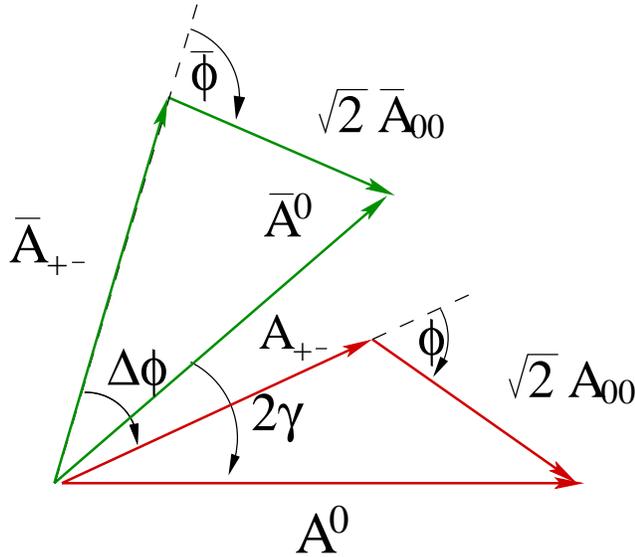
Figure 1.10: *Graphical representation of Eq. (1.47) and Eq. (1.48). The value of the UT angle γ can be calculated if angles ϕ, $\bar{\phi}$ and $\Delta\phi$ are known. These can be measured in the Dalitz plot analysis of $B^0 \to K^+\pi^0\pi^-$ and $B^0 \to K_S^0\pi^+\pi^-$ decays.*

The above calculations have been simplified by not taking into account the electroweak penguin contributions (obtained by exchanging the gluon in the penguin diagrams with a photon). Considering the full (weak, strong and electromagnetic) effective Hamiltonian for the transition, the authors of [27] give the following final expression:

$$R^0 = e^{-i(2\gamma + \arg(1 + \kappa_{\mathrm{EW}}))} \times (1 + \Delta), \qquad (1.50)$$

where Δ is theoretically bound ($\lesssim 0.05$) and κ_{EW} is:

$$\kappa_{\mathrm{EW}} = \frac{3}{2} \frac{C_+^{\mathrm{EW}}}{C_+} \left(1 + \frac{1 - \lambda^2}{\lambda^2 (\rho + i\eta)} + \mathcal{O}(\lambda^2) \right), \qquad (1.51)$$

with C_+^{EW} and C_+ being, respectively, the coefficients of the electroweak and normal QCD 4-quark operators in the effective theory. κ_{EW} is found to be an $\mathcal{O}(1)$ correction to the decay amplitude of the isospin 3/2 final state. Using available results on $B^0 \to K^+\pi^0\pi^-$ and $B^0 \to K_S^0\pi^+\pi^-$ Dalitz plot analyses the authors found that the value of the UT angle γ should be between 39° and 112° and placed the following CKM constraint:

$$\bar{\eta} = \tan\gamma[\bar{\rho} - a \pm b]. \qquad (1.52)$$

Here $a = 0.24$ is the electroweak penguin correction and $b = 0.03$ the error of the electroweak penguin model.

The uncertainty of the UT angle γ, obtained using the described method, is rather large compared to the result obtained using the $B^- \to D^0 K^-$ and $B^- \to \overline{D}^0 K^-$ analyses. The reason for this lies in large uncertainties of ϕ, $\bar{\phi}$ and $\Delta\phi$ angles. Therefore, more precise analyses of $B^0 \to K^+\pi^0\pi^-$ and $B^0 \to K_S^0\pi^+\pi^-$ decays are needed in order to improve the precision of the method, which justifies a Dalitz plot analysis of the $B^0 \to K_S^0\pi^+\pi^-$ decay on the larger data sample.

1.4   Three-body decays

1.4.1   Kinematics of three-body decays

In the case of a B meson decay to three scalar particles: $B \to a_1 + a_2 + a_3$, there are several kinematic constraints which reduce the number of independent variables needed to describe the process to only two. The usual choice is the two squared invariant masses $m_{ij}^2 = p_{ij}^2$, where $p_{ij} = p_i + p_j$, and p_i is the four-momentum of particle i.

In this case, the conservation law of four-momentum gives the following relation:

$$m_{12}^2 + m_{13}^2 + m_{23}^2 = m_B^2 + m_1^2 + m_2^2 + m_3^2, \qquad (1.53)$$

and in the B meson rest frame:

$$m_{ij}^2 = (p_B - p_k)^2 = m_B^2 + m_k^2 - 2m_B E_k$$

$$m_{ij}^2 = (p_i + p_j)^2 = m_i^2 + m_j^2 + 2E_i E_j - 2|\vec{p_i}||\vec{p_j}| \cos\theta_{ij}, \qquad (1.54)$$

where $k \neq i, j$, and θ_{ij} is the angle between $\vec{p_i}$ and $\vec{p_j}$. From the above equations it can be concluded that the energies of daughter particles depend only on the invariant masses of the pairs of daughter particles and also that the relative orientation of the daughter particles' momenta is fixed for known energies, lying in a plane in the B meson rest frame.

The Lorentz invariant phase space for such a decay can be written as:

$$
\begin{aligned}
dN = & \; \delta^4\left(p_B - \sum_{i=1}^{3} p_i\right) \prod_{i=1}^{3} \frac{d^3 p_i}{(2\pi)^3 2E_i} \\
\approx & \; \delta\left(m_B - \sum_{i=1}^{3} E_i\right) \frac{p_1^2 dp_1 p_2^2 dp_2}{2E_1 2E_2 2E_3} d\Omega_1 \Omega_{1-2}, \qquad (1.55)
\end{aligned}
$$

where m_B and p_B are the mass and momentum of the decaying particle respectively, p_i and E_i are the momenta and energies of the daughter particles, and Ω_1 and Ω_{1-2} are the solid angles for the direction of $\vec{p_1}$ and the direction

of $\vec{p_2}$ with respect to $\vec{p_1}$. When the decaying particle is a B meson, its scalar nature leads to a uniform distribution of the decay system, and therefore the direction of one daughter particle's momentum (say $\vec{p_1}$) can be fixed, which gives $\int d\Omega_1 = 4\pi$, and $\int d\Omega_{1-2} = 2\pi d\cos\theta_{12}$, where θ_{12} is the angle between $\vec{p_1}$ and $\vec{p_2}$. Using:

$$E_3 = \sqrt{p_3^2 + m_3^2} = \sqrt{p_1^2 + p_2^2 + 2p_1 p_2 \cos\theta_{12} + m_3^2}, \qquad (1.56)$$

equation Eq. (1.55) can be rewritten as:

$$dN \propto \quad \delta\left(m_B - E_1 - E_2 - \sqrt{p_1^2 + p_2^2 + 2p_1 p_2 \cos\theta_{12} + m_3^2}\right) \times$$
$$d\cos\theta_{12} \frac{p_1^2 dp_1 p_2^2 dp_2}{E_1 E_2 E_3}. \qquad (1.57)$$

Once integrated, this becomes:

$$dN \propto \frac{E_3}{p_1 p_2} \frac{p_1^2 dp_1 p_2^2 dp_2}{E_1 E_2 E_3} = \frac{p_1 dp_1}{E_1} \frac{p_2 dp_2}{E_2}. \qquad (1.58)$$

Finally, since $E_i dE_i = p_i dp_i$, and (from Eq. (1.54)) $dE_k = -dm_{ij}^2/m_B$:

$$dN \propto dE_1 dE_2 \propto dm_{12}^2 dm_{23}^2. \qquad (1.59)$$

Thus, the decay rate of a three-body decay is:

$$\Gamma = |\mathcal{M}| dN \propto |\mathcal{M}| dm_{12}^2 dm_{23}^2, \qquad (1.60)$$

where $|\mathcal{M}|$ is the matrix element for the decay, which holds all information about the decay's dynamics. From the above equation it can be seen that the dynamics of a three-body decay can be visualised by a scatter plot in any two of three m_{ij}^2 variables. Such a plot is often called a Dalitz plot [29]. If $|\mathcal{M}|$ is a constant, the Dalitz plot will have a uniform distribution as the decay proceeds according to phase space only. A distribution which is not uniform indicates a matrix element which has a kinematic dependence, such as an intermediate resonant decay. A resonance will appear as a narrow band in the Dalitz plane at the invariant mass of the resonance. An illustration

of a $B^0 \to K_S^0 \pi^+ \pi^-$ Dalitz plot, using Monte Carlo (MC) data, is shown in Figure 1.11. The kinematical boundaries for a Dalitz plot can be found using Eq. (1.54). For a given value of m_{jk}^2, the maximum of m_{ij}^2 will be reached when the particles i and j are flying back to back, and the minimum when they are at the rest in the ij centre of mass system. Using the same equation, one can find that the centre of the Dalitz plot will be populated with events where the final particles are distributed quite isotropically, while the events in which one of the particles in the final state flies back to back to the other two, populate the edges of the Dalitz plot. A Dalitz plot analysis models signal and backgrounds within the Dalitz plane, fitting for the amplitudes and phases of the various contributions to the signal. This technique correctly models the quantum mechanical interference between the signal contributions and as higher statistics become available it becomes the optimal method for three-body analyses. By measuring the magnitudes and phases of the resonant and nonresonant amplitudes, the analysis becomes sensitive to several CP violating parameters.

1.5   Parametrisation of the Dalitz Plot

Usually, Dalitz-plot amplitudes are parametrized using the isobar model [31, 32, 33], which models the total amplitude as a sum of amplitudes of the individual decay channels:

$$\mathcal{A}(m_{13}^2, m_{23}^2) = \sum_{j=1}^{N} c_j F_j(m_{13}^2, m_{23}^2) \qquad (1.61)$$

$$\overline{\mathcal{A}}(m_{13}^2, m_{23}^2) = \sum_{j=1}^{N} \overline{c}_j \overline{F}_j(m_{13}^2, m_{23}^2). \qquad (1.62)$$

Here $F_j(m_{13}^2, m_{23}^2)$ are the dynamical amplitudes described below and c_j are complex coefficients describing the relative magnitude and phase of the different decay channels. All the weak phase dependence is contained in c_j, and
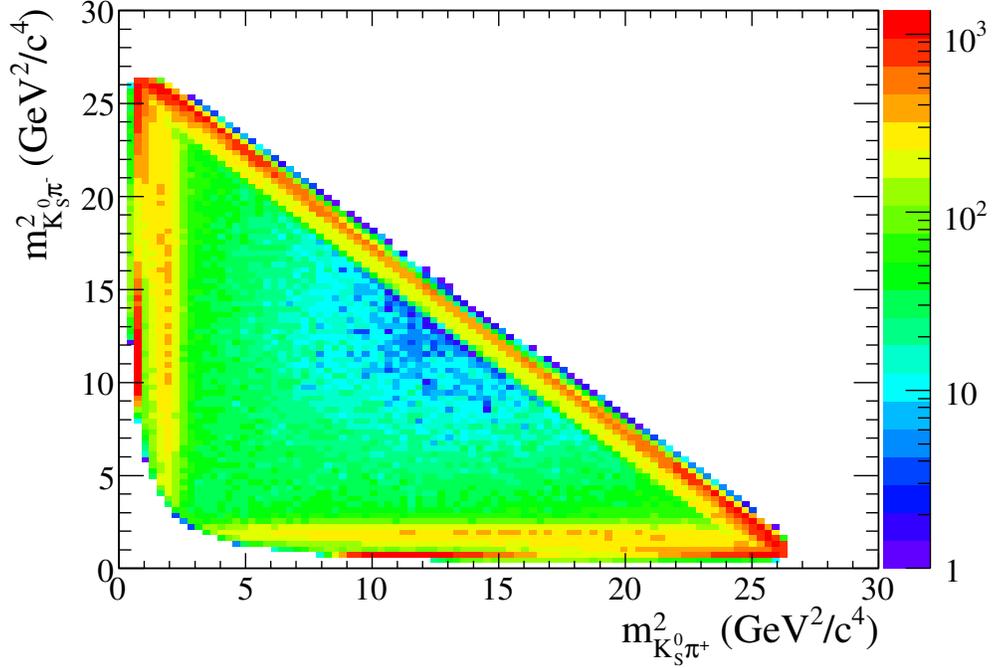
Figure 1.11: *Toy Monte Carlo simulation of $B^0 \rightarrow K^0_S \pi^+ \pi^-$. The resonances $f_0(980)$, $\rho^0(770)$, $K^*(892)$ and $K^*_0(1430)$ have been included, approximately in the proportions found by $\mathcal{B}$elle [30].*

$F_j(m^2_{13}, m^2_{23})$ contains strong dynamics only, therefore:

$$F_j(m^2_{13}, m^2_{23}) \quad = \quad \overline{F}_j(m^2_{13}, m^2_{23}) . \qquad (1.63)$$

1.5.1 Dynamical Amplitude

The resonance dynamics are contained within the F_j term, which is represented by the product of the invariant mass and angular distribution probabilities:

$$F_j(L, m^2_{13}, m^2_{23}) = R_j \times X^B_L \times X^{\text{res}}_L \times T^L_j, \qquad (1.64)$$

where:

- L is the orbital angular momentum of the resonance,

31

- R_j is the resonance mass term,

- X_L are barrier factors,

- T_j^L is the angular probability distribution.

The $F_j(m_{13}^2, m_{23}^2)$ are each normalised such that, over the whole Dalitz plot:

$$\int\int_{DP} \left| F_j(m_{13}^2, m_{23}^2) \right|^2 dm_{13}^2 dm_{23}^2 = 1. \tag{1.65}$$

1.5.2 Resonance mass term

The Breit-Wigner Lineshape

The most common formulation of the resonance mass term is the Breit-Wigner function [34, 35], the relativistic form of which is given below:

$$R_j(m) = \frac{1}{(m_r^2 - m_{ab}^2) - im_r\Gamma(m_{ab})}. \tag{1.66}$$

Here m_{ab} is the invariant mass of the pair of daughter particles produced in the decay $R \to ab$, and m_R and $\Gamma(m_{ab})$ are the resonance pole mass and mass-dependent resonance width, respectively. The mass-dependent width Γ in general depends on the resonance energy:

$$\Gamma(m_{ab}) = \Gamma_R \left(\frac{q}{q_R}\right)^{2L+1} \left(\frac{m_R}{m_{ab}}\right) X_L^2(|\vec{q}|R), \tag{1.67}$$

where q is the momentum of either of the resonance daughters in the rest frame of the resonance (the symbol q_R denotes the value of q when $m_{ab} = m_R$), and $X_L^2(|\vec{q}|r)$ is the Blatt-Weisskopf barrier factor (see below). A Breit-Wigner parametrization best describes isolated, non-overlapping resonances far from the threshold of additional decay channels. The proximity of a threshold to the resonance shape distorts the line shape from a simple Breit-Wigner. In that case the Flatté parametrisation is used.

The Flatté Lineshape

The scenario where another channel opens close to the resonance position is described by the Flatté formulation [36]. An example of this is the $f_0(980)$ resonance, which lies near the $K\bar{K}$ threshold (the mass of the $K\bar{K}$ system at rest is $\sim 990\,\mathrm{MeV}/c^2$). In such a case the proximity of the threshold has to be taken into account:

$$R_j(m) = \frac{1}{(m_R^2 - m^2) - im_R(\Gamma_{\pi\pi}(m) + \Gamma_{KK}(m))}, \tag{1.68}$$

with

$$\Gamma_{\pi\pi}(m) = g_\pi \left(\frac{1}{3}\sqrt{1 - 4m_{\pi^0}^2/m^2} + \frac{2}{3}\sqrt{1 - 4m_{\pi^\pm}^2/m^2} \right), \tag{1.69}$$

$$\Gamma_{KK}(m) = g_K \left(\frac{1}{2}\sqrt{1 - 4m_{K^\pm}^2/m^2} + \frac{1}{2}\sqrt{1 - 4m_{K^0}^2/m^2} \right), \tag{1.70}$$

where g_π and g_K are $\pi\bar{\pi}$ and $K\bar{K}$ coupling constants.

The LASS lineshape

The most poorly understood component of the $K\pi$ spectrum is that of the higher S-wave K^* resonances [37, 38]. The LASS experiment made measurements of $K\pi$ scattering and as part of this study produced a description of the S-wave that consists of the $K_0^*(1430)$ resonance together with an effective range nonresonant component. A detailed description of the LASS parametrisation of the higher S-wave K^* resonancescan be found in [39]. Here some general remarks will be presented. For fits to the LASS data, the $K\pi$ scattering amplitude is described using the following parametrization:

$$A = B\sin(\delta_B + \phi_B)e^{i(\delta_B + \phi_B)} + Re^{i\phi_R}e^{2i(\delta_B + \phi_B)}\sin\delta_R e^{i\delta_R}. \tag{1.71}$$

The first term represents a non-resonant contribution, while the second term represents a resonant component and B, ϕ_B, R and ϕ_R are constants, while the phases δ_B and δ_R depend on $K\pi$ mass.

The mass dependence of δ_B is described by means of an effective range parametrization:

$$\cot \delta_B = \frac{1}{aq} + \frac{1}{2rq},$$ (1.72)

where a denotes the scattering length, r the effective range and

$$q = \sqrt{\frac{(m_{K\pi}^2 - (m_K + m_\pi)^2)(m_{K\pi}^2 - (m_K - m_\pi)^2)}{4m_{K\pi}^2}}.$$

The mass dependence of δ_R is described by means of a Breit-Wigner parametrization of the form:

$$\cot \delta_R = \frac{m_0^2 - m_{K\pi}^2}{m_0 \Gamma(m_{K\pi})},$$ (1.73)

where m_0 is a resonance mass and $\Gamma(m_{K\pi})$ is energy-dependent total width for an S-wave Breit-Wigner. The LASS data indicated that the S-wave remains elastic up to $K\eta'$ threshold. Because of that $B = R = 1$ and $\phi_B = \phi_R = 0$, and the $K\pi$ scattering amplitude has a simpler form:

$$A = \sin(\delta_R + \delta_B)e^{i(\delta_R + \delta_B)}.$$ (1.74)

The above equation can be rewritten as following:

$$A = \frac{1}{\cot \Delta - i},$$ (1.75)

where Δ denotes the $I = 1/2$ (I - isospin) phase shift, so the invariant amplitude describing the $K\pi$ scattering process is:

$$\mathcal{M} \sim \frac{m_0}{q} A.$$ (1.76)

Using $m_0 \Gamma(m_{K\pi}) \sim q/m_{K\pi}$ (the 2-body phase space factor), for an S-wave resonance the invariant amplitude becomes:

$$\mathcal{M} \sim \frac{1}{m_0^2 - m_{K\pi}^2 - im_0 \Gamma(m_{K\pi})}.$$ (1.77)

The numerator has no $m_{K\pi}$-dependence since the coupling at each end of the propagator is S-wave, and hence there is no centrifugal barrier.

34

Modification of the LASS S-wave Amplitude to a Dalitz Analysis Context

In the context of B meson decay to $K\pi P$, where P is a recoil pseudo scalar, both ends of an S-wave propagator again involve an S-wave coupling, and so $\mathcal{M}$ should again contain just the propagator for an amplitude describing decay to an S-wave resonance. The LASS amplitude contains an effective range contribution in addition to the resonant part, therefore in the B decay context the more general expression:

$$\mathcal{M} \sim \frac{m_{K\pi}}{q}A, \tag{1.78}$$

$$A = \sin\delta_B e^{i\delta_B} + e^{2i\delta_B}\sin\delta_R e^{i\delta_R}, \tag{1.79}$$

should be used. Combining the above equations the following expression for the invariant amplitude of the $B \to K\pi P$ process can be written:

$$\mathcal{M} = \frac{m_{K\pi}}{q\cot\delta_B - iq} + e^{2i\delta_B}\frac{m_0\Gamma_0\frac{m_0}{qR}}{m_0^2 - m_{K\pi}^2 - im_{K\pi}\Gamma_0\frac{q}{m_0}\frac{m_{K\pi}}{qR}} \tag{1.80}$$

In the analysis of $B^0 \to K_S^0\pi^+\pi^-$ for the values of the parameters a and r (the scattering length and the effective range) the values measured by LASS are used [39]:

$$a = (2.07 \pm 0.10)\,(\mathrm{GeV}/c)^{-1},\, r = (3.32 \pm 0.34)\,(\mathrm{GeV}/c)^{-1}. \tag{1.81}$$

Non-Resonant Amplitudes

In addition to decays via intermediate resonances, as just described, there are so called nonresonant decays, ie. decays that are not associated with any resonant structure. It is seen in $B^0 \to K^+K^-K^0$ and $B^+ \to K^+K^+K^-$ analysis [40, 41] that such decays can account for a large fraction of events. The precise source and nature of these decays is not well understood. In the $B^0 \to K_S^0\pi^+\pi^-$ analysis a simple model of the nonresonant amplitude with constant magnitude and constant phase is used.

1.5.3 Angular Distribution

The distribution of events across the Dalitz plot decaying through a resonance depends on the spin of the resonance. In the Zemach tensor formalism [42, 43], the resonance angular distribution terms are given by:

$$L = 0 \quad : \quad T^{L=0} = 1, \tag{1.82}$$

$$L = 1 \quad : \quad T^{L=1} = -2\vec{p} \cdot \vec{q}, \tag{1.83}$$

$$L = 2 \quad : \quad T^{L=2} = \frac{4}{3} \left[3(\vec{p} \cdot \vec{q})^2 - (|\vec{p}||\vec{q}|)^2 \right]. \tag{1.84}$$

If the analysed resonant decay is $B \rightarrow Rc$, with $R \rightarrow ab$, $\vec{p}$ denotes the momentum of particle c in the R rest frame, and $\vec{q}$ the momentum of one of the particles produced in a decay of the resonance R in the resonance rest frame.

From Eq. (1.82) it can be seen that in the case of the spin 1 (vector) resonances there is a convention-dependent sign in the Zemach tensor. If the particle a is chosen to represent the resonance $R(\rightarrow ab)$ one has to keep that convention all the time, because switching to the particle b will change the sign of $T^{L=1}$. In the case of $B^0 \rightarrow K_S^0 \pi^+ \pi^-$ analysis this issue is slightly complicated. For resonances in $m_{K_S^0 \pi^+}$ or $m_{K_S^0 \pi^-}$ one can always choose the K_S^0, since one only gets B^0 decaying to resonances in $m_{K_S^0 \pi^+}$ and $\bar{B}^0$ to resonances in $m_{K_S^0 \pi^-}$. For resonances in $m_{\pi^+ \pi^-}$ one would like to choose the pion such that the same choice is maintained. However, in this case since both B^0 and $\bar{B}^0$ decay to $(\pi^+ \pi^-)_{\text{res}} K_S^0$ the flavour of the B meson can not be inferred from the resonance itself. One of the solutions for this problem is to use π^+ for the $B^0 \rightarrow (\pi^+ \pi^-)_{\text{res}} K_S^0$ decays and π^- for $\bar{B}^0 \rightarrow (\pi^+ \pi^-)_{\text{res}} K_S^0$. In that case, if the variables labelling the axes of the Dalitz plot are chosen to be $m_{K_S^0 \pi^+}$ and $m_{K_S^0 \pi^-}$ the Dalitz plot will be symmetric with respect to the diagonal in the absence of direct CP violation.

1.5.4　Blatt-Weisskopf Barrier Factors

For a decay of the resonance R into particles a and b, the probability of a particle a (or b) to escape the potential barrier of the resonance is usually called the Blatt-Weisskopf barrier factor (or the transmission coefficient) [44]. The Blatt-Weisskopf barrier factor is a function of a daughter particle momentum ($|\vec{q}|$), angular momentum (L) and the radius of the barrier (r). For angular momentum L, the form of the Blatt-Weisskopf barrier factor is the following:

$$B_{L=0}(z) = 1, \tag{1.85}$$

$$B_{L=1}(z) = \sqrt{\frac{1 + z_0^2}{1 + z^2}}, \tag{1.86}$$

$$B_{L=2}(z) = \sqrt{\frac{z_0^4 + 3z_0^2 + 9}{z^4 + 3z^2 + 9}}, \tag{1.87}$$

where $z = \left(|\vec{q}|r\right)^2$ and z_0 is the value that z takes when $\vec{q}$ is evaluated at the resonance pole mass. In the $B^0 \to K_S^0 \pi^+ \pi^-$ analysis for the radius of the barrier the value of 4 $\text{GeV}^{-1} \approx 0.8$ fm is taken. This value is chosen using experimental measurements of the radii of the barriers of K^* and ρ resonances [45, 37].

1.5.5　Isobar Coefficients

As mentioned inSection 1.5 the dynamical amplitudes, either resonant or non-resonant, are multiplied by complex coefficients (isobar coefficients) that describe the relative strengths of the components. A Dalitz plot analysis models signal and backgrounds within the Dalitz plane fitting for the amplitudes and phases of the various contributions to the signal. This means that the final results of such an analysis are values of the isobar coefficients.

There are several ways of parameterising the isobar coefficients. The most natural choice is to use polar coordinates. Polar coordinates have the advantage that the fitted parameters are the magnitude and phase, which are intuitive measures. However, since the magnitudes are positive definite quantities it

can lead to non-Gaussian errors in the region close to zero. This in turn can lead to fit bias. Because of that in the $B^0 \to K_S^0 \pi^+ \pi^-$ analysis the Cartesian coordinates parametrisation is used:

$$
\begin{aligned}
c_j &= (x_j + \Delta x_j) + i(y_j + \Delta y_j) & (1.88) \\
\overline{c}_j &= (x_j - \Delta x_j) + i(y_j - \Delta y_j) . & (1.89)
\end{aligned}
$$

In this case, one has 4 free parameters per one resonant term. In the terms of the isobar coefficients, for each resonance, the CP violating parameters defined in Eq. (1.41) can be written as:

$$
\begin{aligned}
\mathcal{S}^j &= 2\,\mathrm{Im}\left[c_j \overline{c}_j^* e^{-i\phi_{\mathrm{mix}}}\right] / \left(|c_j|^2 + |\overline{c}_j|^2\right) , & (1.90) \\
\mathcal{C}^j &= \left(|c_j|^2 - |\overline{c}_j|^2\right) / \left(|c_j|^2 + |\overline{c}_j|^2\right) , & (1.91)
\end{aligned}
$$

which in the Cartesian coordinates parametrisation become:

$$
\begin{aligned}
\mathcal{S}^j &= \frac{2(x_j \Delta y_j - y_j \Delta x_j)\cos\phi_{\mathrm{mix}} - \left(x_j^2 - \Delta x_j^2 + y_j^2 - \Delta y_j^2\right)\sin\phi_{\mathrm{mix}}}{\left(x_j^2 + \Delta x_j^2 + y_j^2 + \Delta y_j^2\right)} & (1.92) \\
\mathcal{C}^j &= 2(x_j \Delta x_j + y_j \Delta y_j) / \left(x_j^2 + \Delta x_j^2 + y_j^2 + \Delta y_j^2\right) . & (1.93)
\end{aligned}
$$

The parameters $\mathcal{S}^j$ and $\mathcal{C}^j$ are used to describe the CP eigenstate channels. For the flavour specific final states (ie a $K_S^0 \pi^\pm$ resonance plus $\pi^\mp$ in the case of the $B^0/\bar{B}^0 \to K_S^0 \pi^+ \pi^-$ decay) the parameter $\mathcal{A}_{CP}^j$ defined as $\mathcal{A}_{\mathrm{CP}}^j = -\mathcal{C}^j$ is used. From Eq. (1.92) and Eq. (1.93) it can be seen that if there is no CP violation in decay (ie. $\Delta x_j = \Delta y_j = 0$), $\mathcal{C}^j = 0$ and $\mathcal{S}^j = -\eta_{CP}\sin\phi_{\mathrm{mix}}$, as expected. Since the choice of normalisation, phase convention and amplitude formalism may not always be the same for different analyses, fit fractions are presented in addition to the isobar coefficients to allow a more meaningful comparison of results. The fit fraction is defined as the integral of a single decay amplitude squared divided by the coherent matrix element squared for

38

the complete Dalitz plot:

$$FF_j = \frac{\int \int_{DP} |c_j F_j(x,y)|^2 \, dxdy}{\int \int_{DP} \left|\sum_j c_j F_j(x,y)\right|^2 \, dxdy}. \qquad (1.94)$$

$$\overline{FF}_j = \frac{\int \int_{DP} |\bar{c}_j \overline{F}_j(x,y)|^2 \, dxdy}{\int \int_{DP} \left|\sum_j \bar{c}_j \overline{F}_j(x,y)\right|^2 \, dxdy}.$$

Here, $\overline{FF}_j$ is the fit fraction of the conjugate amplitude.

The Square Dalitz Plot

Instead of using squared invariant masses of pairs of daughter particles as the generalized coordinates to describe a 3-body decay, very often the square Dalitz plot coordinates are used [46]. In the case of the $B^0 \rightarrow K_S^0 \pi^+ \pi^-$ decay they are defined as:

$$
\begin{aligned}
m' &\equiv \frac{1}{\pi} \arccos\left(2\frac{m_{\pi^+\pi^-} - m_{\pi^+\pi^-}^{min}}{m_{\pi^+\pi^-}^{max} - m_{\pi^+\pi^-}^{min}} - 1\right), &(1.95)\\
\theta' &\equiv \frac{1}{\pi}\theta_{\pi^+\pi^-},
\end{aligned}
$$

where $m_{\pi^+\pi^-}$ is the invariant mass of the two pion candidates, $m_{\pi^+\pi^-}^{max} = m_{B^0} - m_{K_S^0}$ and $m_{\pi^+\pi^-}^{min} = 2m_\pi$ are the boundaries of $m_{\pi^+\pi^-}$ and $\theta_{\pi^+\pi^-}$ is the angle between the π^+ and the negative B momentum in the $\pi^+\pi^-$ rest frame. Using the square Dalitz plot instead of the classical Dalitz plot, resolves a problem related to appropriate binning of the histograms used to describe background distributions. Since decays of the B meson proceed mostly through low mass resonances, the most populated areas of the classical Dalitz plot are those close to the edges. Also, the combinatoric nature of background means that their density also peaks around the edges. In such a case, the ideal binning of histograms describing the Dalitz plot distributions is fine binning around the edges, and coarse binning around the centre. Additionally, the shapes of most of the classical Dalitz plots are such that the bins on the edges of the plots contain both kinematically allowed and kinematically forbidden areas.

Using the square Dalitz plot solves both problems. The effect of the transformation of the classical Dalitz plot into the square Dalitz plot is a magnification of the areas of interest, and since both m' and θ' have validity ranges between 0 and 1, the problem of having bins which partially cover the kinematically forbidden areas is avoided. Figure 1.12 shows the conventional and the square Dalitz plots for toy Monte Carlo events.

Because of the explained advantages, in this analysis of the $B^0 \rightarrow K_S^0 \pi^+ \pi^-$ decay, the square Dalitz plots have been used.
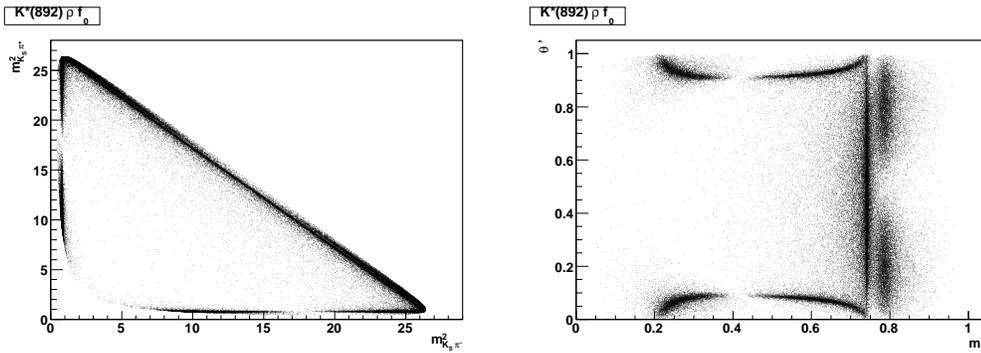
Figure 1.12: *Conventional (left) and square (right) $B^0 \rightarrow K_S^0 \pi^+ \pi^-$ Dalitz plots obtained from toy Monte Carlo without detector simulation. The generated model includes $K^*(892)$, $\rho^0(770)$ and $f_0(980)$ resonances only.*

Chapter 2

BABAR and PEP-II

In order to measure CP asymmetries in B mesons one has to be able to determine the flavour (i.e. B^0, $\overline{B}^0$, B^+ or B^-) of the decaying meson and compare the decay rates of opposite flavours. Detection of charged B mesons is relatively straightforward, but the real challenge is to determine the flavour of neutral B mesons. One of methods is to use the pairs of $B^0\overline{B}^0$ mesons produced in an entangled quantum mechanical state, one of them decaying to the channel of interest, and the other one to a final state that uniquely determines its flavour. The entanglement implies that, when one of the B mesons decays in a flavour-dependent state, the flavour of the other B meson can be deduced to be opposite at that exact same instant.

An additional experimental challenge for measurements of CP asymmetries in B mesons is their short lifetime ($\tau_B \sim 1.5$ ps). In order to extend the distances which B mesons travel in a detector into the measurable range, the idea of building an *asymmetric e^+e^-* collider in which any produced particle would move in the laboratory frame with a relativistic boost, was suggested [22].

These requirements drove the design of the *BABAR* detector [47] and the PEP-II [48] accelerator.

2.1   The PEP-II accelerator

The PEP-II B Factory [48] is a high luminosity[1] ($L \geq 3 \times 10^{33} \mathrm{cm}^{-2} \mathrm{s}^{-1}$) e^+e^- collider at the Stanford Linear Accelerator Center (SLAC), that uses SLAC's three-kilometre linear accelerator complex as the injector. It is designed to operate at the centre-of-mass (CM) energy of 10.58 GeV, on the $\Upsilon(4S)$ resonance. At this energy the cross section for $b\bar{b}$ ($\Upsilon(4S)$) production is approximately 1 nb, while those for continuum $q\bar{q}$ ($q = u,\ d,\ c,\ s$) and τ production are 3.4 nb and 0.9 nb respectively. The main final states of e^+e^- collisions at the $\Upsilon(4S)$ resonance, together with their cross sections, are listed in Table 2.1 [22].

$e^+e^- \rightarrow$	Cross Section (nb)
$b\bar{b}$	1.05
$c\bar{c}$	1.30
$s\bar{s}$	0.35
$u\bar{u}$	1.39
$d\bar{d}$	0.35
$\tau^+\tau^-$	0.94
$\mu^+\mu^-$	1.16
e^+e^-	~ 40

Table 2.1: *Some final states of e^+e^- collisions at the energy of 10.58 GeV.*

The $\Upsilon(4S)$ resonance decays almost exclusively into a $B^0\bar{B}^0$ or a B^+B^- pair with approximately equal probabilities. Since the threshold for $B\bar{B}$ production is just below the $\Upsilon(4S)$ energy, the produced B mesons are almost at rest in

---

[1]The luminosity (L) of the machine depends on several parameters:

$$L = \frac{n f N_1 N_2}{A}, \tag{2.1}$$

where n is the number of bunches in a ring, f is the bunch crossing frequency, $N_{1,2}$ are the number of particles in each bunch, and A is their overlap section.

the CM frame.

The PEP-II accelerator was designed to collide electron and positron beams with energies of 9.0 GeV and 3.1 GeV, respectively. The asymmetry in the energies of the electron and the positron beams provides a Lorentz boost of the $\Upsilon(4S)$ resonance of $\beta\gamma = 0.56$ in the laboratory frame. The asymmetry of the machine was motivated by the need to separate the decay vertices of the two B mesons, which is crucial for time-dependent CP asymmetry determination. The boost allows the separation and reconstruction of the decay vertices of both B mesons, the determination of their relative decay length Δz_{CM}, the difference of their decaying times and thus the measurement of time dependent asymmetries.

During the PEP-II running time (October 1999 - April 2008) around 82% of the data was collected at the energy of the $\Upsilon(4S)$ resonance (so called on-peak data), 10% at an energy 40 MeV below the $\Upsilon(4S)$ resonance (off-peak data) in order to allow studies of background from continuum events, while the remaining 8% was collected at the $\Upsilon(3S)$ and $\Upsilon(2S)$ resonances. The distribution of the integrated luminosity delivered by PEP-II and collected by BABAR during its period of running is shown in Figure 2.1.

Figure 2.2 shows the beam interaction region (IR). Electron and positron beams have to be brought into focus for collisions just before the interaction point (IP) and separated directly afterwards, to avoid secondary collisions. At BABAR the collisions are made with no crossing angle. To focus the beams a set of quadrupole magnets (QD and QF) is used. The QD4 and QF5 magnets are used for focusing the high energy electron beam, whilst QF2 is responsible for focusing the lower energy positron beam. The QD1 quadrupole is the final focus for both the electron and positron beams. A strong dipole (B1) in close proximity to the IP is used for bringing the beams together and separating them after collision.

BaBar
Run 1-7
PEP II Delivered Luminosity: 553.48/fb
BaBar Recorded Luminosity: 531.43/fb
BaBar Recorded Y(4s): 432.89/fb
BaBar Recorded Y(3s): 30.23/fb
BaBar Recorded Y(2s): 14.45/fb
Off Peak Luminosity: 53.85/fb

Delivered Luminosity
Recorded Luminosity
Recorded Luminosity Y(4s)
Recorded Luminosity Y(3s)
Recorded Luminosity Y(2s)
Off Peak
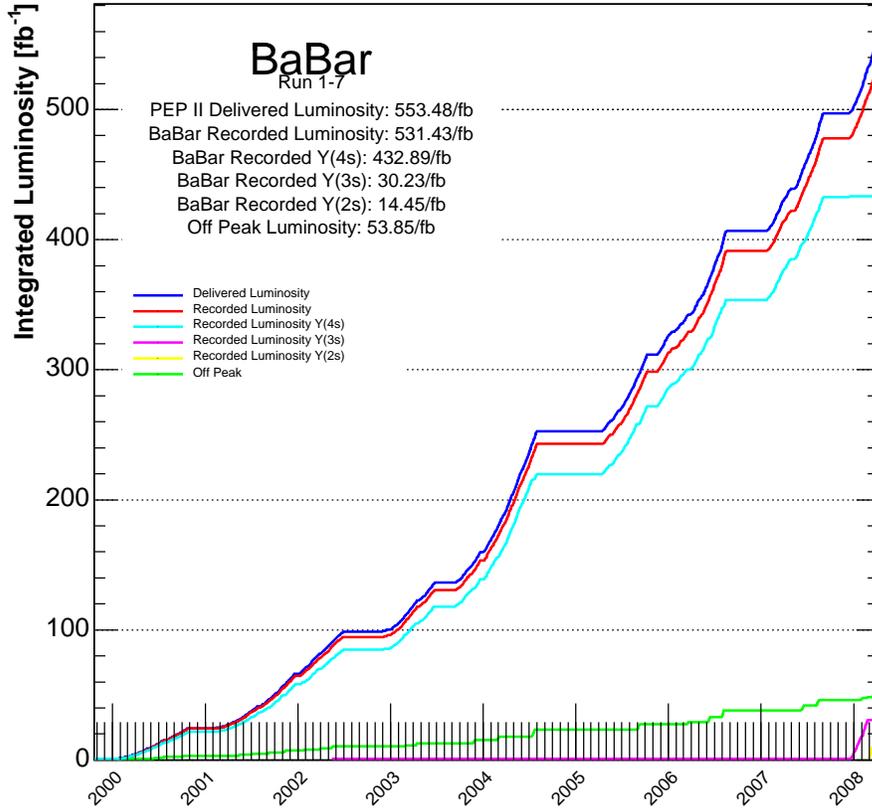
Figure 2.1: *Plot showing the integrated luminosity as delivered by PEP-II (blue), total luminosity recorded by* BABAR *(red) and* BABAR *recorded luminosity at* $\Upsilon(4S)$, $\Upsilon(3S)$ *and* $\Upsilon(2S)$ *resonances (cyan, magenta and yellow respectively), as well as off-peak luminosity.*

2.2 The *BABAR* detector

The very small branching ratios of B meson decays to CP eigenstates, typically of order 10^{-4}, the need for full reconstruction of final states with two or more charged particles and several neutral pions, plus the need to determine the flavour (tag) of the second neutral B meson, place strict requirements on the *BABAR* detector. Its asymmetrical design (the centre of the *BABAR* detector

44
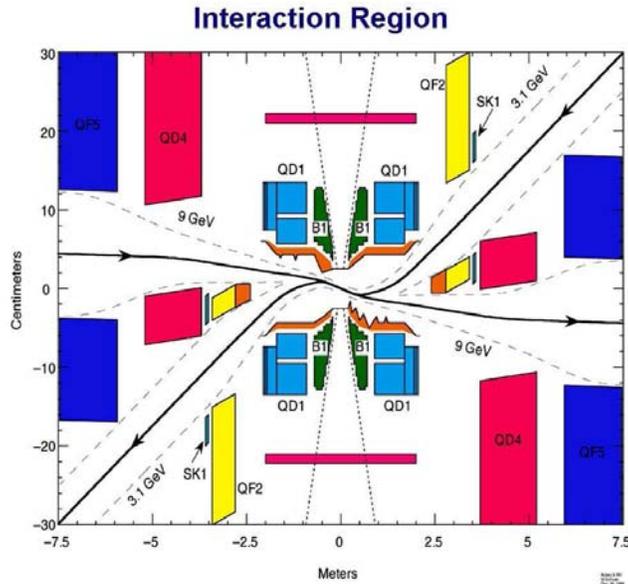
Figure 2.2: *Schematic view of the interaction region. The components labelled QD and QF are focusing quadrupoles, and those labelled B1 are dipoles used to separate the beams after collision.*

is displaced by 37 cm from the interaction point) is a consequence of the asymmetrical collider and the need for uniform acceptance in the CM frame. In order to provide measurements of CP asymmetries and rare B meson decays, the following requirements needed to be met:

- A large and uniform acceptance down to small polar angles relative to the boost direction;

- Excellent reconstruction efficiency for charged particles down to 60 MeV and for photons to 20 MeV;

- Very good momentum resolution to separate small signals from background;

- Excellent energy and angular resolution for the detection of photons from π^0 and η^0 decays, and from radiative decays in the range from 20 MeV

45

to 4 GeV;

- Very good vertex resolution, both transverse and parallel to the beam direction;

- Efficient electron and muon identification, with low misidentification probabilities for hadrons (this feature is crucial for tagging the B flavour);

- Efficient and accurate identification of hadrons over a wide range of momenta for B flavour tagging, and for the reconstruction of exclusive states;

- A flexible and selective trigger system;

- Low-noise electronics and a reliable, high bandwidth data-acquisition and control system;

- Detailed monitoring and automated calibration;

- An on-line computing and network system that can control, process and store the high volume of data;

- Detector components that can tolerate significant radiation doses and operate reliably under high background conditions.

The final design of the BABAR detector is illustrated in Figure 2.3. It consists of five sub-detectors: the silicon vertex tracker (SVT), the drift chamber (DCH), the detector of internally reflected Čerenkov radiation (DIRC), the electromagnetic calorimeter (EMC) and the instrumented flux return (IFR). The first four sub-detectors are enclosed in the 1.5 T magnetic field, created by a superconducting magnetic coil. A conventional right-handed coordinate system is defined: the $z-$axis coincides with the principal axis of the DCH and points in the direction of the electron beam, while the $y-$axis points upward. The polar angle coverage extends down to 0.35 rad in the forward direction and to $(\pi-0.4)$ rad in the backward direction. These limits are determined by

the permanent dipole and quadrupole magnets of PEP-II. In order to improve the coverage of the forward region, the whole detector is offset relative to the interaction point by 37 cm in the forward direction.

In the next few sections the individual detector components will be described in more details.

2.2.1 Tracking System

The charged particles detection and track parameters determination system consists of two components: the Silicon Vertex Tracker and the Drift Chamber. The angles and positions measured by the SVT are used for determination of the B meson decay vertices, whereas the track curvature from the DCH is used to detect particles' momenta. Tracks reconstructed in the SVT and DCH are extrapolated to the other detector components (DIRC, EMC and IFR). Since the average momentum of charged particles is less than 1 GeV, the precision of the measured track parameters is mostly affected by multiple Coulomb scattering in the detector material. Thus special attention has been devoted to the components' design in order to limit the overall amount of active material in the tracking region.

Silicon Vertex Tracker

The Silicon Vertex Tracker provides a precise reconstruction of charged particle trajectories and decay vertices as close as possible to the interaction point. It is designed to make precise measurements of the z position of tracks in order to measure the separation of the two B decay vertices, which is essential for time-dependent CP violation studies. Various Monte Carlo studies [49] have shown that the resolution required for such measurements is $\approx 80\,\mu$m. An additional role of the SVT is tracking low transverse momenta particles ($p_T < 120\,$MeV), which can not be reliably detected by the DCH. This is particularly important for the reconstruction of slow pions and D mesons coming from D^* decays, since these are used for B meson tagging. This places

47
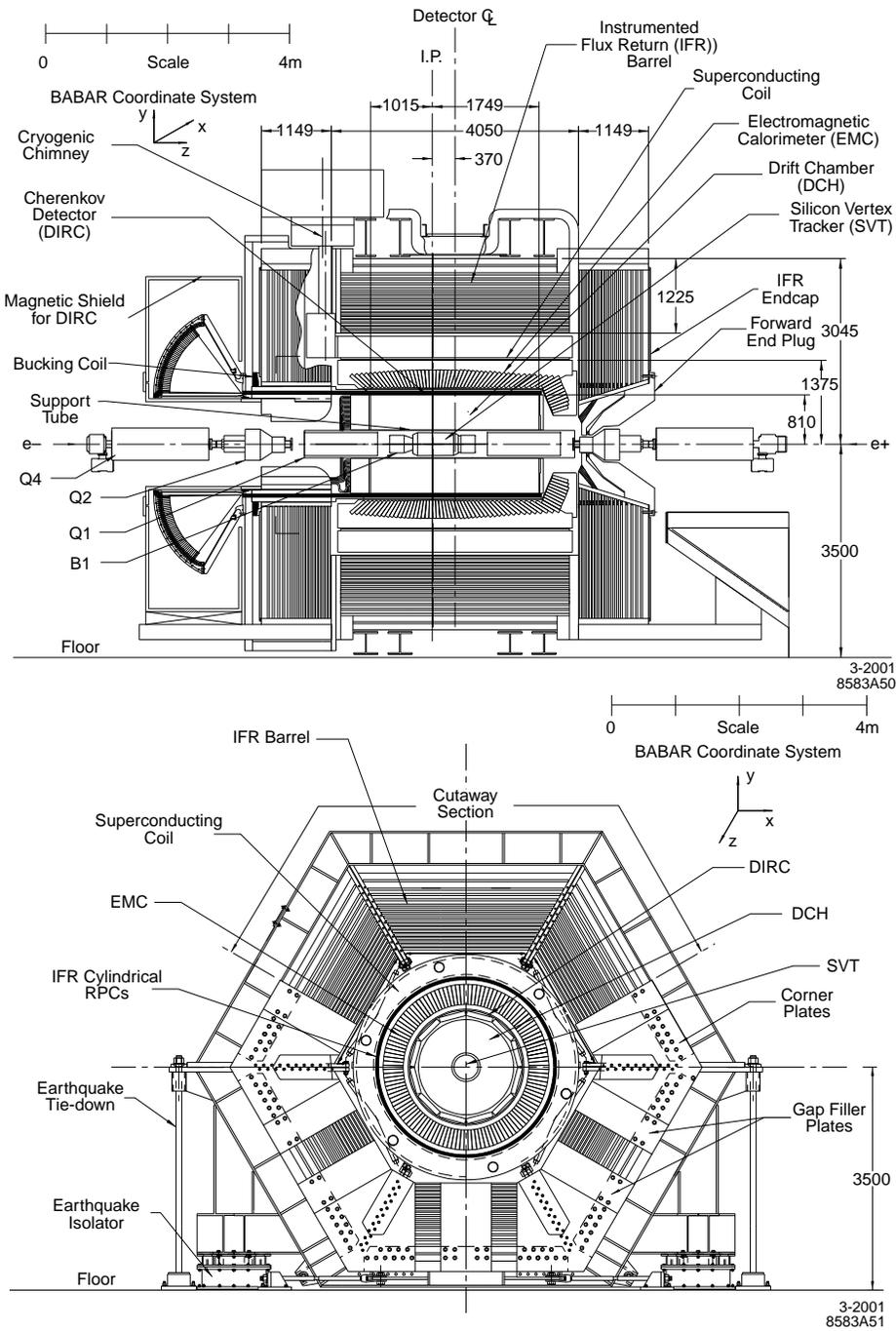
Figure 2.3: *Longitudinal (top) and end view (bottom) of the BABAR detector.*

the requirement of a resolution of $\approx 100 \, \mu$m in the x–y plane. Finally, the SVT is used in particle identification, by measuring the rate of energy loss,

and giving the best determination of the polar angle of high momentum tracks. The SVT (a schematic view of which is given in Figure 2.4) is located inside the support tube and was designed taking into account both the physical requirements and constraints imposed by the PEP-II interaction region. The latter limits the detector angular acceptance to 350 mrad in the forward direction and 520 mrad in the backward direction. The SVT consists of five concentric cylindrical layers of double-sided silicon strip detectors. Each layer is divided in azimuth into modules. The inner three layers are made of 6 modules each, while the outer layers have 16 and 18 modules respectively. The silicon strip detectors in layers 4 and 5 are arch-shaped in order to reduce the amount of active material. The role of the inner SVT layers is precise vertex reconstruction, while measurements from the outer layers are used for matching tracks to those found by the DCH. In total there are 340 silicon detectors covering an area of 1 m^2 and about 150×10^3 readout channels.

Drift Chamber

The Drift Chamber is the main tracking device in the *BABAR* detector. It supplies high precision descriptions of charged particles' momenta and angles through measurements of track curvature inside a 1.5 T magnetic field. It also contributes to particle identification by measuring the energy loss due to ionisation (dE/dx). The DCH is designed to achieve a resolution of $\sigma_{p_T}/p_T < 0.3\%$, so that reconstruction of B and D mesons will be possible, and a spatial resolution of 140 μm. Also, in order to reconstruct the vertices of long lived particles (such as K_S meson) the uncertainty of the longitudinal position measurement should not be larger than 1 mm.

A schematic view of the DCH is shown in Figure 2.5. It is a compact, 280 cm long cylinder with an inner radius of 23.6 cm and outer radius of 80.9 cm. As the active gas a mixture of helium and isobutane, with a small amount of water vapour is used. The DCH is formed of 40 layers of hexagonal drift cells, with each 4 layers grouped into a superlayer. Every cell is formed of a sense

Beam Pipe 27.8mm radius

Layer 5a

Layer 5b

Layer 4b

Layer 4a

Layer 3

Layer 2

Layer 1

580 mm

Space Frame

Bkwd. support cone

520 mrad

Fwd. support cone

350 mrad

e^-

e^+

Front end electronics

Beam Pipe
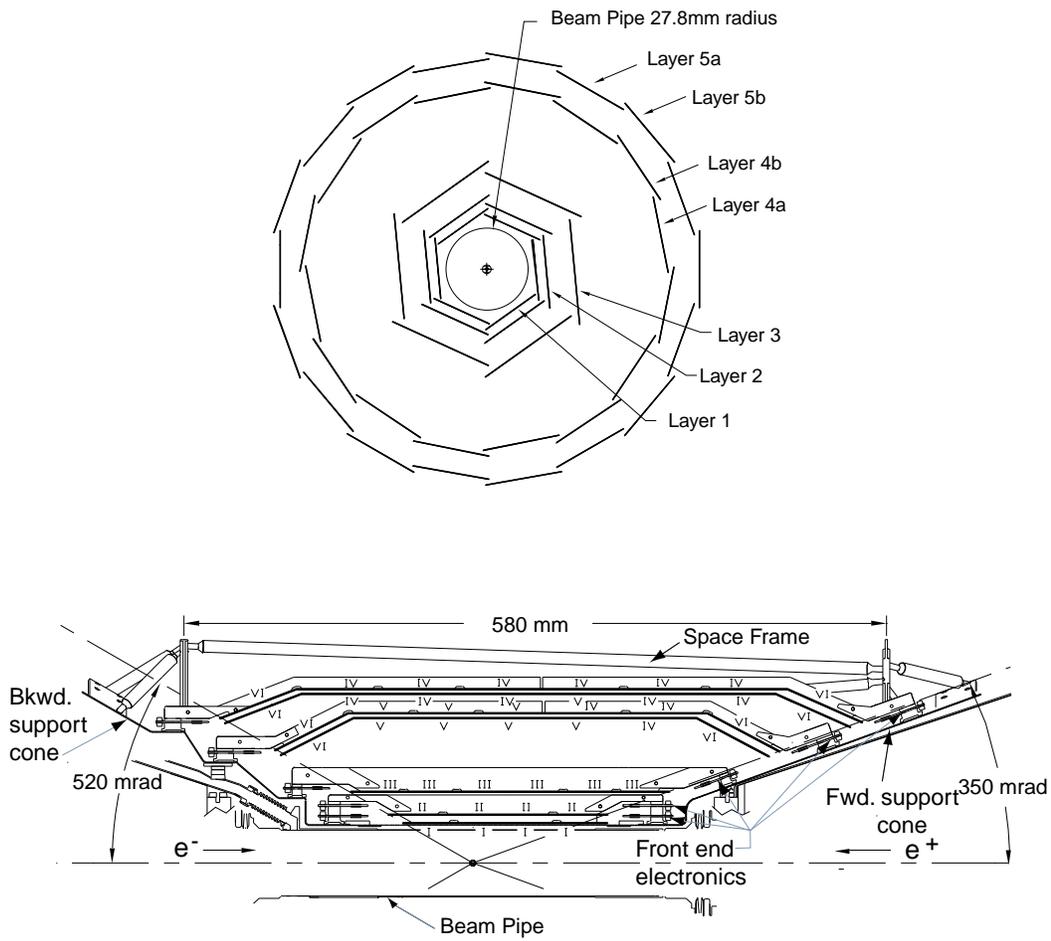
Figure 2.4: *End (top) and side (bottom) views of the Silicon Vertex Tracker.*

wire placed in the centre of the cell, held at a high voltage (1930 V), and 6 grounded, field wires.
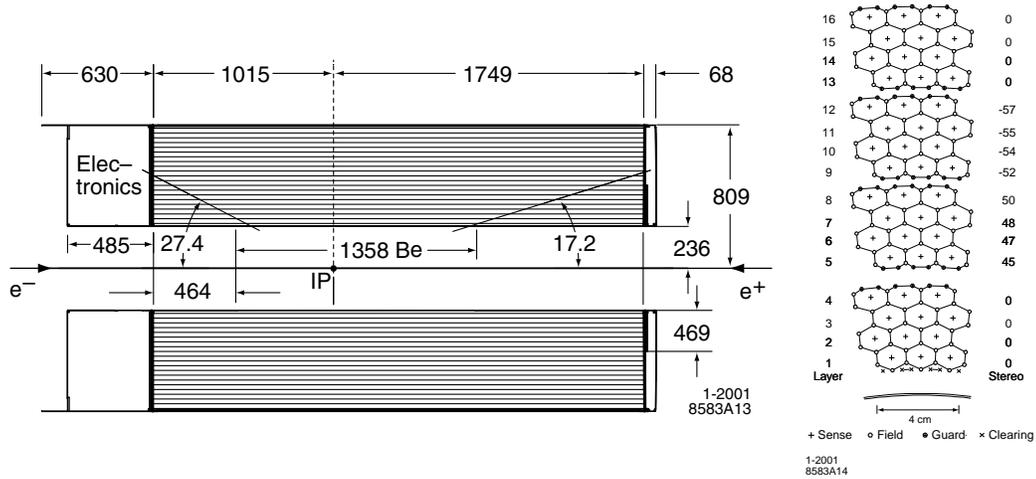
Figure 2.5: *Side view of the drift chamber (left) and cell layout in first four superlayers (right). The angle in* mrad *of the stereo layers with the z axis is written on the right of each layer.*

Each sequential layer is staggered by half a cell as shown in Figure 2.5, which permits left-right ambiguities to be resolved within a superlayer even if one out of four signals is missing, as well as allowing local segment finding. Six out of the ten superlayers are orientated at a small angle to the z-axis in order to permit longitudinal position calculation.

The readout electronics are mounted on the backward end-plate, minimising in this way the amount of material in the forward direction and thus preventing performance degradation for the outer *BABAR* detector components. Since momentum resolution is limited by multiple scattering in the inner cylinder, the DCH is built using light materials: low-mass wires and a helium-based gas mixture.

Detector of Internally Reflected Čerenkov Light

Above ~ 700 MeV the dE/dx information from DCH does not allow pions and kaons to be distinguished (see Figure 2.6). For this purpose *BABAR* uses
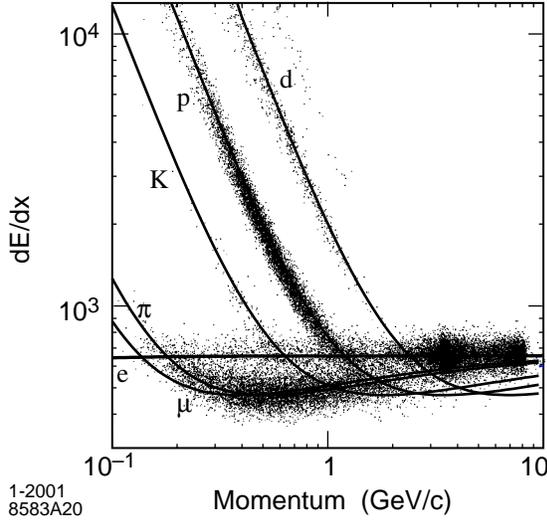
Figure 2.6: dE/dx measurements in the DCH shown as a function of track momentum. The overlaid curves are Bethe–Bloch predictions calculated from control samples of each of the labelled particle types [47].

the Detector of Internally Reflected Čerenkov light. It was designed to be able to provide π/K separation of $\sim 3\sigma$ or greater for all tracks from B meson decays, which reach momenta up to $4.2\,\mathrm{GeV}/c$. For muons, the DIRC must complement the IFR, whose effectiveness falls for momenta below $750\,\mathrm{MeV}/c$. Čerenkov light emission is widely used in particle detectors' technology. A charged particle traversing a medium with a velocity v greater than the speed of light in that medium ($v/c = \beta \geq 1/n$; n is the medium refraction index and c is the velocity of light in the vacuum) emits electromagnetic radiation (called Čerenkov light). The angle between the emitted photon and the track direction is determined by the velocity of the particle with the relation:

$$\cos\theta_c = 1/n\beta, \tag{2.2}$$

In this way, the measurement of θ_c determines β and knowing the particle's momentum (measured in the DCH) the mass of the particle can be obtained. The DIRC is placed in front of the electromagnetic calorimeter. In order to minimise the impact on the energy resolution, it has been designed to be
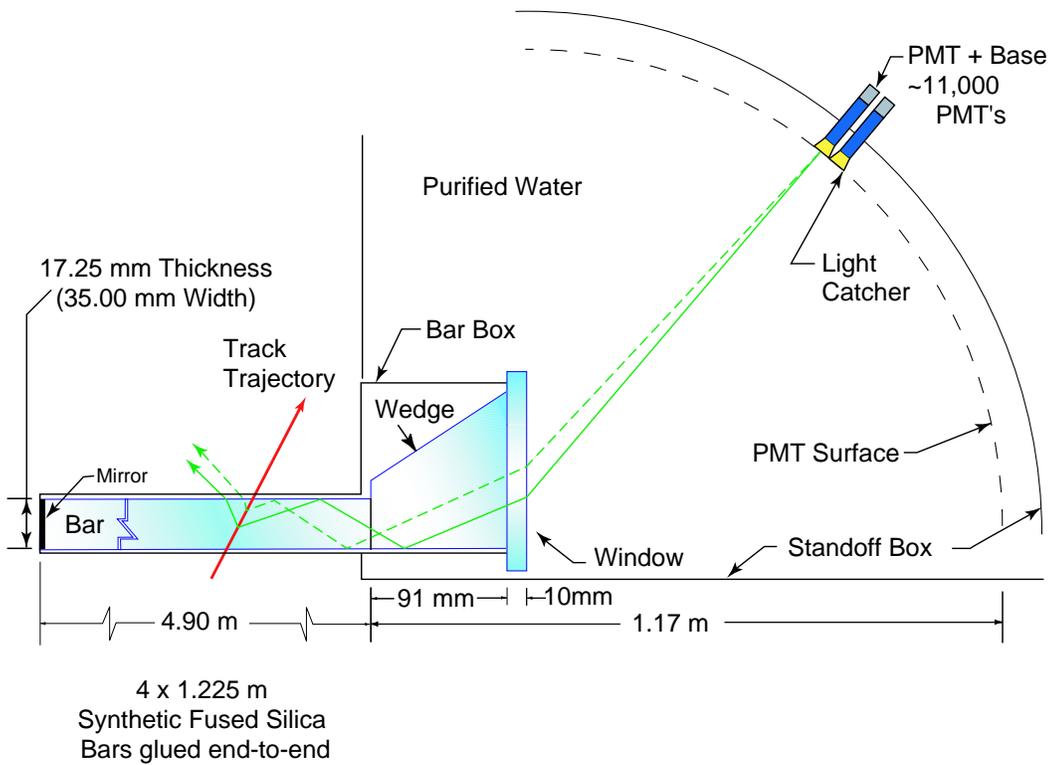
Figure 2.7: *Diagram illustrating the operating principles of the DIRC.*

thin and uniform in terms of radiation lengths. Figure 2.7 shows a schematic view of the DIRC geometry and basic principles of Čerenkov light production, transport and image reconstruction. Charged particles, exiting from the DCH, cross a matrix of 144 thin quartz bars, arranged longitudinally to form a 12-sided polygonal barrel. These 12 modules (bar-boxes) are placed with a mirror in the forward region and with a semi-toroidal water tank in the backward side. Photons emitted by particles above the Čerenkov threshold are trapped inside the bars due to the total reflection mechanism, which preserves angular information, and finally enter the water tank that optically couples them with the photomultiplier matrix. The photomultiplier tubes (PMTs) are placed on a semi-toroidal surface with an inner radius of 1.2 m and an outer radius of 3 m.

The DIRC is intrinsically a three-dimensional imaging device, giving the po-

sition and arrival time of the PMT signals. The three-dimensional vector pointing from the center of the bar end to the center of the PMT is computed, and then extrapolated into the radiator bar in order to extract the Čerenkov angle.

The angle and time resolution of the DIRC are calibrated using dimuon events. The Čerenkov angle resolution for a track is 2.5 mrad, giving separation of over 4σ at $3\,\mathrm{GeV}/c$.

2.2.2 Electromagnetic Calorimeter

Many of the B decays used to study CP violation have at least one neutral pion in the final state and have small branching ratios. Thus, an electromagnetic calorimeter with high efficiency for detection of low energy photons along with good energy and angular resolution is required to accurately reconstruct these final states and improve their signal-to-background ratios. Additionally the EMC should be efficient in identifying electrons.

A schematic view of the BABAR electromagnetic calorimeter is shown in Figure 2.8. It is built as a finely segmented array of 6580 thallium-doped cesium iodide (CsI(Tl)) crystals (with Molière radius of 3.8 cm) and covers the polar angle region from 15.8° to 141.8°. The crystal size varies from 16 radiation lengths in the backward direction to 17.5 radiation lengths in the forward endcap, since these crystals receive impacts from the more energetic Lorentz-boosted particles. Their exposed area is $\sim 5\,\mathrm{cm}^2$, so a typical electromagnetic shower will spread over several crystals.

The photon energy resolution of the EMC is found to be a quadratic sum of an energy dependent and a constant term:

$$\frac{\sigma_E}{E} = \frac{(2.32 \pm 0.30)\%}{E^{1/4}} \oplus (1.85 \pm 0.12)\%. \tag{2.3}$$

where the energy E is measured in GeV. The first term in the sum is dominant at low energies and arises primarily from fluctuations in photon statistics, noise of the photon detectors and electronics, or from noise due to the beam-

Figure 2.8: *A longitudinal cross section of the EMC (only the top half is shown) indicating the arrangement of the 56 crystal rings. The detector is axially symmetric around the z-axis. All dimensions are given in mm.*

generated background. The second term dominates at energies above 1 GeV and arises from non-uniformity in light collection, from leakage or absorption in the material between and in front of the crystals and from uncertainties in the calibration.

The photon angular resolution is determined by the transverse crystal size and the distance from the interaction point. It can be empirically parameterized as a sum of an energy dependent and a constant term consistent with zero within 4%:

$$\sigma_\theta = \sigma_\phi = [\frac{(3.87 \pm 0.07)\%}{\sqrt{E(GeV)}} + (0.00 \pm 0.04)]\,\mathrm{mrad}. \qquad (2.4)$$

The design of the *BABAR* EMC allows detection of electromagnetic showers with excellent energy and angular resolution in the range from 20 MeV (for photons from decays of slow π^0 or η^0 mesons) to 4 GeV (for photons and electrons from QED processes).

2.2.3 The Instrumented Flux Return

High efficiency and good purity muon detection is crucial for flavour tagging of B mesons via semileptonic decays, for reconstruction of vector mesons (like J/ψ) and for the study of semileptonic and rare decays involving leptons from B and D mesons and τ leptons. For this purpose, the muon subdetector needs to have a large solid angle coverage, good efficiency and high background rejection for muons down to momenta around $1\,\text{GeV}$.

The outer part of the *BABAR* detector is built of layers of steel plates. The main purpose of this iron structure is magnetic field shielding and support for the rest of the detector. The detector function is performed by equipping the gaps between steel layers with resistive plate chambers (RPCs), so that the whole structure acts as a muon detector and a primitive hadron calorimeter. Two additional cylindrical RPCs are placed between the EMC and the magnet to detect particles leaving the EMC and to link any EMC clusters to IFR energy deposits. A schematic view of the *BABAR* IFR and the design of the RPC are shown in Figure 2.9. The resistive plate chambers consist of two
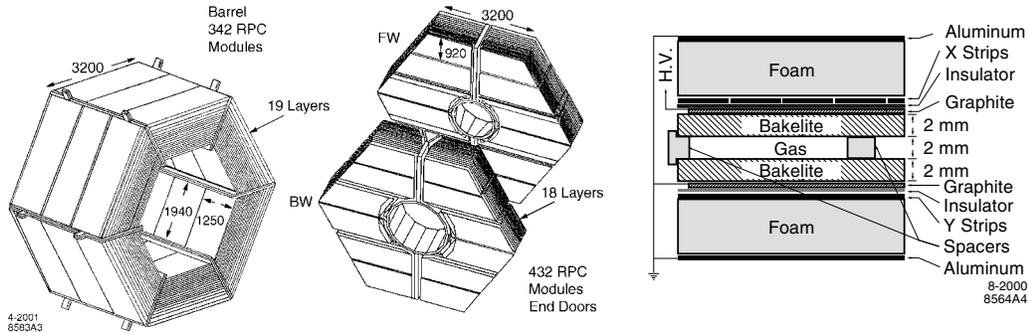
Figure 2.9: *Overview of the IFR (left) and design of the RPC (right).*

graphite electrodes separated by two 2 mm thick sheets of bakelite. The gap between these is filled with a mixture of gases: argon, chlorofluorocarbon (freon) and isobutane. Readout strips are located next to the graphite and are placed orthogonally, providing three-dimensional positional information when combined with the distance of the RPC to the interaction point. The whole

system works as a capacitor (one of the graphite electrodes is grounded and the other set to 8 kV voltage). The passage of a charged particle or a hadronic shower induce temporary changes in the charge accumulated at each electrode. Hits from different layers in coincidence with an event are grouped into a charged cluster if they can be associated to a track detected in the SVT and the DCH. The track is extrapolated to the IFR taking into account the non-uniform magnetic field, the multiple scattering and the average energy loss. Then the projected intersections with the RPC planes are computed, and finally all the hits within a predefined distance from the predicted intersection are associated to the track.

Studies of the efficiency of muon detection, performed during BABAR's first year of running, showed that for a muon efficiency of 90%, pion misidentification is at the level of 8%. Also, studies of the angular resolution and efficiency of the detection of neutral hadrons showed efficiencies between 20 and 40%, and angular resolutions around 60 mrad for K_L^0 mesons that did not interact in the EMC. Over the course of Run 1 it was seen that the muon efficiency was degrading rapidly in many RPCs, so the RPCs in the endcaps were replaced by new RPCs built with more stringent quality constraints and the barrel RPCs were substituted by limited streamer tubes.

Limited Streamer Tubes

A conducting wire with a 100 μm diameter, playing the role of the anode, is placed in a long grounded cell (the tube). The volume between them is filled with a gas that is ionized with the passage of a charged particle, which alters the charge distribution in the cylindrical capacitor. The signal is then read either by external strips attached to both sides, or from the wires directly. In Figure 2.10 a photograph of an limited streamer tube is shown. The efficiency of the LSTs is monitored using dimuon events and cosmic rays. The averaged value of the efficiency is around 90%, without any noticeable degradation over time.
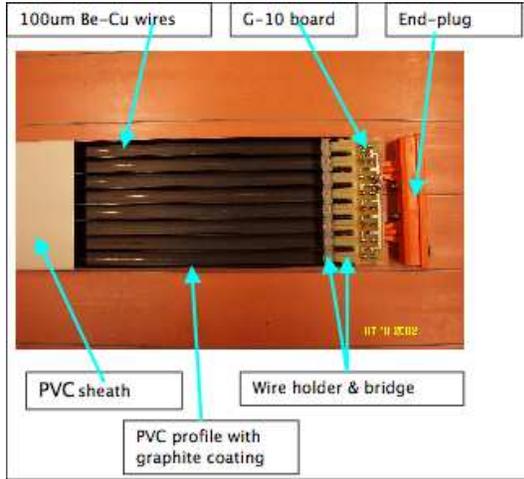
Figure 2.10: *An LST tube with the top cover pulled back to reveal the major components.*

2.2.4   Trigger System

The *BABAR* trigger system consists of two independent stages: the Level 1 (LT1) trigger, implemented in hardware, and the Level 3 (LT3) in software.

The LT1 trigger interprets incoming detector signals and recognises and removes beam-induced background, Bhabha ($e^+e^- \rightarrow e^+e^-$) and cosmic rays to a level acceptable for the subsequent stage. The basic LT1 requirement is the selection of events of interest with a high, stable and well-understood effciency, while rejecting background events and keeping the total event rate under 1 kHz. Also, the total trigger efficiency must exceed 99% for all $B\bar{B}$ events and at least 95% for continuum events. The LT1 trigger decision is based on outputs coming from three specialized hardware processors: charged tracks above a preset transverse momentum in the DCH, showers in the EMC, and tracks detected in the IFR. The DCH trigger identifies tracks down to $p_t = 120$ MeV. The EMC trigger works with energy deposits above a threshold of 20 MeV for each crystal, and the IFR trigger requires only single clusters or back-to-back coincidences. The latter select cosmic ray events for calibration purposes, and $\mu^+\mu^-$ events.

The LT3 trigger software consists of event reconstruction and classification, a set of event selection filters, and monitoring. It receives the output from LT1, performs a second stage reduction for the main physics sources and identifies and flags the special categories of events needed for luminosity determination, diagnostic and calibration purposes.

Chapter 3

Analysis Techniques

In Chapter 1 the production rate for a $B^0\bar{B}^0$ system which decays into final states f_1 and f_2, one of which is a state of interest and the other is any flavour dependent state, was shown to be:

$$\Gamma(t_{\text{tag}}, t) \approx Ce^{-\Gamma(t_{\text{tag}}-t)}|A_{\text{tag}}|^2[(|A|^2 + |\bar{A}|^2)q_{\text{tag}}-$$

$$q_{\text{tag}}(|A|^2 - |\bar{A}|^2)\cos(\Delta M(t_{tag} - t))+$$

$$q_{\text{tag}}2Im[\bar{A}A^*e^{-i\phi_{mix}}]\sin(\Delta M(t_{tag} - t))]. \quad (3.1)$$

This formula was derived with assumptions of perfect knowledge of the B meson's flavour and the time elapsed between decays of the two B mesons ($\Delta t = t_{\text{tag}} - t$). However, in real life these two variables have to be obtained experimentally and the formula has to be rewritten in order to reflect the experimental uncertainties on these measurements.

In this chapter, techniques used to determine the B meson flavour and Δt will be described. Also, techniques for signal event reconstruction, signal and background discrimination and maximum likelihood fits will be discussed.

3.1 Flavour Tagging

The flavour of a neutral B meson can be determined in a situation when it decays to a final state which is only accessible to either a b or $\bar{b}$ quark. For

example, a positively charged lepton from $B^0 \to D^{*-}l^+\nu$ identifies the presence of a $\bar{b}$ quark and allows the B meson to be tagged as a B^0. The exclusive reconstruction of $B\overline{B}$ pairs in order to determine the B meson flavour is not effective, and combined with the small branching fractions of decays of interest is impractical. A more efficient approach for b-flavour tagging is the analysis of inclusive methods. Combining kinematics and particle identification it is possible to select particles with charges that are likely to correlate with the b quark flavour.

The BABAR flavor tagging algorithm [50] consists of two layers of decisions, both employing the Neural Network (NN) technique [51]. The first layer consists of 9 NN algorithms (so called sub-taggers) optimised to recognise specific decays of neutral B meson (so called tagging channels). These sub-taggers use kinematic and particle identification information to identify the signature of B meson's flavour. The outputs of the sub-taggers are then combined in a larger NN (named `Tag04`) and an overall probability is assigned to the event. The magnitude of the assigned probability represents the confidence in the estimation while the sign indicates the flavour of the meson (ie. NN=+1 $\Rightarrow B_{\text{tag}} = B^0$, $q_{\text{tag}} = +1$). The event is then assigned to one of six mutually exclusive categories that group events with similar mis-tag fractions (the probability of wrongly assigning a flavour to B_{tag}) and similar underlying physics. These categories are: `Lepton, KaonI, KaonII, Kaon-Pion, Pion, Other` and `Untagged`. The `Untagged` is reserved for events without reliable tagging information.

In order to characterise the quality of tagging the following variables are used:

- **Tagging efficiency** ϵ_{tag}: fraction of events for which a B tag is calculated;

- **Mis-tag fraction** ω ($\bar{\omega}$): fraction of B^0 ($\bar{B}^0$) events tagged wrongly as $\bar{B}^0$ (B^0) events by the tagging algorithm;

- **Dilution** $\mathcal{D} = 1 - 2\omega$ ($\bar{\mathcal{D}} = 1 - 2\bar{\omega}$): attenuation of the CP asymmetry

62

due to imperfect tagging;

- **Effective tagging efficiency** $Q = \epsilon_{\text{tag}}(1 - 2\omega)^2$**:** quality factor that summarises the performance of tagging. This variable describes the effective loss of statistic in a given measurement (it can be shown that the statistical error on a measurement scales with $1/\sqrt{Q}$).

Also, the following quantities are often in use:

$$\langle w \rangle = \frac{1}{2}(w + \bar{w}) \quad , \quad \Delta w = (w - \bar{w}) \tag{3.2}$$

$$\langle \mathcal{D} \rangle = \frac{1}{2}(\mathcal{D} + \bar{\mathcal{D}}) = 1 - (w + \bar{w}) \quad , \quad \Delta\mathcal{D} = (\mathcal{D} - \bar{\mathcal{D}}) = -2(w - \bar{w}). \tag{3.3}$$

Here, $\Delta\mathcal{D}$ (and Δw) parameterizes a possible difference in performance of the tagging procedure for the two tags, B^0 and $\overline{B}^0$.

The performance of *BABAR*'s `Tag04` tagging algorithm, described by the tagging efficiencies and mis-tag rates for each tagging category measured using $B^0 \to D^{(*)\pm}\pi^{\mp}$, $B^0 \to D^{(*)\pm}\rho^{\mp}$ and $B^0 \to D^{(*)\pm}a_1^{\mp}$ samples (together known as B_{flav} sample) is shown in Table 3.1.

Table 3.1: *Performance of BABAR's* `Tag04` *tagging algorithm [52]. The tagging efficiencies and mistag rates are measured on the B_{flav} sample. The values are given for each tagging category. $\Delta\epsilon_{tag}$ and ΔQ are defined analogously to Δw (see Eq. (3.2)).*

Category	$\epsilon_{tag}(\%)$	$\Delta\epsilon_{tag}(\%)$	$w(\%)$	$\Delta w(\%)$	$Q(\%)$	$\Delta Q(\%)$
Lepton	8.69 ± 0.07	-0.0 ± 0.2	3.1 ± 0.3	-0.1 ± 0.6	7.66 ± 0.12	0.04 ± 0.41
KaonI	10.96 ± 0.08	0.2 ± 0.2	5.2 ± 0.4	-0.1 ± 0.7	8.78 ± 0.16	0.21 ± 0.50
KaonII	17.23 ± 0.10	0.1 ± 0.3	15.4 ± 0.4	-0.5 ± 0.6	8.26 ± 0.18	0.29 ± 0.54
Kaon-Pion	13.78 ± 0.09	-0.3 ± 0.3	23.5 ± 0.5	-1.8 ± 0.7	3.88 ± 0.14	0.43 ± 0.38
Pion	14.37 ± 0.09	-0.7 ± 0.3	32.9 ± 0.5	5.1 ± 0.7	1.67 ± 0.10	-1.08 ± 0.26
Other	9.57 ± 0.08	0.3 ± 0.2	41.8 ± 0.6	4.6 ± 0.9	0.26 ± 0.04	-0.28 ± 0.10
Total	74.61 ± 0.12	-0.4 ± 0.6			30.5 ± 0.3	-0.4 ± 1.0

3.1.1 Lepton sub-tagger

The semi-leptonic $B \rightarrow Xl\nu$ ($l = e$, μ) decays (Figure 3.1) constitute roughly 20% [23] of the B branching fraction. The flavour of the B meson can be found by measuring the charge of the primary electron or muon produced in such a decay. Since the primary lepton comes from a decay of a virtual W boson emitted from a b or a $\bar{b}$ quark, its charge has to be of the same sign as the b ($\bar{b}$) quark charge.
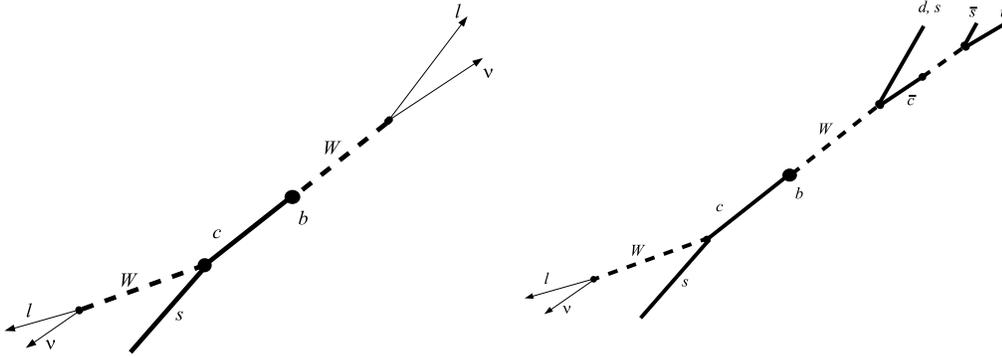
Figure 3.1: *Diagrams representing b decays likely to produce a* `Lepton` *tag (left) and a* `Kaon` *tag (right).*

In order to distinguish between primary and secondary leptons that could arise further along the decay chain, the lepton sub-trigger employs a set of discriminating variables:

- **The CM momentum of the leptonic track.** The momentum spectrum of a primary lepton is harder than that of a secondary lepton;

- **The cosine of the angle between the missing momentum ($\vec{p}_{\mathrm{miss}} = \vec{p}_B - \vec{p}_X - \vec{p}_l$) and the lepton's momentum.** The angle between the missing momentum and lepton momentum is a function of lepton's energy. Its value decreases with increasing energy of the lepton.

64

- **The energy contained in the hemisphere defined by the direction of the virtual $W^{\pm}$.** For primary leptons, the W recoils against a c quark in the CM frame, leading to a virtually empty hemisphere, whereas in the case of secondary leptons, the c quark that emits the W has recoiled from the decay of the b with an appreciable boost, and all its decay products will be boosted in the same direction (see Figure 3.1).

From the Table 3.1 can be seen that tagging using leptons is not very efficient ($\epsilon_{\text{tag}} \approx 9\%$), but it is very accurate ($w \approx 3\%$), resulting in an effective tagging efficiency of $Q \approx 8\%$.

3.1.2   Kaon sub-tagger

The kaon sub-tagger exploits events in which one or more charged kaons are produced in the decay of the B_{tag}. In decays of neutral B mesons most charged kaons are produced via the $b \to c \to s$ transition. The charge of the kaon produced in this process can be correlated with the flavour of the decaying B meson: the presence of a K^+ indicates a B^0, while K^- indicates a $\bar{B}^0$. The main problem in B meson flavour identification using kaons is multiple kaon production. A significant fraction of B meson decay into final states with more than one charged kaon, or into states with both neutral and charged kaons (see Figure 3.1).

In order to distinguish between different kaons the kaon sub-tagger combines information on the charge and PID of the best three charged kaon candidates in the event, the number of K^0_S mesons observed in the decay and the sum of the squared transverse momenta of each kaon, Σp_t^2. The latter helps to discriminate kaons originating from a W rather than from a charmed object, whereas a non-zero number of K^0_S mesons decreases the certainty of the tag, since the strange quark from the cascade $b \to c \to s$ could have formed a neutral rather than a charged kaon, providing no information on the B_{tag} flavour.

3.1.3 Slow Pion sub-tagger

Slow pions provide another source of B flavour identification. Slow pions of interest come from decays of $B^0/\bar{B}^0 \to D^{*\pm}X$, where $D^{*\pm}$ decays to $D^0(\bar{D}^0)\pi^\pm$. Because of the small mass difference between the D^* and D mesons the pion will carry a very low momentum, with an average of around 100 MeV/c. Also, the pion and the D will be emitted almost at rest in the D^* CM frame, and therefore the D^* boost will strongly correlate the directions of the tracks originating from the D^0 to that of the pion. To recognise slow pions coming from the $B^0 \to D^{*-}X$ ($D^{*\pm} \to D^0\pi^\pm$) the slow pion sub-tagger combines information about the pion's momentum, the cosine of the angle between the pion's track and the thrust axis of B_{tag} (see Section 3.3) and PID information.

3.1.4 Kaon-Slow Pion sub-tagger

This is an improved version of the previous sub-tagger. It exploits the fact that the favoured decay for a D^0 is $D^0 \to K^-X$ ((53 ± 4)% [23]), and that the D^0 decay products fly along the same direction as the slow pion. Therefore, by combining the output of the slow pion sub-tagger with PID information for a kaon candidates and the angle between their tracks, a cleaner tag can be obtained.

3.1.5 Highest p^* sub-tagger

The charge of the decay products of a virtual high momentum W boson emitted from a b quark can also be used for B flavour tagging, since the charge of such a W boson is directly correlated to that of the B meson. The variables used for NN training are the momentum of the track, p^*, the cosine of the angle between the fast particle and the thrust axis of B_{tag} and the track impact parameter in the xy plane, since the W decays very fast so its daughter particles originate from the B_{tag} vertex.

3.1.6 Fast-Slow correlation sub-tagger

One another aspect of the decay $b \to cW^-$ that can be used for B flavour tagging is the correlation between directions of the decay products of the W and the charmed meson formed by the c quark. The discriminating variables used in this case are the momenta of the slow and fast tracks, the cosine of their angles with the thrust axis of B_tag, the cosine of the angle between the tracks, and PID information about the slow track (to eliminate the possibility that the slow track is a kaon).

3.1.7 Lambda sub-tagger

This sub-tagger is used for identification of $b \to c \to s$ decays where the strange quark later forms a Λ baryon. The branching fraction for this type of decays is very small, but the decay itself has a very clean signature. To select these events a number of standard variables for neutral, long-lived objects are used (mass of the Λ baryon candidate; cosine of the angle between its momentum and its flight direction; flight length; momentum of the candidate; probability for the fit of the $\Lambda \to p\pi$ decay vertex) as well as PID information for the proton.

3.2 Measurement of Δt and resolution

3.2.1 Measurement of Δt

The two B mesons, produced in a $\Upsilon(4S)$ resonance decay, fly back-to-back in the centre of mass frame with an average momentum of $340\,\text{MeV}/c$. With a lifetime of approximately $1.5\,\text{ps}$, these B mesons are separated by around 35-40 μm along each Cartesian axis before decaying (in the centre of mass frame). Thanks to the asymmetry of the PEP-II accelerator the $\Upsilon(4S)$ resonance is boosted in the electon beam direction by the boost factor of $\beta\gamma = 0.56$, so looking from the laboratory frame the separation along the z-axis between

67

the decay vertices of the two B mesons is around $\beta\gamma c\tau_{B^0} = 257\,\mu$m. This distance is larger than the SVT vertex resolution and therefore permits a measurement of Δz.

Therefore, in order to measure Δt the vertices of both B mesons in an event have to be measured. When analysing a specific decay usually one of the B mesons (B_{rec}) is fully reconstructed, so its vertex is well known, while the other (B_{tag}) is reconstructed inclusively, in order to keep the efficiencies at a reasonable level.

This method of reconstruction is the main cause of the poor resolution for the B_{tag} vertex, which dominates the overall resolution in Δz. In the case of B_{rec} the average resolution in z is $\sim 65\,\mu$m for more than 99% of the candidates (and as good as $\sim 45\,\mu$m for more than 80%). In the case of B_{tag} this value is $\sim 190\,\mu$m.

Once Δz is measured, in the approximation of negligible B momenta in the $\Upsilon(4S)$ rest frame, Δt can be calculated as:

$$\Delta t = \frac{\Delta z}{\beta\gamma c}, \tag{3.4}$$

where $\beta\gamma$ is the boost factor of the $\Upsilon(4S)$ resonance in the laboratory frame, calculated from the beam energies which are monitored continuously. The approximation of negligible B momenta in the $\Upsilon(4S)$ rest frame is not completely correct. The B mesons do have a small momentum in the $\Upsilon(4S)$ rest frame ($p_B^* \approx 340\,\text{MeV}/c$), so the correct relation between Δt and Δz is the following:

$$\Delta z = \beta\gamma\gamma_{\text{rec}}^* c\Delta t + \gamma\beta_{\text{rec}}^*\gamma_{r\text{rec}}^* \cos\theta_{\text{rec}}^* c\left(t_{\text{rec}} + t_{\text{tag}}\right). \tag{3.5}$$

Here, $\gamma_{\text{rec}}^* = 1.002$, $\beta_{\text{rec}}^* = 0.064$ and θ_{rec}^* are, respectively, the boost factor of the reconstructed B meson, its velocity, and its angle with respect to the z axis, all in the CM frame.

The above equation introduces the quantity: $t_{\text{rec}} + t_{\text{tag}}$, which is not directly measurable. Its value can be obtained from the transverse displacement of one B meson with respect to the other, but the value of this displacement is rather

68

small (~ 35-$40\,\mu$m) compared to the resolution of the B_{tag} vertex. Instead of that, the averaged value can be used. Since both t_{rec} and t_{tag} are positive, the minimum value of $t_{\text{rec}} + t_{\text{tag}}$ is $|\Delta t|$. By integrating $t_{\text{rec}} + t_{\text{tag}}$ from $|\Delta t|$ to infinity, we get:

$$\langle t_{\text{rec}} + t_{\text{tag}} \rangle = \tau_B + |\Delta t|, \tag{3.6}$$

which after returning into Eq. (3.5) gives:

$$\Delta z = \beta\gamma\gamma^*_{\text{rec}}c\Delta t + \gamma\beta^*_{\text{rec}}\gamma^*_{\text{rec}}\cos\theta^*_{\text{rec}}c\left(\tau_B + |\Delta t|\right), \tag{3.7}$$

and can be solved for Δt. The value of Δt is corrected by only ~ 0.02 ps relative to Eq. (3.4). The use of Eq. (3.7) improves the resolution for Δt by about 5% and removes a correlation existing in signal data between the true value of Δt and its resolution.

Δt resolution model

The behavior of the Δt residual ($\delta t = \Delta t - \Delta t_{\text{true}}$) is modelled as the sum of three gaussians, known as the core, tail and outlier:

$$\begin{aligned}\mathcal{R}_{\text{sig}}(\delta t,\ \sigma_{\Delta t}) \;=\;& (1 - f_{\text{tail}} - f_{\text{outlier}})G\left(\delta t;\ b_{\text{core}}\sigma_{\Delta t},\ s_{\text{core}}\sigma_{\Delta t}\right) \tag{3.8}\\ &+ f_{\text{tail}}G\left(\delta t;\ b_{\text{tail}}\sigma_{\Delta t},\ s_{\text{tail}}\sigma_{\Delta t}\right) + f_{\text{outlier}}G\left(\delta t;\ b_{\text{outlier}},\ s_{\text{outlier}}\right).\end{aligned}$$

Here, $\sigma_{\Delta t}$ is the event-by-event error on Δt extracted from the fit of the B meson vertex and the G functions are gaussians:

$$G\left(\delta t;\ \mu,\ \sigma\right) = \frac{1}{\sigma\sqrt{2\pi}}\exp\left(-\frac{(\delta t - \mu)^2}{2\sigma^2}\right). \tag{3.9}$$

From Eq. (3.8) it can be seen that the parameters of the core and tail gaussians are scaled by the event-by-event error $\sigma_{\Delta t}$. Studies of the B^0 lifetime [53] showed that the mean and RMS of the Δt resolution are linearly correlated with the error $\sigma_{\Delta t}$. The reason for this behaviour comes from the correlation between measurements of the z position of the B_{tag} vertex and the flight directions of charmed particles used for B_{tag} vertex reconstruction. An illustration of this effect is shown in Figure 3.2.
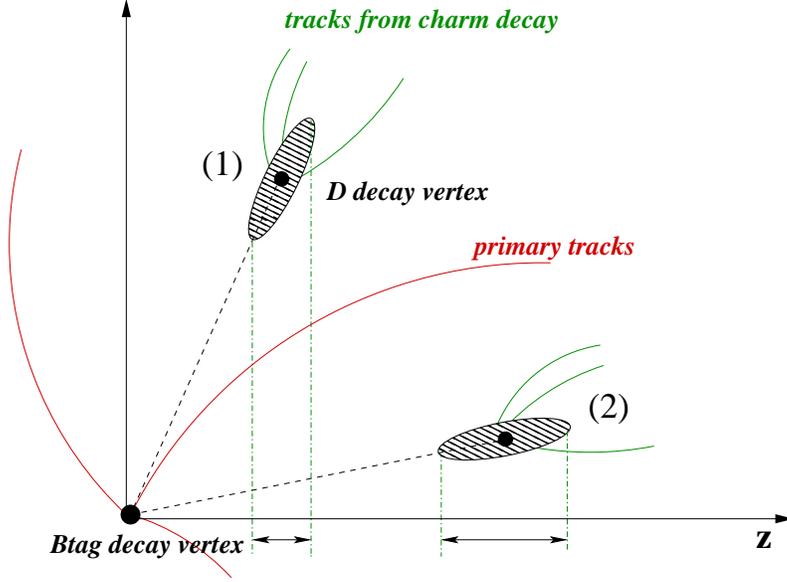
Figure 3.2: *A B_{tag} meson decay where one of its daughter particles is a D meson. Two possible flight directions of the D meson are given (1) and (2). The secondary tracks from the D vertex are distributed uniformly in a cone around the D flight direction and the ellipse around the D decay vertex illustrates the error ellipse on the decay vertex that can be reconstructed from the secondary tracks. In the case when the D meson travels in the forward direction (2) the flight length in z tends to be large compared to the case when the D meson flight path is almost orthogonal to the z axis (1). Also, if the error ellipse has the same size in both cases, then its projection on the z axis is larger for the D meson that travels in the forward direction.*

The outlier gaussian is independent of $\sigma_{\Delta t}$ and is used to describe the small fraction of events ($< 1\%$) for which at least one of the two vertices is badly reconstructed.

The Δt resolution model Eq. (3.8) was developed in studies of the charmonium $\sin 2\beta$ analyses [54]. Since the dominant contribution to the Δt error comes from the poor determination of the B_{tag} vertex, and the algorithm for finding the B_{tag} vertex is independent of the channel into which B_{rec} decays, it can

70

be, to a good approximation, assumed that the obtained Δt resolution model is valid for all B_{rec} channels. In the case of the $B^0 \to K^0_S \pi^+ \pi^-$ analysis this assumption was checked using MC events and good agreement was found. The values of the resolution parameters used in the $B^0 \to K^0_S \pi^+ \pi^-$ analysis are listed in Table 3.2. Since the lepton tagged events do not suffer from the correlation between the event-per-event error $\sigma_{\Delta t}$ and the bias on Δz, different values of the core gaussian parameters are used for the lepton and non-lepton tagged events.

In order to implement the Δt resolution effects the expected signal distribution Eq. (1.38) (see Section 1.2.2), has to be convolved with the resolution function:

$$
\begin{aligned}
\mathcal{P}^{\text{observed}}\ (x,\ y,\ \Delta t) &= \left(\mathcal{P}^{\text{theory}} \otimes \mathcal{R}_{\text{sig}}\right)(x,\ y,\ \Delta t) \qquad\qquad (3.10) \\
&= \int_{-\infty}^{+\infty} \mathcal{P}^{\text{theory}}\ (x,\ y,\ \Delta t_{\text{true}})\, \mathcal{R}_{\text{sig}}(\Delta t - \Delta t_{\text{true}})d\Delta t_{\text{true}}\ .
\end{aligned}
$$

Table 3.2: *Parameters that describe the resolution in Δt for signal events, extracted from the B_{flav} sample for the charmonium $\sin 2\beta$ analyses [55], and used for $B^0 \to K^0_S \pi^+ \pi^-$.*

	Lepton	Other categories
b_{core}	-0.0666 ± 0.0264	-0.1916 ± 0.0124
s_{core}	1.0142 ± 0.0418	1.0973 ± 0.0206
f_{core}	0.8744 ± 0.0079	
b_{tail}	-0.9674 ± 0.0987	
s_{tail}	3.0 fixed	
f_{outlier}	0.0026 ± 0.0005	
b_{outlier}	0.0 fixed	
s_{outlier}	8.0 ps^{-1} fixed	

3.3 Signal and Background separation

In order to separate signal events from the background, the standard approach in most *BABAR* analyses is to use appropriate variables which exploit the different kinematic and topological signatures of signal and background events. In the case when the distribution of a discriminating variable lies in a certain range for signal events and in a different range for background events, it is possible to apply a cut to the distribution in such a way that most of the background events are rejected and the signal to background ratio is increased. In the case when applying a cut is not efficient all events can be accepted, and a weight or probability of belonging to the signal or background can be assigned to each event.

In $B^0 \rightarrow K_S^0 \pi^+ \pi^-$ analysis, loose cuts are applied on three discriminating variables: m_{ES}, ΔE and MLP (definitions of these variables are given in the following sections). However, their distributions are also used in the fit to optimise the separation.

3.3.1 Kinematic variables

In this analysis two discriminating kinematic variables, m_{ES} and ΔE [56] are used. The first one is the beam-energy substituted mass, defined as:

$$m_{\mathrm{ES}} \equiv m_B = \sqrt{E_X^2 - \vec{p}_B^{\,2}}, \tag{3.11}$$

where $\vec{p}_B$ is the momentum of the reconstructed B meson and E_X is the energy of the B meson derived using the beam-energy:

$$p_B^2 = p_{\bar{B}}^2 \quad \text{and} \quad p_{\mathrm{beam}} = p_B + p_{\bar{B}}$$
$$\Rightarrow 0 = p_{\mathrm{beam}}^2 - 2p_{\mathrm{beam}}p_{\bar{B}} \Rightarrow 0 = s - 2(E_{\mathrm{beam}}E_B + \vec{p}_B\vec{p}_{\mathrm{beam}})$$

$$\Rightarrow E_X \equiv E_B = \frac{\frac{s}{2} - 2\vec{p}_B\vec{p}_{\mathrm{beam}}}{E_{\mathrm{beam}}}.$$

Here, p_{beam}, p_B and $p_{\bar{B}}$ are the four momenta of the beam and B mesons, and $\sqrt{s}$ is the CM energy.

The reason for using the beam-energy constrained derived energy of the B meson is that the candidate is formed from a number of tracks and neutral clusters whose energies are not as accurately measured as the beam energy. For signal events, m_{ES} yields the mass of the B meson, and its distribution peaks at the B mass ($5.279\,\mathrm{GeV}/c^2$). For background coming from continuum production of light quarks ($e^+e^- \to q\bar{q}$ events, where q is a u, d, s or c quark), the only way of reaching the B rest mass is by associating tracks randomly. Because of that, their distribution slowly varies over the m_{ES} range of interest. Another advantage of using the knowledge of the beam conditions is that it gives a possibility to construct another kinematic variable, ΔE. The analysis of m_{ES} and ΔE variables shows that the correlations between these two variables is rather small [56]. ΔE is defined as difference between reconstructed and beam-derived energies of the B candidate:

$$\Delta E \;=\; E_B - E_X. \tag{3.12}$$

Since m_{ES} is calculated only from the beam four-momentum and the momentum of the B candidate it is independent of the mass hypothesis of the B daughter tracks. On the other hand, ΔE does depend on the mass hypothesis since it uses the reconstructed energy of the B candidate. For well reconstructed B mesons ΔE should peak at zero. Plots of both variables for signal and background are shown in the next Chapter (Figure 4.23 and Figure 4.24).

3.3.2 Event-shape variables

Another way to distinguish between the signal and the background is to exploit differences in the signal and background events topology.

In $q\bar{q}$ events the mesons are produced with large kinetic energy, therefore, two highly collimated jets will be formed around the axes of the original quark and anti-quark (angular distribution of jet particles roughly $\propto (1 + \cos^2 \theta)$, where θ is the CM angle of a jet with respect to the beam axis [57]).

Unlike the $q\bar{q}$ events, the $B\bar{B}$ events are produced almost at rest in the CM

73

frame, and since the B mesons are pseudo-scalars they decay isotropically. Therefore the distributions of their daughters in the $\Upsilon(4S)$ centre-of-mass frame will be approximately spherical. Furthermore, the $\Upsilon(4S) \to B\bar{B}$ decay is a decay of a vector particle to pseudo-scalar particles so the angular distribution of B candidates with respect to the beam axis follows a $\sin^2 \theta_{B\mathrm{mom}}$ distribution ([23]).

In the $B^0 \to K_S^0 \pi^+ \pi^-$ analysis the following topological variables have been used:

- Angle between the B momentum and the beam axis;

- Angle between the thrust axis of the B candidate and the z axis;

- Ratio of the zeroth and second order Legendre polynomials of the rest of event (ROE) momentum distribution, where the ROE is the collection of all tracks and neutral objects remaining after the B candidate reconstruction.

Individually these variables do not provide a large amount of discrimination but using a Neural Network [51] to combine them yields a powerful separating variable.

Angle between the B momentum and the beam axis

The distributions of $|\cos \theta_{B\mathrm{mom}}|$ for signal and $q\bar{q}$ background events are shown in Figure 3.3. As mentioned before, the distribution of the B momentum direction with respect to the beam axis for $B\bar{B}$ events has a parabolic shape, $\sin^2 \theta_{B_{mom}} = 1 - \cos^2 \theta_{B_{mom}}$. In the case of $q\bar{q}$ events this distribution is approximately uniform, since in the process of reconstruction only a random combination of tracks coming from the $q\bar{q}$ events can form a B candidate.

Angle between the thrust axis of the B candidate and the z axis

The thrust axis of a collection of particles is the axis along which the sum of the projections of the momenta of the particles has maximal value. Since the

distributions of the daughters of true B events is approximately spherical in the $\Upsilon(4S)$ centre-of-mass, the thrust axis of a true B candidate is essentially random. On the other hand $q\bar{q}$ events are strongly collimated, therefore the thrust axis of such events will have approximately the same direction as the momentum of the emitted quark. In the $B^0 \rightarrow K_S^0 \pi^+ \pi^-$ analysis the cosine of the angle between the thrust axis of the B candidate and the z axis is used. Distributions of $|\cos \theta_{B_\text{trust}}|$ for $B\overline{B}$ and $q\bar{q}$ events are shown in Figure 3.3.
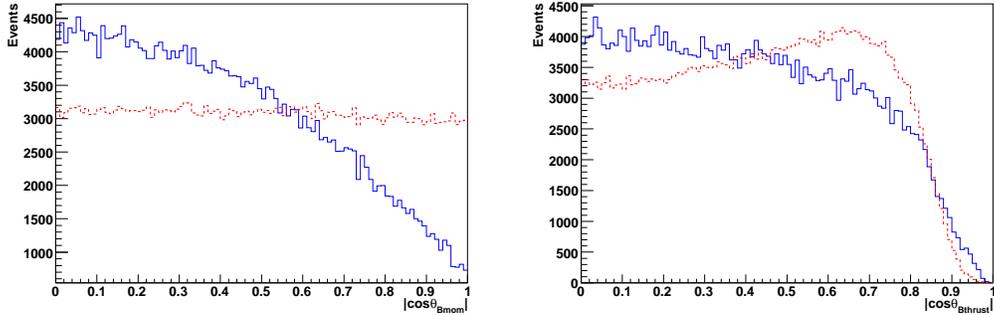
Figure 3.3: *Distributions of $|\cos \theta_{B_{mom}}|$ and $|\cos \theta_{B_{thrust}}|$ for non-resonant $B^0 \rightarrow K_S^0 \pi^+ \pi^-$ signal MC (blue, solid) and off-peak data (red, dashed). The shapes seen in the figure on the right differ somewhat from those discussed in the text due to detector acceptance effects.*

The ROE and Legendre polynomials

The momenta of the tracks remaining after a B candidate is reconstructed can also be used to distinguish between signal and continuum background events. In the $B^0 \rightarrow K_S^0 \pi^+ \pi^-$ analysis the ratio of the second-order to the zeroth-order Legendre polynomials L_2/L_0 is used, where:

$$L_0 = \sum_i^{\text{ROE}} p_i, \tag{3.13}$$

$$L_2 = \sum_i^{\text{ROE}} p_i \times \frac{1}{2}(3\cos^2(\theta_i) - 1). \tag{3.14}$$

Here, p_i and θ_i are the momentum and polar angle of each track and neutral cluster in the ROE. The distributions of these variables are shown in Figure 3.4.
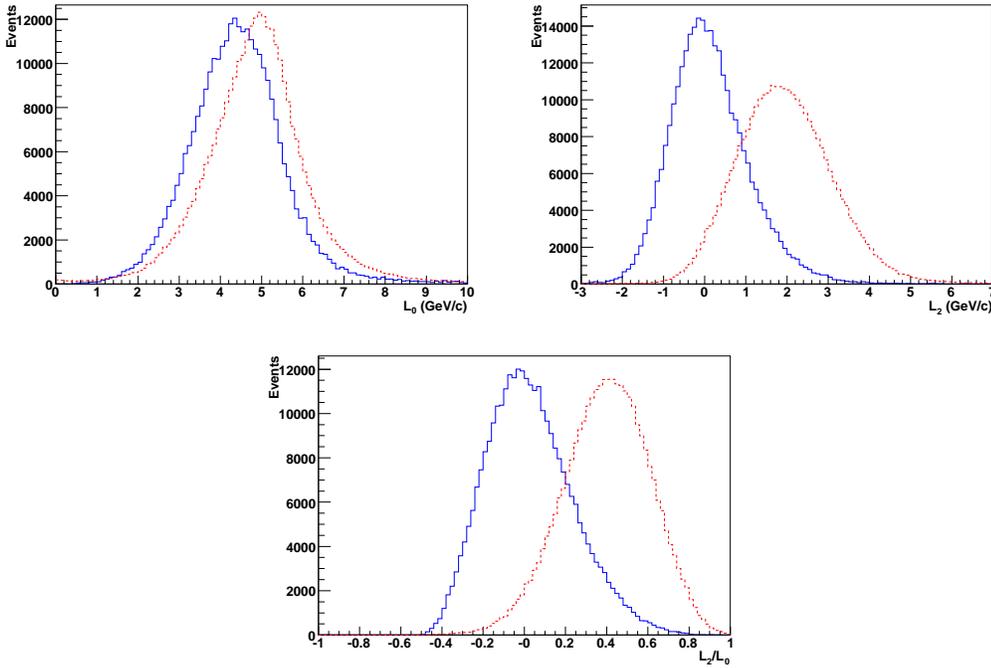
Figure 3.4: *Distributions of the zeroth and second order components in the Legendre polynomials of the momentum flow in the rest of the event. The bottom plot shows the distribution of the ratio of the second-order to the zeroth-order polynomials. Non-resonant $B^0 \to K_S^0 \pi^+ \pi^-$ signal MC is displayed in blue (solid) and off-peak data in red (dashed).*

The MLP Neural Network

Artificial neural networks are data modelling tools that are inspired by the learning processes that take place in biological systems. They have been developed in order to help processing complex input/output relations. The architecture of the neural networks follows the architecture of its biological counterparts: a large number of interconnected artificial neurons, each performing a weighted sum of its inputs, and then firing a binary signal if the

76

total input exceeds a certain level. In biological systems when a learning process happens the strength of synaptic connections changes. In the artificial neural network modelling the synapse strength modification rules are derived by applying mathematical optimisation methods.

There are many types of neural network models. Perhaps the most common one is the Multilayer Perceptron (MLP) neural network [58]. This type of neural network is known as a supervised network because it requires a desired output in order to learn. The goal of this type of network is to create a model that correctly maps the input to the output using historical data so that the model can then be used to produce the output when the desired output is unknown. A graphical representation of an MLP is shown in Figure 3.5.

$$y_k^1 = \frac{1}{1 + e^{w_k^1 x - a_k^1}}, k = 1, 2, 3$$

$$y_k^2 = \frac{1}{1 + e^{w_k^2 x - a_k^2}}, k = 1, 2$$

$$y_{out} = \sum_{k=1}^{2} w_k^3 y_k^2$$
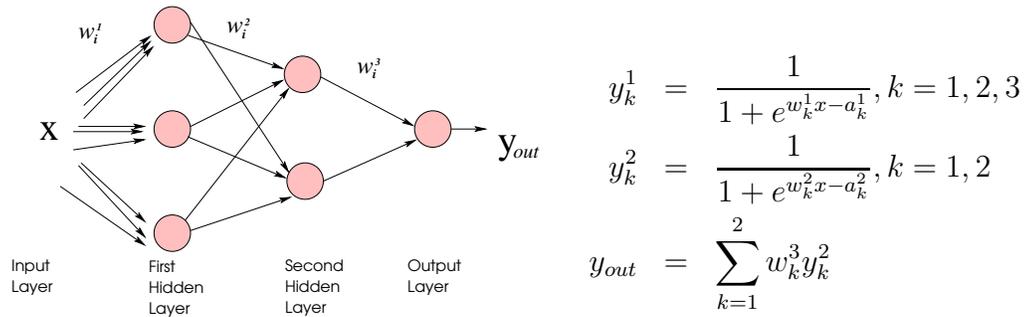
Figure 3.5: *Graphical representation of a two hidden layer (MLP) neural network. The inputs are fed into the input layer and get multiplied by interconnection weights as they are passed from the input layer to the first hidden layer. Within the first hidden layer, they get summed then processed by a nonlinear function. As the processed data leaves the first hidden layer, again it gets multiplied by interconnection weights, then summed and processed by the second hidden layer. Finally the data is multiplied by interconnection weights then processed one last time within the output layer to produce the neural network output.*

The output of the MLP neural network where the input variables are $|\cos\theta_{B_{mom}}|$, $|\cos\theta_{B_{thrust}}|$ and L_2/L_0 for off-peak (background) data and signal MC data is shown in Figure 3.6. The discrimination power of each of the variables used

to build the MLP is weak, but using the MLP to combine them yields a powerfully separating variable. To use discriminating variables in the likelihood Dalitz plot fit one has either use histogrammed distributions of the variables or find analytical functions which model the distributions. To find analytical functions that describe the distributions of the MLP variable for signal and continuum background shown in Figure 3.6 is rather difficult. Because of that the following was done:

- Firstly, a loose cut is applied, such that around 90% of signal events are selected, while around 66% of background events are rejected ($\mathrm{MLP}_{\mathrm{cut}} = 0.367$).

- Secondly, the MLP distributions are transformed using the following function:

$$\log\left(\frac{\mathrm{MLP} - \mathrm{MLP}_{\mathrm{cut}}}{\mathrm{MLP}_{\mathrm{max}} - \mathrm{MLP}}\right) \equiv \mathrm{MLP}_{\mathrm{transf}}, \qquad (3.15)$$

where $\mathrm{MLP}_{\mathrm{cut}}$ is the cut value and $\mathrm{MLP}_{\mathrm{max}}$ is the maximal value of the MLP found using signal Monte Carlo events and off-peak data. In Figure 3.6 the transformed MLP distributions ($\mathrm{MLP}_{\mathrm{transf}}$) are also shown. It can be seen that these distributions are far easier to fit than the originals. More detail about the MLP and its analytical shape is given in Chapter 4. Thereafter in the text the acronym MLP will denote the transformed value of the MLP ($\mathrm{MLP}_{\mathrm{transf}}$).

3.4   Monte Carlo Simulation

Simulated (Monte Carlo) data are used in order to analyse detector effects, study backgrounds and signal as well as various other aspects of an analysis. In order to enable these types of studies, MC data include full detector simulation: generation of the event, simulation of the passage of the particles through the detector, the response of the detection material and the detector electronics.
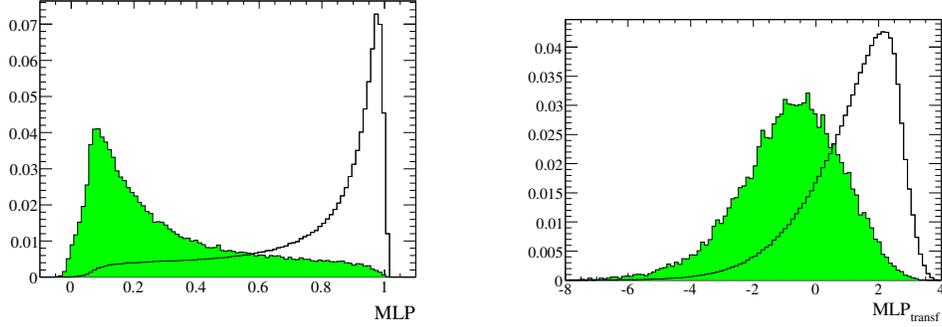
Figure 3.6: *(left) Normalised distributions of the* MLP *discriminant for signal (empty histogram) and continuum background (green, filled histogram). The variables from which it is constructed are* $|\cos\theta_{B_{mom}}|$, $|\cos\theta_{B_{thrust}}|$ *and* L_2/L_0. *(right) The distributions of transformed* MLP (MLP$_{transf}$) *(obtained after the MLP cut is applied) for signal and continuum background events.*

At the *BABAR* experiment various software packages are used for MC data production. For the simulation of B decays the `EvtGen` [59] package in combination with the `JETSET` [60] and `PHOTOS` [61] generators are used. `EvtGen` provides a number of detailed models important for B physics, like CP violation, angular correlations in sequential decays and specialised matrix elements for rare decays. The `JETSET` package is responsible for the simulation of jet-like events (for example $q\bar{q}$ event), while `PHOTOS` is used to generate initial and final state radiation effects.

The simulation of each particle's passage through the detector is done using the *BABAR* code, which is based on the `GEANT4` package [62]. A model of the *BABAR* detector, highly detailed in terms of geometry and of materials, is constructed and the behaviour of the particles as they traverse the detector material, including how they trigger the actual detection systems, is simulated. Each interaction with a detector system is recorded, and simulation of the detector signals performed.

The next stage is a full software implementation of the *BABAR* electronics. This simulates the processing of the detector signals through the front end

79

electronics and the dataflow crates to the data acquisition system. It also includes a full software simulation of the trigger system allowing determination of when an event would be triggered on and stored.

In order to fully mimic real data, machine backgrounds and electronic noise have to be added. This is done by adding prerecorded background conditions of the detector. During normal operations the *BABAR* trigger system issues so called cyclic triggers at regular intervals, causing the data acquisition system to read out its event buffers. The probability that an interesting physics event is in progress in these randomly selected moments is negligible and so they represent a good sample of the background conditions in the detector.

The final stage of the MC simulation is the reconstruction, where the same code used to reconstruct real data is applied.

Toy Monte Carlo

Toy MC events are events simulated using very simplified models of particle decays and their interactions. Many decay characteristics are ignored (like detector response effects or passage of the particles through the detector), and only those relevant for a specific problem are taken into account.

Toy MC events are usually used to identify potential problems in the maximum likelihood fit. A large number of toy MC samples generated with given PDFs is fitted using the same PDFs, and for each fitted variable, a so called *pull* distribution is plotted:

$$\text{pull} = \frac{a_i^{fit} - a_i^{true}}{\sigma_i^{fit}} \ . \tag{3.16}$$

Here a_i^{true} and a_i^{fit} are the generated and the fitted value of the parameter a_i respectively, and σ_i^{fit} is the fit error. Ideally, these pull distributions should be gaussian shaped, with the centre around zero and the unit width. Any discrepancy will point towards problems such as defective likelihood, mistake in the calculations or the low statistics.

3.5 Reconstruction

Event reconstruction at *BABAR* is performed in two stages. In the first stage, the so called Offline Prompt Reconstruction (OPR), the tracks from hits in the Drift Chamber and the Silicon Vertex Tracker, and crystals with energy deposits in the Electromagnetic Calorimeter are found. The collected information, together with Čerenkov photons and dE/dx information is then used for particle identification.

In the second stage, previously collected information is used to construct the composites, ie. particle candidates that are not directly observable by the detector (for an example a B meson).

3.5.1 Tracking algorithms

The *BABAR* tracking algorithm is based on a Kalman filter [63], an algorithm for optimal recursive data processing. This algorithm incorporates all information that is provided to it and prosses all available measurements, regardless of their precision, to estimate values of variables of interest.

The algorithm starts from the DCH hits found by the Level 3 Trigger (see Section 2.2.4) to form a track, and further hits are added if they are observed to be consistent with that track. The remaining DCH hits are searched in order to find tracks that did not originate from the IP (such as those from secondary particles, like K_S^0 mesons) or that do not cross the whole chamber. Afterwards, SVT hits are examined and those which can be linked to the existing DCH tracks are added to these tracks. The rest of the SVT hits are searched to locate any low momentum, SVT-only track. Once a track is found a fit is performed, so that physics information, like momentum, charge and position and direction at the impact point can be extracted.

A charged particle moving in a homogeneous magnetic field follows a circular motion in the plane perpendicular to the field. The momentum component along the magnetic field is left unchanged, therefore the particle's trajectory

81

is a helix. To describe a helix one needs five parameters. At the *BABAR* exper-
iment these parameters are defined at the point of closest approach (POCA)
of the track to the z-axis:

- d_0, the distance in the xy plane to the z-axis;

- z_0, the coordinate along the z-axis;

- ϕ_0, the azimuthal angle of the track;

- λ, the dip angle of the track with respect to the transverse (xy) plane;

- $\omega = 1/R$, the curvature of the track projection in the xy plane, where R
  is the distance between the helix centre and the POCA.

A schematic view of tracks parameters defined at the POCA is shown in Fig-
ure 3.7.
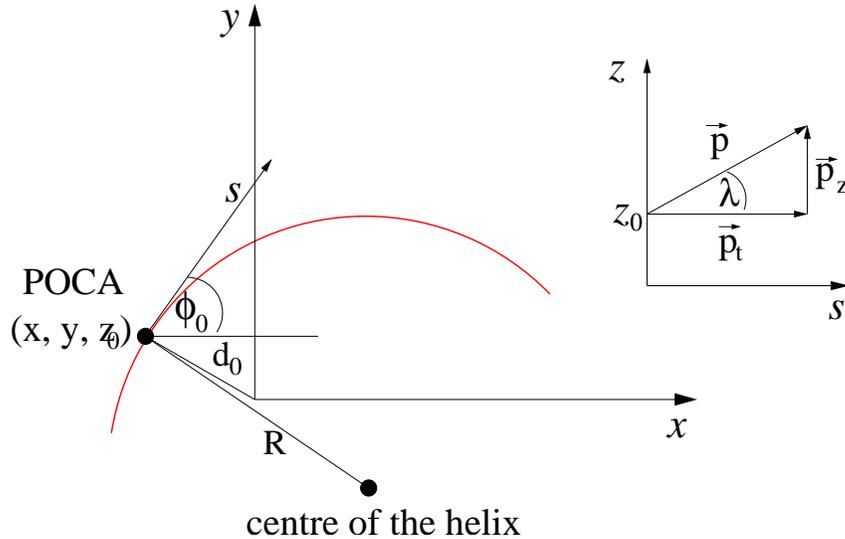
Figure 3.7: *Schematic view of the track parameters.*

The reconstructed tracks are then classified and stored in lists according to
different selection criteria. As an example, in the $B^0 \to K_S^0 \pi^+ \pi^-$ analysis, the
pion candidates are required to meet the conditions of the `GoodTracksLoose`
list:

- $p_t > 0.1\,\mathrm{GeV}/c$

- $p < 10.0\,\mathrm{GeV}/c$

- at least 12 hits in the DCH

- $d_0 < 1.5$ cm

- $|z_0| < 10$ cm

The K_S^0 candidates are formed from any two oppositely charged tracks (often not meeting the `GoodTracksLoose` requirements above), assumed to be pions, and whose mass, after performing a vertex constrain, is within $25\,\mathrm{MeV}/c^2$ of the PDG value of the K_S^0 meson mass [23].

3.5.2 Calorimeter algorithms

The electromagnetic showers created by particles traversing the Electromagnetic Calorimeter usually spread over more than one crystal. Also, the showers induced by different particles often overlap, so the task for the EMC reconstruction algorithms is to reconstruct the right shape of the electromagnetic shower and measure the energy of the particle that created the shower. The algorithm first searches for crystals with energy deposits greater than $10\,\mathrm{MeV}$. Such crystals are "seeds" for the EM shower reconstruction. Crystals surrounding the seed crystal, with energy above $1\,\mathrm{MeV}$ are then added. If the energy deposit in those crystals is greater than $3\,\mathrm{MeV}$ their neighbouring crystals are added as well. This process is iterated until no further crystals meet the above requirements. Once the cluster is completed a maxima finding algorithm is run over all its constituent crystals. This algorithm is designed to find local maxima within the cluster since a single cluster may be caused by two or more overlapping showers. At the end, tracks are projected onto the calorimeter, and if their position and entrance angle are consistent with one of the maxima, they are linked and considered as a single particle. The remaining maxima are assumed to be associated with neutral objects.

3.5.3   Particle Identification

The step after track and the shower reconstruction is particle identification (PID). Five types of particle may be detected as a charged track in the *BABAR* detector: pions, kaons, electrons, muons and protons. In order to link a track with the appropriate type of particle, selectors are developed. Each selector uses probability density functions (PDFs) to form a per-track likelihood for its particle type.

Special attention is given to pion and kaon identification, since electrons and muons can often be separated from the other types of particles by their signatures in the Electromagnetic Calorimeter and the Instrumented Flux Return, while protons are quite scarce. Kaon and pion identification combine the measurements of the Čerenkov angle and the number of photons in the DIRC with dE/dx information from the SVT and DCH. A total likelihood is formed as a product of SVT and DCH likelihoods because it is assumed that the PDFs from these sources are uncorrelated. Once the likelihoods for the different particle hypotheses have been calculated, cuts on their values are applied, and the track is entered into different lists according to the criteria satisfied: `VeryLoose`, `Loose`, `Tight` and `VeryTight` for pions, and `NotPion`, `VeryLoose`, `Loose`, `Tight` and `VeryTight` in the case of kaons. For the analysis described in this thesis, `piLoose` was chosen (see Section 4.1). The reconstruction efficiency of pions passing the `piLoose` list requirements is above 95% in most of the kinematical range, with kaon contamination between 5% and 10% depending on the particle's momentum. All PID selectors have been developed and maintained by the *BABAR* PID group. Further details can be found in [64, 65]. The likelihoods used for particle identification are built using different sets of variables, like dE/dx, lateral shower development, number of hits in DCH and SVT... One variable that can provide additional PID information is the longitudinal shower distribution. The Electromagnetic Calorimeter at *BABAR* is a crystal calorimeter, which means that the longitudinal shower development can not be directly measured, but it can be extracted combining information

from the tracking system and the electromagnetic calorimeter. A new method for extracting longitudinal shower development information from longitudinally unsegmented calorimeters, which has been implemented as a part of the *BABAR* final particle identification algorithm, was developed by the author in collaboration with Gagan Mohanty and David Brown [66]. It significantly improved low momenta electron, kaon and muon identification at *BABAR*. Details about this method are given in Appendix A.

3.5.4 Vertexing of candidates

Composite candidates are particles that are not directly detected in the *BABAR* detector but are reconstructed from their decay products. A good example of this is the B meson, which has to be reconstructed using daughter particles. Composite candidates are formed combining tracks and neutral objects that match the decay daughters of the particle. How the vertexing proceeds depends on the analysed decay itself. As an example, in the reconstruction of the $B^0 \to K_S^0 \pi^+ \pi^-$ decay, any intermediate states that may appear, like ρ^0 or $K^{*+}(892)$ mesons, have decays that are governed by the strong force and these have very short lifetimes. This means that their vertices are indistinguishable from that of the B meson and their presence can only be observed by structure in the Dalitz phase space. Therefore, the only composites in this particular analysis are the K_S^0 and the B meson itself. Once the composite candidates are constructed, their vertices are calculated using the `TreeFitter` package, which performs a global fit to the whole decay chain by applying the Kalman filter technique [63]. This approach allows implementation of corrections due to energy loss of the particles or inhomogeneities of the magnetic field.

The fitting procedure is performed twice. In the first stage an unconstrained fit is performed. This allows extraction of the kinematical background-rejecting variables m_{ES} and ΔE. After this a constraint on the B meson candidate mass is applied, the fitting is repeated, and the Dalitz-plot coordinates and related event shape variables are calculated.

3.5.5   *B* Counting

If the cross section for $\Upsilon(4S)$ production in e^+e^- collisions was known with satisfactory accuracy, it would be possible to infer the number of produced $B\overline{B}$ pairs from the luminosity. Instead, the number of $B\overline{B}$ pairs ($N_{B\overline{B}}$) is calculated by a method known as B counting.

The number of $B\overline{B}$ pairs is calculated from the number of multi-hadronic events (N_{MH}) recorded at the $\Upsilon(4S)$ resonance (on-peak) and 40 MeV below the $\Upsilon(4S)$ resonance energy (off-peak).

The difference between these numbers must be entirely due to $\Upsilon(4S)$ production, since lowering by 40 MeV takes the energy below $B\overline{B}$ production threshold. Assuming that the branching fraction of $\Upsilon(4S) \rightarrow B\overline{B}$ is 100%, $N_{B\overline{B}}$ is given by:

$$N_{B\overline{B}} = \frac{1}{\epsilon_{B\overline{B}}} \left(N_{MH}(\text{on}) - N_{MH}(\text{off}) \kappa \frac{N_\mu(\text{on})}{N_\mu(\text{off})} \right). \qquad (3.17)$$

Here $\epsilon_{B\overline{B}}$ is the efficiency with which $B\overline{B}$ events pass the multi-hadronic selection cuts (determined from MC simulation), $\kappa \sim 1$ is a factor to correct for possible variations in cross section and efficiencies with center of mass energy. $N_\mu(\text{on})$ and $N_\mu(\text{off})$ are numbers of muon pairs produced in the process $e^+e^- \rightarrow \mu^+\mu^-$ at $\Upsilon(4S)$ energy and 40 MeV below, respectively. Their ratio accounts for the different integrated luminosities of the on-peak and off-peak samples.

Applying this procedure to the data used in this analysis yields a value of:

$$N_{B\overline{B}} = (465.0 \pm 5.1) \times 10^6. \qquad (3.18)$$

3.6   Maximum Likelihood fits

In most physics analyses we deal with measurements of a parameter or set of parameters (which are assumed to have some fixed, but unknown values) based on a limited number of experimental observations. The usual approach

is to construct an unbiased estimator[1], a function of the observations, which has a numerical value that converges toward the true value of the parameter as the number of observations increases. A quantity with such characteristics can be constructed using the law of large numbers:

$$N^{-1} \sum_{i=1}^{N} a(X_i) \xrightarrow[N \to \infty]{} E[a(X)] = \int a(X) \mathcal{P}(X, \theta) dX. \qquad (3.19)$$

Here $a(X)$ is any function of X with finite variance, and we assume that N observations X_i have been made of a random variable X with probability density function $\mathcal{P}(X, \theta)$, where θ is an unknown parameter.

The three most usual methods of estimation, each making use of the law of the large numbers are: *the moments method, the least squares method and the maximum likelihood method.* Complete discussions about these methods can be found in many books about statistics [67, 68]. Here, some details about the maximum likelihood method will be given.

The maximum likelihood estimate of the parameter θ is that value $\hat{\theta}$ for which the likelihood function $L(X|\theta)$ has its maximum, given the particular observations X. Here, the likelihood function for a set of N independent observations X_i is defined as:

$$L(X|\theta) = \prod_{i=1}^{N} \mathcal{P}(X_i, \theta) . \qquad (3.20)$$

The likelihood function represents the probability of drawing the N measurements of the random variable given a certain set of values for the parameters θ, so optimizing this quantity should yield the parameter values that best describe the sample. The PDFs can be quite complicated, reflecting several hypotheses for the source of the measurement (e.g. whether it is signal or background), or the fact that the outcome of the experiment requires several random variables to be described:

---

[1]Unbiased in this context means that the deviation of the expectation of an estimator of parameter θ from the true value of that parameter θ_0 is zero for any number of measurements

$$\mathcal{P}\left(X_i, Y_i; \theta\right) = \sum_{j=1}^{M} \mathcal{P}_j\left(X_i, Y_i; \theta\right) = \sum_{j=1}^{M} \mathcal{Q}_j\left(X_i; \theta_{\mathcal{Q}}\right) \mathcal{R}_j\left(Y_i; \theta_{\mathcal{R}}\right) \qquad (3.21)$$

where M is the number of hypotheses, X_i and Y_i are the outcomes of the i-th experiment and in the last equality it has been assumed that the two random variables are uncorrelated and, therefore, that their joint PDF $\mathcal{P}$ can be written as a product of their individual PDFs $\mathcal{Q}$ and $\mathcal{R}$.

Eq. (3.20) is not usually applied as such, but with a slight modification to ease its computation. Taking logarithms, it can be rewritten as

$$\ell = -\log L = -\sum_{i=1}^{N} \log \mathcal{P}\left(X_i, \theta\right), \qquad (3.22)$$

where the sum of logarithms is far more manageable in terms of machine precision than the previous product. The minus sign has been introduced so that the optimization of the likelihood function is performed by minimizing ℓ. In the likelihood fitting package `Laura++` [69], used in the $B^0 \rightarrow K_S^0 \pi^+ \pi^-$ analyses, this is carried out numerically via an interface to `Minuit` [70, 71] through `ROOT` [72]. It should be noted that $\hat{\theta}$ is also a random variable, since it is a function of the X_i. If a second sample is taken, $\hat{\theta}$ will have a different value and so on. The estimator is thus also described by a probability distribution. This leads to a question what is the uncertainty of the estimator. In general the error is given by the standard deviation of the estimator distribution. This can be calculated from L since L is just the probability for observing the sampled values X_1, X_2,..., X_N. Since these values are used to calculate $\hat{\theta}$, L is related to the distribution of $\hat{\theta}$. Therefore, the variance is then:

$$\sigma^2(\hat{\theta}) = \int (\hat{\theta} - \theta)^2 L(X|\theta) dX_1 dX_2...dX_N. \qquad (3.23)$$

This formula, unfortunately, can be solved analytically only for a few simple cases. An easier, but only approximate method which works in the limit of large numbers, is to calculate the inverse second derivative of the log-likelihood

function evaluated at the maximum [67]:

$$\sigma^2(\hat{\theta}) \simeq \left(\frac{d^2 \ln L}{d\theta^2} \right)^{-1}. \tag{3.24}$$

If there is more than one parameter, the matrix of the second derivatives must be formed:

$$U_{ij} = -\frac{\partial^2 \ln L}{\partial \theta_i \partial \theta_j}. \tag{3.25}$$

The diagonal elements of the inverse matrix then give the approximate variances:

$$\sigma^2(\hat{\theta}_i) \simeq (U^{-1})_{ii}. \tag{3.26}$$

Because of these limitations these methods for the estimator error determination could not be used in analyses such as $B^0 \to K_S^0 \pi^+ \pi^-$. Instead, the so called *likelihood ratio* and *likelihood integral* methods are used. In the likelihood ratio approach the *zeta*% confidence interval is found by finding the points where the logarithm of the likelihood function falls by an amount $d(\zeta)$ from its maximum value (for a 68% confidence level $d(\zeta) = 1/2$). In the likelihood integral approach the ζ% confidence interval is determined by finding points which contain ζ% of the area under the likelihood function. Which one of these methods will be used depends on many factors. It can be shown [73] that the likelihood ratio approach is in general better since even in the situation where likelihood is not an approximately normal distribution this approach can give the correct result.

There is an additional problem concerning unbinned likelihood fits, which is the goodness of fit. The value of the likelihood does not provide the goodness of fit between the data and the PDF. If the analysed sample is large, it is convenient to bin the values in a histogram in order to estimate the goodness of fit. It can be shown [23] that in order to compare two hypotheses the difference between values of the corresponding likelihood fits can be used, since the distribution $-2\Delta \ln L(X|\theta)$ follows the χ^2 distribution with degrees of freedom equal to the difference in the number of parameters between the two models.

3.6.1 Extended Maximum Likelihood fits

The above descriptions all take the normalisation of the PDFs to be unity. In fact it is often the case that the normalisation depends on an event yield, which is distributed according to a Poisson distribution with mean ν. In these circumstances it is better to use the *extended* likelihood function [67]:

$$\mathcal{L}(\nu|\theta) = \frac{\nu^N e^{-\nu}}{N!} \prod_{i=1}^{N} P(X_i, \theta) = \frac{e^{-\nu}}{N!} \prod_{i=1}^{N} \nu \, P(X_i, \theta), \qquad (3.27)$$

or:

$$l = -\log \mathcal{L}(\nu|\theta) = \nu + \log N! - \sum_{i=1}^{N} \log \nu P(X_i, \theta). \qquad (3.28)$$

3.7 The $_s\mathcal{P}lot$ technique

The $_s\mathcal{P}lot$ technique is a statistical tool which allows to unfold a distribution of events of interest in a given variable, when these events are part of the data sample populated by several sources of events (i.e signal, background...) [74]. This technique is applicable in the case when the data sample is analysed using a maximum Likelihood method. As explained earlier, to construct a likelihood function (Eq. (3.20)), one usually starts from a set of discriminating variables for which the distribution of all the sources of the events is known. Once the likelihood fit has been performed and the values of fitted parameters found, using the $_s\mathcal{P}lot$ technique it is possible to reconstruct the distributions of other (control) variables for which one does not have any a priory knowledge. That is possible for each of the various sources of events.

Except for the possibility to find information about a priori unknown characteristics of different types of events, the $_s\mathcal{P}lot$ technique gives a possibility to perform a quality check of the Likelihood fit by examining the distribution of control variables. If the distribution of one of the control variables is known for at least one of the sources of events, simple comparison between the fitted and

known distribution can give us the quality of the fit. If that is not the case, one of the discriminating variables can always be removed from the Likelihood function, the fit performed, distribution of the removed variable unfolded and compared to the one expected from the data sample.

Taking into account that the analysed data sample consists of events coming from the different sources, the log-Likelihood function (Eq. (3.28)) can be rewritten as following:

$$-l = \log \mathcal{L} = \sum_{e=1}^{N} \log \sum_{j=1}^{N_s} \nu_j P_j(y_e) - \sum_{j=1}^{N_s} \nu_j, \qquad (3.29)$$

where

- N is the total number of events in the data sample,

- N_s is the number of the species of events populating the data sample,

- ν_j is the number of events expected on average for the jth species,

- y_j is the set of discriminating variables,

- P_j is the PDF of the discriminating variables for the jth species,

- $P_j(y_e)$ is the value of the PDF P_j for event e.

It can be shown (details of the calculation are given in [74]) that the true distribution $(\mathbf{M_n}(x))$ of a control variable x for events of nth species can be derived from the x-distribution $(\tilde{M}_n(x))$ obtained by histograming events:

$$\left\langle \nu_n \tilde{M}_n(\bar{x}) \right\rangle = \nu_n \mathbf{M_n}(\bar{x}). \qquad (3.30)$$

The x-distribution $\tilde{M}_n$ is defined as:

$$\nu_n \tilde{M}_n(\bar{x}) \delta x \equiv \sum_{e \subset \delta x} \mathbf{s P_n}(y_e), \qquad (3.31)$$

where the sum $\sum_{e \subset \delta x}$ runs over the $\nu_{\delta x}$ events for which the value of the variable x lies in the bin centred on the $\bar{x}$ and of total width δx. The values

$\mathbf{sP_n}(y_e)$ are weights (so called sWeights), which in the case when the control variable x is not correlated with the discriminating variables y, are defined as:

$$\mathbf{sP_n}(y_e) = \frac{\nu_n P_n(y_e)}{\sum_{k=1}^{N_s} \nu_k P_k(y_e)}, \qquad (3.32)$$

In the case when the control variable can be expressed as a function of discriminating variables the weights should be calculated as follows:

$$\mathbf{sP_n}(y_e) = \frac{\sum_{j=1}^{N_s} \mathbf{V}_{nj} P_j(y_e)}{\sum_{k=1}^{N_s} \nu_k P_k(y_e)}, \qquad (3.33)$$

where $\mathbf{V}_{nj}$ is variance matrix $(\partial^2(-l)/\partial\nu_n\partial\nu_j)$.

Also, the authors show that for the expected number of events per x-bin indicated by $_s\mathcal{P}lots$, the statistical uncertainties are calculated simply as:

$$\sigma\left[\nu_n \tilde{M}_n(\bar{x})\delta x\right] = \sqrt{\sum_{e \subset \delta x} (\mathbf{sP_n})^2}. \qquad (3.34)$$

Chapter 4

Analysis Method

In this chapter a detailed analysis of the $B^0/\bar{B}^0 \to K_S^0\pi^+\pi^-$ decay is presented. It starts with the event selection procedure, followed by the analysis of signal and background events. The models used to describe the different species of events will be given and the construction of the likelihood function used to fit the $B^0/\bar{B}^0 \to K_S^0\pi^+\pi^-$ Dalitz plot will be explained. This will be followed by the results of the tests performed to ensure that the fit is performed correctly. The $B^0/\bar{B}^0 \to K_S^0\pi^+\pi^-$ transition is a charmless B meson decay. Since the most probable way for a B meson to decay is via the $b \to c$ quark transition, charmless B meson decays suffer from small branching fractions (usually of the order of 10^{-6}). Because of that special attention is paid to the study of background events. Background events will be mentioned many times in the following chapters so the different types of background events are listed here. Two types of background are considered:

- **Continuum events.** These events originate from the $e^+e^- \to q\bar{q}$ processes, where q is a light quark (u, d, c or s quark).

- $B\overline{B}$ **background events.** These events originate from $B\overline{B}$ decays to the channels different from $K_S^0\pi^+\pi^-$, but because their topology is similar to the signal channel they can be misinterpreted as signal events.

4.1 Event Selection

The selection of $B^0/\bar{B}^0 \to K_S^0 \pi^+ \pi^-$ events is performed in two stages. First, the B candidates are formed from a K_S candidate and two oppositely charged particles which satisfy the `GoodTracksLoose` list criteria (see Chapter 3). As described in Chapter 3, a K_S candidate is constructed from any two oppositely charged tracks (assumed to be pions) whose invariant mass is within 25 MeV/c^2 of the PDG value of the K_S meson mass. The initial cuts that a B candidate has to pass are:

- $m_{\mathrm{ES}} > 5.2\,\mathrm{GeV}/c^2$,

- $4.99\,\mathrm{GeV} < E^* < 5.59\,\mathrm{GeV}$,

- total energy of the event $E_{\mathrm{TOTAL}} < 20.0\,\mathrm{GeV}$.

Here E^* is the centre-of-mass energy of the B candidate.

In the next stage, additional cuts on K_S^0-quality related variables and background discriminating variables are applied:

- The decay vertex of the K_S^0 candidate is required to be separated from the B meson decay vertex by at least twenty times the uncertainty in the measurement of the separation of the vertex positions. This value is found to be the optimal after the distributions of $\tau_{K_S^0}/\sigma_{\tau_{K_S^0}}$ for signal MC and continuum background events were compared. Here $\tau_{K_S^0}$ denotes K_S^0 meson lifetime.

- The cosine of the angle between the momentum of the K_S^0 and the line that joins its decay vertex with that of the B candidate must be greater than 0.999.

- The mass requirement on the K_S^0 candidate is tightened to $|m_{\pi^+\pi^-} - m_{K_S^0}| < 15\,\mathrm{MeV}/c^2$. Here, π^+ and π^- correspond to the pions used to reconstruct the K_S^0 candidate.

- The K_S^0 vertex probability is required to be greater than 10^{-6}.

- The charged tracks are required to satisfy the `PiLoose` requirements (Section 3.5.3). Comparing different PID selectors it was found that the choice of `PiLoose` maximizes the signal sensitivity, defined as $\sqrt{S}/\sqrt{S+B}$ (S and B denote the number of signal and background events passing the selection criteria, respectively). At the same time, the `PiLoose` list criteria minimises possibility that charged tracks likely to be electrons are selected.

- Very loose cuts on Δt and its error are applied, following the standard *BABAR* procedure: $|\Delta t| < 20\,\mathrm{ps}$ and $\sigma_{\Delta t} < 2.5\,\mathrm{ps}$.

- The MLP variable is calculated and required to be MLP > 0.367, so that the background coming from the light quark production (continuum background) is lowered to 30% of its original size. This cut decreases the number of signal events by only around 10%.

- Cuts on the kinematic variables m_{ES} and ΔE are applied to select three regions of interest in the m_{ES}-ΔE plane (see Figure 4.1):

  a) the **signal region**, where true $B^0 \to K_S^0 \pi^+ \pi^-$ decays are expected, is defined as a three-standard deviation window around the m_{ES} and ΔE peaks: $5.272\,\mathrm{GeV}/c^2 < m_{\mathrm{ES}} < 5.286\,\mathrm{GeV}/c^2$ and $-0.075\,\mathrm{GeV} < \Delta E < 0.075\,\mathrm{GeV}$;

  b) the **grand sideband**:
  $5.20\,\mathrm{GeV}/c^2 < m_{\mathrm{ES}} < 5.26\,\mathrm{GeV}/c^2$ and $-0.075\,\mathrm{GeV} < \Delta E < 0.075\,\mathrm{GeV}$;

  c) the **upper sideband**:
  $5.20\,\mathrm{GeV}/c^2 < m_{\mathrm{ES}} < 5.286\,\mathrm{GeV}/c^2$ and $0.1\,\mathrm{GeV} < \Delta E < 0.3\,\mathrm{GeV}$.

  Events in the grand sideband and upper sideband are used to study the continuum distributions (see Section 4.4).

- Events with:

$$m_{K_S^0 \pi^+} \text{ (or } m_{K_S^0 \pi^-}) \in [1.744, 1.944] \text{ GeV}/c^2$$

or

$$m_{\pi^+ \pi^-} \in [3.037, 3.157] \cup [3.626, 3.746] \text{ GeV}/c^2,$$

are rejected. In these regions a large number of background events coming from decays of B mesons into charm and charmonium resonances are expected (more details in Section 4.3).

In about 5% of the selected events it was possible to construct more than one B candidate that satisfies the above criteria. In that case, the candidate with the highest B-vertex probability from the mass-unconstrained fit (see Section 3.5.4) was chosen.

The efficiency of each of these cuts, as well as the overall efficiency, has been evaluated from a phase space MC (flat distribution of signal events over Dalitz plot) and from the MC generated according to the Dalitz plot model described in [75] (resonant MC). The results are shown in Table 4.1.

4.1.1 Event selection efficiency and self cross feed events

The total event selection efficiency is defined as the fraction of signal events that have passed the selection criteria. The event selection efficiency is not uniform over the Dalitz plot, because events with different kinematic properties populate the different areas of the Dalitz plot. As mentioned in Section 1.4.1, the corners of the Dalitz plot are populated with events in which one of the final particles has very low momentum. The low momentum particles are difficult to reconstruct, so it should be expected that the event selection efficiency is lower in the corners than in the centre of the Dalitz plot. Such a trend can be seen in Figure 4.2, where the plot on the left shows the event selection efficiency as a function of the Dalitz coordinates.

The difficulties in the reconstruction of the low momentum tracks make misreconstruction of these tracks likely. The poor quality of reconstruction increases the probability of them being assigned to the wrong B candidate. This can

Table 4.1: *Summary of cut efficiencies evaluated from MC with no structure across the Dalitz Plot (left) and with a resonant structure taken from [76] (right). The efficiency for each selection criterion is calculated relative to the sample of events passing the previous requirement. The last three rows show the absolute efficiency for the three regions of interest in the m_{ES}-ΔE plane. The overall efficiency depends on the resonant content of the Dalitz plot, and is only known after the fit to data is performed, so the quoted uncertainties are statistical only.*

| | Efficiency (%) for $B^0 \to K^0_S \pi^+ \pi^-$ | |
Selection requirement	Phase space MC	Resonant MC
First stage selection,	40.8	42.2
vertexing and reconstruction		
Pion PID requirements	93.8	94.0
Electron veto	97.1	97.3
$E_{\mathrm{tot}} < 20\,\mathrm{GeV}$	99.1	99.0
$\mathrm{MLP} > 0.367$	90.2	89.9
$|m_{\pi^+\pi^-} - m_{K^0_S}| < 15\,\mathrm{MeV}/c^2$	96.3	96.7
$\tau_{K^0_S}/\sigma_{\tau_{K^0_S}} > 20$	91.3	92.0
$\cos\alpha_{K^0_S} > 0.999$	98.5	98.4
K_S vertex probability $> 10^{-6}$	97.7	97.6
$|\Delta t| < 20\,\mathrm{ps}$	98.0	98.0
$\sigma_{\Delta t} < 2.5\,\mathrm{ps}$	97.9	98.0
$5.20\,\mathrm{GeV}/c^2 < m_{\mathrm{ES}} < 5.286\,\mathrm{GeV}/c^2$	99.2	99.2
$-0.075\,\mathrm{GeV} < \Delta E < 0.3\,\mathrm{GeV}$	93.2	93.1
Veto D, J/ψ and $\psi(2S)$	84.1	86.6
Signal Region:	19.981	19.773
$\pm$ statistical uncertainty	0.014	0.032
Upper Sideband:	0.294	0.829
$\pm$ statistical uncertainty	0.002	0.007
Grand Sideband:	0.279	0.580
$\pm$ statistical uncertainty	0.002	0.006
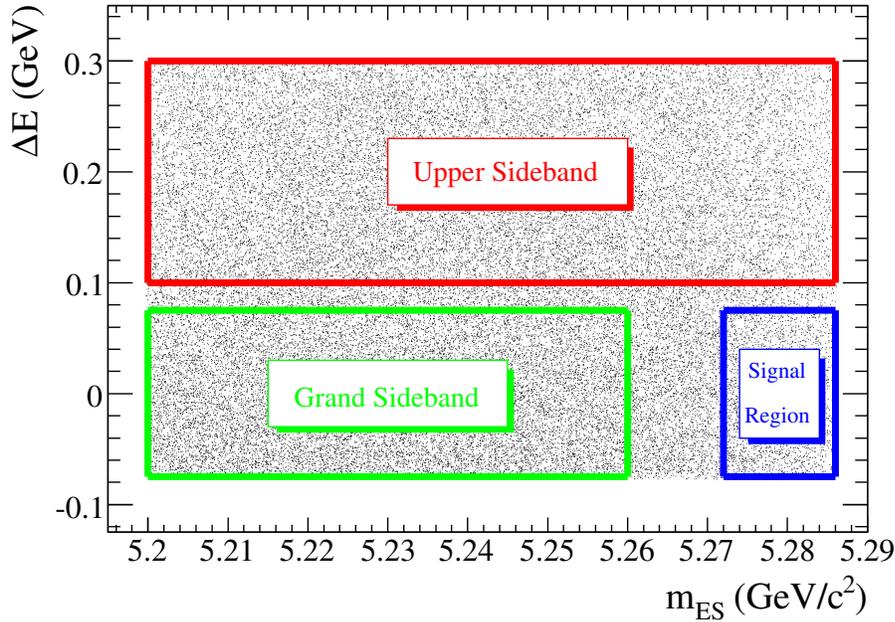
Figure 4.1: *Signal region (blue), grand sideband (green) and upper sideband (red). Events in the signal region are used for the full time-dependent amplitude fit. Events from the grand and upper sidebands are used to extract the continuum distributions of the variables used in the fit.*

either make a background event match the $K_S^0\pi^+\pi^-$ final state (resulting in selection of that event as signal candidate), or change the properties of a true $B^0 \to K_S^0\pi^+\pi^-$ event. If a true signal event is misreconstructed the assignment of an incorrect track to the candidate will change the balance of energy and momentum among the three particles in the final state, and such an event will be reconstructed at the wrong Dalitz plot position. The misreconstructed signal is usually called *self cross feed* (SCF). A schematical interpretation of the misreconstruction of the low momentum particles is shown in Figure 4.3.

The fraction of this kind of events, calculated across the Dalitz plot, defined as the number of events that are reconstructed as self cross feed divided by the total number of events that are reconstructed, is plotted in Figure 4.2
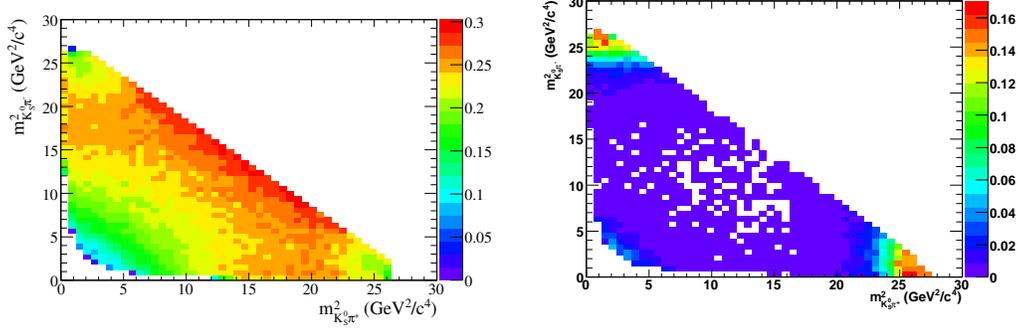
Figure 4.2: *Efficiency (left) and self cross feed fraction (right) as a function of the Dalitz coordinates. The drop in the efficiency in the corners of the Dalitz plot is clearly visible. Higher misreconstruction probability of the low momentum tracks results in a higher fraction of self cross feed in the slow pion corners ($m^2_{K^0_S \pi^\pm} > 23\,\mathrm{GeV}/c^2$) of the Dalitz plot. The small fraction of self cross feed events in the low K^0_S momentum corner of the Dalitz plot is a result of the selection requirements on the K^0_S lifetime significance and the K^0_S-vertex probability.*
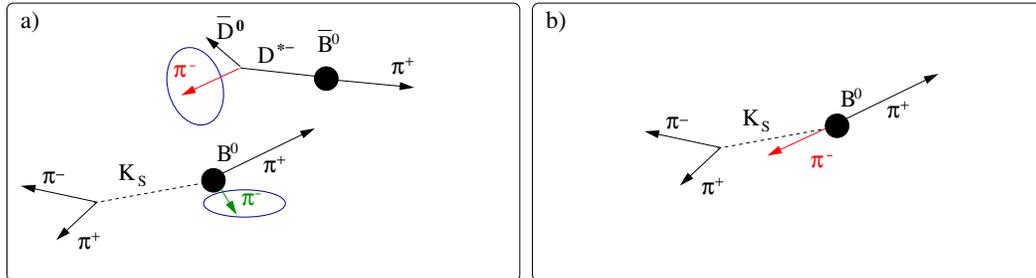
Figure 4.3: *Example of a self cross feed event. a) One of the B mesons from the $e^+e^- \rightarrow B^0\bar{B}^0$ event decays into the signal, $K^0_S \pi^+\pi^-$ final state, while the other decays into the $D^{*-}\pi^+$ final state. Instead of reconstructing the low momentum π^- (green) as a part of the signal, a negative pion from the other B meson decay (red) is reconstructed. The reconstructed signal candidate is shown in b).*

(right). The fraction of self cross feed events is larger in the corners of the Dalitz plot, the areas most sensitive to the interference between the resonances. Consequently it is necessary to analyse the impact of the self cross feed events on the reconstruction of the phases between the resonant components of the signal. Fits to MC simulated events, reconstructed in exactly the same way as real data, showed that the extraction of the phases is not affected by neglecting the presence of the SCF events (Section 5.1.2).

4.2   Signal Events

The aim of this Dalitz plot analysis is to extract the relative magnitudes and phases of all sub-processes that lead to the desired final state, and from these to calculate the asymmetries. In this analysis of $B^0 \to K_S^0 \pi^+ \pi^-$, an unbinned maximum likelihood fit of the Dalitz plot is performed. Since events that pass the selection criteria are a mixture of signal and background events, the total likelihood function is built from parts that model different event species. The likelihood function used to describe the signal events is the following:

$$
\mathcal{L}\left(m_{K_S^0\pi^+}^2, m_{K_S^0\pi^-}^2, \Delta t, q_{\text{tag}}\right) \;=\; \frac{1}{\mathcal{N}} \sum_c f_c \frac{e^{-|\Delta t|/\tau_{B^0}}}{4\tau_{B^0}} \times \tag{4.1}
$$

$$
\left[\left(|\mathcal{A}|^2 + |\overline{\mathcal{A}}|^2\right)\left(1 + q_{\text{tag}}\frac{\Delta \mathcal{D}^c}{2}\right) \right.
$$

$$
- q_{\text{tag}}\langle \mathcal{D}\rangle^c \left(|\mathcal{A}|^2 - |\overline{\mathcal{A}}|^2\right)\cos\left(\Delta m_d \Delta t\right)
$$

$$
+ q_{\text{tag}}\langle \mathcal{D}\rangle^c 2\mathrm{Im}\left[\overline{\mathcal{A}}\mathcal{A}^* e^{-i\phi_{\text{mix}}}\right]\sin\left(\Delta m_d \Delta t\right)
$$

$$
\left. \right] \otimes \mathcal{R}_{sig}^c(\Delta t,\ \sigma_{\Delta t}),
$$

$$
\mathcal{N} = \int_{DP}\left(|\mathcal{A}|^2 + |\overline{\mathcal{A}}|^2\right) dm_{K_S^0\pi^+}^2\, dm_{K_S^0\pi^-}^2. \tag{4.2}
$$

Here, c labels the tagging categories, f_c is the fraction of the events in tagging category c, $\mathcal{D}$ and $\Delta \mathcal{D}$ are the dilution and dilution difference (see Chapter

3) and $\mathcal{R}_{sig}(\Delta t,\ \sigma_{\Delta t})$ is the Δt resolution function. This formula is derived from the production rate formula of the $B^0\bar{B}^0$ system, and dilution, dilution difference and Δt resolution function are introduced in order to reflect the experimental realities of the tagging and the Δt measurements. As mentioned in Chapter 1, the Dalitz amplitudes $\mathcal{A}$ (for $B^0 \to K_S^0\pi^+\pi^-$ decay) and $\bar{\mathcal{A}}$ (for $\bar{B}^0 \to K_S^0\pi^+\pi^-$ decay) are parameterized as a sum of all resonances included in the model:

$$\mathcal{A}\left(m^2_{K_S^0\pi^+}, m^2_{K_S^0\pi^-}\right) = \sum_{j=1}^{N} c_j F_j\left(m^2_{K_S^0\pi^+}, m^2_{K_S^0\pi^-}\right), \qquad (4.3)$$

$$\bar{\mathcal{A}}\left(m^2_{K_S^0\pi^+}, m^2_{K_S^0\pi^-}\right) = \sum_{j=1}^{N} \bar{c}_j F_j\left(m^2_{K_S^0\pi^+}, m^2_{K_S^0\pi^-}\right), \qquad (4.4)$$

where F_j is the Dalitz plot PDF shape of the resonance j, and c_j (isobar coefficients) are complex numbers, whose values are the final result of the Dalitz plot fit. In this analysis the signal model was established containing the following resonances:

- $B^0 \to f_0(980)K_S^0$, $f_0(980)\to \pi^+\ \pi^-$,

- $B^0 \to \rho^0(770)K_S^0$, $\rho^0(770)\to \pi^+\ \pi^-$,

- $B^0 \to K^{*+}(892)\pi^-$, $K^{*+}(892)\to K_S^0\ \pi^+$,

- $B^0 \to K_0^{*+}(1430)\pi^-$, $K_0^{*+}(1430)\to K_S^0\ \pi^+$,

- $B^0 \to f_0(1300)K_S^0$, $f_0(1300)\to \pi^+\ \pi^-$,

- $B^0 \to f_2(1270)K_S^0$, $f_2(1270)\to \pi^+\ \pi^-$,

- $B^0 \to \chi_{c0}K_S^0$, $\chi_{c0} \to \pi^+\ \pi^-$,

- $B^0 \to K_S^0\ \pi^+\ \pi^-$, non resonant

With seven resonances and one non resonant term in the model there are 30 parameters (four for each mode, see Chapter 1; two parameters for the $K^*(892)$ resonance(δX and ΔY) are fixed) that the fit has to return in order to describe

101

the signal. The number of parameters is a good indication of the complexity of the fit.

4.2.1   Treatment of Self Cross Feed

As already mentioned, assigning a wrong track to the signal event changes the properties of that event. The Dalitz plot coordinates of such an event will differ from the true values. The SCF events can either be treated as a background to the properly reconstructed signal events, or used to extract the physics information still available by statistically tracing their true Dalitz plot positions. The second option is used to model the SCF events in the Dalitz plot fitter `Laura++`. In order to recognise SCF events, having in mind that their main characteristic is that they migrate over the Dalitz plot, the distribution of the following variable is used:

$$\delta p_i = \frac{|p_i^{\mathrm{reco}}| - |p_i^{\mathrm{true}}|}{\sigma_i^{\mathrm{reco}}} \quad i = K_S^0, \pi^+, \pi^-, \tag{4.5}$$

where $|p_i^{\mathrm{reco}}|$ is the momentum of the reconstructed daughter particle i, $|p_i^{\mathrm{true}}|$ is the true value of the particle's momentum, and σ_i^{reco} is the uncertainty of $|p_i^{\mathrm{reco}}|$. The distribution of δp for correctly reconstructed B meson daughter particles should peak sharply around zero, while the values of δp for misreconstructed particles should significantly differ from zero. The distribution of this variable for reconstructed π^+ mesons is shown in Figure 4.4. Using δp, an event is defined as SCF if the absolute value of δp for any of the B meson daughter particles is greater than 15:

$$|\delta p_i| = \left| \frac{|p_i^{\mathrm{reco}}| - |p_i^{\mathrm{true}}|}{\sigma_i^{\mathrm{reco}}} \right| > 15. \tag{4.6}$$

The optimal value of the cut on $|\delta p|$ is chosen by looking at the distributions of ΔE and m_{ES} for the selected SCF events. If a too tight cut on $|\delta p|$ is applied the distributions of ΔE and m_{ES} for events selected as SCF will resemble the distribution of correctly reconstructed signal events (see Section 4.5.4) The distribution of events selected as SCF, applying the above value of the cut on
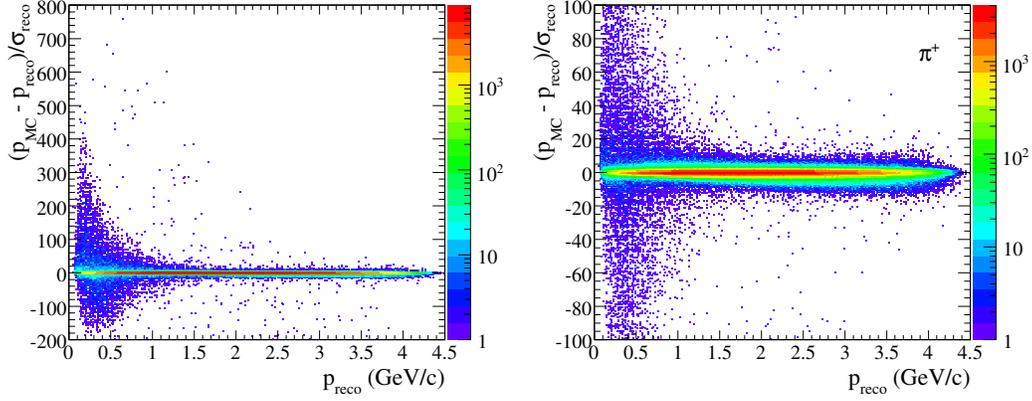
Figure 4.4: *Plots showing the ratio of reconstructed minus true momentum over the reconstruction error for the pion candidates: on the left, the whole range and on the right, a zoom in the central region, where it can be seen that for most pions, the absolute value of the ratio is below 15.*

$|\delta p|$ is shown in Figure 4.5. From Figure 4.6 it can be seen that the chosen cut
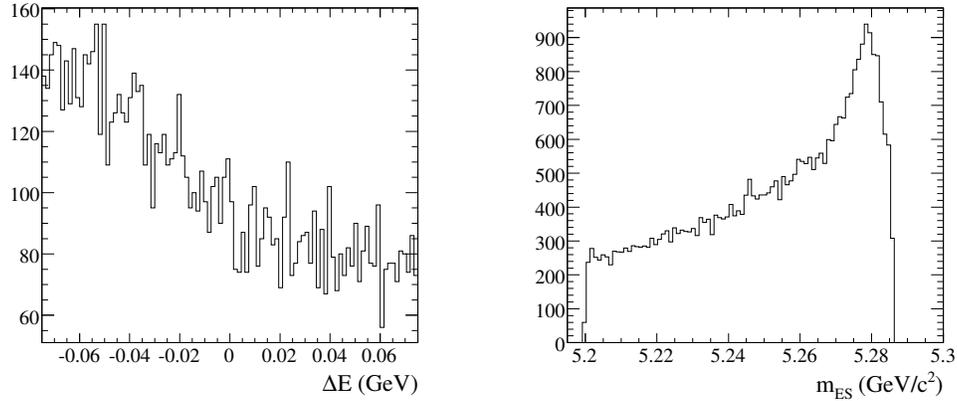
Figure 4.5: ΔE *(left) and* m_{ES} *(right) distributions for self cross feed events. The latter peaks at* $5.28\,\mathrm{GeV}/c^2$*, as signal should,but presents a long tail due to the misreconstruction.* ΔE *exhibits an even more combinatorial profile, and shows no enhancement at the origin, which proves the correct separation of SCF from TM.*

value ensures that an event classified as self cross feed migrates significantly over the Dalitz plot. The events in which migration can be neglected (*truth-matched*), are assumed to have been reconstructed with perfect experimental resolution in the Dalitz plot coordinates. This assumption is valid as long as the distances between their true and reconstructed positions are small compared to the typical widths of the Dalitz plot structures. In the case of the $B^0 \to K_S^0 \pi^+ \pi^-$ analysis, the narrowest resonance is the $K^*(892)$, with a width of $(50.8 \pm 0.9)\,\mathrm{MeV}/c^2$ [23], and the previous assumption on the resolution is guaranteed to hold by the above inequalities (Figure 4.6).

Defining the SCF events in this way makes it possible to calculate the migration probability for these events (probability that an event which originates at $(x_{\mathrm{true}}, y_{\mathrm{true}})$ position in the Dalitz plot migrates to $(x_{\mathrm{reco}}, y_{\mathrm{reco}})$ position). In Figure 4.7 the migration probability histogram for events originating from the same bin of the Dalitz plot is shown.
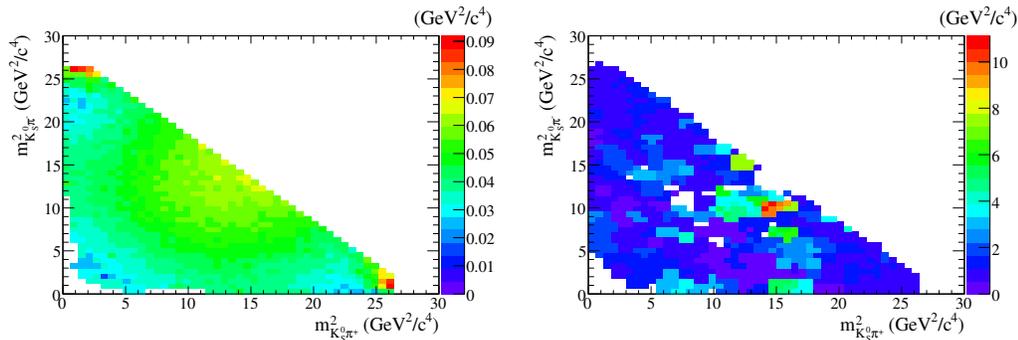
Figure 4.6: *Average distance between the reconstructed and the true position of truth-matched (left) and self cross feed (right) events, plotted at the reconstructed position. For the former it is rather small, demonstrating the validity of neglecting the experimental resolution. In the case of SCF it takes on average values around $1 - 2\,\mathrm{GeV}^2/c^4$ for events originating in the corners, occasionally reaching $\sim 10\,\mathrm{GeV}^2/c^4$.*
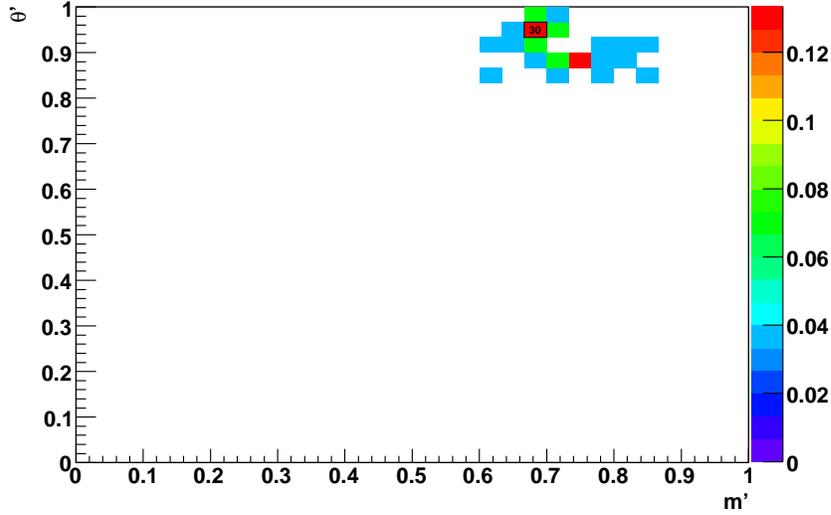
Figure 4.7: *One migration probability histogram is plotted (in the square Dalitz plot), depicting the probability of migration for a single bin. The number in the bin near the top right corner is the number of self cross feed events found in the MC originating at that bin. (i.e. $x_{\text{true}}, y_{\text{true}}$). The coloured bins around it represent the probability for those events to migrate to each of the bins.*

Formalism

The experimentally measured distribution of any of the variables used to describe a physical process differs from the true distribution of that variable. This is a consequence of the experimental uncertainties of the measurements. The experimentally obtained distribution of a variable can be written as:

$$\mathcal{P}^{\text{observed}} = \mathcal{P}^{\text{true}} \otimes \mathcal{R}^{\text{total}}. \tag{4.7}$$

Here, $\mathcal{P}^{\text{true}}$ is the true distribution of the variable and $\mathcal{R}^{\text{total}}$ is a resolution function which describes the detector and reconstruction effects, and the symbol $\otimes$ denotes operation of convolution of functions $\mathcal{P}^{\text{true}}$ and $\mathcal{R}^{\text{total}}$.

In the case when different contributions to the resolution function are not

correlated, the resolution function can be split into several parts:

$$\mathcal{R}^{\text{total}} = \epsilon\left(x, y\right) \mathcal{R}^{\text{migration}} \mathcal{R}^{\Delta t} . \tag{4.8}$$

Here, ϵ represents the Dalitz plot-dependent efficiency, and $\mathcal{R}^{\Delta t}$ is the Δt resolution function for signal events described in Section 3.2.

Having in mind that SCF events migrate significantly over the Dalitz plot, unlike the correctly reconstructed events, the part of the resolution function describing events migration can be written as:

$$
\begin{aligned}
\mathcal{R}^{\text{migration}} &\left(x_{\text{reco}}, y_{\text{reco}}; x_{\text{true}}, y_{\text{true}}\right) = \\
&\left(1 - f_{\text{SCF}}\left(x_{\text{true}}, y_{\text{true}}\right)\right) \delta\left(x_{\text{reco}} - x_{\text{true}}\right) \delta\left(y_{\text{reco}} - y_{\text{true}}\right) + \\
&f_{\text{SCF}}\left(x_{\text{true}}, y_{\text{true}}\right) \mathcal{R}^{\text{SCF}}\left(x_{\text{reco}}, y_{\text{reco}}; x_{\text{true}}, y_{\text{true}}\right)
\end{aligned}
\tag{4.9}
$$

where f_{SCF} is the fraction of self cross feed events, and the function $\mathcal{R}^{\text{SCF}}$ represents the probability for a self-cross-feed event originally at $\left(x_{\text{true}}, y_{\text{true}}\right)$ to migrate to $\left(x_{\text{reco}}, y_{\text{reco}}\right)$ (Figure 4.7). Assuming the same Δt resolution model for truth-matched and self cross feed, $\mathcal{P}^{\text{observed}}$ becomes:

$$
\begin{aligned}
&\mathcal{P}^{\text{observed}}\left(x_{\text{reco}}, y_{\text{reco}}, \Delta t\right) = \\
&\frac{\epsilon\left(1 - f_{\text{SCF}}\right) \mathcal{P}^{\text{true}} + \iint_{\text{DP}} \mathcal{P}^{\text{true}} \epsilon f_{\text{SCF}} \mathcal{R}^{\text{SCF}} dx_{\text{true}} dy_{\text{true}}}{\iint_{\text{DP},\Delta t, q_{\text{tag}}} \mathcal{P}^{\text{observed}} dx dy} \otimes \mathcal{R}^{\Delta t},
\end{aligned}
\tag{4.10}
$$

where $\mathcal{P}^{\text{true}}$ is the PDF given by Eq. (4.1) without the normalisation factor.

Tests on MC

The formalism described above was implemented in the fitting package `Laura++`, by Pablo del Amo Sánchez, who also performed the extensive tests of the described model. Figure 4.8 shows comparison between the distribution of the SCF events selected from the full resonant MC sample which model consists of 3 resonances ($K^{*\pm}(892)\pi^{\mp}$, $\rho^0(770)K_S^0$ and $f_0(980)K_S^0$) and the distribution of the SCF events generated using the model described previously. It can be seen that the implemented method nicely describes the SCF events.
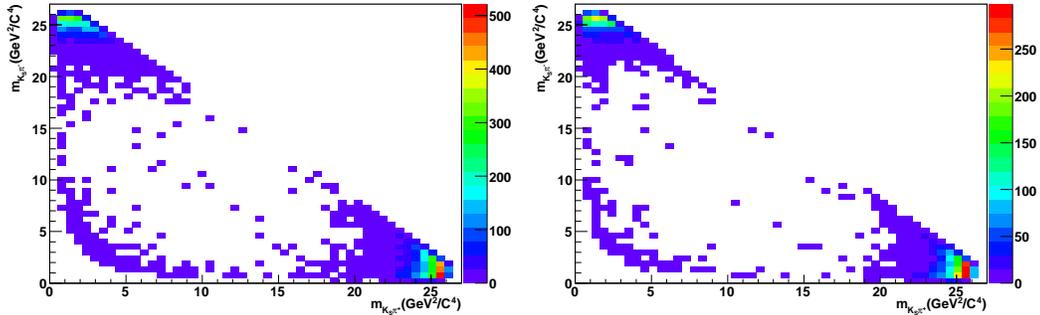
Figure 4.8: *Self cross feed events in full MC (left) and in toy MC generated by the implementation of the procedure described in the text (right).*

Since the number of the excepted SCF events for this analysis was estimated to be small, around $\sim 1\%$ of the total number of events passing the selection criteria, the additional tests on the full MC data are performed in order to see if adding the description of the SCF events improves the fit quality. The signal MC is fitted with and without accounting for the self cross feed events, and the obtained results are compared. It was noticed that the quality of the fit moderately improves when the SCF model is included (the pull plots of the fitted variables were more gausian-like distributed), but the obtained improvements were small compared to the statistical uncertainties on the fitted parameters, which is visible from Table 4.2.

Due to the large increase in computing time in the case when the SCF model was taken into account, compared to the rather small improvement to the fit, it was decided not to treat self cross feed and truth-matched events separately for the present iteration of the $B^0 \rightarrow K_S^0 \pi^+ \pi^-$ analysis.

4.3 Background from B Decays

The $B\overline{B}$ background arises from decays of B mesons to final states different from $K_S^0 \pi^+ \pi^-$, but with kinematic and topological properties similar to the

Table 4.2: *Comparison between fits to full MC with and without separating self cross feed and truth-matched events. The MC was generated according to a three resonance model: $K^{*\pm}(892)\pi^{\mp}$, $\rho^0(770)K_S^0$ and $f_0(980)K_S^0$. The shifts in fitted parameters are shown.*

Parameter	shift = (withSCF - noSCF)
$K^*(892)$ ΔX	-0.04 ± 0.22
$K^*(892)$ ΔY	-0.02 ± 0.16
$\rho^0(770)$ X	0.17 ± 0.23
$\rho^0(770)$ Y	0.15 ± 0.22
$\rho^0(770)$ ΔX	0.02 ± 0.11
$\rho^0(770)$ ΔY	0.13 ± 0.13
$f_0(980)$ X	-0.16 ± 0.18
$f_0(980)$ Y	-0.13 ± 0.20
$f_0(980)$ ΔX	0.05 ± 0.16
$f_0(980)$ ΔY	-0.03 ± 0.14

$B^0 \to K_S^0\pi^+\pi^-$ decay. They are not as abundant as the continuum background (see Section 4.4), but still the expected number of these events in the signal region of the m_{ES}-ΔE plane is estimated to be around 1/3 of that for the signal. These events share many of the characteristics of the signal events. Their distributions of the m_{ES}, ΔE and MLP variables peak close to or at the same point, as those of true $B^0 \to K_S^0\pi^+\pi^-$ events. Therefore, an accurate model of the distributions of the $B\overline{B}$ events is needed. In order to ease the analysis of these events they were split in three groups, according to their Δt properties:

1) **Charged $B\overline{B}$ events**. They decay with a lifetime of the same order of magnitude as that of the signal, but do not mix.

2) **Neutral decays to flavour eigenstates**. They do oscillate, but their final state determines the flavour of the B.

3) **Neutral decays to CP eigenstates**. Their Δt dependence is similar to that of the signal.

In order to identify the most dominant $B\overline{B}$ background modes, generic B^+B^- and $B^0\bar{B}^0$ Monte Carlo samples were analysed. It was found that the expected number of background events coming from a few specific B decay modes is of the same size, or even larger, as the signal. Since the phase spaces of these channels are far smaller compared to the phase space of the charmless $B^0 \to K_S^0\pi^+\pi^-$ decay, it was decided that the corresponding areas of the Dalitz plot should be vetoed.
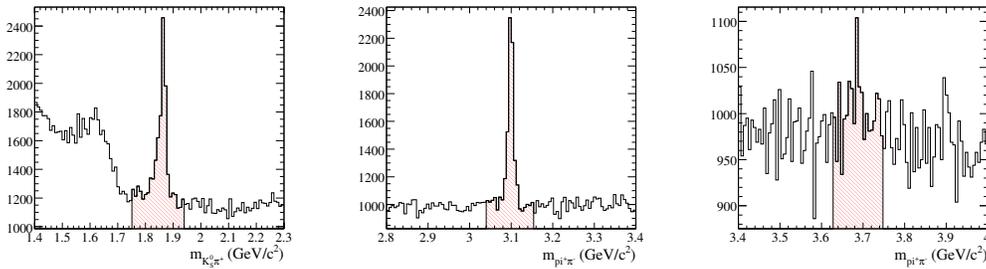
Figure 4.9: *Plots showing the $m_{K_S^0\pi^+}$ and $m_{\pi^+\pi^-}$ ranges in which vetoes are applied. Hatched areas represent the excluded ranges. The first and most prominent one shows the D veto, the second one is the J/ψ veto, and the last one, the $\psi(2S)$ veto.*

In Table 4.3 the vetoed regions of the Dalitz plot are given together with the list of B-background modes that dominate in these regions.

The charmed mode $B^0 \to D^- (\to K_S^0\pi^-)\, \pi^+$, for instance, has a branching fraction greater than that of signal, and similar efficiency, while the charmonium modes $B^0 \to J/\psi\, (\to \ell^+\ell^-)\, K_S^0$ and $B^0 \to \psi(2S)\, (\to \ell^+\ell^-)\, K_S^0$, are background for the $B^0 \to K_S^0\pi^+\pi^-$ mode because the leptons coming from J/ψ and $\psi(2S)$

Table 4.3: *Dalitz-plot vetoes employed against B-backgrounds.*

Decay Mode	Veto Region (GeV/c^2)
$D^{\pm} \to K_S^0 \pi^{\pm}$	$1.744 < m_{K_S^0 \pi^{\pm}} < 1.944$
$J/\psi \to \ell^+ \ell^-$	$3.037 < m_{\pi^+ \pi^-} < 3.157$
$\psi(2S) \to \ell^+ \ell^-$	$3.626 < m_{\pi^+ \pi^-} < 3.746$

can be misreconstructed as pions. Plots showing the $m_{K_S^0 \pi^+}$ and $m_{\pi^+ \pi^-}$ ranges in which vetoes are applied are shown in Figure 4.9.

After applying identical reconstruction and selection algorithms as for the signal, the generic $B^0 \overline{B}^0$ and $B^+ B^-$ MC samples were again searched for remaining B-background modes. All modes contributing more than one event were studied in detail using exclusive MC samples, from which all the PDFs were extracted. The remaining background events are grouped together forming a rather combinatoric-like contribution, without much structure in any of the variables (see Figure 4.10).

In Table 4.4, Table 4.5 and Table 4.6 summaries of the analysed $B^+ B^-$ and $B^0 \overline{B}^0$ background modes are given.
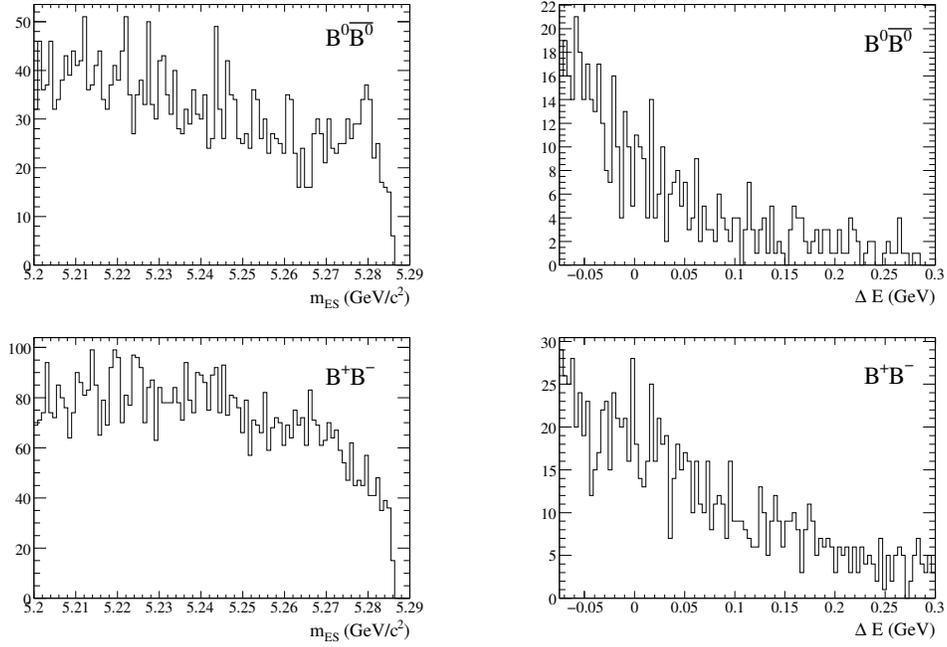
Figure 4.10: *Distributions of* m_{ES}, *(left) and* ΔE, *(right) for combinatoric* $B\overline{B}$ *background. Top (bottom) plots show* m_{ES} *and* ΔE *distributions for combinatoric background coming from neutral (charged) B meson decays.*

Table 4.4: *Summary of B^+B^- background. The values of the branching fractions are taken from either [26] or [23]. The errors on the expected numbers of events arise from the uncertainties on the branching fractions and the statistically limited samples used to evaluate the efficiencies.*

Mode (*CP* conjugate included)	Efficiency	Branching Fraction	Expected events in Signal Region
$B^+ \to \overline{D}^0\pi^+, \overline{D}^0 \to K^+\pi^-$	$(2.62 \pm 0.10) \times 10^{-4}$	$(1.85 \pm 0.07) \times 10^{-4}$	22.5 ± 1.2
$B^+ \to \overline{D}^0\pi^+, \overline{D}^0 \to K^+\pi^-\pi^0$	$(4.08 \pm 0.46) \times 10^{-5}$	$(6.53 \pm 0.35) \times 10^{-4}$	12.4 ± 1.6
$B^+ \to \overline{D}^0\pi^+, \overline{D}^0 \to K^0_S\pi^+\pi^-$	$(4.07 \pm 0.22) \times 10^{-4}$	$(1.39 \pm 0.10) \times 10^{-4}$	26.4 ± 2.4
$B^+ \to D^{*0}\pi^+, D^{*0} \to D^0\pi^0, D^0 \to K^-\pi^+$	$(1.25 \pm 0.13) \times 10^{-4}$	$(1.23 \pm 0.09) \times 10^{-4}$	7.1 ± 0.9
$B^+ \to D^{*0}\pi^+, D^{*0} \to D^0\pi^0, D^0 \to K^-\pi^+\pi^0$	$(6.72 \pm 1.86) \times 10^{-6}$	$(4.34 \pm 0.35) \times 10^{-4}$	1.4 ± 0.4
$B^+ \to D^{*0}\pi^+, D^{*0} \to D^0\pi^0, D^0 \to K^0_S\pi^+\pi^-$	$(8.48 \pm 0.66) \times 10^{-5}$	$(9.25 \pm 0.88) \times 10^{-5}$	3.7 ± 0.5
$B^+ \to D^{*0}\pi^+, D^{*0} \to D^0\gamma, D^0 \to K^-\pi^+$	$(1.43 \pm 0.14) \times 10^{-4}$	$(6.55 \pm 0.70) \times 10^{-5}$	5.2 ± 0.7
$B^+ \to D^{*0}\pi^+, D^{*0} \to D^0\gamma, D^0 \to K^-\pi^+\pi^0$	$(1.24 \pm 0.25) \times 10^{-5}$	$(2.67 \pm 0.27) \times 10^{-4}$	1.5 ± 0.4
$B^+ \to D^{*0}\pi^+, D^{*0} \to D^0\gamma, D^0 \to K^0_S\pi^+\pi^-$	$(8.92 \pm 0.68) \times 10^{-5}$	$(5.69 \pm 0.64) \times 10^{-5}$	2.4 ± 0.3
$B^+ \to D^0\rho^+, D^0 \to K^-\pi^+$	$(3.15 \pm 0.40) \times 10^{-5}$	$(5.12 \pm 0.69) \times 10^{-4}$	7.5 ± 1.4
$B^+ \to a^0_1\pi^+$	$(1.16 \pm 0.11) \times 10^{-4}$	$(2.04 \pm 0.58) \times 10^{-5}$	1.1 ± 0.3
$B^+ \to K^0_S\pi^+$	$(1.49 \pm 0.06) \times 10^{-3}$	$(7.99 \pm 0.35) \times 10^{-6}$	5.6 ± 0.3
$B^+ \to \rho^+\rho^0$ (Longitudinal)	$(2.10 \pm 0.12) \times 10^{-4}$	$(1.82 \pm 0.30) \times 10^{-5}$	1.8 ± 0.3
$B^+ \to \pi^+\pi^+\pi^-$	$(1.72 \pm 0.15) \times 10^{-4}$	$(1.62 \pm 0.15) \times 10^{-5}$	1.3 ± 0.2
$B^+ \to \rho^0 K^{*+}, K^{*+} \to K^0_S\pi^+$ (Longitudinal)	$(4.38 \pm 0.11) \times 10^{-3}$	$(5.08 \pm 5.08) \times 10^{-7}$	1.0 ± 1.0
$B^+ \to \pi^0\pi^+K^0_S$	$(8.78 \pm 0.05) \times 10^{-3}$	$(1.65 \pm 1.65) \times 10^{-5}$	67.4 ± 67.4
Combinatorics			243.9 ± 2.4
Total Charged B backgrounds			413.4 ± 67.6

Table 4.5: *Summary of the $B^0 \to (flavour\ eigenstate)$ background modes. Whenever a generic decay, e.g. $D^- \to X$, and some of its subdecays are listed, the latter have been subtracted from the former in the calculation of the efficiencies and branching fractions.*

Mode (CP conjugate included)	Efficiency	Branching Fraction	Expected events in Signal Region
$B^0 \to D^-\pi^+, D^- \to K_S^0\pi^-\pi^0$	$(3.45 \pm 0.13) \times 10^{-4}$	$(1.88 \pm 0.14) \times 10^{-4}$	30.1 ± 2.5
$B^0 \to D^-\pi^+, D^- \to K_S^0\pi^-$	$(7.63 \pm 0.20) \times 10^{-4}$	$(3.94 \pm 0.24) \times 10^{-5}$	14.0 ± 1.0
$B^0 \to D^-\pi^+, D^- \to K_S^0 K^-$	$(2.55 \pm 0.08) \times 10^{-3}$	$(7.90 \pm 0.64) \times 10^{-6}$	9.4 ± 0.8
$B^0 \to D^-\pi^+, D^- \to X$	$(1.55 \pm 0.09) \times 10^{-4}$	$(2.44 \pm 0.12) \times 10^{-3}$	176.1 ± 13.5
$B^0 \to D^{*+}\pi^-, D^{*+} \to D^0\pi^+, D^0 \to K^-\pi^+$	$(2.88 \pm 0.22) \times 10^{-4}$	$(7.14 \pm 0.36) \times 10^{-5}$	9.6 ± 0.9
$B^0 \to D^{*+}\pi^-, D^{*+} \to D^0\pi^+, D^0 \to K_S^0\pi^0$	$(6.45 \pm 0.18) \times 10^{-4}$	$(2.11 \pm 0.25) \times 10^{-5}$	6.4 ± 0.7
$B^0 \to D^{*+}\pi^-, D^{*+} \to D^0\pi^+, D^0 \to X$	$(2.48 \pm 0.20) \times 10^{-5}$	$(1.39 \pm 0.18) \times 10^{-3}$	20.5 ± 1.9
$B^0 \to D^{*+}\pi^-, D^{*+} \to D^+\pi^0, D^+ \to K_S^0\pi^+$	$(1.02 \pm 0.02) \times 10^{-3}$	$(1.25 \pm 0.08) \times 10^{-5}$	5.9 ± 0.4
$B^0 \to D^{*+}\pi^-, D^{*+} \to D^+\pi^0, D^+ \to X$	$(3.99 \pm 0.32) \times 10^{-5}$	$(8.35 \pm 0.42) \times 10^{-4}$	15.5 ± 1.5
$B^0 \to D^+\rho^-, D^+ \to K_S^0\pi^+$	$(2.33 \pm 0.14) \times 10^{-4}$	$(1.10 \pm 0.18) \times 10^{-4}$	11.9 ± 2.1
$B^0 \to D^+\rho^-, D^+ \to X$	$(8.42 \pm 1.20) \times 10^{-6}$	$(7.39 \pm 1.18) \times 10^{-3}$	28.9 ± 6.2
$B^0 \to D^0 K_S^0$	$(3.60 \pm 0.04) \times 10^{-3}$	$(2.60 \pm 0.35) \times 10^{-5}$	43.5 ± 6.0
Combinatorics			128.6 ± 2.0
Total $B^0 \to (flavour\ eigenstate)$ backgrounds			470.1 ± 16.8

Table 4.6: *Summary of $B^0 \to (CP$ eigenstate) background modes. Although $a_1^+ \pi^-$, $B^0 \to K^0 \mu^+ \mu^-$ and $B^0 \to \pi^+ \pi^- \pi^0$ are not CP eigenstates, they are not flavour eigenstates either, since the final states can be reached from a $\overline{B}^0$ too. However, for this purpose they can be treated as CP eigenstates.*

Mode	Efficiency	Branching Fraction	Expected events in Signal Region
$B^0 \to \eta' K_s^0, \eta' \to \rho^0 \gamma$	$(1.42 \pm 0.01) \times 10^{-2}$	$(9.54 \pm 0.54) \times 10^{-6}$	62.8 ± 3.7
$B^0 \to a_1^+ \pi^-$ & $B^0 \to a_1^- \pi^+$	$(1.62 \pm 0.05) \times 10^{-4}$	$(3.17 \pm 0.37) \times 10^{-5}$	2.4 ± 0.3
$B^0 \to K_s^0 K_s^0$	$(3.46 \pm 0.04) \times 10^{-2}$	$(3.32 \pm 0.70) \times 10^{-7}$	5.3 ± 1.2
$B^0 \to a_1^0 K_s^0$	$(1.42 \pm 0.06) \times 10^{-3}$	$(2.42 \pm 2.42) \times 10^{-6}$	1.6 ± 1.6
$B^0 \to K^0 \mu^+ \mu^-$	$(1.12 \pm 0.01) \times 10^{-1}$	$(5.69 \pm 2.2) \times 10^{-7}$	29.8 ± 11.5
$B^0 \to \pi^+ \pi^- \pi^0$	$(1.77 \pm 0.10) \times 10^{-4}$	$(3.6 \pm 3.6) \times 10^{-4}$	29.6 ± 29.6
Total *CP* Neutral B backgrounds			161.6 ± 32.0

4.3.1 $B\overline{B}$ Background PDFs

As already mentioned, $B\overline{B}$ background modes were split in three groups, according to their Δt properties. For each group, an appropriate Δt-Dalitz plot model is built.

Charged B background

Since these events do not mix, their Δt dependence is modelled as an exponential decay with an effective lifetime. Their likelihood function is then given as the product of the Δt and Dalitz plot PDFs, convoluted with the usual resolution function:

$$
\begin{aligned}
\mathcal{P}^{j,c}_{B^+B^-} \;=\; & \left[\left(\frac{1 - q_{\text{tag}} A^c_j}{2} \right) \omega^c \frac{P^j_{B^+B^-}(-q_{\text{tag}}; x, y)}{\int \int_{DP} \, P^j_{B^+B^-}(-q_{\text{tag}}; x, y) \, dxdy} \right. \\
& + \left(\frac{1 + q_{\text{tag}} A^c_j}{2} \right) (1 - \omega^c) \frac{P^j_{B^+B^-}(q_{\text{tag}}; x, y)}{\int \int_{DP} \, P^j_{B^+B^-}(q_{\text{tag}}; x, y) \, dxdy} \\
& \left. \right] \times \frac{e^{-|\Delta t^{true}|/\tau_j}}{4\tau_j} \otimes \mathcal{R}^c_{B^+B^-}.
\end{aligned}
\tag{4.11}
$$

Here, the index j refers to the background category, and index c to the tagging category. Different background categories group those $B\overline{B}$ background modes with similar ΔE and m_{ES} distributions. In this analysis the B^+B^- background was split into four different categories. The A_j are tagging category-dependent asymmetries that take into account possible differences between numbers of B^0 and $\overline{B}^0$ tags, $P^c_{B^+B^-}$ are tagging category-dependent Dalitz plot PDFs (two-dimensional histograms), and ω^c are mistag fractions extracted from the MC. Misreconstruction effects cause the (effective) lifetimes τ_j to be mode-dependent and mildly different from the nominal value for charged B mesons. The values of τ_j for different groups are extracted from the MC. The Δt resolution model is taken from the $\sin 2\beta$ analyses [55]. The main contributors to this kind of background are charmed decays of the B^+ meson (as it can be seen from Table 4.4). The $K^0_S \pi^+ \pi^-$ final state is reached through the loss of a

photon or a π^0 during the reconstruction, or through misreconstruction of the low momentum tracks. As an example, in the reconstruction of $B^+ \to \pi^0\pi^+K_S^0$ as $B^0 \to K_S^0\pi^+\pi^-$ the π^0 meson is lost and a charged, low momentum pion from the other B meson in the event is added. The number of events expected in this channel is rather large (~ 70), but it comes with a large error. This is due is the uncertainty on its branching fraction, for which only an upper limit exists. Distributions of m_{ES}, ΔE, MLP and the Dalitz plot for $B^+ \to \pi^0\pi^+K_S^0$ are shown in Figure 4.11.
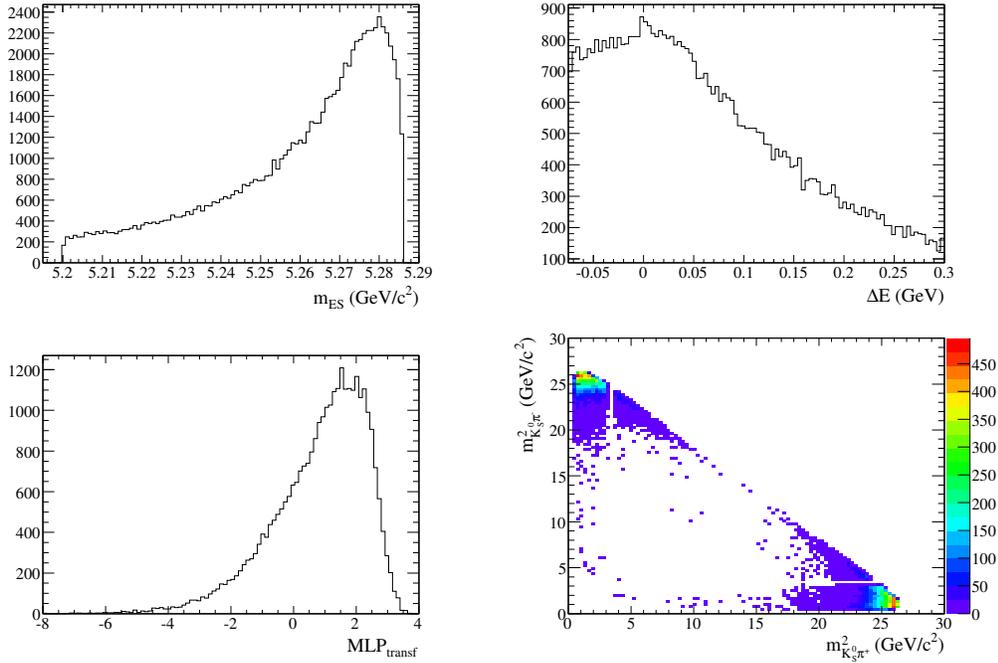
Figure 4.11: *Distributions of (top left) m_{ES}, (top right) ΔE, MLP (bottom left) and Dalitz plot (bottom right) for $B^+/B^- \to \pi^0\pi^\pm K_S^0$. The areas of the Dalitz plot populated by the background events are the low momentum pion corners, indicating that the misreconstruction of $B^+ \to \pi^0\pi^+K_S^0$ as $B^0 \to K_S^0\pi^+\pi^-$ happens when the π^0 meson from the $B^+ \to \pi^0\pi^+K_S^0$ decay is lost, and a charged, low momentum pion from the other B meson in the event is included in the reconstructed $B^0 \to K_S^0\pi^+\pi^-$ candidate.*

Neutral B to flavour eigenstates background

The likelihood function used to model this type of background is given below. It is similar to the charged B backgrounds likelihood, except that here the mixing term appears.

$$
\mathcal{P}_{B_{flav}}^{j,c} = \frac{e^{-|\Delta t|/\tau_j}}{4\tau_j} \left[\left(1 + q_{\text{tag}}\frac{\Delta\mathcal{D}_j^c}{2} + \langle\mathcal{D}_j^c\rangle\cos\left(\Delta m_{d,j}\Delta t\right)\right) \right. \tag{4.12}
$$

$$
\times \frac{P_{B_{flav}}^j(q_{\text{sig}} = -q_{\text{tag}}; x, y)}{\int\int_{DP} P_{B_{flav}}^j(q_{\text{sig}} = -q_{\text{tag}}; x, y)\ dxdy} \tag{4.13}
$$

$$
+ \left(1 + q_{\text{tag}}\frac{\Delta\mathcal{D}_j^c}{2} - \langle\mathcal{D}_j^c\rangle\cos\left(\Delta m_{d,j}\Delta t\right)\right) \tag{4.14}
$$

$$
\times \frac{P_{B_{flav}}^j(q_{\text{sig}} = +q_{\text{tag}}; x, y)}{\int\int_{DP} P_{B_{flav}}^j(q_{\text{sig}} = +q_{\text{tag}}; x, y)\ dxdy} \tag{4.15}
$$

$$
\left. \right] \otimes \mathcal{R}_{B_{flav}}^c. \tag{4.16}
$$

Here $q_{\text{sig}} = 1(-1)$ when $B_{\text{rec}} = B^0(\overline{B}^0)$, $\mathcal{D}_j^c$, $\Delta\mathcal{D}_j^c$, τ_j and $\Delta m_{d,j}$ represent mode-dependent effective dilutions, lifetimes and oscillation frequencies that may vary from those of correctly reconstructed signal. In the case of the neutral B to flavour eigenstates background, since the final state of the background mode is a flavour eigenstate, events coming from opposite flavours will group into opposite regions of the Dalitz plot. Because of that, instead of using histograms to model the Dalitz plot distribution of each tag flavour, histograms for each signal B flavour were used. Also, neutral B to flavour eigenstates background was split into four different groups with similar m_{ES} and ΔE distributions. A list of the background modes that belong to this category is in Table 4.5. As an example of this type of background the distributions of m_{ES}, ΔE, MLP and the Dalitz plot for $B^0 \rightarrow D^-\pi^+, D^- \rightarrow K_S^0 K^-$ are shown in Figure 4.12.

117

Neutral B to CP eigenstates background

For these events the Δt PDF is expected to be similar to that for signal events (Eq. (1.38)). The direct CP violation of the main contributors to this background are consistent with zero [26], therefore the following expression for the likelihood function is used:

$$
\mathcal{P}_{B_{CP}}^{j,c} = f_c \frac{P_{B_{CP}}^j(x,y)}{\int\int_{DP} P_{B_{CP}}^j(x,y)\,dxdy} \frac{e^{-|\Delta t|/\tau_j}}{4\tau_j} \tag{4.17}
$$
$$
\times \left[\left(1 + q_{\text{tag}}\frac{\Delta \mathcal{D}^c}{2}\right) + q_{\text{tag}}\langle \mathcal{D}\mathcal{S}_{\text{eff}}\rangle^{j,c} \sin\left(\Delta m_{d,j}\Delta t\right) \right] \otimes \mathcal{R}_{B_{CP}}^c.
$$

Here, $\langle \mathcal{D}\mathcal{S}_{\text{eff}}\rangle^{j,c}$ is a tagging category-dependent parameter which describes the time-dependent asymmetry $\mathcal{S}$ and the effective dilution at the same time. In the analyses each of the neutral B to CP eigenstates background modes is treated as a separate group.

A list of the background modes that belong to this category is in Table 4.6. The most prominent channel is $B^0 \to \eta' K_S^0$ with $\eta' \to \rho^0\gamma$. Misreconstruction happens when the photon is lost. Distributions of m_{ES}, ΔE, MLP and the Dalitz plot for this background channel are given in Figure 4.13. The m_{ES} and MLP distributions are signal like, but the ΔE distribution is shifted toward lower ΔE values compared to the signal, because the energy carried by the photon is missing.

4.4   Continuum Background

The most dominant source of background for the analysed channel is light quark production (continuum background). To study this type of background, data collected $50\,\text{MeV}$ below the $\Upsilon(4S)$ resonance are used. Such a data sample is ideal to characterise this kind of background, since it does not contain any B meson decay. In order to estimate the number of expected continuum background events the signal selection criteria are applied to the off-peak data
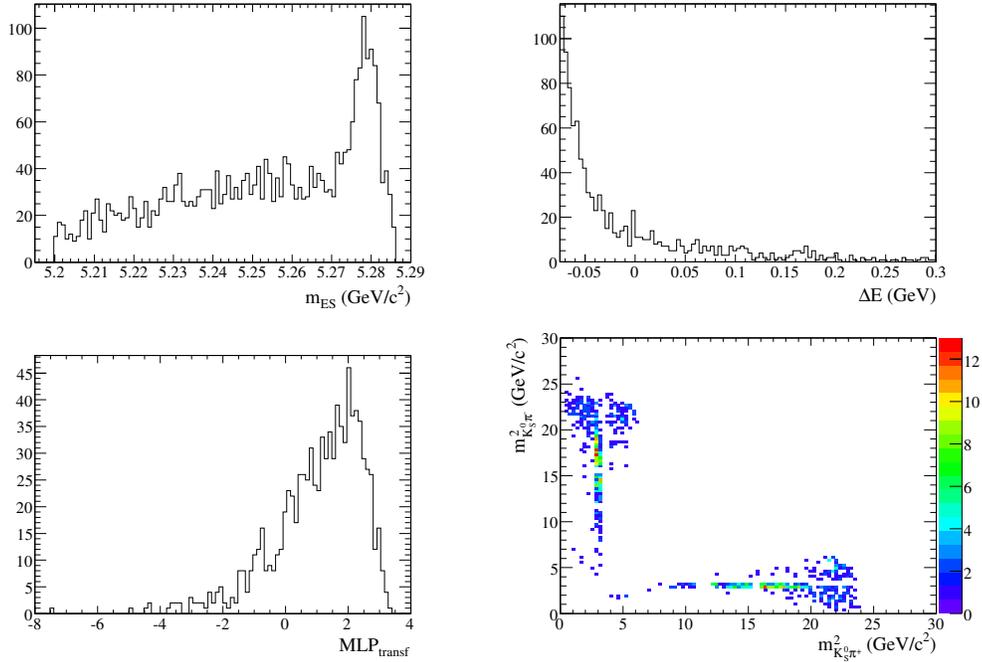
Figure 4.12: *Distributions of m_{ES} (top left), ΔE (top right), MLP (bottom left) and Dalitz plot (bottom right) for $B^0 \to D^-\pi^+, D^- \to K_S^0 K^-$. The areas of the Dalitz plot populated by the background events are close to the D-veto bands. Since the final state of the background mode is a flavour eigenstate, events coming from the opposite flavours are grouped into opposite regions of the Dalitz plot. The m_{ES} distribution peaks at $5.28\,\mathrm{GeV}/c^2$, as signal should, but has a long tail due to misreconstruction.*

sample and the number of selected events is multiplied by a factor of 9.65 to account for the different integrated luminosities of the off-peak and on-peak samples. In such a way the number of continuum events expected in the signal region is estimated to be around 13500, which is almost six times more than the number of expected signal events. Because of that, it was essential to develop an accurate model of the distributions of the continuum events.

The small size of the off-peak sample gives a poor estimation of the shapes of its distributions. In order to enrich the off-peak sample of continuum events,
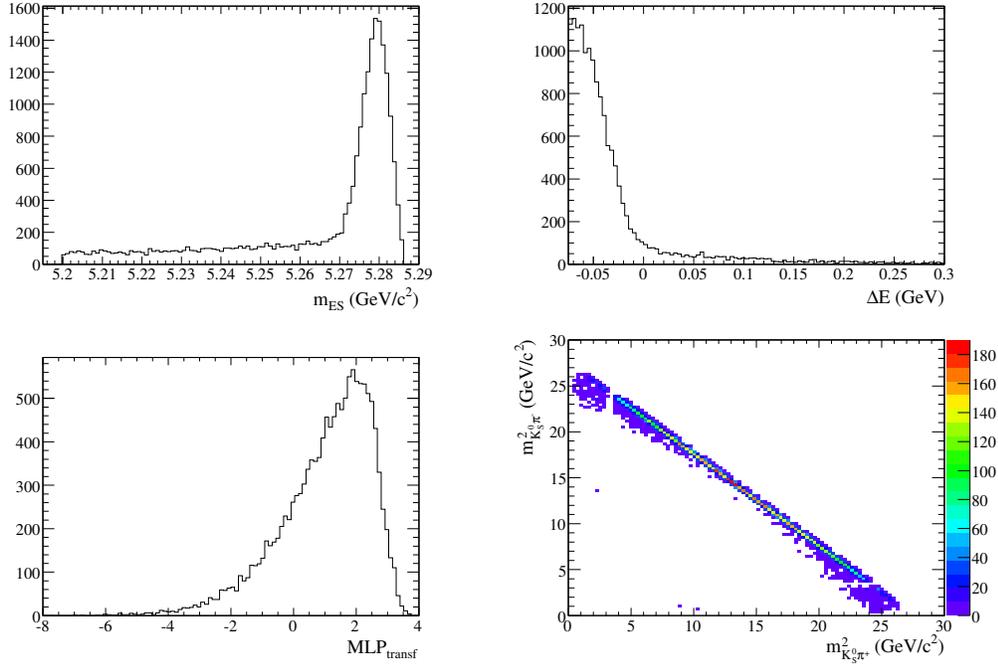
Figure 4.13: *Distributions of m_{ES} (top left), ΔE (top right,) MLP (bottom left) and Dalitz plot (bottom right) for $\eta' \to \rho^0 \gamma$. The m_{ES} distribution peaks at $5.28\,\mathrm{GeV}/c^2$, but the ΔE peak is shifted toward lower ΔE value compared to the signal, because the energy carried by the photon is missing.*

events from the upper and grand side bands of the m_{ES}-ΔE plane (see Section 4.1), are used as well.

However, the sideband regions of the m_{ES}-ΔE plane are populated not only by continuum events, but also by $B\overline{B}$ background events. The level of this contamination is studied using both generic and exclusive $B\overline{B}$ MC samples, described in Section 4.3.1. It was found that 6905.9 ± 262.4 $B\overline{B}$ events are expected to contribute to the on-resonance sideband, which is around 3% of the reconstructed sideband events. The $B\overline{B}$ background contamination is histogrammed and bin-by-bin subtractions from the histograms of the sideband data are then performed in order to use this data to analyse the continuum distributions.

The invariant mass squared distributions for the sideband events ($B\overline{B}$ events are subtracted from the sample), together with the distribution of off-peak events are shown in Figure 4.14. These plots show that the two distributions are consistent, and therefore the combined sample of off-peak and on-peak sideband events can be used to analyse the continuum events.
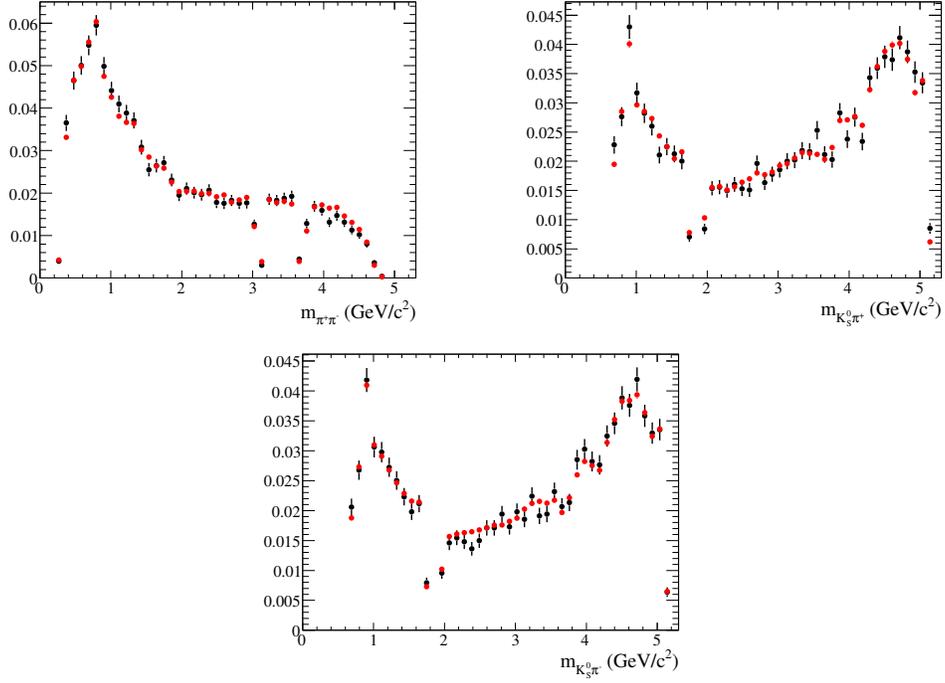
Figure 4.14: *Projections on the three invariant masses of the Dalitz plot distributions of off-peak data (black) and on-peak sidebands (red). Since good agreement is observed, both samples are used in the extraction of the continuum PDFs.*

Using the combined sample, two-dimensional histograms ($P_{q\overline{q}}^{c,q_{\text{tag}}}$) describing the Dalitz plot distribution of continuum events (in principle one for each flavour tag q_{tag} and tagging category c) are constructed and used to build the Δt-Dalitz plot PDF:

$$\mathcal{P}_{q\bar{q}}^{c,q_{\text{tag}}} = \frac{P_{q\bar{q}}^{c,q_{\text{tag}}}(x,y)}{\int\int_{DP} P_{q\bar{q}}^{c,q_{\text{tag}}}(x,y)\ dxdy} \times$$
$$\left(f_{\text{prompt}}\delta(\Delta t_{\text{true}}) + (1 - f_{\text{prompt}})\frac{e^{-|\Delta t_{\text{true}}|/\tau_{q\bar{q}}}}{2\tau_{q\bar{q}}} \right) \otimes \mathcal{R} \qquad (4.18)$$

The Δt behaviour is modelled as two components, with zero (*prompt*) and non-zero lifetimes, convolved with a customised resolution function $\mathcal{R}$ extracted from off-peak data and consisting of three gaussians (similar to the Δt signal resolution function). In Figure 4.15 Δt distribution of off-peak data is shown.
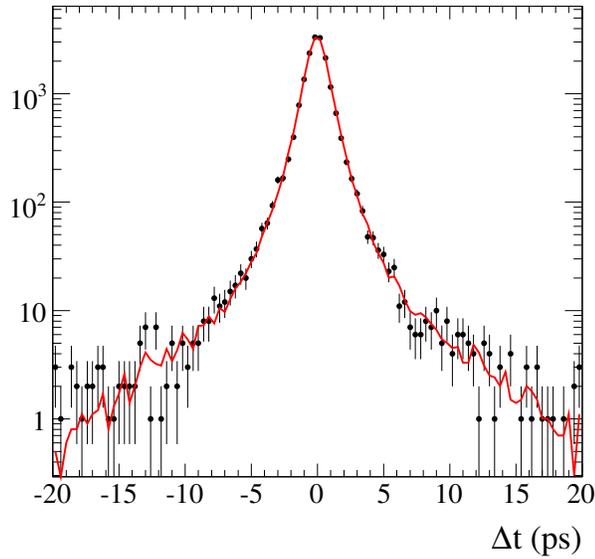
Figure 4.15: *Off-peak data are used to extract a resolution function in Δt for continuum events, as well as the fraction of events that have a non-negligible lifetime and the value of that lifetime. A measurable fraction is expected, since charmed resonances are produced in the continuum with lifetimes comparable to those of the B meson (e.g. ($\tau_{D^\pm} = (1.04 \pm 0.07)$ ps). They are found to be $1 - f_{\text{prompt}} = 0.11 \pm 0.01$ and $\tau_{q\bar{q}} = (1.37 \pm 0.12)$ ps.*

4.5 Analysis of the discriminating variables

In order to analyse distributions of discriminating variables, their correlations, as well as Dalitz plot, tag and tagging category dependence, the fully simulated nonresonant Monte Carlo sample of $B^0 \to K_S^0 \pi^+ \pi^-$ events was used.

4.5.1 Dependence on tagging categories

Analysis of m_{ES}, ΔE and MLP distributions for different tagging categories showed no dependence on tagging categories for m_{ES} and ΔE (see Figure 4.16).
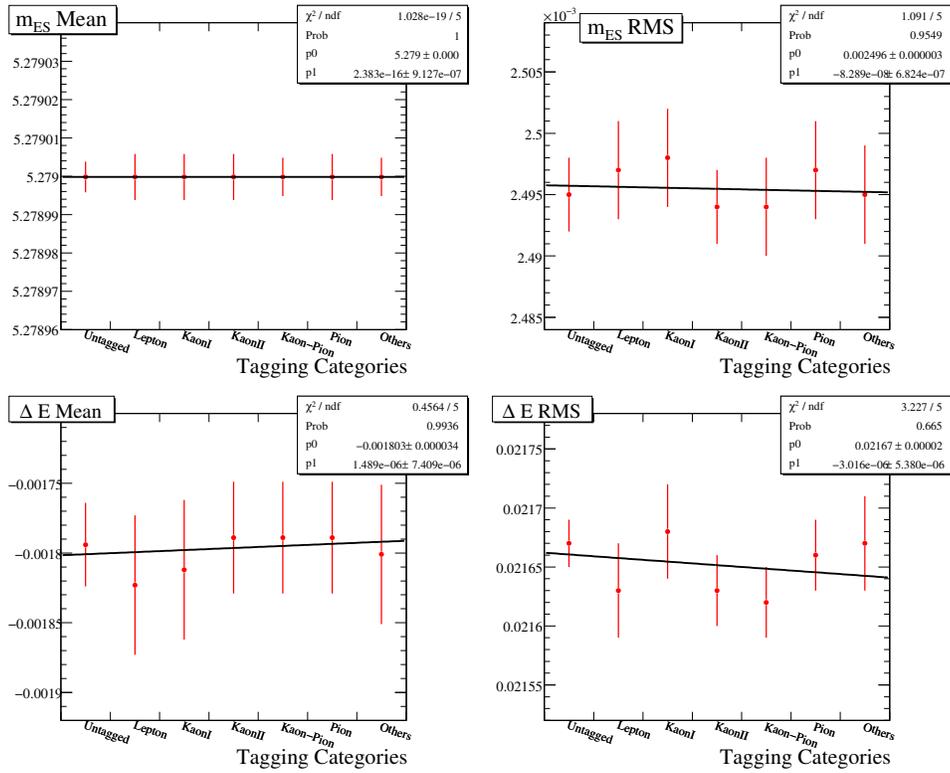
Figure 4.16: *The m_{ES} (top) and ΔE (bottom) dependence on tagging categories. On the left, the distributions of the m_{ES} and ΔE mean calculated for different tagging categories are shown. On the right, the distributions of m_{ES} and ΔE RMS as a function of tagging categories are plotted. No dependence can be observed.*

On the other hand, a strong dependence of the MLP discriminant was observed (Figure 4.17). This dependence is not unexpected. The MLP discriminant is built using the event-shape variables ($\cos\theta_{B_{\mathrm{mom}}}$, L_2/L_0 and $\cos\theta_{B_{\mathrm{thrust}}}$; see Section 3.3.2), which use information about the tagging B meson in an $e^+e^- \to B^0\bar{B}^0$ event. Each tagging category corresponds to a specific group of tagging B meson decays, so differences among tagging B meson decays translate into the observed dependence of the MLP with tagging categories.
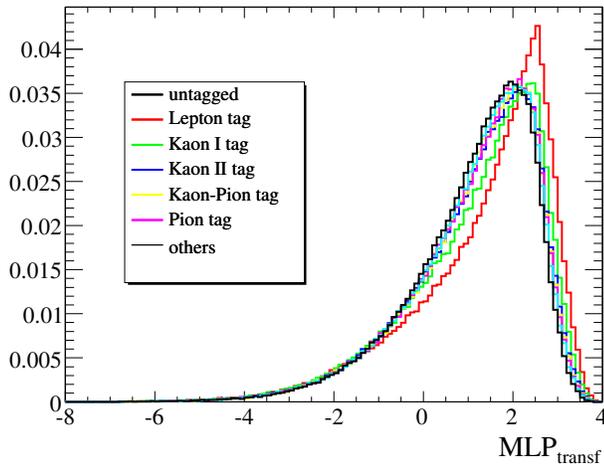
Figure 4.17: *Distribution of MLP discriminant for different tagging categories.*

In order to allow the variable dependence on the tagging categories the different parameters are employed for each tagging category in the signal hypothesis.

4.5.2 Flavour dependence

The flavour-dependence of m_{ES}, ΔE and MLP distributions is also analysed. The analysis showed no flavour-dependence neither for signal nor for the different kinds of backgrounds. Therefore, identical PDFs are used to model m_{ES}, ΔE and MLP for both flavours in each species. The plots showing the ratio between the discriminating variable distribution plotted for the signal candidates tagged as B^0 mesons and the signal candidates tagged as $\bar{B}^0$ mesons (for

MC signal events), are shown in Figure 4.18. It can be seen that all plotted distributions are consistent with unity.
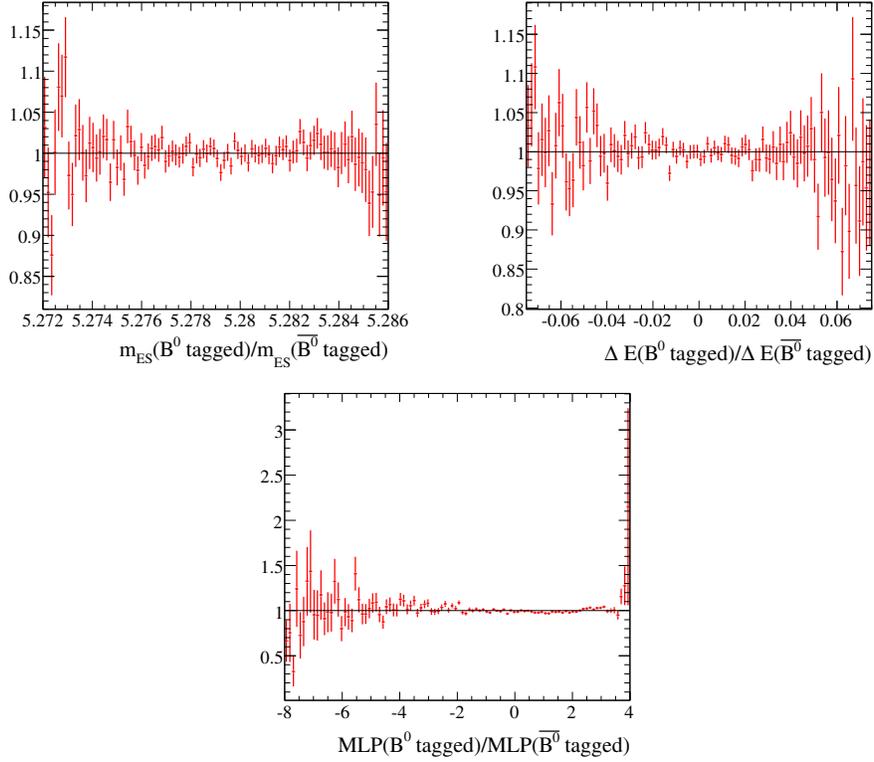
Figure 4.18: *The flavour-dependence of the signal m_{ES}, ΔE and MLP distributions. In each plot the ratio between the discriminating variable distribution plotted for the signal candidates tagged as B^0 mesons and the signal candidates tagged as $\bar{B}^0$ mesons is shown.*

4.5.3 Dependence on Dalitz plot position

In order to study correlations of m_{ES}, ΔE and the MLP discriminant with the Dalitz plot position, for each bin in the Dalitz plot the mean and RMS of the discriminating variables were calculated. In Figure 4.19, Figure 4.20 and Figure 4.21 results of the analysis for signal events are shown. It can be seen that the plotted distributions are uniform across the Dalitz plot for m_{ES} and

MLP, while in the case of ΔE, the RMS shows some dependence on the Dalitz plot position. However, since the variation over the Dalitz plot is smaller than the average value of the RMS, this dependence can be neglected (Figure 4.19). Results for the mean of ΔE are shifted by adding 0.075. This done because the ΔE distribution is centred around zero, and without adding the shift a plot of the mean of ΔE as a function of the Dalitz plot position will have many zero entry bins. Also, in order to avoid the zero entry bins, the results for the mean of MLP discriminant are shifted by adding 8.0.
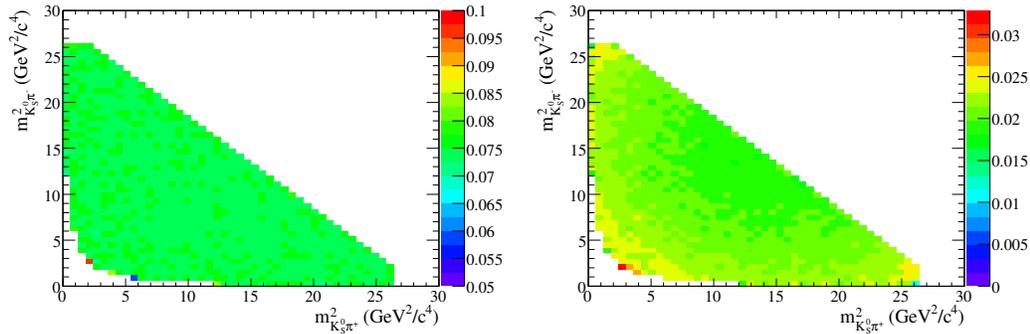
Figure 4.19: *The plot of the variation in mean (left) and RMS (right) of ΔE over the Dalitz plot for signal events. The RMS shows some dependence on the Dalitz plot position, but since the variation over the Dalitz plot is smaller than the average value of the RMS, this dependence can be neglected.*

A similar analysis was performed for continuum background events. Examination of the m_{ES} and ΔE distributions for continuum events in the off-peak sample did not show any dependencies. However, the MLP distribution was observed to vary for events in the centre of the Dalitz plot compared to those at the edges (see Figure 4.22). As in the case of the MLP dependence on the tagging categories, this behaviour was expected. The event-shape variables used in the MLP quantify the jet-like structure of the B candidates. Since the centre of the Dalitz plot is populated with the $B^0 \to K_S^0 \pi^+ \pi^-$ candidates in which the directions of the three daughter particles are distributed quite

126
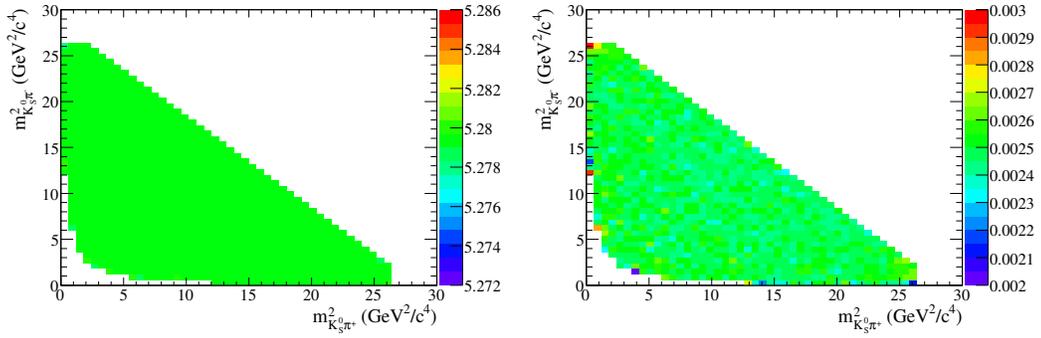
Figure 4.20: *Plot of the variation in mean (left) and RMS (right) of m_{ES} over the Dalitz plot for signal events. Plotted distributions are uniform across the Dalitz plot.*
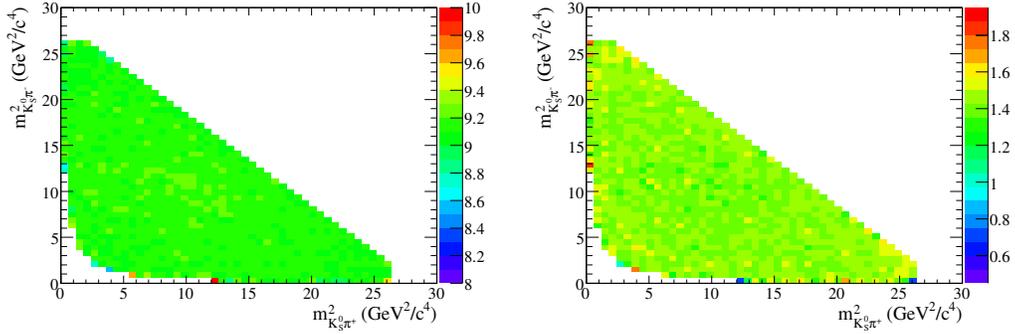
Figure 4.21: *Plot of the variation in mean (left) and RMS (right) of MLP discriminant over the Dalitz plot for signal events. Plotted distributions are uniform across the Dalitz plot.*

isotropically, and the candidates in which one of the particles in the final state flies back to back to the other two populate the edges of the Dalitz plot, more jet-like events will be distributed on the edges of the Dalitz plot, while the less jet-like events will be grouped in the centre of the Dalitz plot. These changes translate into the observed dependence of the mean and the width of the MLP distribution of continuum background events on the distance from the Dalitz plot centre.
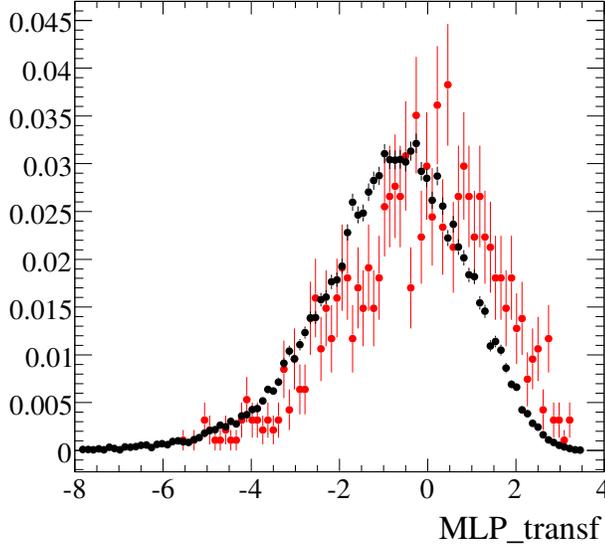
Figure 4.22: *Continuum background MLP distribution dependence on the distance from the centre of the Dalitz plot. In red, events contained in the central area of the Dalitz plot, defined as $m_{ij}^2 > 2\,\mathrm{GeV}/c^2$ for all three pairs of particles. In black, events outside that region.*

In order to account for the observed dependence an attempt to model the continuum MLP distribution as a function of the distance from the centre of the Dalitz plot is made. The Dalitz plot is binned into annular regions around the centre (defined as a point in the Dalitz plot where $m_{12}^2 = m_{13}^2 = m_{23}^2$), with the first bin covering the central area of the Dalitz plot (defined as $m_{ij}^2 > 2\,\mathrm{GeV}/c^2$). In each of these bins, the MLP discriminant is fitted as the sum of two bifurcated Gaussians. No differences among distributions of the MLP variable in bins outside of the central area of the Dalitz plot were noticed. Because of that the following dependence of the fitted parameters (par_k) of the bifurcated Gaussians on the distance of the Dalitz plot centre is assumed:

$$
par_k = \begin{cases} \alpha_k, & m_{ij}^2 > 2\,\mathrm{GeV}/c^2 \\ \alpha_k + step_k, & m_{ij}^2 < 2\,\mathrm{GeV}/c^2, \end{cases}
$$

128

where α_k is the fitted value of the parameter par_k inside the central area of the Dalitz plot, and $step_k$ is the difference between the fitted values of par_k inside and the outside of the central area of the Dalitz plot.

The MLP distribution of the continuum background events fitted in such a way is shown in Figure 4.26.

4.5.4   Probability density functions

In Figure 4.23 the m_{ES} distributions of signal, self cross feed and continuum background events are shown. The m_{ES} signal distribution is modelled by the sum of two Gaussians, the distribution of SCF events as the sum of Crystal Ball and ARGUS functions, while continuum background events are parameterized by an ARGUS function.
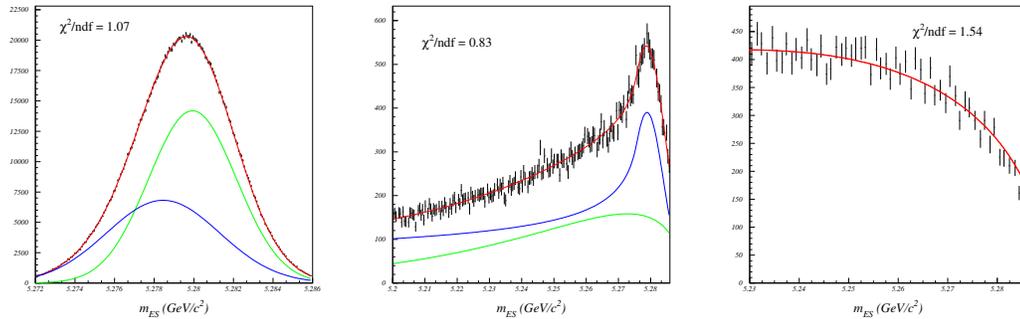
Figure 4.23: m_{ES} *distributions of signal (left), SCF (middle) and continuum background (right) events. In all plots the black histogram represents MC data (or the off peak data in the case of continuum background), while the red curve is the fit. The signal m_{ES} distribution is modelled as the sum of two Gausians (shown as the blue and the green curves), the SCF distribution as sum of a Crystal Ball (blue) and an ARGUS (green) function. An ARGUS function is used to parameterize the continuum background distribution.*

In the case of the ΔE distributions, the signal ΔE distribution is modelled by the sum of two Gausians, while for the SCF and continuum background,

linear functions are used (see Figure 4.24).
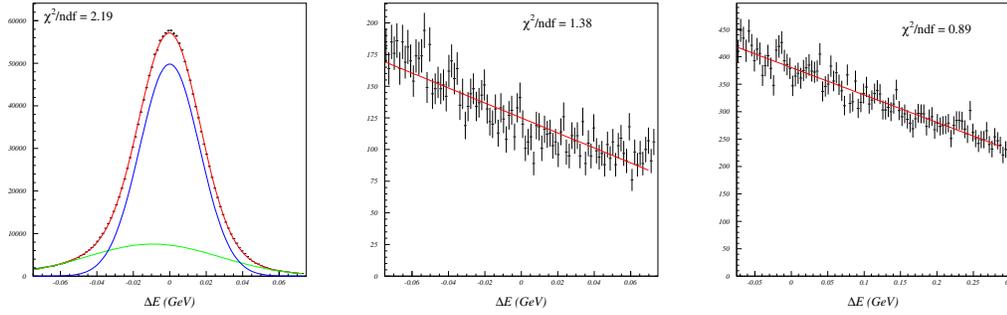
Figure 4.24: ΔE distribution of signal (left), SCF (middle) and continuum background (right) events. As before, the black histogram represents MC data (or the off peak data in the case of continuum background), while the red curve is the fit.

Since it was found that the distribution of the MLP discriminant depends on tagging categories, separate fits are performed for each tagging category. In all cases the sum of three bifurcated Gaussians is used to model the MLP distribution. The examples of fits to `Lepton`, `KaonI` and `Untagged` events are shown in Figure 4.25.

The MLP distributions of SCF and continuum background events are shown in Figure 4.26. The SCF distribution is parameterised by the sum of two bifurcated Gaussians, while for the distribution of continuum background events the sum of two bifurcated Gaussians, with parameters depending on the distance from the Dalitz plot centre, is used.

The exact functional forms of PDFs used in the fit are given, together with the values of the fitted PDF parameters are given in Chapter E.

4.5.5 Control sample

Since the Monte Carlo does not give a perfect representation of the data, the probability density functions extracted from the MC samples should be

130
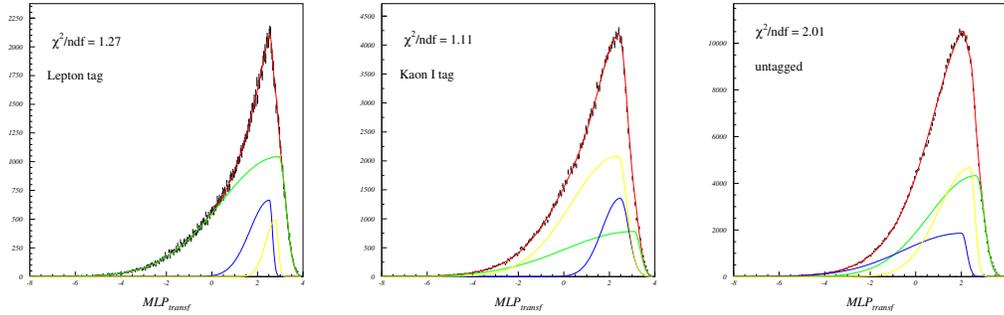
Figure 4.25: *Signal MLP distributions for* `Lepton` *(left),* `KaonI` *(middle) and* `Untagged` *(right) events. In all plots the black histogram represents MC data (the off peak data in the case of continuum background), while the red curve is the fit.*

verified. One of the ways to accomplish the verification is to analyse a B meson decay channel similar to the one of interest. The signal PDF parameters should be extracted from MC simulation of the control channel, and then compared to
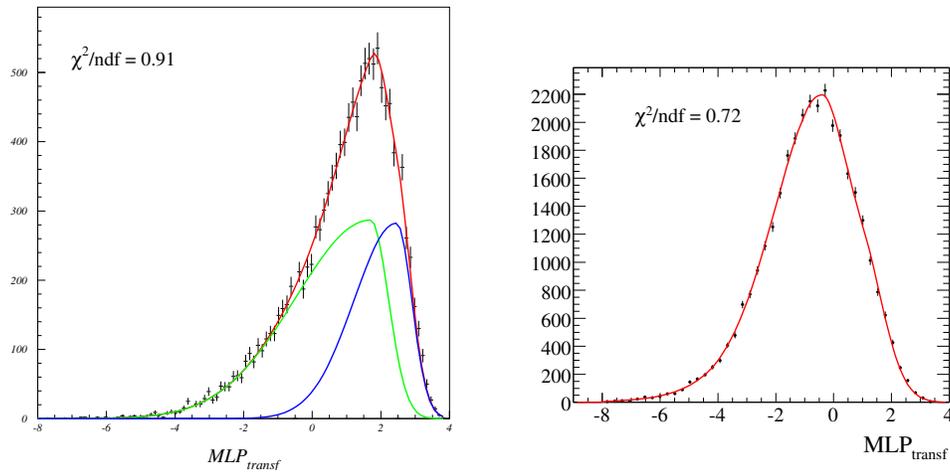
Figure 4.26: *The MLP distribution for SCF (left) and continuum background (right) events. The black histogram represents MC data (the off peak data in the case of continuum background), while the red curve is the fit.*

those extracted from the data. As the control channel for the $B^0 \to K_S^0 \pi^+ \pi^-$ decay, the decay of a neutral B meson to $D^{\mp} \pi^{\pm}$ with $D^{\mp} \to K_S^0 \pi^{\mp}$ is chosen. This channel is an excellent choice, since its final state is identical to that of the charmless $B^0 \to K_S^0 \pi^+ \pi^-$.

If signal statistics are sufficient, one can overcame this problem by floating the signal parameters in the fit to data. Nevertheless, the study of the control sample is useful to provide a handle on the possible size of related systematic effects.

For the signal MC sample the m_{ES} and ΔE distributions are parameterised by the sum of two Gaussian functions. The same functions are used to describe signal m_{ES} and ΔE distributions in the control data sample. The $B\overline{B}$ background has been neglected in both variables, while the presence of continuum background in the data sample is taken into account by including a background component with the same m_{ES} and ΔE PDFs as described in Section 4.5.4.

Results of this analysis are summarised in Table 4.7, and plots showing comparisons of the m_{ES} and ΔE PDF shapes in MC and data are given in Figure 4.27. The results show good agreement in both cases, making unnecessary any correction of the PDF parameters extracted from MC.

In the case of ΔE both means show small shifts $((-3 \pm 2)\mathrm{MeV})$ and $((3.6 \pm 0.6)\mathrm{MeV})$, which is expected due to the unaccounted $B\overline{B}$ background. The ratios of the widths for data and MC are compatible with unity, and any differences are therefore neglected. In the case of m_{ES}, a small shift in one of the means is observed $((1.2 \pm 0.2)\mathrm{MeV/c^2})$, while the ratios of the widths for data and MC are compatible with unity. All noticed shifts are treated as a source of systematic error.

4.6 Total likelihood

As mentioned before, the variables used to describe an event that passed the selection criteria listed in Section 4.1 are m_{ES}, ΔE, MLP, Δt and the position

Table 4.7: *Differences between MC and the data m_{ES} and ΔE fit parameters for $B^0 \to D^- \pi^+$ control sample.*

	m_{ES}	ΔE
$\mu 1_{\mathrm{data}} - \mu 1_{\mathrm{MC}}$	$(0.0 \pm 0.1)\mathrm{MeV}/\mathrm{c}^2$	$(-3 \pm 2)\mathrm{MeV}$
$\mu 2_{\mathrm{data}} - \mu 2_{\mathrm{MC}}$	$(1.2 \pm 0.2)\mathrm{MeV}/\mathrm{c}^2$	$(3.6 \pm 0.6)\mathrm{MeV}$
$\sigma_{\mathrm{data}}/\sigma_{\mathrm{MC}}$	1.03 ± 0.07	0.98 ± 0.01
$\sigma_{\mathrm{data}}/\sigma_{\mathrm{MC}}$	0.98 ± 0.05	1.04 ± 0.03

of the event in the Dalitz plot. In the case of uncorrelated variables the total likelihood function for an event is given as the product of the individual PDFs (see Section 3.6). Previous studies have shown that the m_{ES} and ΔE variables are mostly uncorrelated [56], while the results presented in Section 4.5 show that in the case of $B\bar{B}$ events (both signal and background) no correlation between Dalitz plot position and m_{ES}, ΔE and MLP can be seen. Therefore, the likelihood for a $B\bar{B}$ event can be written in the following form:

$$\mathcal{P}_{B\bar{B}}\left(x, y, \Delta t, m_{\mathrm{ES}}, \Delta E, \mathrm{MLP}\right) = \mathcal{P}\left(x, y, \Delta t\right) \mathcal{P}\left(m_{\mathrm{ES}}\right) \mathcal{P}\left(\Delta E\right) \mathcal{P}\left(\mathrm{MLP}\right).$$

(4.19)

Here, $\mathcal{P}\left(x, y, \Delta t\right)$ is the joint PDF for the Dalitz plot coordinates and the time difference Δt. On the other hand, in the case of continuum background events, a correlations between the MLP distribution with the Dalitz plot coordinates was observed. Because of that, the likelihood for a continuum event has the following form:

$$\mathcal{P}_{q\bar{q}}\left(x, y, \Delta t, m_{\mathrm{ES}}, \Delta E, \mathrm{MLP}\right) = \mathcal{P}\left(x, y, \mathrm{MLP}\right) \mathcal{P}\left(\Delta t\right) \mathcal{P}\left(m_{\mathrm{ES}}\right) \mathcal{P}\left(\Delta E\right)$$

(4.20)

Using the previous expressions for the likelihoods of the signal and background events, the total likelihood for an event α in tagging category c is given by:

$$\mathcal{L}\left(\vec{n}, \vec{a}\right) = \frac{e^{-\left(n_{\mathrm{sig}} + n_{q\bar{q}} + n_{B^+B^-} + n_{B_{flav}} + n_{B_{CP}}\right)}}{N!} \prod_{e=1}^{N} \mathcal{L}_{\alpha}^{e},$$

(4.21)
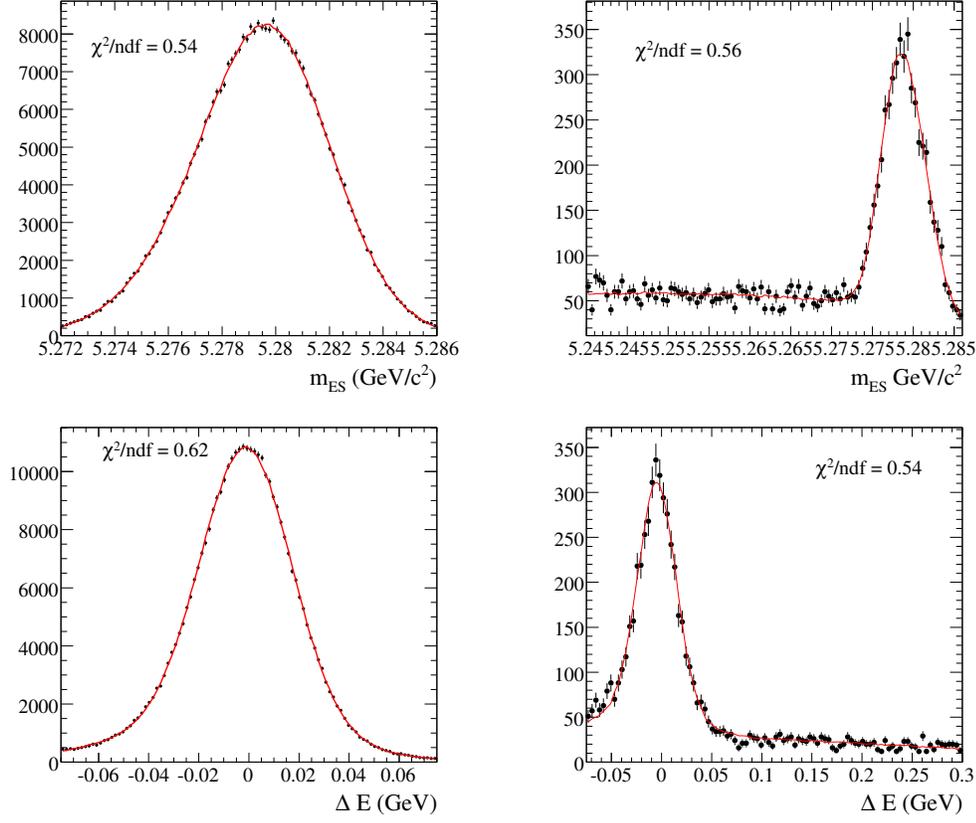
Figure 4.27: *Comparison between MC (left) and data (right) fit of m_{ES} (top) and ΔE (bottom) for the $B^0 \to D^-\pi^+$, $D^- \to K_S^0\pi^-$ control sample. The results show good agreement between MC and data fit in both cases, which can be seen from Table 4.7, making unnecessary any correction of the PDF parameters extracted from MC.*

where $\mathcal{L}_\alpha^c$ is:

$$
\begin{aligned}
\mathcal{L}_\alpha^c \;=\;& n_{\mathrm{sig}} f_{\mathrm{sig}}^c \mathcal{P}_{\mathrm{sig},\alpha} \\
&+ n_{q\bar{q}} f_{q\bar{q}}^c \mathcal{P}_{q\bar{q},\alpha} + \sum_{j=1}^{n_{\mathrm{class}}^{B^+B^-}} n_j f_j^c \mathcal{P}_{B^+B^-,j,\alpha} \\
&+ \sum_{k=1}^{n_{\mathrm{class}}^{B_{flav}}} n_k f_k^c \mathcal{P}_{B_{flav},k,\alpha} + \sum_{l=1}^{n_{\mathrm{class}}^{B_{CP}}} n_l f_l^c \mathcal{P}_{B_{CP},l,\alpha}\,.
\end{aligned}
\tag{4.22}
$$

134

Here, the n_i represent the numbers of events of each species and the sums for each of the three types of $B\overline{B}$ background run over the different classes of background channels within that type.

Chapter 5

Analysis Results and Conclusions

In this chapter results of the fit to the data are presented. The chapter starts with a discussion of results of various toy MC tests and fully simulated MC tests.

5.1 MC tests

5.1.1 Toy MC tests

In order to test the stability of the fit and check for potential errors in the models used to describe different event species a number of toy MC tests are performed. The toy MC events are generated according to the PDFs described in the previous chapter. These generated events are then fitted using the same PDFs. The fit results are compared with the generated values by calculating biases, the differences between the means of the distributions of fitted values and the true values, for the all fitted parameters. Three different sets of toy MC tests are performed: toy MC tests with signal only events, toy MC tests with signal and continuum background events and finally, toy MC tests with signal, continuum background and $B\bar{B}$ background events. For each toy

MC test 500 samples of the analysed set of events are generated (each one containing the amounts of different event species expected in the on-peak data sample). Because of the large number of the fitted parameters it is expected that the fit will not always converge to the global maximum. Therefore, each of the generated samples is fitted 100 times with randomized initial values of the fitted parameters. Results of the toy tests showed that almost 100% of these fits converge, despite their often highly incorrect starting points, and a majority (often $> 80\%$) will converge to the solution with the best likelihood. Examining all the different possible solutions in toy experiments it was found that this most favoured and best-likelihood solution is always the one closest to the generated parameters. The adopted practice for dealing with the multiple solutions behaviour is therefore to perform multiple randomised fits and to extract the solution with the best likelihood value.

In signal only tests it was found that biases among the fitted parameters are either non existent or very small, not larger than 15% of the expected statistical error. In the case of signal, continuum background and $B\bar{B}$ background MC toy tests, slightly larger biases (20%) are noticed in only 2 out of 32 fitted parameters.

In Figure B.1-B.6, given in Appendix B, pull plots (see Section 3.4) for the signal only and signal, continuum background and $B\bar{B}$ background toy MC tests are given.

5.1.2   Fully simulated MC tests

Fully simulated MC events are used to check whether any neglected effects, such as self cross feed or correlations between variables, are more important than initially estimated. For this purpose, the existing true MC $B^0 \rightarrow K_S^0 \pi^+ \pi^-$ model is used. In this model neutral B mesons decay to the $K_S^0 \pi^+ \pi^-$ final state via 5 resonances ($f_0(980)K_S^0$, $\rho^0(770)K_S^0$, $K^*(892)\pi$, $K_0^*(1430)\pi$ and $f_0(1300)K_S^0$) and two different non resonant terms. 250 data samples in which the true MC events are mixed with generated continuum and $B\overline{B}$ background

138

events are made and each of them is fitted 100 times (with randomized initial values of the fitted parameters) using signal, continuum and $B\overline{B}$ PDFs described in the previous chapter. As before, the best fit is chosen according to its likelihood function value. Figures C.1 to C.3 in Appendix B show the distributions of the fitted variables and the values used for the generation. It can be seen that the agreement between fitted and generated values is very good. The same conclusion can be made from the isobar coefficients distributions shown in Figure 5.1. In this figure the generated values of the isobar coefficients (which are complex numbers) and the values returned by the fits are shown in the complex plane. For each of the resonances, distributions of the best fits for 250 samples are shown (see the colour code) together with the mean fit value (black dot marker) and the generated value (black star marker).

5.2   Results of the fit to data

After obtaining satisfactory results of the toy MC and true MC tests, a fit to data is performed using the signal model containing the following resonances:

- $B^0 \rightarrow f_0(980)K_S^0$, $f_0(980) \rightarrow \pi^+ \pi^-$,

- $B^0 \rightarrow \rho^0(770)K_S^0$, $\rho^0(770) \rightarrow \pi^+ \pi^-$,

- $B^0 \rightarrow K^{*+}(892)\pi^-$, $K^{*+}(892) \rightarrow K_S^0 \pi^+$,

- $B^0 \rightarrow K_0^{*+}(1430)\pi^-$, $K_0^{*+}(1430) \rightarrow K_S^0 \pi^+$,

- $B^0 \rightarrow f_0(1300)K_S^0$, $f_0(1300) \rightarrow \pi^+ \pi^-$,

- $B^0 \rightarrow f_2(1270)K_S^0$, $f_2(1270) \rightarrow \pi^+ \pi^-$,

- $B^0 \rightarrow \chi_{c0}K_S^0$, $\chi_{c0} \rightarrow \pi^+ \pi^-$,

- $B^0 \rightarrow K_S^0 \pi^+ \pi^-$, non resonant
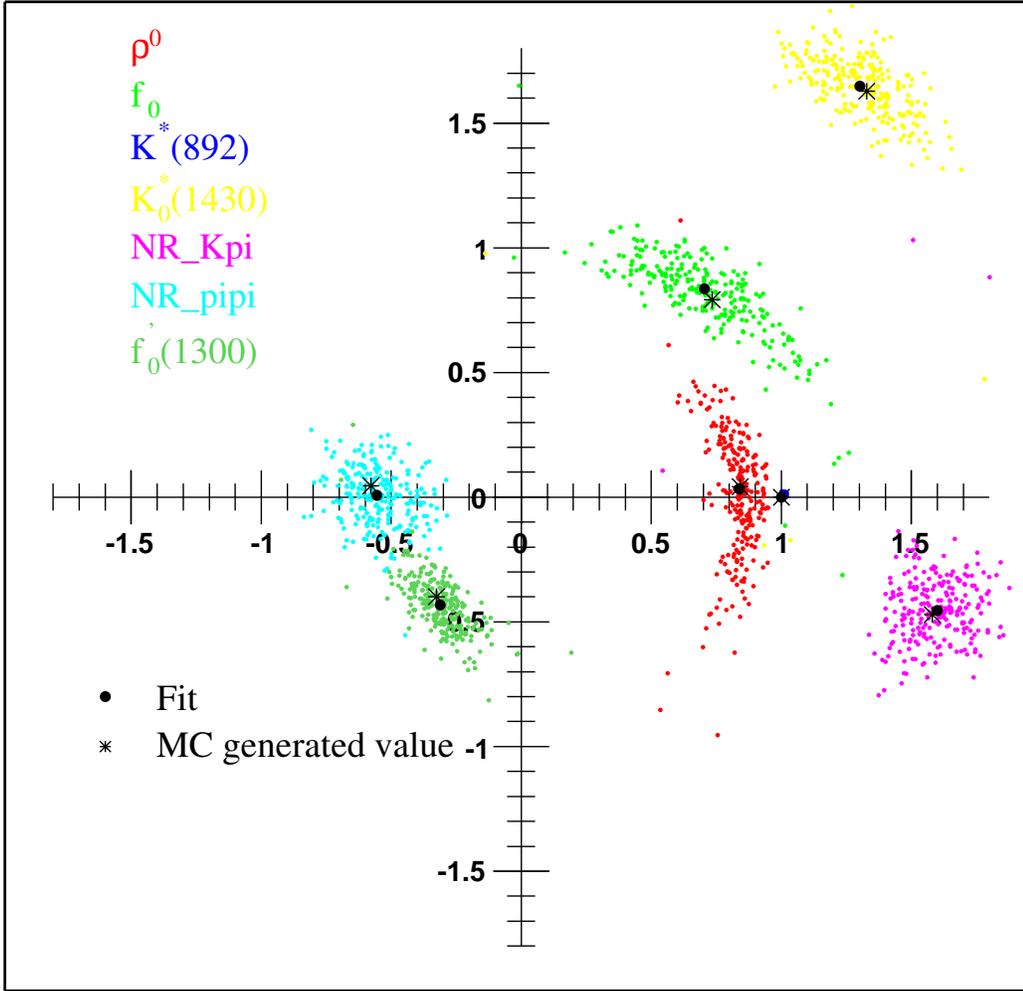
Figure 5.1: *Results of the fully simulated MC tests. In total, 250 samples containing the true $B^0 \to K^0_S \pi^+ \pi^-$ MC events are fitted. Values of the isobar coefficient returned by the fits are shown in different colours as "clouds" of the solutions. The mean value of each "cloud" is shown as a black-dot marker, while the generated value is shown as a black-star marker. A very good agreement between generated values and the values returned by the fit is visible.*

This model was established in *BABAR*'s previous analysis of the $B^0 \to K^0_S \pi^+ \pi^-$ decay on a smaller $B\overline{B}$ dataset [77] where it was thoroughly checked and found that it describes the Dalitz plot structure of the $B^0 \to K^0_S \pi^+ \pi^-$ decay well.

Because of that, it was decided that there is no need to repeat the model selection procedure studies. For most of the resonances a relativistic Breit-Wigner distribution is used for the lineshape, except for $f_0(980)$ and $K_0^*(1430)$ for which Flatté and LASS lineshapes are employed, respectively. For the reasons discussed above, data sample is fitted 100 times with randomised initial values of the fit parameters.

5.2.1 $_s\mathcal{P}lot$s

After the fit to data is performed, the $_s\mathcal{P}lots$ are examined (see Section 3.7) and agreement between the fitted distributions in each variable of interest for signal and continuum events with those obtained using the $_s\mathcal{P}lot$ technique is checked. In Figure 5.2 comparisons between the fit and $_s\mathcal{P}lot$ distributions of ΔE, m_{ES}, MLP and the Dalitz plot variables for signal events are shown. It can be seen that they agree well. In the Dalitz plot distribution (lower right) plot, which is obtained when only m_{ES}, ΔE and MLP variables are used to separate signal from background, heavily populated bands in the $m_{\pi^+\pi^-}$ and $m_{K_S^0\pi}$ spectra are visible.

A similar set of plots for continuum background events is shown in Figure 5.3. As in the case of signal events it can be said that there is a good agreement between the fit and $_s\mathcal{P}lots$. The only visible discrepancy exists between the MLP shape predicted by the fit and one given by the $_s\mathcal{P}lot$ (lower left plot in Figure 5.3).

This can be explained by the fact that the MLP distribution of the continuum events depends on the distance from the Dalitz plot centre (see Section 4.4). In the situation when only the m_{ES}, ΔE and Dalitz plot variables are used in the fit (and all of them are assumed to be uncorrelated) it is likely that some of the continuum $B\overline{B}$ background events are recognised as continuum $(q\bar{q})$ background events. This can happen because the distribution of m_{ES}, ΔE and Dalitz plot variables for continuum $B\overline{B}$ background and $(q\bar{q})$ background events are similar, and the only variable that can distinguish between them is
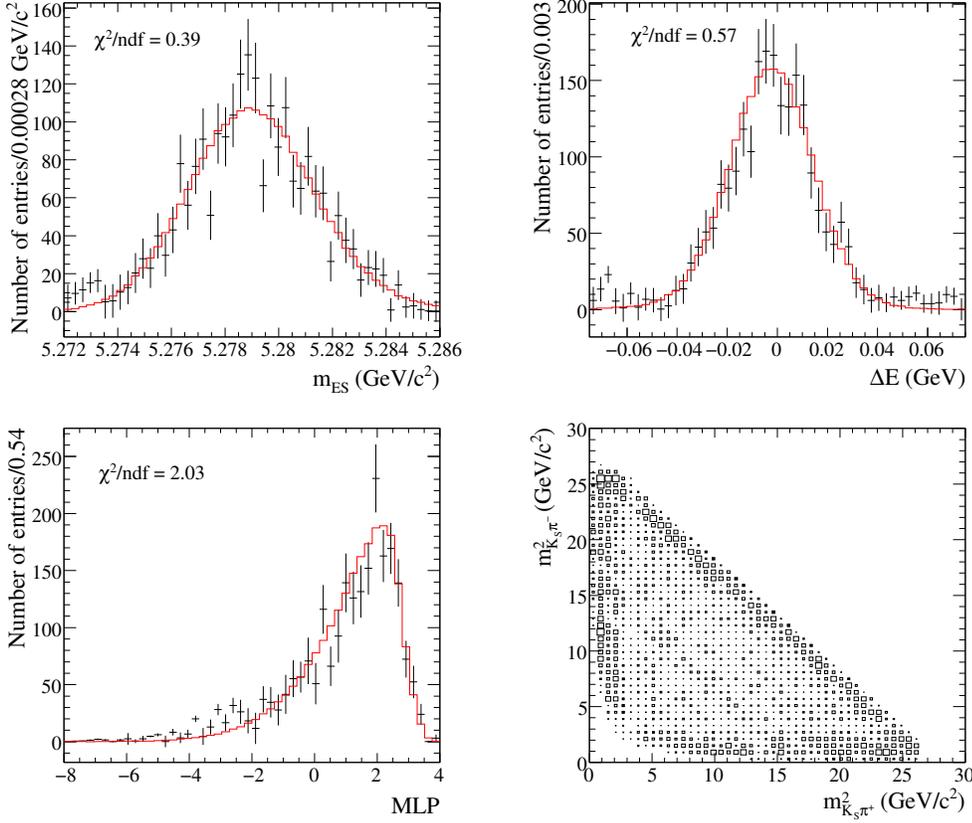
Figure 5.2: $_s\mathcal{P}lots$ distributions for the signal events given by the three background discriminating variables included in the fit, m_{ES}, ΔE and MLP and the Dalitz plot variable. The points with errors in a given variable represent the signal distribution as determined from data by a fit in which all the variables but the one plotted are used to separate signal and backgrounds. The red histograms are the distributions predicted by the results of the total fit.

MLP. Distribution of the MLP variable for the $B\bar{B}$ events (see Section 4.3.1) is centred around higher values of MLP than the corresponding distribution of the continuum background events, and that is the region of the MLP values where the difference between the $_s\mathcal{P}lot$ and the fit is visible.

The next two figures (Figure 5.4 and Figure 5.5) show projections on the $m_{K_S^0\pi}$ and $m_{\pi^+\pi^-}$ invariant masses of the $_s\mathcal{P}lots$ Dalitz distribution for the signal and

142

continuum background events.

There is good agreement between the global fit and the prediction on the Dalitz plot PDF, especially for the signal events. In the case of the continuum background events a slight underestimation of the peaks at low $m_{K_S^0 \pi}$ invariant mass is visible. The reason for this lies in the usage of the on-peak sideband data to model the continuum background distributions. The resonances in the on-peak sideband coming from the continuum events are smoothed by the misreconstruction. This effect can be seen in a plot shown earlier (Figure 4.14), where the off-peak and the on-peak sidebands are compared, and this issue
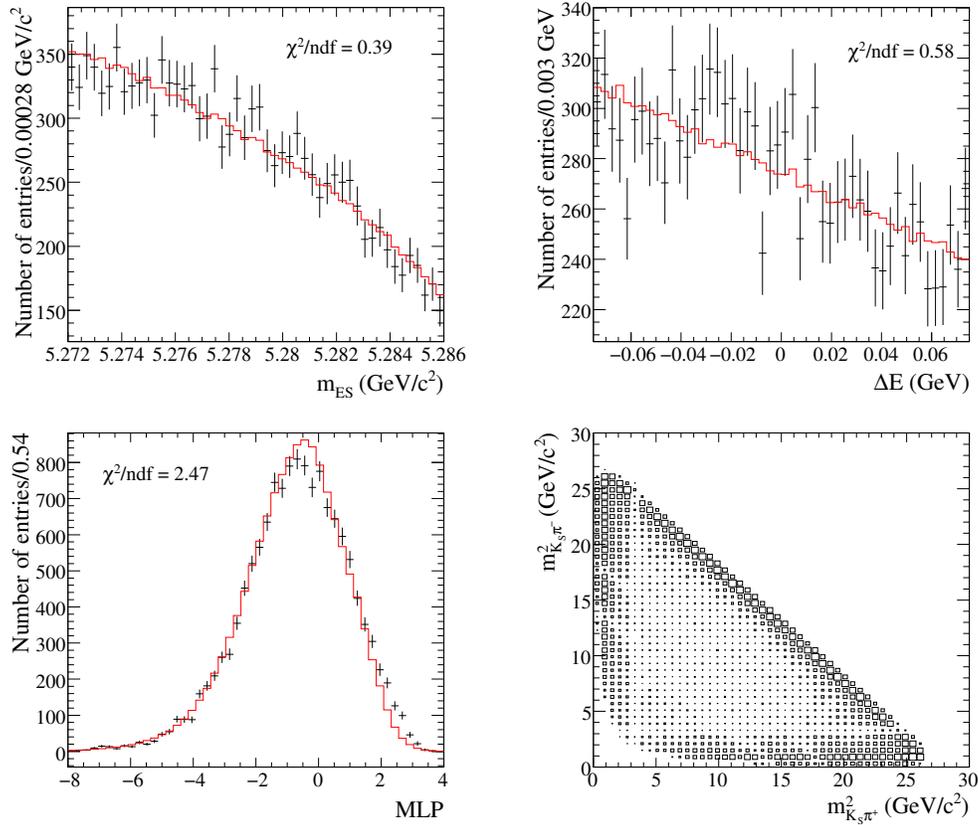
Figure 5.3: $_s\mathcal{P}lots$ distributions for the continuum background events given by the three background discriminating variables included in the fit, $m_{\rm ES}$, ΔE and MLP, and the Dalitz plot variable.
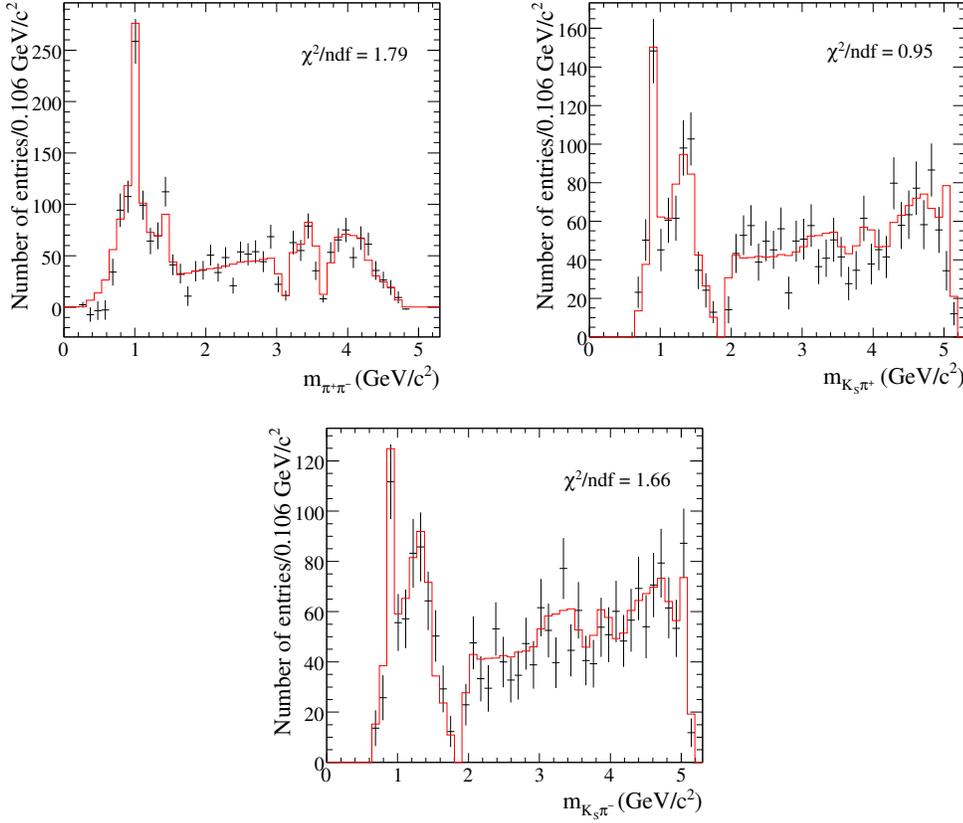
Figure 5.4: *Projections on the $m_{\pi^+\pi^-}$ and $m_{K_S^0\pi}$ invariant masses of the $_s\mathcal{P}lots$ Dalitz distribution for the signal events. Good agreement between the global fit and the prediction of the Dalitz plot PDF from the fit only to the three discriminating variables m_{ES}, ΔE and MLP is observed.*

was addressed in the systematic error studies.

Finally, a comparison of the global fit and the prediction for the distribution of the Δt variable (made by using only m_{ES}, ΔE and MLP discriminating variables) for signal events is shown in Figure 5.6. Again, a very good agreement can be observed.
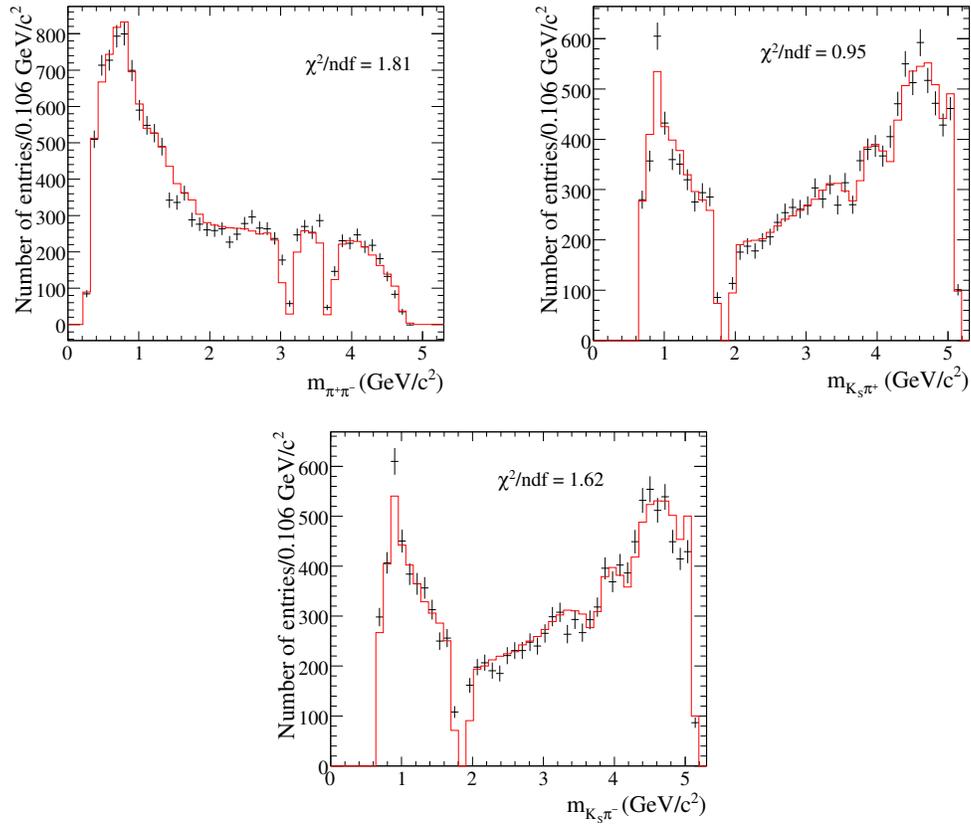
Figure 5.5: *Projections on the $m_{\pi^+\pi^-}$ and $m_{K_S^0\pi}$ invariant masses of the $_s\mathcal{P}lots$ Dalitz distribution for the continuum background events. Good agreement between the global fit and the prediction on the Dalitz plot PDF from the fit only to the three discriminating variables m_{ES}, ΔE and MLP is observed.*
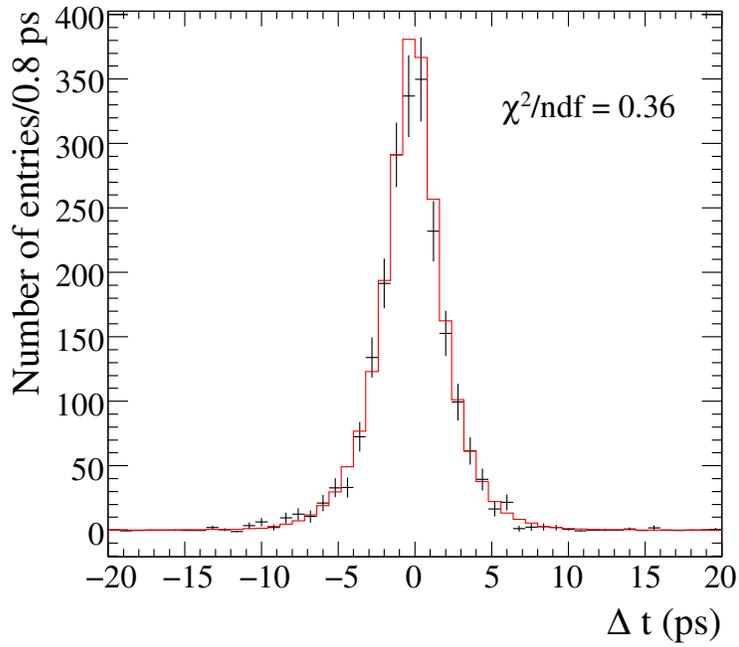
Figure 5.6: *Comparison of the global fit and the prediction on distribution of Δt made by using m_{ES}, ΔE and MLP variables, for signal events.*

5.2.2 Mass projection plots

The histograms shown below have been created to illustrate the fit results in the projection variables $m_{K_S^0 \pi^\pm}$ and $m_{\pi^+\pi^-}$. These histograms are made with the requirement that the orthogonal invariant masses are greater than $2\,\mathrm{GeV}$ (in order to remove the contribution of the orthogonal resonances; see at example a typical Dalitz plot distribution in Figure 1.11) and that the MLP variable is greater than 0.0. A tighter cut on MLP variable is applied in order to reduce continuum background and enhance signal events. In each of the plots the data are shown as the black points with error bars, the lower solid red histogram is the continuum background component, the middle solid green histogram is the $B\overline{B}$ background contribution, while the upper blue histogram shows the total fit result. The empty histogram shows the signal contribution. As well as the full spectrum plots (Figure 5.7), additional plots are constructed to show particular regions of the invariant mass spectra, such as $K^*(892)$, $K_0^*(1430)$, χ_{c0}, $\rho^0(770)$ and $f_0(980)$ (Figure 5.8). From these plots, it can be concluded that the fit describes data well. A quick estimation of the number of events in the region of the χ_{c0} resonance, which is visible as a small peak in the bottom plot in Figure 5.7 (a larger plot of this region is given in Figure 5.8), gives a value of 14 ± 6 events. Therefore, this structure cannot be interpreted as signature of the χ_{c0} resonance at the 3σ level.

5.2.3 Isobar coefficients and event yields

In the fit isobar coefficients for the different components of the signal model, together with signal and continuum background events yields, are directly measured. The results are given together with their statistical errors in Table 5.1. The measured isobar coefficient are used to extract the quasi-two-body parameters (Q2B) and fit fractions, defined earlier in Section 1.2.2 and Section 1.5.5.

Their definitions are repeated below:

$$S^j = \frac{2\left(x_j\Delta y_j - y_j\Delta x_j\right)\cos\phi_{\text{mix}} - \left(x_j^2 - \Delta x_j^2 + y_j^2 - \Delta y_j^2\right)\sin\phi_{\text{mix}}}{\left(x_j^2 + \Delta x_j^2 + y_j^2 + \Delta y_j^2\right)} \quad (5.1)$$

$$C^j = 2\left(x_j\Delta x_j + y_j\Delta y_j\right)/\left(x_j^2 + \Delta x_j^2 + y_j^2 + \Delta y_j^2\right), \quad (5.2)$$

and:

$$FF_j = \frac{\int\int_{DP}\left|c_jF_j(m^2_{K_S\pi^+}, m^2_{K_S\pi^-})\right|^2 dm^2_{K_S\pi^+}dm^2_{K_S\pi^-}}{\int\int_{DP}\left|\sum_j c_jF_j(m^2_{K_S\pi^+}, m^2_{K_S\pi^-})\right|^2 dm^2_{K_S\pi^+}dm^2_{K_S\pi^-}}, \quad (5.3)$$

where $\phi_{\text{mix}} = 2\beta$ and $c_j = (x_j + \Delta x_j) + i(y_j + \Delta y_j)$. The parameters S^j and C^j are used to describe the CP eigenstate channels. For the flavour specific intermediate resonances the parameter A^j_{CP} defined as $A^j_{\text{CP}} = -C^j$ is used.
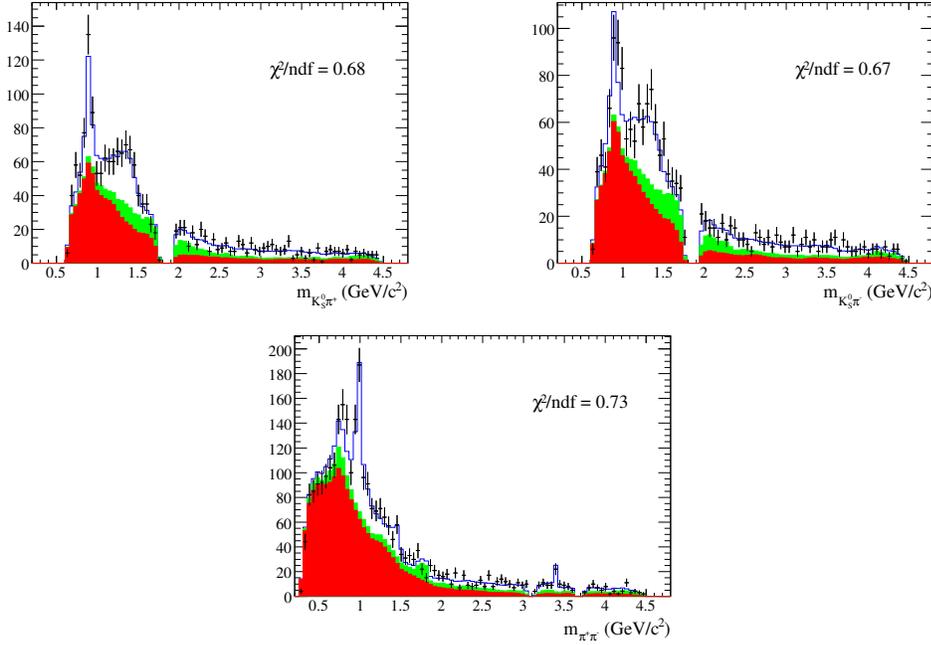
Figure 5.7: *Invariant mass plots for the $B^0 \rightarrow K^0_S\pi^+\pi^-$ fit. The upper plots shows the $K^0_S\pi^\pm$ mass spectrum; The bottom plot shows the $\pi^+\pi^-$ mass spectrum; The large dips in the spectra correspond to the vetoes described in Section 4.3. Note the small χ_{c0} component in the $\pi^+\pi^-$ mass spectrum plot.*

148
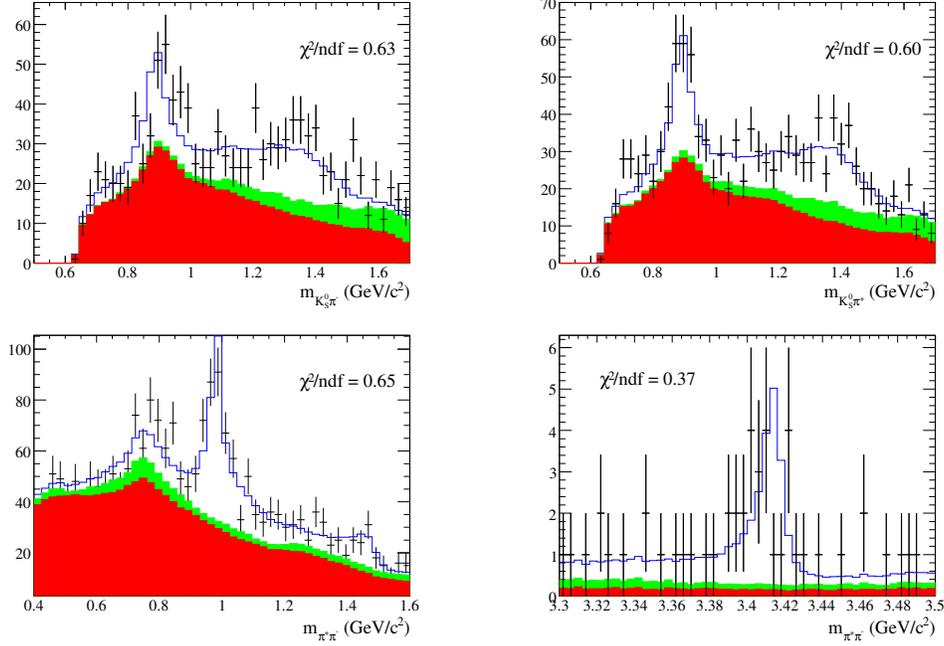
Figure 5.8: *Invariant mass plots for the* $B^0 \to K_S^0 \pi^+ \pi^-$ *fit. The upper plots show the* $K_S^0 \pi^\pm$ *mass spectrum in the region of the* $K^*(892)$ *and* $K_0^*(1430)$ *resonances; Bottom plots show the* $\pi^+\pi^-$ *mass spectrum in the regions of* $f_0(980)$ *and* $\rho^0(770)$ *resonances (left) and* χ_{c0} *resonance (right);*

In addition to these parameters, for each resonance A^k the phase between that resonance and its conjugate $\bar{A}^k$, is also calculated. For the flavour specific final states, which in the case of $B^0 \to K_S^0 \pi^+ \pi^-$ decay do not overlap in the Dalitz plot, this phase is denoted as $\Delta\phi(A^k)$, while in the case of the CP eigenstates as $\phi(A^k)$.

It is important to mention that by the convention used in this analysis the value of the mixing angle ϕ_{mix} was fixed to the world average value $(21.1 \pm 0.9)°$ [26], so the definition of the above mentioned phase is the same as the definition of the effective mixing angle:

$$2\beta_{\text{eff}}(A^k) = \arg(\bar{c}_k c_k^* e^{i\phi_{\text{mix}}}). \tag{5.4}$$

Although the same by definition, they differ in their physical interpretation.

149

Table 5.1: *Results of the fit to data for the isobar coefficients and event yields with statistical uncertainties only.*

Resonance	x	y	Δx	Δy
$f_0(980)K_S^0$	0.87 ± 0.17	-0.70 ± 0.22	0.24 ± 0.15	0.28 ± 0.16
$\rho^0(770)K_S^0$	0.59 ± 0.15	0.44 ± 0.17	-0.03 ± 0.12	-0.01 ± 0.10
$f_0(1300)K_S^0$	0.13 ± 0.11	0.39 ± 0.10	0.12 ± 0.13	-0.05 ± 0.11
NR	0.67 ± 0.18	0.63 ± 0.17	0.14 ± 0.14	-0.06 ± 0.15
$K^*(892)\pi$	$1\ (fixed)$	$0\ (fixed)$	0.09 ± 0.05	-0.05 ± 0.19
$K_0^*(1430)\pi$	-2.04 ± 0.15	0.05 ± 0.23	-0.02 ± 0.09	-0.51 ± 0.31
$f_2(1270)K_S^0$	0.30 ± 0.08	-0.05 ± 0.10	0.11 ± 0.09	0.02 ± 0.11
$\chi_{c0}K_S^0$	0.30 ± 0.06	0.05 ± 0.11	0.04 ± 0.09	-0.04 ± 0.09
signal yield	2240 ± 58			
continuum yield	13719 ± 118			

The $2\beta_{\text{eff}}(A^k)$ quantifies the time-dependent, mixing-induced CP asymmetry, and the $\Delta\phi(A^k)$ describes flavour-specific modes, for which there is no interference in decays with and without mixing. For such modes, sensitivity to $\Delta\phi(A^k)$ is provided indirectly by the interference between these resonances with other modes that are accessible to both B^0 and $\bar{B}^0$ decays. These parameter can only be measured in a Dalitz plot analysis.

The Cartesian coordinates parametrisation of the isobar coefficients used in this analysis is not the most natural parametrisation for the complex numbers. It makes difficult any estimation of the size of resonance magnitudes and phases. Since the Q2B parameters are the parameters of the most interest, instead of giving estimations of the systematics and model errors for x, y, Δx and Δy, they will be given for Q2B parameters.
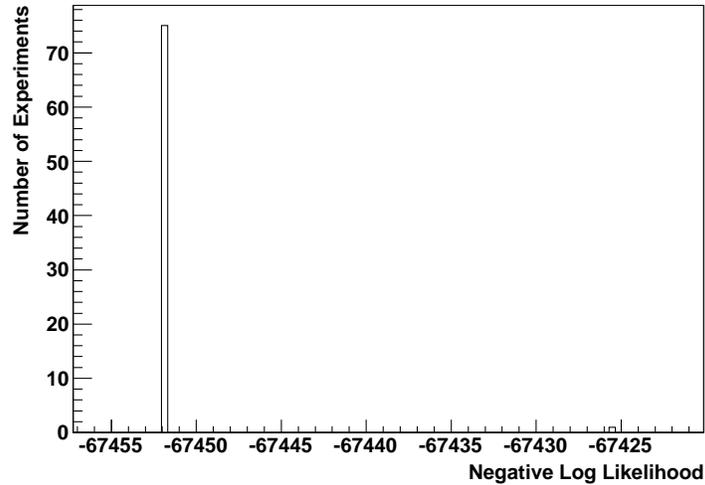
Figure 5.9: *Multiple solutions in the amplitude fit.*

Multiple solution

As mentioned before, the MC toy tests showed that since the likelihood space is highly non-trivial, the fit can easily become stuck in a local minimum. In order to check for multiple solutions, the distribution of the values of the negative log-likelihood function for 100 different fits of data sample is plotted. The plot is shown in Figure 5.9. It can be seen that 76 out of 100 fits converged and that out of these 75 converged to the solution with the best likelihood. Also, the secondary solution is sufficiently far from the preferred one, so that there is no need to be worried about a possible solution degeneracy.

Correlations

In Figure 5.10 the correlation matrix of the fitted parameters is shown, while the numerical values of the correlation matrix can be found in Chapter D. As expected, some of the parameters are highly correlated. A large correlation can be seen between $f_0(980)$ and $\rho^0(770)$ parameters as well as between non-resonant amplitude and $f_0(980)$ and $\rho^0(770)$. Also a large negative cor-

151

relation between $K^*(1430)$ and $f_0(980)$ is visible. The signal and continuum background yields do not appear to be correlated with other parameters.

$(1,2,3,4) \equiv f_0(980)(X, Y, \Delta X, \Delta Y)$ $(5,6,7,8) \equiv \rho^0(770)(X, Y, \Delta X, \Delta Y)$

$(9,10,11,12) \equiv f_0(1300)(X, Y, \Delta X, \Delta Y)$ $(13,14,15,16) \equiv NR(X, Y, \Delta X, \Delta Y)$

$(17,18) \equiv K^*(892)(\Delta X, \Delta Y)$ $(19,20,21,22) \equiv K^*(1430)(X, Y, \Delta X, \Delta Y)$

$(23,24, 25, 26) \equiv f_2(1270)(X, Y, \Delta X, \Delta Y)$ $(27, 28, 29\ 30) \equiv \chi_{c0}(X, Y, \Delta X, \Delta Y)$

$(31) \equiv$ signal yield $(32) \equiv$ continuum background yield

Figure 5.10: *Correlations between the parameters varied in the fit. z axis shows the values of the correlation coefficients. The x and y axises are labeled in such a way that the label value corresponds to the particular fitted parameter. The transcription between the label values and the fitted parameters is given below the plot.*

5.3 Systematic uncertainties

There are several sources of systematics uncertainty in this analysis. The dominant sources and the methods used to estimate the systematic uncertainties on the results presented in Section 5.2.3, will be described in more details.

5.3.1 Fixed PDF parameters

All parameters of the m_{ES} and ΔE PDFs for signal and continuum background hypotheses are kept fixed in the fit, as are the contents of histograms describing corresponding distributions of $B\overline{B}$ background.

For the signal hypothesis the associated systematic uncertainty is determined by varying incoherently each parameter of m_{ES} and ΔE PDFs up and down by 1σ according to the discrepancies observed between data and MC in the channel $B^0 \to D^{\mp}\pi^{\pm}$ ($D^{\mp} \to K_S^0 \pi^{\mp}$), described in Section 4.5.5.

For the continuum background hypothesis a similar procedure is carried out for the ARGUS shape parameter that describes the continuum m_{ES} distribution. It is varied incoherently in accordance with the difference observed between the on-peak sideband data and off-peak data, or the error from these fits, whichever is larger.

$B\overline{B}$ m_{ES} and ΔE shapes for all groups of $B\overline{B}$ background (14 groups in total) are described by histograms. In order to estimate the systematics coming from the fact that these have been fixed in the fit, the content of each bin of these histograms is fluctuated independently according to the associated statistic error. In this way 100 sets of m_{ES} and ΔE $B\overline{B}$ histograms are made, each differing slightly form the original set used in the fit. The fit is then repeated. Each of the $B\overline{B}$ m_{ES} and ΔE histogram sets is fitted 20 times with randomized initial values of the fitted parameters, after which the fit with the highest value of the likelihood function is selected as the best. Once this procedure is applied on all histogram sets, the distribution of each parameter of interest is plotted and the RMS of the distribution is taken as the absolute

systematic uncertainty. Systematic uncertainties for all three described cases are given in Table 5.3 - Table 5.5.

5.3.2 Δt parameter fluctuations

The parameters of the signal Δt resolution function (the same resolution function is used for $B^0 \bar{B}^0$ background events), dilutions and dilution differences are kept fixed in the fit. The associated systematic uncertainty is determined by varying each parameter of the resolution model (scale factors, biases, fractions, dilutions, dilution differences) up and down by 1σ. Since these parameters are largely correlated they are varied coherently, according to the correlations between parameters obtained in the studies of the charmonium $\sin 2\beta$ analyses [54]. For each set of varied parameters the fit is repeated 20 times with randomized initial values of the fitted parameters, after which the best fit is chosen, distributions of parameters of interest are plotted and for each RMS is taken as the absolute systematic uncertainty. Results of this study are given in Table 5.6.

A procedure similar to the one described above is performed in order to analyse the systematic uncertainties arising from the non-floating continuum background Δt resolution function parameters. These are varied coherently, according to the correlations between them obtained from the fit to the off-peak data (see Section 4.4). The values of the associated systematics are given in Table 5.7.

5.3.3 Tag-side interference effects

When analysing decays used for tagging it is usually assumed that the individual tagging states can be reached only from a B^0 or $\bar{B}^0$ meson. This assumption is valid only for the lepton tags. In the case of the non-leptonic tagging decays there is a possibility of suppressed contributions to the tag-side final state.

One of the examples is the $D^+\pi^-$ final state, with $D^+ \to K^-\pi^+\pi^+$, which is usually associated with $\bar{B}^0$ meson since the charge of the kaon has the same sign as charge of a b quark. However, this final state can also be reached from a B^0 meson through a $\bar{b} \to c\bar{u}\bar{d}$ decay. Its amplitude is CKM suppressed relative to the dominant $\bar{B}^0$ decay amplitude ($|V_{ub}^*V_{cd}/V_{cb}V_{ud}^*| \approx 0.02$) and has a relative weak phase difference of γ.

In order to evaluate the systematic effects on the measured signal amplitudes due to the interference between CKM-favoured $b \to c\bar{u}d$ and doubly-CKM-suppressed $\bar{b} \to c\bar{u}d$ tagging amplitudes, the formula of the decay rate of a pair of coherently produced neutral B mesons, which subsequently decay to the arbitrary final states f_t and f_r was used:

$$F(\Delta t) = e^{-\Gamma|\Delta t|}[R + C\cos(\Delta m\Delta t) + S\sin(\Delta m\Delta t)]. \tag{5.5}$$

Here the coefficients R, C and S are given by:

$$
\begin{aligned}
R &= \frac{1}{2}\left(|a_+|^2 + |a_-|^2\right), \\
C &= \frac{1}{2}\left(|a_+|^2 - |a_-|^2\right), \\
S &= Im\left(a_+^*a_-\right),
\end{aligned}
\tag{5.6}
$$

where:

$$
\begin{aligned}
a_+ &= \bar{A}_t A_r - A_t \bar{A}_r, \tag{5.7} \\
a_- &= -\left(\frac{q}{p}\bar{A}_t \bar{A}_r - \frac{p}{q}A_t A_r\right), \tag{5.8}
\end{aligned}
$$

and $A_k(\bar{A}_k)$ is the $B^0(\bar{B}^0)$ decay amplitude to the final state f_k. The detailed derivation of this formula can be found in [78]. Equations Eq. (5.7) and Eq. (5.8) can be usefully rewritten in the following form:

$$
\begin{aligned}
a_+ &= -A_t\left(\bar{A}_r - \lambda_t A_r\right), \tag{5.9} \\
a_- &= \frac{p}{q}A_t\left(A_r - \left(\frac{q}{p}\right)^2 \lambda_t \bar{A}_r\right). \tag{5.10}
\end{aligned}
$$

155

Here:

$$\lambda_t = \frac{\bar{A}_t}{A_t} = re^{-i\gamma}e^{i\delta}; \qquad r = \left| \frac{V_{ub}^* V_{cd}}{V_{cb} V_{ud}^*} \right| \approx 0.02, \qquad (5.11)$$

where γ and δ are relative weak and strong phase differences respectively. Now assume that the tagged final state has a contribution from only one amplitude and that at the moment $t = t_{tag}$ the tagged meson is identified as a B^0. In this case $\bar{A}_t = 0$ and the coefficients a_+ and a_- become:

$$a_+ = -A_t \bar{A}_r, \qquad (5.12)$$

$$a_- = \frac{p}{q} A_t A_r. \qquad (5.13)$$

Comparing Eq. (5.12) with Eq. (5.9) and Eq. (5.13) with Eq. (5.10) it can be conclude that in the case when the contribution of the doubly-CKM-suppressed (DCS) amplitude to the tagged final state is taken into account the signal decay amplitudes $\bar{A}_r$ and A_r are shifted by factors of $-\lambda_t A_r$ and $-(\frac{q}{p})^2 \lambda_t \bar{A}_r$ respectively, compared to the situation where this contribution is not taken into account. Contributions of the doubly-CKM-suppressed amplitude to the time dependence of tagged decays is given in Table 5.2. To quantify the effect

Table 5.2: *Contributions of the doubly-CKM-suppressed amplitude to the time dependence of tagged decays.*

	DCS off	DCS on
a_+	$-A_t \bar{A}_r$	$-A_t \left(\bar{A}_r - \lambda_t A_r \right)$
a_-	$\frac{p}{q} A_t A_r$	$\frac{p}{q} A_t \left(A_r - \left(\frac{q}{p}\right)^2 \lambda_t \bar{A}_r \right)$
A_r	A_r	$A_r - (\frac{q}{p})^2 \lambda_t \bar{A}_r$
$\bar{A}_r$	$\bar{A}_r$	$\bar{A}_r - \lambda_t A_r$

of DCS decays on the isobar coefficients 500 samples where generated with parameters r, δ and γ generated randomly in the ranges:

- r uniform in $[0.00, 0.04]$,

- δ uniform in $[0, 2\pi]$,

- γ uniform in $[39^0, 80^o]$.

After fitting the samples the mean shift in each amplitude was calculated. Results of these calculations are given in Table 5.8.

5.3.4 Dalitz plot histograms

The fact that the $B\overline{B}$ background, continuum background and efficiency Dalitz plot histograms are all fixed in the fit introduces sources of systematic uncertainty. The same procedure as in the case of m_{ES} and ΔE $B\overline{B}$ background histograms is applied here in order to estimate systematics uncertainties. The results are given in Table 5.9, Table 5.10 and Table 5.11.

An additional source of systematics come from the assumption that the Dalitz plot distribution of continuum background in the on-peak sideband is the same as in the signal region. This is tested by creating histograms from the sideband and signal region of a continuum MC sample. The signal region histogram is used to generate a sample toy MC, which is then fitted using both the signal and sideband histograms. The difference observed in the fitted parameters between these two cases is taken to be the systematic uncertainty. The results of this analysis are given in Table 5.12.

5.3.5 $B\overline{B}$ background yield fluctuations

Although the continuum background yield is extracted from the fit and therefore does not contribute to the systematic uncertainties, the number of $B\overline{B}$ background events across the different categories, as well as asymmetries are fixed from the MC studies. To estimate the effect of this uncertainty on the fit parameters, fits to the data are performed. In each of the 10 largest $B\overline{B}$ background categories both its yield and CP asymmetry are floated. Variations in the other fitted parameters are determined and the variations from ten different fits are added in quadrature to give the overall systematics uncertainty from the $B\overline{B}$ background yield and asymmetries. The results are

shown in Table 5.13.

5.3.6   Fit biases

To search for possible biases in the fitting procedure a number of toy and full MC tests are performed (see Section 5.1). To estimate this systematic the differences between the true and the fitted (biased) values from full MC tests can be taken. From the results of these tests it can bee seen that the differences are rather small. Any large bias is accounted for in the systematics errors. This is done by the assigning a systematic uncertainty of half of the value of the bias added in quadrature with the uncertainty with which the bias is known.

Table 5.3: *Systematic uncertainties - fixed signal m_{ES} and ΔE parameters.*

Resonance	$\mathcal{A}_{CP}$	$\mathcal{S}$	$\Delta\phi$ (rad)	$\overline{B}^0$ fraction	B^0 fraction
$f_0(980)K_S^0$	0.0045	0.0062	0.0369	0.0019	0.0022
$\rho^0(770)K_S^0$	0.0141	0.0295	0.0420	0.0011	0.0010
$f_0(1300)K_S^0$	0.0584		0.0295	0.0057	0.0019
NR	0.0297		0.0229	0.0026	0.0034
$K^*(892)\pi$	0.0019		0.0133	0.0003	0.0010
$K_0^*(1430)\pi$	0.0065		0.0009	0.0003	0.0038
$f_2(1270)K_S^0$	0.0568		0.0187	0.0006	0.0008
$\chi_{c0}K_S^0$	0.0067		0.0118	0.0003	0.0005

Table 5.4: *Systematic uncertainties − fixed continuum background m_{ES} parameters.*

Resonance	$\mathcal{A}_{CP}$	$\mathcal{S}$	$\Delta\phi$ (rad)	$\overline{B}^0$ fraction	B^0 fraction
$f_0(980)K_S^0$	0.0001	0.0001	0.0005	0.0000	-0.0001
$\rho^0(770)K_S^0$	0.0007	0.0001	0.0002	0.0002	0.0000
$f_0(1300)K_S^0$	0.0014		0.0006	0.0001	0.0000
NR	0.0004		0.0004	0.0001	0.0001
$K^*(892)\pi$	0.0002		0.0010	0.0000	0.0000
$K_0^*(1430)\pi$	0.0001		0.0015	0.0002	0.0000
$f_2(1270)K_S^0$	0.0002		0.0009	0.0001	0.0001
$\chi_{c0}K_S^0$	0.0003		0.0006	0.0000	0.0000

Table 5.5: *Systematic uncertainties - fixed $B\bar{B}$ background m_{ES} and ΔE parameters.*

Resonance	$\mathcal{A}_{CP}$	$\mathcal{S}$	$\Delta\phi$ (rad)	$\overline{B}^0$ fraction	B^0 fraction
$f_0(980)K_S^0$	0.0039	0.0027	0.0119	0.0010	0.0008
$\rho^0(770)K_S^0$	0.0054	0.0082	0.0113	0.0005	0.0004
$f_0(1300)K_S^0$	0.0172		0.0223	0.0006	0.0003
NR	0.0142		0.0216	0.0017	0.0013
$K^*(892)\pi$	0.0017		0.0385	0.0003	0.0005
$K_0^*(1430)\pi$	0.0026		0.0333	0.0006	0.0011
$f_2(1270)K_S^0$	0.0128		0.0337	0.0001	0.0003
$\chi_{c0}K_S^0$	0.0113		0.0204	0.0002	0.0002

Table 5.6: *Systematic error arising from the non-floating signal ($B^0\bar{B}^0$ background) resolution function parameters.*

Resonance	$\mathcal{A}_{CP}$	$\mathcal{S}$	$\Delta\phi$ (rad)	$\overline{B}^0$ fraction	B^0 fraction
$f_0(980)K_S^0$	0.0026	0.0014	0.0063	0.0005	0.0003
$\rho^0(770)K_S^0$	0.0014	0.0042	0.0058	0.0001	0.0002
$f_0(1300)K_S^0$	0.0031		0.0058	0.0001	0.0001
NR	0.0017		0.0017	0.0002	0.0003
$K^*(892)\pi$	0.0002		0.0069	0.0001	0.0000
$K_0^*(1430)\pi$	0.0003		0.0062	0.0003	0.0002
$f_2(1270)K_S^0$	0.0029		0.0115	0.0000	0.0001
$\chi_{c0}K_S^0$	0.0015		0.0024	0.0000	0.0000

Table 5.7: *Systematic error arising from the non-floating continuum background Δt resolution function parameters.*

Resonance	$\mathcal{A}_{CP}$	$\mathcal{S}$	$\Delta\phi$ (rad)	$\overline{B}^0$ fraction	B^0 fraction
$f_0(980)K_S^0$	0.0000	0.0000	0.0100	0.0011	0.0006
$\rho^0(770)K_S^0$	0.0000	0.0100	0.0100	0.0008	0.0011
$f_0(1300)K_S^0$	0.0100		0.0200	0.0008	0.0004
NR	0.0100		0.0100	0.0008	0.0013
$K^*(892)\pi$	0.0000		0.0000	0.0005	0.0009
$K_0^*(1430)\pi$	0.0000		0.0000	0.0002	0.0006
$f_2(1270)K_S^0$	0.0100		0.0100	0.0001	0.0002
$\chi_{c0}K_S^0$	0.0100		0.0100	0.0002	0.0002

Table 5.8: *Systematic error arising from the tag side interference effects.*

Resonance	$\mathcal{A}_{CP}$	$\mathcal{S}$	$\Delta\phi$ (rad)	$\overline{B}^0$ fraction	B^0 fraction
$f_0(980)K_S^0$	0.0028	-0.0018	0.0142	0.0006	0.0003
$\rho^0(770)K_S^0$	0.0074	-0.0330	0.0800	0.0001	0.0002
$f_0(1300)K_S^0$	0.0107		0.0406	0.0008	0.0001
NR	0.0013		0.0265	0.0018	0.0003
$K^*(892)\pi$	-0.0108		-0.0762	0.0003	0.0000
$K_0^*(1430)\pi$	-0.0041		0.0615	0.0020	0.0002
$f_2(1270)K_S^0$	0.0260		-0.0515	0.0005	0.0001
$\chi_{c0}K_S^0$	-0.0159		0.0265	0.0005	0.0000

Table 5.9: *Systematic error arising from the non-floating $B\bar{B}$ background Dalitz plot.*

Resonance	$\mathcal{A}_{CP}$	$\mathcal{S}$	$\Delta\phi$ (rad)	$\overline{B}^0$ fraction	B^0 fraction
$f_0(980)K_S^0$	0.0088	0.0066	0.0204	0.0026	0.0018
$\rho^0(770)K_S^0$	0.0182	0.0227	0.0216	0.0015	0.0015
$f_0(1300)K_S^0$	0.0399		0.0179	0.0028	0.0013
NR	0.0430		0.0276	0.0048	0.0042
$K^*(892)\pi$	0.0055		0.0110	0.0008	0.0012
$K_0^*(1430)\pi$	0.0075		0.0261	0.0020	0.0033
$f_2(1270)K_S^0$	0.0411		0.0151	0.0005	0.0007
$\chi_{c0}K_S^0$	0.0250		0.0310	0.0005	0.0006

Table 5.10: *Systematic error arising from the non-floating continuum background Dalitz plot.*

Resonance	$\mathcal{A}_{CP}$	$\mathcal{S}$	$\Delta\phi$ (rad)	$\overline{B}^0$ fraction	B^0 fraction
$f_0(980)K_S^0$	0.0112	0.0054	0.0230	0.0030	0.0020
$\rho^0(770)K_S^0$	0.0210	0.0181	0.0264	0.0016	0.0017
$f_0(1300)K_S^0$	0.0325		0.0498	0.0011	0.0008
NR	0.0390		0.0379	0.0048	0.0043
$K^*(892)\pi$	0.0083		0.0738	0.0015	0.0013
$K_0^*(1430)\pi$	0.0077		0.0588	0.0028	0.0028
$f_2(1270)K_S^0$	0.0342		0.1144	0.0004	0.0007
$\chi_{c0}K_S^0$	0.0319		0.0390	0.0007	0.0006

Table 5.11: *Systematic error arising from the non-floating signal efficiency histogram content.*

Resonance	$\mathcal{A}_{CP}$	$\mathcal{S}$	$\Delta\phi$ (rad)	$\overline{B}^0$ fraction	B^0 fraction
$f_0(980)K_S^0$	0.0028	0.0013	0.0057	0.0006	0.0005
$\rho^0(770)K_S^0$	0.0071	0.0060	0.0085	0.0006	0.0006
$f_0(1300)K_S^0$	0.0076		0.0119	0.0003	0.0002
NR	0.0067		0.0075	0.0009	0.0006
$K^*(892)\pi$	0.0035		0.0237	0.0005	0.0005
$K_0^*(1430)\pi$	0.0015		0.0195	0.0007	0.0010
$f_2(1270)K_S^0$	0.0131		0.0423	0.0001	0.0003
$\chi_{c0}K_S^0$	0.0082		0.0108	0.0001	0.0001

Table 5.12: *Systematic error caused by assumption that the Dalitz plot distribution of continuum background events in the Grand Side band is almost the same as the Dalitz plot distribution of continuum background events in the Signal Band.*

Resonance	$\mathcal{A}_{CP}$	$\mathcal{S}$	$\Delta\phi$ (rad)	$\overline{B}^0$ fraction	B^0 fraction
$f_0(980)K_S^0$	0.0770	0.0002	0.0334	0.0330	0.0138
$\rho^0(770)K_S^0$	-0.0215	0.0107	0.0155	0.0054	0.0070
$f_0(1300)K_S^0$	0.0407		0.0110	0.0019	-0.0002
NR	-0.0114		-0.0251	-0.0580	-0.0587
$K^*(892)\pi$	0.0334		-0.0021	0.0100	0.0074
$K_0^*(1430)\pi$	-0.0045		-0.0190	0.0028	0.0173
$f_2(1270)K_S^0$	-0.0117		0.0160	-0.0030	-0.0057
$\chi_{c0}K_S^0$	-0.0780		0.0242	0.0011	0.0037

Table 5.13: *Systematic error arising from the non-floating $B\bar{B}$ background yields.*

Resonance	$\mathcal{A}_{CP}$	$\mathcal{S}$	$\Delta\phi$ (rad)	$\overline{B}^0$ fraction	B^0 fraction
$f_0(980)K_S^0$	0.0111	0.0071	0.0311	0.0041	0.0043
$\rho^0(770)K_S^0$	0.0086	0.0195	0.0260	0.0015	0.0017
$f_0(1300)K_S^0$	0.0186		0.0428	0.0011	0.0008
NR	0.0385		0.0225	0.0061	0.0040
$K^*(892)\pi$	0.0039		0.1326	0.0024	0.0032
$K_0^*(1430)\pi$	0.0086		0.1106	0.0018	0.0050
$f_2(1270)K_S^0$	0.0161		0.2277	0.0007	0.0015
$\chi_{c0}K_S^0$	0.0480		0.0647	0.0004	0.0011

5.3.7 Model errors

The Dalitz plot signal model has many associated uncertainties. These are combined into a model error, separate from the other systematics errors. Sources of the model error analysed in this work are listed below:

- The masses and widths of all resonances;

- The LASS parameters;

- The Flatté parameters;

- The Blatt-Weisskopf barrier radius;

- Alternative resonance lineshapes (Gounaris-Sakurai for $\rho^0(770)$).

The masses and widths of all resonances are kept constant in the fit. In order to account for the error of this approach all of them are varied up and down by 1σ according to their statistical errors coming from the PDF fits. The same was done with the LASS parameters.

Table 5.14: *Contribution of the uncertainties of the masses and widths of all resonances to the Dalitz plot model error.*

Resonance	$\mathcal{A}_{CP}$	$\mathcal{S}$	$\Delta\phi$	$\overline{B}^0$ fraction	B^0 fraction
$f_0(980)K_S^0$	0.0051	-0.0013	-0.0015	-0.0006	-0.0025
$\rho^0(770)K_S^0$	0.0003	0.0001	0.0000	-0.0002	0.0001
$f_0(1300)K_S^0$	0.0097		-0.0049	0.0002	-0.0020
NR	0.0021		-0.0030	-0.0018	-0.0021
$K^*(892)\pi$	-0.0002		0.0044	-0.0003	0.0003
$K_0^*(1430)\pi$	-0.0010		-0.0586	0.0022	0.0033
$f_2(1270)K_S^0$	-0.0132		-0.0151	-0.0003	0.0001
$\chi_{c0}K_S^0$	-0.0069		-0.0084	0.0000	-0.0002

The coupling constants g_π and g_K, used in the Flatté parameterisation of the $f_0(980)$ resonance were fixed in the fit. Following results in [79], g_π, the

ratio g_K/g_π and resonance pole mass are varied simultaneously in order to maintain the constant value of the ratio: $(2m_K - m_0)/g_\pi$.

Also, in this analysis, for the radius of the resonance barrier the mean value of experimental measurements of the radii of the barriers of K^* and ρ resonances [45, 37] is used (see Section 1.5.4). The error of such an approach is estimated by fitting the data first with a signal model where the radius of the barrier is set to be 3 GeV^{-1}, and then 5 GeV^{-1}. Differences between these fits and the standard fit are calculated and added in quadrature to give the overall model uncertainty associated with the Blatt-Weisskopf barrier radius.

The results of the listed analysis are given in Table 5.14, Table 5.15, Table 5.17, Table 5.16, and Table 5.18.

Table 5.15: *Contribution of the LASS parameters uncertainties to the Dalitz plot model error.*

Resonance	$\mathcal{A}_{CP}$	$\mathcal{S}$	$\Delta\phi$ (rad)	$\overline{B}^0$ fraction	B^0 fraction
$f_0(980)K_S^0$	0.00291	0.00375	0.01712	0.0006	0.0011
$\rho^0(770)K_S^0$	0.00667	0.00781	0.01166	0.0001	0.0009
$f_0(1300)K_S^0$	0.00904		0.02754	0.0003	0.0004
NR	0.04506		0.01640	0.0022	0.0070
$K^*(892)\pi$	0.00097		0.01083	0.0023	0.0007
$K_0^*(1430)\pi$	0.00111		0.01147	0.0026	0.0039
$f_2(1270)K_S^0$	0.00243		0.01669	0.0000	0.0001
$\chi_{c0}K_S^0$	0.01815		0.01518	0.0001	0.0001

Table 5.16: *Contribution of the Flatté parameters uncertainties to the Dalitz plot model error.*

Resonance	$\mathcal{A}_{CP}$	$\mathcal{S}$	$\Delta\phi$	$\overline{B}^0$ fraction	B^0 fraction
$f_0(980)K_S^0$	0.00350	0.00800	0.03807	0.0062	0.0048
$\rho^0(770)K_S^0$	0.01674	0.03368	0.04861	0.0013	0.0029
$f_0(1300)K_S^0$	0.03775		0.09018	0.0024	0.0008
NR	0.03804		0.02219	0.0036	0.0046
$K^*(892)\pi$	0.00089		0.04638	0.0002	0.0006
$K_0^*(1430)\pi$	0.00151		0.04194	0.0008	0.0032
$f_2(1270)K_S^0$	0.03795		0.01980	0.0006	0.0002
$\chi_{c0}K_S^0$	0.01192		0.02987	0.0001	0.0002

Table 5.17: *Contribution of the Blatt-Weisskopf barrier radius uncertanity to the Dalitz plot model error.*

Resonance	$\mathcal{A}_{CP}$	$\mathcal{S}$	$\Delta\phi$ (rad)	$\overline{B}^0$ fraction	B^0 fraction
$f_0(980)K_S^0$	-0.0057	-0.0034	0.0154	0.0000	0.0019
$\rho^0(770)K_S^0$	0.0102	-0.0245	0.0345	-0.0018	-0.0022
$f_0(1300)K_S^0$	-0.0033		-0.0319	0.0006	0.0007
NR	0.0163		0.0000	0.0043	0.0018
$K^*(892)\pi$	-0.0015		0.0667	-0.0006	-0.0003
$K_0^*(1430)\pi$	0.0032		0.0629	0.0030	0.0004
$f_2(1270)K_S^0$	0.0392		0.0175	0.0003	-0.0007
$\chi_{c0}K_S^0$	0.0050		0.0274	-0.0002	0.0001

Table 5.18: *Contribution of the $\rho^0(770)$ lineshape uncertainty to the Dalitz plot model error* .

Resonance	$\mathcal{A}_{CP}$	$\mathcal{S}$	$\Delta\phi$	$\overline{B}^0$ fraction	B^0 fraction
$f_0(980)K_S^0$	0.0007	-0.0020	0.0088	0.0008	0.0004
$\rho^0(770)K_S^0$	0.0091	-0.0151	0.0217	-0.0007	-0.0015
$f_0(1300)K_S^0$	-0.0013		-0.0257	0.0003	0.0003
NR	0.0001		-0.0035	0.0006	0.0006
$K^*(892)\pi$	-0.0004		0.0094	0.0000	0.0000
$K_0^*(1430)\pi$	-0.0002		0.0073	0.0020	0.0015
$f_2(1270)K_S^0$	0.0005		0.0248	0.0001	0.0002
$\chi_{c0}K_S^0$	0.0011		-0.0003	0.0000	0.0000

5.4   Final results and conclusions

A summary of measurements of the Q2B parameters (the *CP* asymmetries, fit fractions and the relative phases) together with their statistical, systematic and the DP signal model errors is given in Table 5.19, while in Table 5.20 the measurements of the isobar coefficients are listed. The estimation of the statistical errors is made via toy MC studies. The reason for that lies in the fact that the variables of interest (*CP* asymmetries and the fit fractions) are derived from the isobar coefficients (fitted parameters). The isobar coefficients are largely correlated variables (see Figure 5.10) while the *CP* asymmetries and the fit fractions are highly non-linear functions of the isobar coefficients. Consequently, this approach is more suitable for error propagation.

Results obtained in this analysis are the most precise results on $B^0 \rightarrow K_S^0 \pi^+ \pi^-$ decay channel. All Q2B parameters are measured with increased precision and the solutions degeneracy seen in an earlier *BABAR*'s analysis of the same channel [77] is removed.

CP asymmetries

Direct *CP* asymmetries have been measured for all resonances and have been found to be consistent with zero. Measurements of the time-dependent asymmetries coefficients $\mathcal{S}$ and mixing angle β_{eff} have also been made for the *CP* eigenstate channels $B^0 \rightarrow f_0(980)K_S^0$ and $B^0 \rightarrow \rho^0(770)K_S^0$. They are found to be $\mathcal{S}(f_0(980)K_S^0) = -0.97 \pm 0.09 \pm 0.01 \pm 0.01$ and $\mathcal{S}(\rho^0(770)K_S^0) = 0.67 \pm 0.20 \pm 0.06 \pm 0.04$, and $2\beta_{\text{eff}}(f_0(980)K_S^0) = (77.0 \pm 18.5 \pm 4.0 \pm 2.6)°$ and $2\beta_{\text{eff}}(\rho^0(770)K_S^0) = (42.8 \pm 16.6 \pm 5.9 \pm 3.4)°$, respectively. The statistical errors are improved, and a very good agreement with charmonium measurements of $\sin 2\beta$ is obtained, especially for the $\rho^0(770)$ resonance.

Plots of Δt asymmetry in $f_0(980)$ and $\rho^0(770)$ regions are shown in Figure 5.11.

The relative phase between $B^0 \to K^{*+}\pi^-$ and $\overline{B}^0 \to K^{*-}\pi^+$ and the UT angle γ

The relative phase between $B^0 \to K^{*+}\pi^-$ and $\overline{B}^0 \to K^{*-}\pi^+$, needed for the determination of the unitarity triangle angle γ has been measured to be $\Delta\phi(K^*(892)\pi) = (34.9 \pm 23.1 \pm 7.5 \pm 4.7)^\circ$. This phase is only possible to measure in a Dalitz plot analysis, since $B^0 \to K^{*+}\pi^-$ and $\overline{B}^0 \to K^{*-}\pi^+$ amplitudes do not interfere. Sensitivity to this particular phase is provided indirectly by the interference between these resonances with other modes in the Dalitz plot model. The measurement of the relative phase between $B^0 \to K^{*+}\pi^-$ and $\overline{B}^0 \to K^{*-}\pi^+$ allows a new independent determination of the unitarity triangle angle γ, proposed in [27, 28]. The existing result obtained using this new method is $20^\circ < \gamma < 115^\circ$ [80], and it suffers from large experimental uncertainties with which the relative phases, needed for its determination, are known. The new result for the $\Delta\phi(K^*(892)\pi)$ value in a combination with the results expected from the $B^0 \to K^+\pi^0\pi^-$ analysis will improve the overall knowledge of this unitarity triangle angle. Once when the results from $B^0 \to K^+\pi^0\pi^-$ became available, the error on the new determination is expected to be of the order of the typical error on a Dalitz-plot measured phase, i.e. $\sim 20^\circ$.

Future Enhancements

Of course, as with any analysis, there is room for improvement within this one. The self cross feed model could be included, the $B\overline{B}$ bar model could be simplified, or a fit to the data performed without vetoing regions of the Dalitz plot where a large contribution of $B\overline{B}$ background events is expected. But all these changes will not bring significant improvement of the results because the accuracy of the measurements is limited by the statistical error. Considering that the *BABAR* experiment completed data collection in April 2008, these results, which use the final *BABAR* data set, will probably be the final word from *BABAR* on this decay channel and for the possible improvements one has

to wait for results from the Belle experiment or the LHCb experiment.
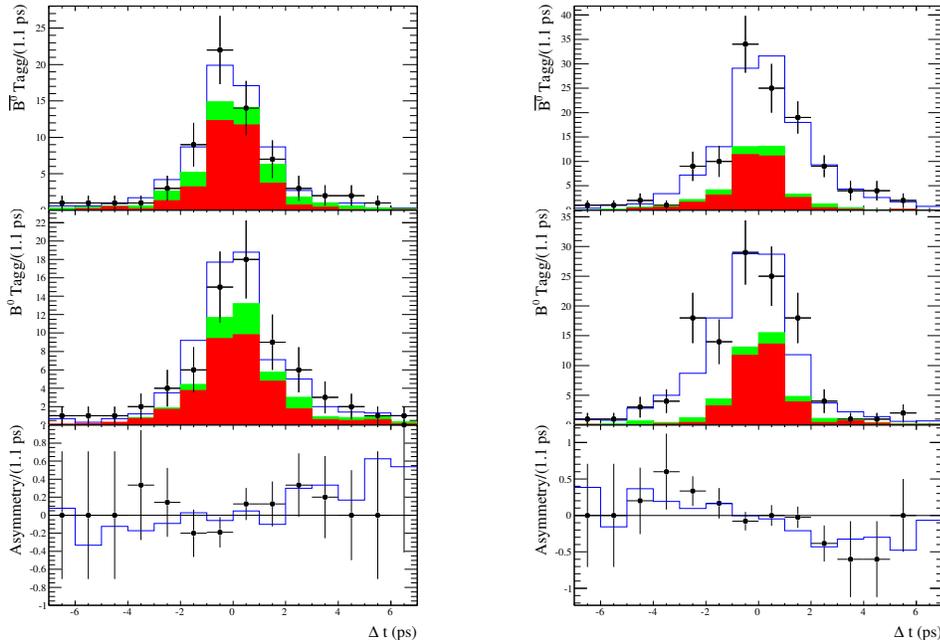
Figure 5.11: *Distributions of Δt when the B^0_{tag} is a B^0 (top), $\overline{B^0}$ (middle) and the derived Δt asymmetry (bottom). Plots on the left (right) hand side, correspond to events in the $f_0(980)K^0_S$ ($\rho^0(770)K^0_S$) region. The blue line is the total PDF, the red histogram is the continuum only PDF, green histogram is the $B\overline{B}$ PDF and points with error bars represent data. These distributions correspond to samples where the very tight cut on MLP is applied in order to enhance the signal contribution.*

Table 5.19: *Summary of measurements of the Q2B parameters. The first uncertainty is statistical, the second is systematic and the third represents the DP signal model error. The fit fraction values are given in percents, and the relative phases in degrees.*

$\mathcal{C}(f_0(980)K_S^0)$	$0.02 \pm 0.14 \pm 0.08 \pm 0.02$	$\mathcal{C}(\rho^0(770)K_S^0)$	$-0.14 \pm 0.27 \pm 0.04 \pm 0.02$
$\mathcal{S}(f_0(980)K_S^0)$	$-0.97 \pm 0.09 \pm 0.01 \pm 0.01$	$\mathcal{S}(\rho^0(770)K_S^0)$	$0.67 \pm 0.20 \pm 0.06 \pm 0.04$
$2\beta_{\mathrm{eff}}(f_0(980)K_S^0)$	$77.0 \pm 18.5 \pm 4.0 \pm 2.6$	$2\beta_{\mathrm{eff}}(\rho^0(770)K_S^0)$	$42.8 \pm 16.6 \pm 5.9 \pm 3.4$
$FF(f_0(980)K_S^0)$	$15.2 \pm 2.4 \pm 1.5 \pm 0.6$	$FF(\rho^0(770)K_S^0)$	$5.2 \pm 1.9 \pm 0.7 \pm 0.4$
$\overline{FF}(f_0(980)K_S^0)$	$16.1 \pm 3.0 \pm 0.3 \pm 0.6$	$\overline{FF}(\rho^0(770)K_S^0)$	$7.6 \pm 1.3 \pm 0.6 \pm 0.2$
$\mathcal{A}_{CP}(K^*(892)\pi)$	$-0.18 \pm 0.10 \pm 0.04 \pm 0.00$	$\mathcal{A}_{CP}((K\pi)_0^*\pi)$	$-0.03 \pm 0.06 \pm 0.02 \pm 0.00$
$\Delta\phi(K^*(892)\pi)$	$34.9 \pm 23.1 \pm 7.5 \pm 4.7$	$\Delta\phi((K\pi)_0^*\pi)$	$67.2 \pm 15.5 \pm 6.4 \pm 5.5$
$FF(K^*(892)\pi)$	$12.6 \pm 1.6 \pm 0.9 \pm 0.1$	$FF((K\pi)_0^*\pi)$	$46.7 \pm 2.9 \pm 1.9 \pm 0.6$
$\overline{FF}(K^*(892)\pi)$	$9.8 \pm 1.4 \pm 1.0 \pm 0.1$	$\overline{FF}((K\pi)_0^*\pi)$	$51.8 \pm 2.6 \pm 0.5 \pm 0.5$
$\mathcal{C}(f_2(1270)K_S^0)$	$0.57 \pm 0.80 \pm 0.09 \pm 0.06$	$\mathcal{C}(f_X(1300)K_S^0)$	$0.01 \pm 0.42 \pm 0.09 \pm 0.04$
$\phi(f_2(1270)K_S^0)$	$58.2 \pm 48.3 \pm 8.4 \pm 2.4$	$\phi(f_X(1300)K_S^0)$	$3.4 \pm 29.8 \pm 5.2 \pm 5.0$
$FF(f_2(1270)K_S^0)$	$1.6 \pm 1.0 \pm 0.6 \pm 0.1$	$FF(f_X(1300)K_S^0)$	$2.0 \pm 1.1 \pm 0.3 \pm 0.2$
$\overline{FF}(f_2(1270)K_S^0)$	$1.4 \pm 0.7 \pm 0.3 \pm 0.1$	$\overline{FF}(f_X(1300)K_S^0)$	$2.1 \pm 1.3 \pm 0.7 \pm 0.2$
$\mathcal{C}(NR)$	$0.14 \pm 0.23 \pm 0.08 \pm 0.06$	$\mathcal{C}(\chi_{c0}K_S^0)$	$-0.20 \pm 0.40 \pm 0.10 \pm 0.02$
$\phi(NR)$	$23.8 \pm 19.2 \pm 4.1 \pm 1.6$	$\phi(\chi_{c0}K_S^0)$	$19.5 \pm 36.2 \pm 5.35 \pm 2.5$
$FF(NR)$	$10.7 \pm 2.7 \pm 1.0 \pm 0.9$	$FF(\chi_{c0}K_S^0)$	$1.4 \pm 0.7 \pm 0.4 \pm 0.1$
$\overline{FF}(NR)$	$8.9 \pm 2.7 \pm 0.6 \pm 0.6$	$\overline{FF}(\chi_{c0}K_S^0)$	$1.0 \pm 0.7 \pm 0.1 \pm 0.1$

Table 5.20: *Results of fit to data for the isobar coefficients and event yields. The first uncertainty is statistical, the second is systematic and the third represents the DP signal model error.*

Resonance	x	y	Δx	Δy
$f_0(980)K_S^0$	$0.87 \pm 0.17 \pm 0.10 \pm 0.08$	$-0.70 \pm 0.22 \pm 0.15 \pm 0.09$	$0.24 \pm 0.15 \pm 0.06 \pm 0.02$	$0.28 \pm 0.16 \pm 0.05 \pm 0.04$
$\rho^0(770)K_S^0$	$0.59 \pm 0.15 \pm 0.11 \pm 0.06$	$0.44 \pm 0.17 \pm 0.15 \pm 0.04$	$-0.03 \pm 0.12 \pm 0.02 \pm 0.02$	$-0.01 \pm 0.10 \pm 0.03 \pm 0.01$
$f_0(1300)K_S^0$	$0.13 \pm 0.11 \pm 0.07 \pm 0.05$	$0.39 \pm 0.10 \pm 0.06 \pm 0.02$	$0.12 \pm 0.13 \pm 0.04 \pm 0.03$	$-0.05 \pm 0.11 \pm 0.02 \pm 0.01$
NR	$0.67 \pm 0.18 \pm 0.11 \pm 0.06$	$0.63 \pm 0.17 \pm 0.15 \pm 0.06$	$0.14 \pm 0.14 \pm 0.06 \pm 0.02$	$-0.06 \pm 0.15 \pm 0.13 \pm 0.01$
$K^*(892)\pi$	$1\ (fixed)$	$0\ (fixed)$	$0.09 \pm 0.05 \pm 0.04 \pm 0.00$	$-0.05 \pm 0.19 \pm 0.12 \pm 0.04$
$K_0^*(1430)\pi$	$-2.04 \pm 0.15 \pm 0.10 \pm 0.01$	$0.05 \pm 0.23 \pm 0.12 \pm 0.06$	$-0.02 \pm 0.09 \pm 0.02 \pm 0.01$	$-0.51 \pm 0.31 \pm 0.20 \pm 0.08$
$f_2(1270)K_S^0$	$0.30 \pm 0.08 \pm 0.04 \pm 0.01$	$-0.05 \pm 0.10 \pm 0.02 \pm 0.01$	$0.11 \pm 0.09 \pm 0.02 \pm 0.01$	$0.02 \pm 0.11 \pm 0.05 \pm 0.03$
$\chi_{c0}K_S^0$	$0.30 \pm 0.06 \pm 0.01 \pm 0.01$	$0.05 \pm 0.11 \pm 0.01 \pm 0.01$	$0.04 \pm 0.09 \pm 0.02 \pm 0.00$	$-0.04 \pm 0.09 \pm 0.02 \pm 0.01$
signal yield		$2240 \pm 58 \pm 40 \pm 4$		
$q\bar{q}$ yield		$13719 \pm 118 \pm 83 \pm 6$		

Appendix A

Longitudinal Shower Depth

This appendix gives more details on a technique for indirect extraction of longitudinal shower development information from a longitudinally unsegmented crystal calorimeter in conjunction with a precise tracking system. This technique was developed for use with the *BABAR* [47] detector, but it can be applied at any detector which combines crystal calorimetry and precision tracking. The analysis was performed by the author in collaboration with Gagan Mohanty and David Brown [66].

The starting point for developing a variable which can give us more information on longitudinal shower development was the fact that most particles do not enter the calorimeter exactly parallel to the crystal axes. A non-zero entrance angle transforms the transverse crystal segmentation into an effective longitudinal segmentation, providing some depth information. However, the effective longitudinal segmentation is poor (often fractional) and different for every particle. Because of that the attempt to have a full parameterization of the longitudinal shower development is not possible. Instead, the shower can be characterised by the first moment of its longitudinal development, so called *Longitudinal Shower Depth* (ΔL). The ΔL value is closely related to, but not identical to, the position of the electromagnetic shower maximum.

The ΔL variable is a geometric quantity which exploits the fact that the track and the cluster both sample different two-dimensional projections of the three-

dimensional shower spatial distribution. When the track direction is not parallel to the crystal axis, these projections are not fully degenerate, and they can be combined to extract the otherwise unobservable, third (longitudinal) dimension.

Three effects are responsible for the fact that the track direction and the crystal axis are not collinear. First, the magnetic field bends the track as it passes through the tracking volume. Second, the width of the beamspot in the beam direction causes tracks from the interaction point (IP) to have a different polar angle from that of the axis of the crystal they strike. Finally, by design, the crystal axes of the *BABAR* calorimeter do not project perfectly back to the nominal IP, which reduces the chance of particles from the IP passing perfectly between crystals.

In order to compute ΔL the calorimeter cluster was described as a directed line segment in space:

- First, the two-dimensional cluster centroid is calculated. (This is done using the standard *BABAR* algorithm, which takes the weighted average of the crystal centre positions at a nominal depth of $12\,\mathrm{cm}$ [81].)

- Then the weighted average direction of the crystal axes is calculated, using the energy in each crystal as (linear) weight.

- The cluster line segment is defined to pass through the cluster centroid, and point in the average crystal direction.

- The starting point of the cluster line segment is taken as the average position of the crystal front faces projected along the average direction.

The next step is to calculate the point of closest approach (POCA) in three dimensions between the extrapolated track trajectory and the cluster line segment. The POCA is the point where the track and cluster projections of the particle trajectory are most consistent. Knowing POCA and the calorimeter cluster, ΔL is computed as the path distance the track travels in the calorimeter's sensitive volume in reaching the POCA. Or in other words, ΔL is the

distance along the cluster line segment of the POCA, divided by the cosine of the angle between the track direction and the cluster line segment direction:

$$\Delta L \equiv \frac{(\vec{r}_{\text{POCA}} - \vec{r}_{\text{Front}}) \cdot \hat{r}_{\text{Cluster}}}{\cos \beta}. \tag{A.1}$$

Here, $\vec{r}_{\text{POCA}}$ is the position of the POCA, $\vec{r}_{\text{Front}}$ is a point on the front face of the crystal, $\hat{r}_{\text{Cluster}}$ is a unit vector in the direction of the cluster line segment, and β is the angle between the track direction and the cluster axis direction. The definition of ΔL is presented graphically in Figure A.1.
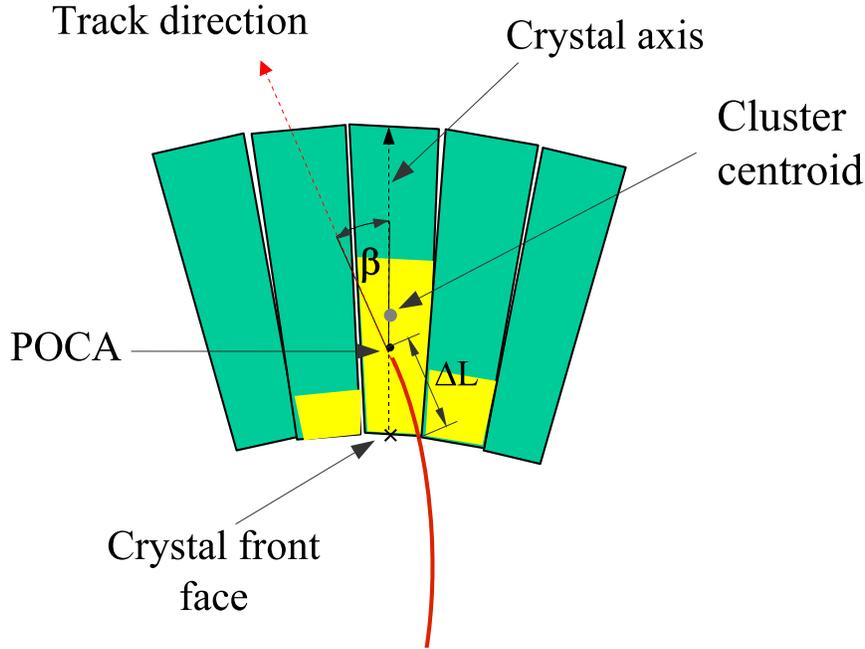
Figure A.1: *Schematic view of how ΔL is calculated.*

The impact of ΔL on electron identification was tested with an electron selector based on two standard variables: the ratio of the shower energy deposited in the calorimeter to the momentum of the track associated with the shower (E/p) and the lateral shower moment, defined as:

$$LAT = \frac{\sum_{i=3}^{N} E_i r_i^2}{\sum_{i=3}^{N} E_i r_i^2 + E_1 r_0^2 + E_2 r_0^2}. \tag{A.2}$$

Here N is the total number of crystals associated to a shower, E_i is the energy deposited in the i-th crystal such that $E_1 > E_2 > .. > E_N$, r_i the lateral distance between center of the shower and i-th crystal, and $r_0 = 5\,\text{cm}$ is approximately the average distance between two crystals. In the first case the electron selector was built using only E/p and LAT variables, and obtained results are compared with results of the selector which used E/p, LAT and ΔL as a set of discriminating variables. In Table A.1 the results of this comparison are shown.

Table A.1: *Comparison of pion misidentification probabilities at 90 % electron identification efficiency in the case where the likelihood function is defined with (or without) ΔL.*

p in	Backward Barrel		Forward Barrel		Endcap	
GeV/c	with	without	with	without	with	without
[0.2, 0.4]	25 %	34 %	16 %	27 %	5 %	7 %
[0.4, 0.6]	19 %	25 %	14 %	22 %		
[0.6, 0.8]	6 %	11 %	8 %	15 %		
[0.8, 1.0]	2 %	3 %	3 %	5 %		
[1.0, 2.0]	2 %	3 %	2 %	3 %	2 %	3 %
> 2.0	3 %	3 %	2 %	2 %		

The results show clear improvement in the performance for the backward and forward barrel regions, while for the endcap region (where high momenta particles are mostly abundant) improvement is marginal. This is because the discrimination power of ΔL diminishes with increasing energy. Figure A.2 shows the electron efficiency *vs.* pion misidentification probability for a typical low momentum bin ($0.2 < p \leq 0.4\,\text{GeV}/c$) in the forward barrel EMC. It is evident that for any given value of electron identification efficiency the likelihood function based on ΔL gives a lower pion misidentification compared to the case where ΔL is not included.
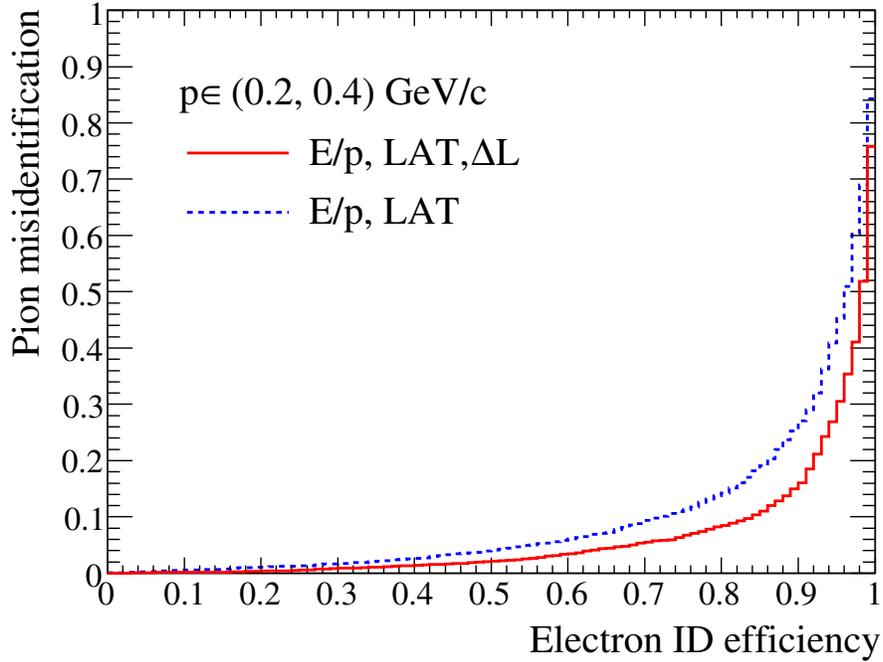
Figure A.2: *Pion misidentification probability as a function of electron identification efficiency in the forward Barrel region for a typical low momentum bin:* $0.2 < p \leq 0.4\,\mathrm{GeV}/c$.

The ΔL variable can also be used to enhance general charged particle identification, as it is sensitive to the differing longitudinal shower development of different particle types. This is demonstrated in Figure A.3, which plots ΔL for different species of particles, broken down into four track-momentum bins. Figure A.3 shows a clear distinction between the ΔL distributions of different particle species, particularly for momenta below 600 MeV/c. These distributions can be basically understood in terms of the different energy loss mechanisms at work; for instance, low momentum protons are highly-ionizing, and so deposit most of their energy early in the crystals. By contrast, electrons deposit their energy near shower maximum (roughly 10 cm), while muons with momenta above 200 MeV/c are minimum ionizing and so distribute their energy uniformly along their path through the EMC. Finally,
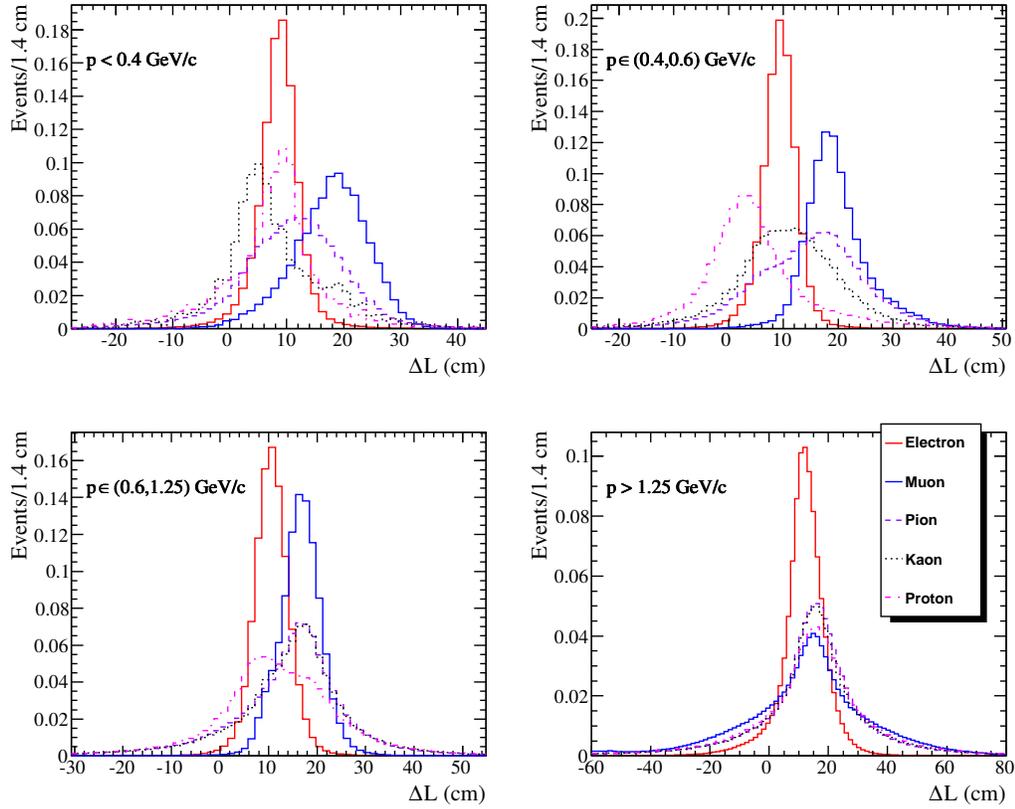
Figure A.3: *Distributions of* ΔL *for different types of particles in different momentum bins. Note the differences in the x-axis range. Each histogram has been normalized to unit area, to better show the* ΔL *distribution shapes.*

pions and kaons produce broad ΔL distributions, corresponding to the large variability of hadronic showers.

In low momentum range ΔL provides $0.8\,\sigma$ pion-muon separation[1], compared to $1.5\,\sigma$ separation from the DIRC, less than $0.1\,\sigma$ separation from either DCH or SVT dE/dx [82], and essentially no separation from E/p. Thus ΔL provides an useful cross-check to the DIRC when identifying muons at these momenta, and provides the best muon-pion separation for the $15\,\%$ of the *BABAR* solid

---

[1] σ is defined as the difference between the average of the muon and pion ΔL distributions divided by the quadratic average of their rms, $\sqrt{(\sigma_\mu^2 + \sigma_\pi^2)/2}$.

angle covered by tracking and calorimetry but not by the DIRC.

At momenta above 1.25 GeV/c, the decrease in magnetic bending reduces the angle between the track direction and the crystal axis, degrading the resolution of ΔL. Additionally, the longitudinal profile of energy deposition for different particle types tends to converge in this momentum region. Some separation power still comes from different widths of ΔL distributions for electrons compared to other particles, but this is a weak discriminant compared to other PID variables available in this momentum region.

The impact of ΔL on muon identification at *BABAR* has been additionally evaluated using a muon selection algorithm which combines many input variables. This algorithm was trained and evaluated using independent subsets of the data control samples. Compared to an older algorithm which does not use ΔL, the minimum muon momentum for which the selector has at least 50 % efficiency (at a fixed pion misidentification probability) was reduced from 800 MeV/c to 270 MeV/c [82]. This improvement in low momentum muon selection efficiency is expected to have a significant impact on several important *BABAR* physics measurements.

Appendix B

Pull plots of toy MC tests

The results of the signal only and signal, continuum background and $B\overline{B}$ background toy MC tests are shown in the plots below. For each of the toy MC tests 500 samples of the analysed set of events are generated and then fitted 100 times. For each of the samples the best fit is chosen and pull plots are made (see Section 5.1.1).
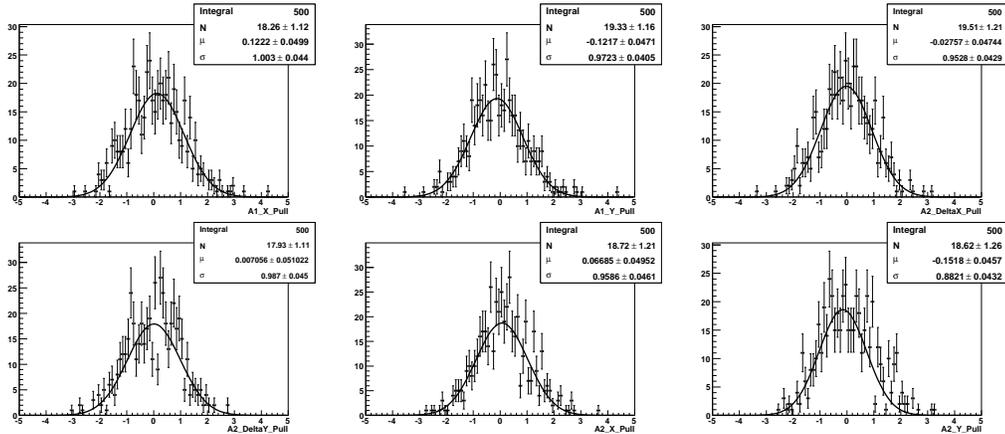
Figure B.1: *Pull plots of the signal only toy MC tests. The legend is the following: A1≡$\rho^0(770)K_S^0$ and A2≡ $f_0(1300)K_S^0$ resonance.*
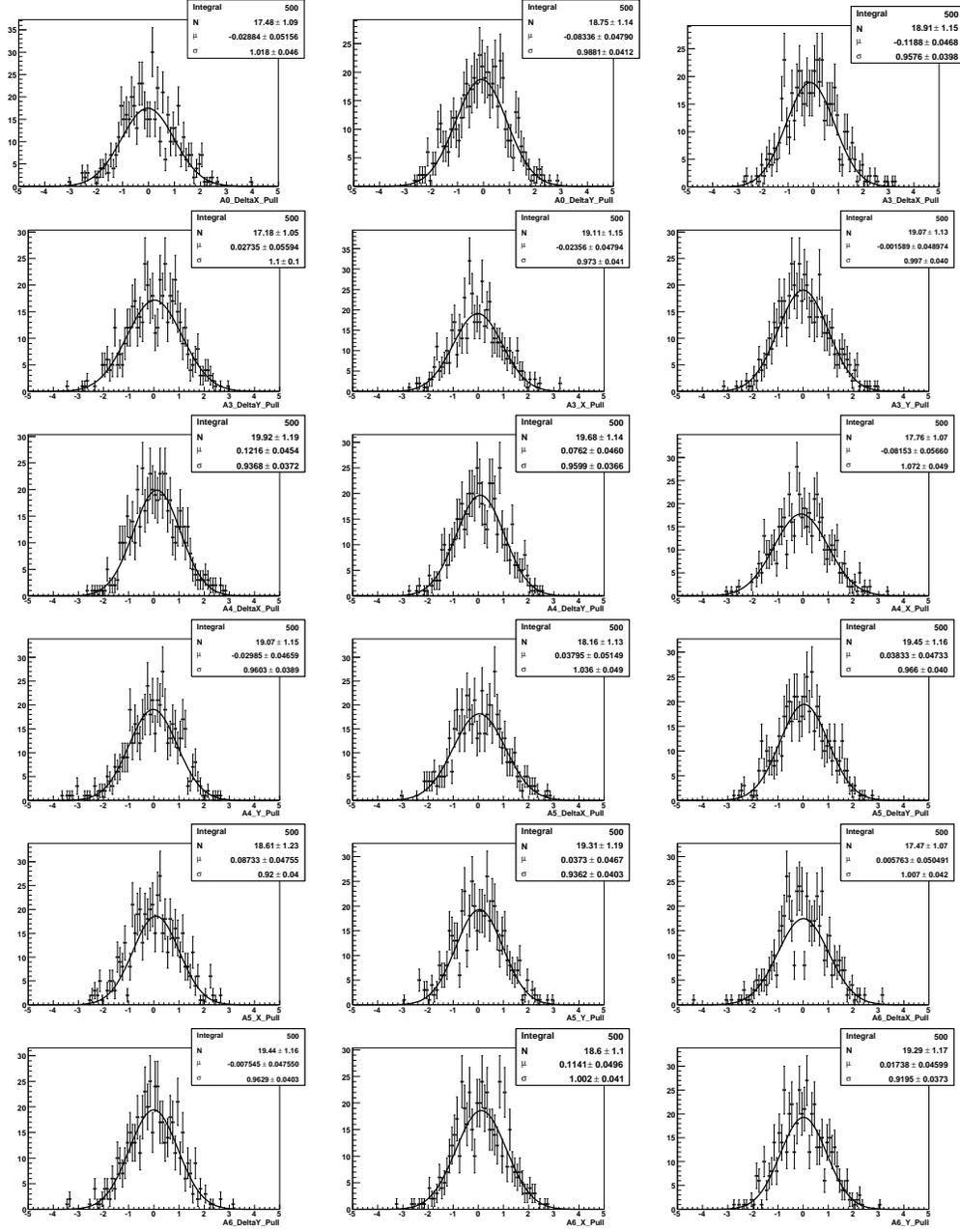
Figure B.2: *Pull plots of the signal only toy MC tests. The legend is the following:* $A0 \equiv f_0(980)K_s^0$, $A3 \equiv NR$, $A4 \equiv K^*(892)\pi$, $A5 \equiv K_0^*(1430)\pi$, *and* $A6 \equiv f_2(1270)K_s^0$ *resonance.*
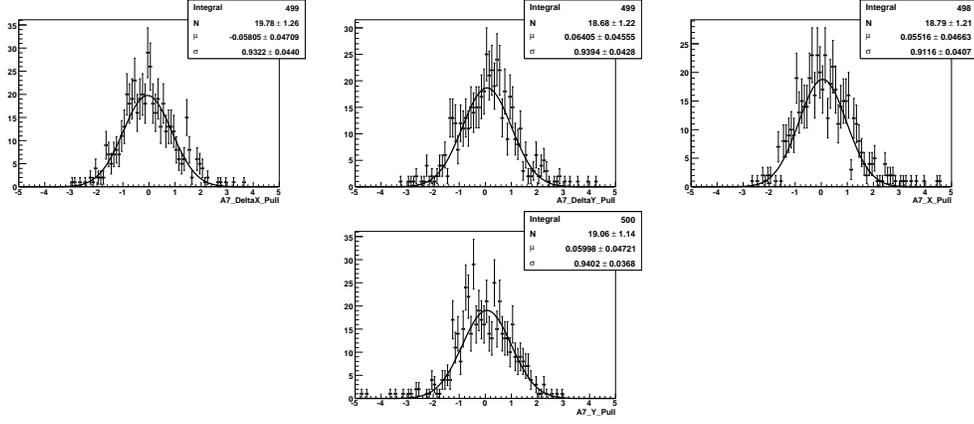
Figure B.3: *Pull plots of the signal only toy MC tests. A7 denotes* $\chi_{c0}K_S^0$ *resonance.*
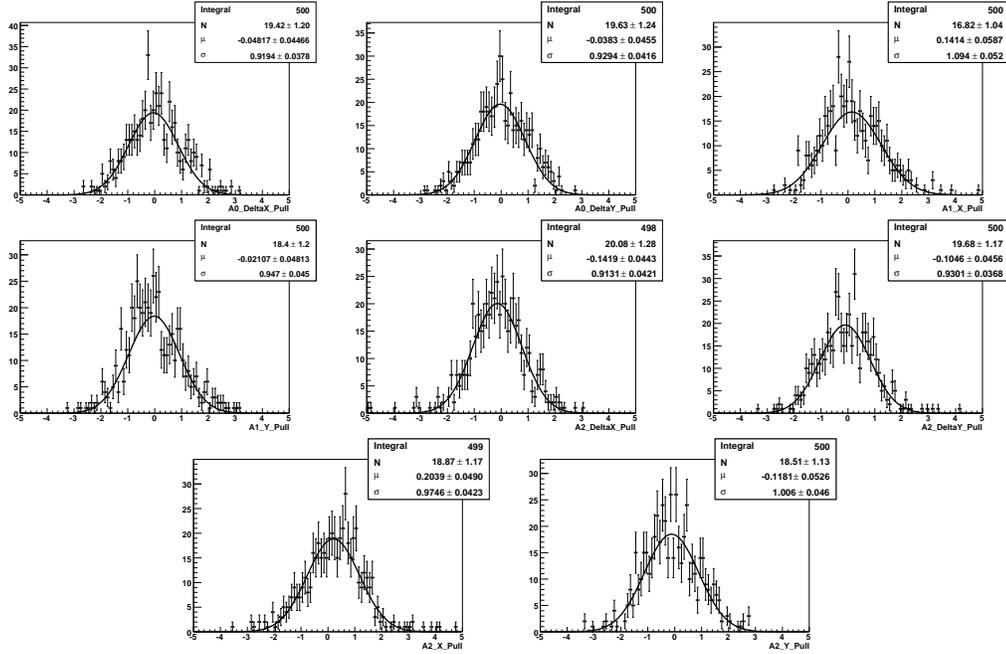
Figure B.4: *Pull plots of the signal, continuum background and* $B\bar{B}$ *background toy MC tests. The legend is the following:* $A0 \equiv f_0(980)K_S^0$, $A1 \equiv \rho^0(770)K_S^0$ *and* $A2 \equiv f_0(1300)K_S^0$ *resonance.*
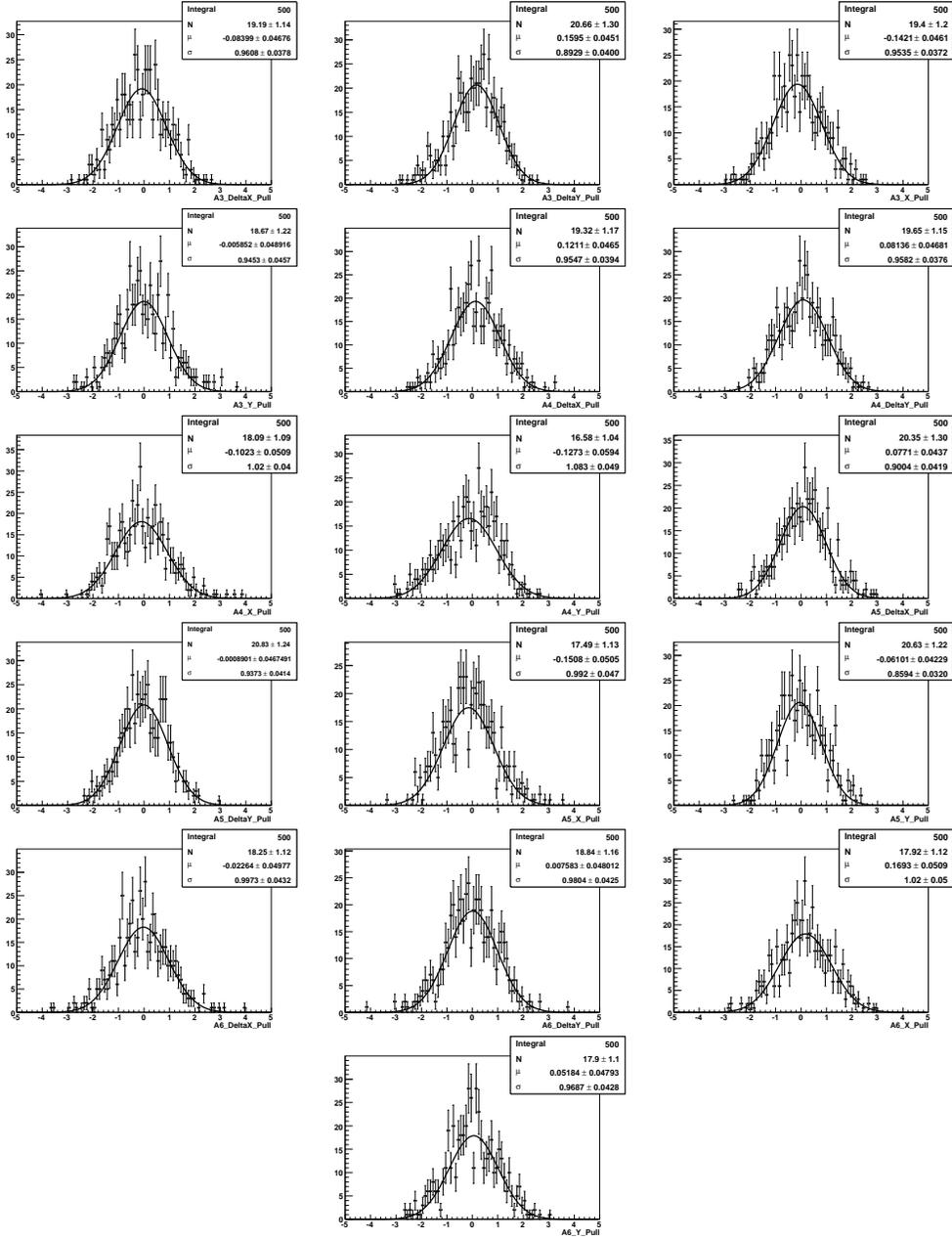
Figure B.5: *Pull plots of the signal, continuum background and $B\bar{B}$ background toy MC tests. The legend is the following: A3≡ NR, A4≡ $K^*(892)\pi$, A5≡ $K_0^*(1430)\pi$, and A6≡ $f_2(1270)K_S^0$ resonance.*
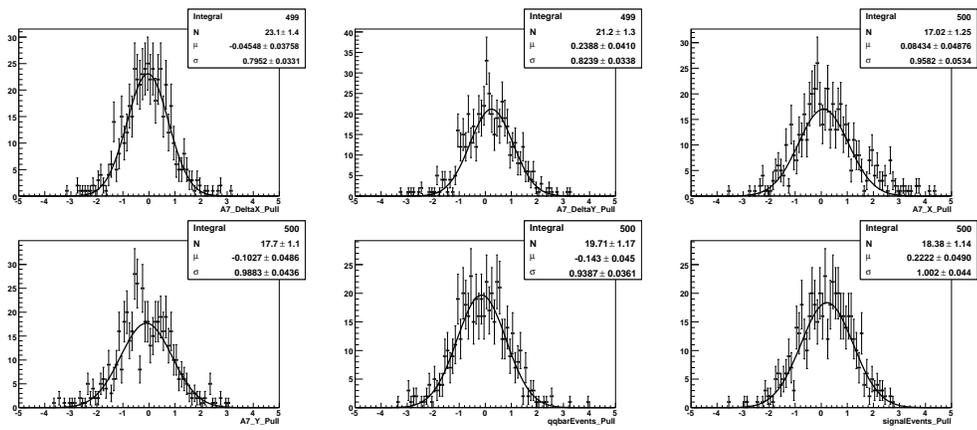
Figure B.6: *Pull plots of the signal, continuum background and $B\bar{B}$ background toy MC tests. A7 denotes $\chi_{c0}K^0_S$ resonance.*

Appendix C

Fully simulated MC tests

The results of the full MC tests are shown in plots below. 250 samples in which the true MC events are mixed with generated continuum and $B\overline{B}$ background events are made and each of them is fitted 100 times. The best fit is chosen according to its likelihood function value, and fitted parameters are plotted.
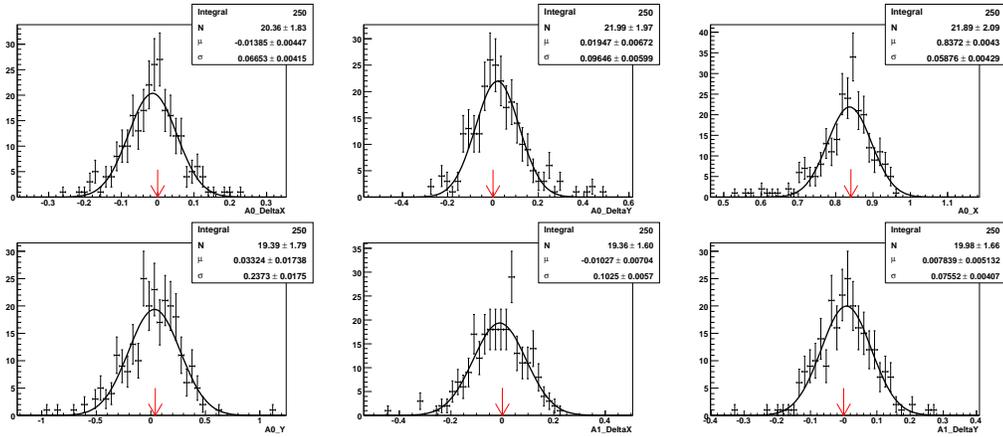
Figure C.1: *Distribution of the fitted parameters in fully simulated MC tests (histograms), gaussian fits to the distributions and the values used for the generation (denoted by the red arrows). The legend is the following: A0≡$\rho^0(770)K_S^0$ and A1≡ $f_0(980)K_S^0$ resonance.*
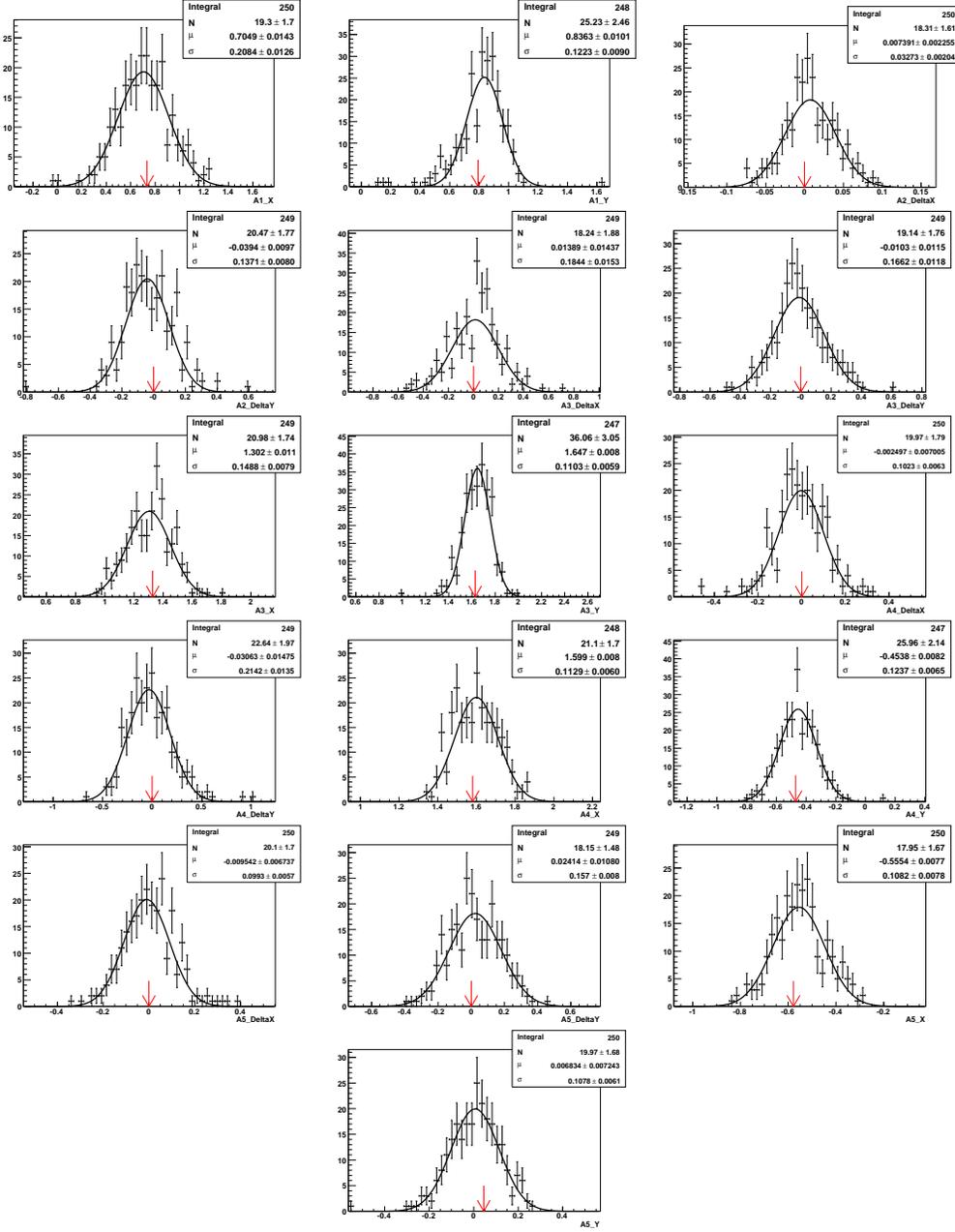
Figure C.2: *Distribution of the fitted parameters in fully simulated MC tests (histograms), gaussian fits to the distributions and the values used for the generation (denoted by the red arrows). The legend is the following: $A1\equiv f_0(980)K_S^0$, $A2\equiv f_0(1300)K_S^0$ $A3\equiv NR$, $A4\equiv K^*(892)\pi$, $A5\equiv K_0^*(1430)\pi$, and $A6\equiv f_2(1270)K_S^0$ resonance.*
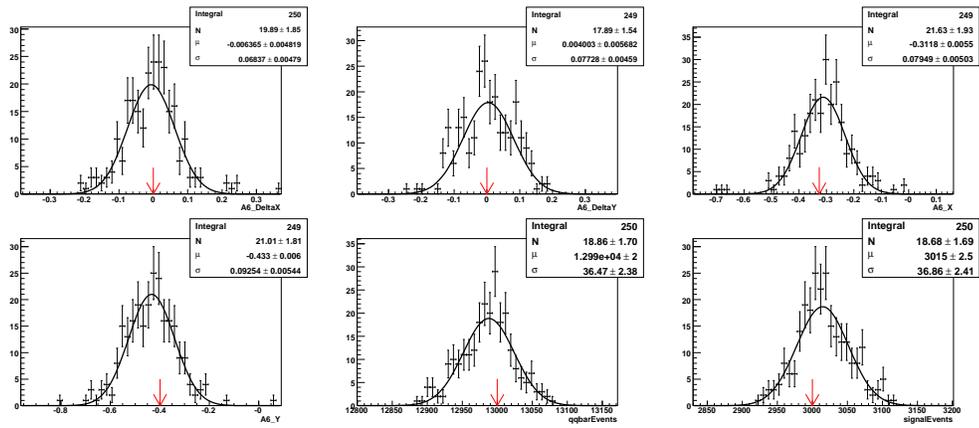
Figure C.3: *Distribution of the fitted parameters in fully simulated MC tests (histograms), gaussian fits to the distributions and the values used for the generation (denoted by the red arrows).*

Appendix D

Correlation Matrix

In the tables below the correlation coefficients among the fitted parameters obtained from the fit to data are given. Each value listed in the first row and column corresponds to the particular fitted parameter. The transcription is the following:

$$
\begin{aligned}
(1,2,3,4) &\equiv f_0(980)(X, Y, \Delta X, \Delta Y) \\
(5,6,7,8) &\equiv \rho^0(770)(X, Y, \Delta X, \Delta Y) \\
(9,10,11,12) &\equiv f_0(1300)(X, Y, \Delta X, \Delta Y) \\
(13,14,15,16) &\equiv NR(X, Y, \Delta X, \Delta Y) \\
(17,18) &\equiv K^*(892)(\Delta X, \Delta Y) \\
(19,20,21,22) &\equiv K^*(1430)(X, Y, \Delta X, \Delta Y) \\
(23,24, 25, 26) &\equiv f_2(1270)(X, Y, \Delta X, \Delta Y) \\
(27,28, 29\ 30) &\equiv \chi_{c0}(X, Y, \Delta X, \Delta Y) \\
(31) &\equiv \text{signal yield} \\
(32) &\equiv \text{continuum background yield}
\end{aligned}
$$

Table D.1: *The correlation matrix*

parm	1	2	3	4	5	6	7	8	9	10	11	12	13	14	15	16
1	1.000	0.751	-0.503	0.099	-0.525	0.615	0.111	-0.149	-0.425	0.257	0.219	0.115	-0.469	0.755	0.073	-0.028
2	0.751	1.000	-0.265	0.410	-0.709	0.632	-0.098	0.069	-0.449	0.312	0.205	0.130	-0.445	0.725	-0.079	0.106
3	-0.503	-0.265	1.000	0.375	0.156	-0.216	-0.439	0.193	0.218	-0.019	-0.096	-0.190	0.279	-0.299	0.002	0.052
4	0.099	0.410	0.375	1.000	-0.377	0.345	-0.472	0.373	-0.227	0.277	0.302	0.022	-0.160	0.313	0.127	0.290
5	-0.525	-0.709	0.156	-0.377	1.000	-0.818	0.210	0.023	0.375	-0.246	-0.205	-0.102	0.344	-0.512	-0.024	-0.137
6	0.615	0.632	-0.216	0.345	-0.818	1.000	-0.117	-0.098	-0.382	0.290	0.214	0.097	-0.417	0.629	0.067	0.130
7	0.111	-0.098	-0.439	-0.472	0.210	-0.117	1.000	-0.331	0.002	-0.073	-0.082	-0.039	-0.025	-0.026	-0.133	-0.235
8	-0.149	0.069	0.193	0.373	0.023	-0.098	-0.331	1.000	-0.009	0.085	-0.026	0.054	0.123	-0.056	-0.239	0.252
9	-0.425	-0.449	0.218	-0.227	0.375	-0.382	0.002	-0.009	1.000	-0.665	-0.555	-0.083	0.474	-0.518	0.048	-0.072
10	0.257	0.312	-0.019	0.277	-0.246	0.290	-0.073	0.085	-0.665	1.000	0.420	0.067	-0.099	0.305	-0.105	0.089
11	0.219	0.205	-0.096	0.302	-0.205	0.214	-0.082	-0.026	-0.555	0.420	1.000	-0.065	-0.165	0.221	0.142	-0.050
12	0.115	0.130	-0.190	0.022	-0.102	0.097	-0.039	0.054	-0.083	0.067	-0.065	1.000	-0.115	0.128	0.102	-0.023
13	-0.469	-0.445	0.279	-0.160	0.344	-0.417	-0.025	0.123	0.474	-0.099	-0.165	-0.115	1.000	-0.734	-0.189	-0.082
14	0.755	0.725	-0.299	0.313	-0.512	0.629	-0.026	-0.056	-0.518	0.305	0.221	0.128	-0.734	1.000	0.102	0.079
15	0.073	-0.079	0.002	0.127	-0.024	0.067	-0.133	-0.239	0.048	-0.105	0.142	0.102	-0.189	0.102	1.000	-0.180
16	-0.028	0.106	0.052	0.290	-0.137	0.130	-0.235	0.252	-0.072	0.089	-0.050	-0.023	-0.082	0.079	-0.180	1.000

Table D.2: *The correlation matrix*

parm	17	18	19	20	21	22	23	24	25	26	27	28	29	30	31	32
1	0.119	0.003	-0.231	-0.523	0.280	-0.002	0.283	0.299	0.080	0.157	-0.092	0.341	0.080	-0.007	0.013	-0.009
2	0.036	0.292	0.242	-0.535	0.350	-0.282	0.082	0.276	0.073	0.330	-0.223	0.317	0.093	0.146	-0.014	0.002
3	-0.058	0.113	0.108	0.270	-0.097	-0.142	-0.052	-0.058	-0.005	0.016	0.112	-0.155	-0.011	0.066	-0.023	0.010
4	0.037	0.231	0.146	-0.173	0.103	-0.263	0.136	0.169	0.053	0.147	-0.035	0.123	0.040	0.136	-0.026	0.010
5	-0.019	-0.191	-0.206	0.391	-0.214	0.173	-0.086	-0.269	0.013	-0.218	0.190	-0.228	-0.055	-0.098	0.027	-0.009
6	0.079	0.074	-0.064	-0.437	0.205	-0.076	0.156	0.283	-0.025	0.142	-0.111	0.283	0.057	0.040	0.021	-0.009
7	-0.004	-0.062	-0.069	-0.030	0.068	0.078	0.023	0.008	-0.143	-0.145	0.001	0.004	0.017	-0.047	0.012	-0.006
8	-0.011	0.346	0.319	0.073	0.008	-0.389	-0.093	0.003	0.022	0.263	0.040	-0.035	0.008	0.189	-0.025	0.009
9	-0.023	-0.185	-0.151	0.374	-0.216	0.187	0.006	-0.346	0.083	-0.221	0.154	-0.243	-0.065	-0.093	0.050	-0.017
10	0.031	0.209	0.088	-0.184	0.154	-0.243	0.085	0.161	-0.083	0.207	0.008	0.116	0.051	0.111	-0.050	0.018
11	0.018	-0.036	-0.048	-0.104	0.068	0.023	0.085	0.099	-0.022	0.002	-0.043	0.084	0.033	-0.016	-0.016	0.007
12	0.026	0.076	0.071	-0.109	0.135	-0.076	-0.077	0.098	0.091	0.114	-0.044	0.060	0.037	0.042	-0.003	-0.002
13	-0.052	0.100	0.127	0.604	-0.197	-0.136	-0.088	-0.279	0.013	-0.020	0.236	-0.410	-0.048	0.050	-0.001	0.007
14	0.115	0.080	-0.160	-0.565	0.258	-0.084	0.213	0.276	0.037	0.181	-0.202	0.417	0.088	0.031	0.034	-0.012
15	0.123	-0.444	-0.414	-0.063	-0.090	0.508	0.148	-0.039	0.049	-0.275	-0.056	0.040	-0.035	-0.231	0.022	-0.008
16	-0.008	-0.055	-0.006	-0.138	-0.335	0.012	0.004	0.095	0.026	-0.043	-0.019	0.072	-0.148	0.001	-0.009	0.005

Table D.3: *The correlation matrix*

parm	17	18	19	20	21	22	23	24	25	26	27	28	29	30	31	32
17	1.000	-0.044	-0.112	-0.043	0.123	0.009	0.064	0.042	-0.022	-0.041	0.024	0.037	-0.002	-0.030	0.003	0.000
18	-0.044	1.000	0.760	0.019	0.262	-0.937	-0.182	0.077	-0.064	0.571	0.018	0.014	0.133	0.454	-0.047	0.014
19	-0.112	0.760	1.000	0.054	0.205	-0.753	-0.330	0.047	-0.091	0.464	-0.112	-0.068	0.079	0.374	-0.072	0.023
20	-0.043	0.019	0.054	1.000	-0.518	-0.056	-0.158	-0.314	-0.004	-0.050	0.180	-0.376	-0.079	-0.013	-0.005	0.004
21	0.123	0.262	0.205	-0.518	1.000	-0.248	0.021	0.161	-0.034	0.253	-0.063	0.152	0.118	0.142	-0.001	-0.003
22	0.009	-0.937	-0.753	-0.056	-0.248	1.000	0.178	-0.069	0.050	-0.598	-0.054	-0.006	-0.131	-0.464	0.046	-0.013
23	0.064	-0.182	-0.330	-0.158	0.021	0.178	1.000	0.099	0.156	-0.237	0.043	0.095	0.007	-0.092	0.032	-0.005
24	0.042	0.077	0.047	-0.314	0.161	-0.069	0.099	1.000	-0.089	-0.037	-0.068	0.157	0.034	0.042	-0.022	0.007
25	-0.022	-0.064	-0.091	-0.004	-0.034	0.050	0.156	-0.089	1.000	0.077	0.018	0.011	-0.005	-0.027	0.010	-0.005
26	-0.041	0.571	0.464	-0.050	0.253	-0.598	-0.237	-0.037	0.077	1.000	-0.017	0.060	0.093	0.281	-0.023	0.004
27	0.024	0.018	-0.112	0.180	-0.063	-0.054	0.043	-0.068	0.018	-0.017	1.000	-0.130	-0.199	0.234	-0.034	0.015
28	0.037	0.014	-0.068	-0.376	0.152	-0.006	0.095	0.157	0.011	0.060	-0.130	1.000	0.124	-0.058	0.002	-0.003
28	-0.002	0.133	0.079	-0.079	0.118	-0.131	0.007	0.034	-0.005	0.093	-0.199	0.124	1.000	0.095	-0.010	0.002
30	-0.030	0.454	0.374	-0.013	0.142	-0.464	-0.092	0.042	-0.027	0.281	0.234	-0.058	0.095	1.000	-0.023	0.007
31	0.003	-0.047	-0.072	-0.005	-0.001	0.046	0.032	-0.022	0.010	-0.023	-0.034	0.002	-0.010	-0.023	1.000	-0.173
32	0.000	0.014	0.023	0.004	-0.003	-0.013	-0.005	0.007	-0.005	0.004	0.015	-0.003	0.002	0.007	-0.173	1.000

Appendix E

PDF parameters

In this chapter the exact functional forms of PDFs used in the fit are given, together with the values of the fitted PDF parameters. All PDFs are normalised ($\int_a^b P(x)dx = 1$). Also, note, that since the SCF model has not be used in the fit, the PDF parameters of the SCF distributions shown in Section 4.5.4 are not listed here.

Signal m_{ES}

$$
\begin{aligned}
P(x) &= f_1 G_1(x; \mu_1, \sigma_1) + (1 - f_1) G_2(x; \mu_2, \sigma_2) \\
G(x; \mu, \sigma) &= \frac{1}{\sqrt{2\pi}\sigma} e^{-\frac{1}{2}\frac{(x-\mu)^2}{\sigma^2}}
\end{aligned}
$$

$q\bar{q}$ background m_{ES}

$$
t = \begin{cases}
t_1 = (1.0 + \frac{x}{m_0})(1.0 - \frac{x}{m_0}), & t_1 > 0 \\
0, & t_1 < 0
\end{cases}
$$

$$
P(x) = \frac{x}{m_0}\sqrt{t}e^{-x_i t}
$$

Table E.1: *The signal m_{ES} PDF parameters.*

Parameter	Value
f_1	0.914 ± 0.006
μ_1	5.27971 ± 0.00002
σ_1	$(0.2346 \pm 0.0008)10^{-2}$
μ_2	5.2759 ± 0.0002
σ_2	$(0.233 \pm 0.008)^{-2}$

Table E.2: *The $q\bar{q}$ background m_{ES} PDF parameters.*

Parameter	Value
m_0	$5.2900 \ (fixed)$
x_i	21.1 ± 0.6

Signal ΔE

$$
\begin{aligned}
P(x) &= f_1 G_1(x; \mu_1, \sigma_1) + (1 - f_1) G_2(x; \mu_2, \sigma_2) \\
G(x; \mu, \sigma) &= \frac{1}{\sqrt{2\pi}\sigma} e^{-\frac{1}{2}\frac{(x-\mu)^2}{\sigma^2}}
\end{aligned}
$$

Table E.3: *The signal ΔE PDF parameters.*

Parameter	Value
f_1	0.245 ± 0.004
μ_1	$(-0.95 \pm 0.02)10^{-2}$
σ_1	$(0.374 \pm 0.002)10^{-1}$
μ_2	$(-0.34 \pm 0.02)10^{-2}$
σ_2	$(0.1632 \pm 0.0003)^{-1}$

$q\bar{q}\ \Delta E$

$$P(x) = sx + 1.0/(b - a)$$

The fitted parameter (s) is the slope of a liner function and x is defined in the interval $[a, b]$.

Table E.4: *The $q\bar{q}\ \Delta E$ PDF parameters.*

Parameter	Value
s	-8.8 ± 0.2

Signal and $q\bar{q}$ MLP

For the $q\bar{q}$ MLP lineshape the sum of two bifurcated Gaussians is used:

$$
\begin{aligned}
P(x) &= f_1 B_1(x; \mu_1(m_{K_S^0\pi^+, K_S^0\pi^-}), \sigma_{L1}, \sigma_{R1}) \\
&+ (1 - f_1)B_2(x; \mu_2(m_{K_S^0\pi^+, K_S^0\pi^-}), \sigma_{L2}, \sigma_{R2}) \\
B(x; \mu, \sigma_L, \sigma_R) &=
\begin{cases}
\frac{1}{\sqrt{2\pi}\sigma_L} e^{-\frac{1}{2}\frac{(x-\mu)^2}{\sigma_L^2}}, & x < \mu \\
\frac{1}{\sqrt{2\pi}\sigma_R} e^{-\frac{1}{2}\frac{(x-\mu)^2}{\sigma_R^2}}, & x > \mu
\end{cases}
\end{aligned}
$$

The parameters μ_1 and μ_2 depend on the Dalitz plot position. The dependence is found to be of the following form:

$$
\mu_k =
\begin{cases}
\alpha_k, & m_{ij}^2 > 2\,\mathrm{GeV}/c^2 \\
\alpha_k + 0.65, & m_{ij}^2 < 2\,\mathrm{GeV}/c^2,
\end{cases}
$$

where α_k (fitted value) is the value of the μ_k in the Dalitz plot centre.

A strong dependence of the MLP discriminant on tagging categories was observed. Because of that the different parameters are employed for each tagging category in the signal hypothesis. In all cases the sum of three bifurcated Gaussians is used:

197

Table E.5: *The $q\bar{q}$ MLP PDF parameters.*

Parameter	Value
f_1	0.496 ± 0.002
μ_1	1.62 ± 0.05
σ_{L1}	2.826 ± 0.002
σ_{R1}	0.79 ± 0.03
μ_1	-0.523 ± 0.006
σ_{L2}	1.52 ± 0.01
σ_{R2}	0.907 ± 0.004

$$
\begin{aligned}
P(x) &= f_2[f_1 B_1(x; \mu_1, \sigma_{L1}, \sigma_{R1}) + (1 - f_1)B_2(x; \mu_2, \sigma_{L2}, \sigma_{R2})] \\
&+ (1 - f_2)B_3(x; \mu_3, \sigma_{L3}, \sigma_{R3}) \\
B(x; \mu, \sigma_L, \sigma_R) &= \begin{cases} \frac{1}{\sqrt{2\pi}\sigma_L} e^{-\frac{1}{2}\frac{(x-\mu)^2}{\sigma_L^2}}, & x < \mu \\ \frac{1}{\sqrt{2\pi}\sigma_R} e^{-\frac{1}{2}\frac{(x-\mu)^2}{\sigma_R^2}}, & x > \mu \end{cases}
\end{aligned}
$$

Table E.6: *The signal MLP PDF parameters.*

Parameter	Value						
	Lepton	KaonI	KaonII	Kaon-Pion	Pion	Other	Untagged
f_1	0.857 ± 0.002	0.287 ± 0.005	0.271 ± 0.007	0.808 ± 0.003	0.719 ± 0.003	0.208 ± 0.005	0.586 ± 0.003
f_2	0.828 ± 0.003	0.831 ± 0.002	0.779 ± 0.001	0.582 ± 0.004	0.840 ± 0.002	0.725 ± 0.001	0.417 ± 0.006
μ_1	2.756 ± 0.02	3.13 ± 0.03	3.04 ± 0.03	2.69 ± 0.03	2.60 ± 0.02	3.05 ± 0.04	2.69 ± 0.02
σ_{R1}	0.22 ± 0.01	0.24 ± 0.01	0.27 ± 0.01	0.35 ± 0.01	1.97 ± 0.06	0.24 ± 0.01	0.33 ± 0.002
σ_{L1}	2.52 ± 0.01	3.12 ± 0.06	3.04 ± 0.08	1.88 ± 0.07	0.370 ± 0.008	3.15 ± 0.01	1.18 ± 0.04
μ_2	3.16 ± 0.04	2.40 ± 0.06	2.20 ± 0.03	2.17 ± 0.04	2.09 ± 0.06	2.11 ± 0.03	1.87 ± 0.03
σ_{R2}	0.24 ± 0.01	0.40 ± 0.02	0.44 ± 0.02	0.25 ± 0.03	0.23 ± 0.05	0.44 ± 0.02	0.19 ± 0.03
σ_{L2}	0.56 ± 0.05	2.10 ± 0.03	2.01 ± 0.03	0.90 ± 0.07	2.63 ± 0.06	2.01 ± 0.03	2.64 ± 0.04
μ_3	2.55 ± 0.02	2.43 ± 0.09	2.45 ± 0.03	2.47 ± 0.02	2.47 ± 0.02	2.42 ± 0.02	2.30 ± 0.01
σ_{R3}	0.12 ± 0.01	0.39 ± 0.02	0.35 ± 0.04	0.18 ± 0.01	0.15 ± 0.01	0.36 ± 0.02	0.27 ± 0.012
σ_{L3}	0.80 ± 0.03	0.77 ± 0.06	1.06 ± 0.03	2.5 ± 0.03	1.04 ± 0.06	1.10 ± 0.03	1.86 ± 0.03

<u>$q\bar{q}$ Δt</u>

The Δt-Dalitz plot PDF is given by Eq. (4.18). The behavior of the Δt resolution function for $q\bar{q}$ events is modelled as the sum of three gaussians,

$$
\begin{aligned}
\mathcal{R}(\delta t,\ \sigma_{\Delta t}) \ =\ & (1 - f_1 - f_2)G\left(\delta t;\ b_0,\ s_0\sigma_{\Delta t}\right) \\
& + f_1 G\left(\delta t;\ b_1,\ s_1\right) + f_2 G\left(\delta t;\ b_2,\ s_2\right).
\end{aligned}
$$

Here, $\sigma_{\Delta t}$ is the event-by-event error on Δt extracted from the fit of the B meson vertex and the G functions are gaussians. The resolution function parameters, together with the parameters zero (*prompt*) and non-zero lifetimes components of the Δt-Dalitz plot PDF (see Eq. (4.18)), are extracted from the continuum background data.

Table E.7: *The $q\bar{q}$ Δt resolution parameters*

Parameter	Value
b_0	-0.066 ± 0.025
s_0	1.28 ± 0.04
b_1	0.0 fixed
s_1	8.0 ps^{-1} fixed
b_2	0.0 fixed
s_2	0.36 ± 0.03
f_1	0.030 ± 0.002
f_2	$0.046e \pm 0.005$
f_{prompt}	0.892 ± 0.008

References

[1] K. Lande, E. T. Booth, J. Impeduglia, L. M. Lederman, and W. Chinowsky. Observation of Long-Lived Neutral V^0 Particles. *Phys. Rev.*, 103:1901–1904, 1956.

[2] C. S. Wu, E. Ambler, R. W. Hayward, D. D. Hoppes, and R. P. Hudson. *Phys. Rev.*, 105:1413, 1956.

[3] T. D. Lee and C. N. Yang. *Phys. Rev.*, 104:254, 1956.

[4] J. H. Christenson, J. W. Cronin, V. L. Fitch, and R. Turlay. Evidence for the 2π Decay of the K_2^0 Meson. *Phys. Rev. Lett.*, 13:138–140, 1964.

[5] J.W. Cronin. *Rev. Mod. Phys.*, 53:373, 1981.

[6] V.L. Fitch. *Rev. Mod. Phys.*, 53:376, 1981.

[7] N. Cabibbo. Unitary Symmetry and Leptonic Decays. *Phys. Rev. Lett.*, 10:531–532, 1963.

[8] M. Kobayashi and T. Maskawa. *CP* Violation in the Renormalizable Theory of Weak Interaction. *Prog. Theor. Phys.*, 49:652–657, 1973.

[9] S.F. King, S. Moretti, and R. Nevzorov. Theory and phenomenology of an exceptional supersymmetric standard model. *Phys. Rev.*, D73:035009, 2006.

[10] A. D. Sakharov. Violation of *CP* invariance, *C* asymmetry, and Baryon Asymmetry of the Universe. *Pisma Zh. Eksp. Teor. Fiz.*, 5:32–35, 1967.

[11] C. Burgess and G. Moore. *The Standard Model.* A Primer, 2006.

[12] L. Wolfenstein. Parametrization of the Kobayashi-Maskawa Matrix. *Phys. Rev. Lett.*, 51:1945, 1983.

[13] N. Lockyer et al. Measurement of the Lifetime of Bottom Hadrons. *Phys. Rev. Lett.*, 51:1316, 1983.

[14] M. Bona et al. The 2004 UTfit Collaboration Report on the Status of the Unitarity Triangle in the Standard Model. *JHEP*, 07:028, 2005. Updated results and plots available at: http://www.utfit.org/.

[15] J. Charles et al. CP violation and the CKM matrix: Assessing the impact of the asymmetric B factories. *Eur. Phys. J.*, C41:1–131, 2005. Updated results and plots available at: http://ckmfitter.in2p3.fr.

[16] H. Albrecht et al. Observation of B^0-$\overline{B}^0$ Mixing. *Phys. Lett.*, B192:245, 1987.

[17] A. Abulencia et al. Measurement of the B_s^0 - $\bar{B}_s^0$ Oscillation Frequency. *Phys. Rev. Lett.*, 97:062003, 2006.

[18] B. Aubert et al. Evidence for D^0-$\overline{D}^0$ mixing. *Phys. Rev. Lett.*, 98:211802, 2007.

[19] M. Staric et al. Evidence for D^0-$\overline{D}^0$ Mixing. *Phys. Rev. Lett.*, 98:211803, 2007.

[20] Ikaros I. Y. Bigi and A. I. Sanda. Cp violation. *Camb. Monogr. Part. Phys. Nucl. Phys. Cosmol.*, 9:1–382, 2000.

[21] I. Y. Bigi and A. I. Sanda. *CP Violation.* Cambridge, UK: Cambridge University Press, 2000.

[22] P.F. Harrison and H.R. Quinn. (editors).The *BABAR* physics book: Physics at an asymmetric B factory. Papers from Workshop on Physics at

an Asymmetric B Factory (BaBar Collaboration Meeting), Rome, Italy, 11-14 Nov 1996, Princeton, NJ, 17-20 Mar 1997, Orsay, France, 16-19 Jun 1997 and Pasadena, CA, 22-24 Sep 1997.

[23] W.-M. Yao et al. Review of Particle Physics. *J. Phys.*, G33:1–1232, 2006.

[24] A.J. Davies, G.C. Joshi, and Matsuda M. Exact calculation of the scalar-induced gluonic penguin diagram in the two-Higgs-doublet model. *Phys. Rev.*, D44:2114–2117, 1991.

[25] B. Aubert et al. Measurement of the CP Asymmetry Amplitude $\sin 2\beta$ with B^0 Mesons. *Phys. Rev. Lett.*, 89:201802, 2002.

[26] E. Barberio et al. Averages of B-hadron properties at the end of 2007. 2008. Unpublished. arXiv:0808.1297v1 [hep-ex].

[27] M. Ciuchini, M. Pierini, and L. Silvestrini. New bounds on the CKM matrix from $B \rightarrow K\pi\pi$ Dalitz plot analyses. *Phys. Rev.*, D74:051301, 2006.

[28] M. Gronau, D. Pirjol, A. Soni, and J. Zupan. Improved method for CKM constraints in charmless three-body B and B_s decays. *Phys. Rev.*, D75:014002, 2007.

[29] R. H. Dalitz. On the Analysis of τ-Meson Data and the Nature of the τ-Meson. *Phil. Mag.*, 44, 1953.

[30] A. Garmash et al. Dalitz analysis of the three-body charmless decays $B^+ \rightarrow K^+\pi^+\pi^-$ and $B^+ \rightarrow K^+K^+K^-$. *Phys. Rev.*, D71:092003, 2005.

[31] G. N. Fleming. *Phys. Rev.*, 135:551, 1964.

[32] D. Morgan. *Phys. Rev.*, 166:1731, 1968.

[33] D. Herndon, P. Soding, and R. J. Cashmore. *Phys. Rev.*, D11:3165, 1975.

[34] G. Breit and E. Wigner. Capture of slow neutrons. *Phys. Rev.*, 49:519, 1936.

[35] G. Breit. *Handbuch der Physik XLI/1.* Springer, 1959.

[36] S. M. Flatté. Coupled - Channel Analysis of the $\pi\eta$ and $K\overline{K}$ systems near $K\overline{K}$ threshold. *Phys. Lett.*, B63:224, 1976.

[37] D. Aston et al. A Study of $K^-\ \pi^+$ Scattering in the Reaction $K^-p \rightarrow K^-\pi^+n$ at 11 GeV/c. *Nucl. Phys.*, B296:493, 1988.

[38] D. V. Bugg. *Phys. Lett.*, B572:1–7, 2003.

[39] W. Dunwoodie. http://www.slac.stanford.edu/∼wmd/kpi_swave/kpi_swave_fit.note.

[40] B. Aubert et al. Measurements of CP-Violating Asymmetries in the Decay $B^0 \rightarrow K^+K^-K^0$. *Phys.Rev.Lett.*, 99:161802, 2007. arXiv:0706.3885 [hep-ex].

[41] B. Aubert et al. Dalitz plot analysis of the decay $B^+ \rightarrow K^\pm\ K^\pm\ K^\mp$. *Phys. Rev.*, D74:032003, 2006.

[42] C. Zemach. *Phys. Rev.*, 133:B1201, 1964.

[43] C. Zemach. *Phys. Rev.*, 140:B97, 1965.

[44] J. Blatt and V. E. Weisskopf. *Theoretical Nuclear Physics.* J. Wiley (New York), 1952.

[45] T. Jansen et al. Radiative decay width of the ρ meson. *Phys.Rev.*, D27:26–46, 1983.

[46] B. Aubert et al. An amplitude analysis of the decay $B^\pm \rightarrow \pi^\pm\pi^\pm\pi^\mp$. *Phys. Rev.*, D72:052002, 2005.

[47] B. Aubert et al. The *BABAR* detector. *Nucl. Instrum. Meth.*, A479:1–116, 2002.

[48] W. Kozanecki. *Nucl. Instrum. Meth.*, A446:59–64, 2000.

[49] A. Snyder. *BABAR* Note #177, 1994.

[50] D. Lange et al. A *B* Flavour tagging algorithm for *CP* violation measurements with the *BABAR* experiment. *BABAR* Analysis Document #1025. Unpublished.

[51] B. Denby and D. Perret-Gallix. New Computing Techniques in Physics Research IV, page 793, Pisa, April 1995.

[52] B. Aubert et al. Improved measurement of CP asymmetries in $B^0 \rightarrow (c\bar{c})K^{(*)0}$ decays. *Phys. Rev. Lett.*, 94:161803, 2005.

[53] B. Aubert et al. Simultaneous Measurement of the B^0 Meson Lifetime and Mixing Frequency with $B^0 \rightarrow D^{*-}l^+\nu$ Decays. *Phys.Rev.*, D67:072002, 2003.

[54] B. Aubert et al. A study of time dependent CP-violating asymmetries and flavor oscillations in neutral B decays at the $\Upsilon(4S)$. *Phys. Rev.*, D66:032003, 2002.

[55] B. Aubert et al. Improved Measurement of CP Violation in Neutral B decays to $c\bar{c}s$. *Phys. Rev. Lett*, 99:171803, 2007.

[56] W. Ford. Choice of Kinematic Variables in B Meson Reconstruction. *BABAR* Analysis Document #53. Unpublished.

[57] S S. Nandi and W. W. Walter. Jet angular distribution from quantum chromodynamics. *Phys. Rev.D*, 21:76–81, 1980.

[58] B.D. Ripley. *Pattern Recognition and Neural Networks*. Cambridge University Pres, 1996.

[59] D. J. Lange. The EvtGen particle decay simulation package. *Nucl. Instrum. Meth.*, A462:152–155, 2001.

[60] T. Sjöstrand. High-energy physics event generation with PYTHIA 5.7 and JETSET 7.4. *Comput. Phys. Commun*, 82:74, 1994.

[61] E. E. Barberio, B. van Eijk, and Z. Was. PHOTOS: A universal monte carlo for qed radiative corrections in decays. *Comput. Phys. Commun.*, 66:115, 1991.

[62] S. Agostinelli et al. GEANT4: A simulation toolkit. *Nucl. Instrum. Meth.*, A506:250–303, 2003.

[63] P. Billoir. Track Fitting with Multiple Scattering: A New Method. *Nucl. Instr. Meth.*, A225:352, 1984.

[64] S. Spanier and G. Mancinelli. *BABAR* Analysis Document #116.

[65] T. Brandt. *BABAR* Analysis Document #396.

[66] D. N. Brown, J. Ilic, and G. B. Mohanty. Extracting longitudinal shower development information from crystal calorimetry plus tracking. *Nucl. Instrum. Meth.*, A592:254–260, 2008.

[67] R. Barlow. *Statistics: A Guide to the Use of Statistical Methods in the Physical Sciences*. Wiley, 1989.

[68] G. Cowan. *Statistical Data Analysis*. Oxford University Press, 1998.

[69] P. Harrison et al. LAURA++ - Likelihood Analysis Unbinned Reconstruction of Amplitudes. *BABAR* Analysis Document #806. Unpublished.

[70] F. James and M. Roos. 'MINUIT', a system for function minimization and analysis of the parameter errors and correlations. *Comput. Phys. Commun.*, 10:343–367, 1975.

[71] F. James. MINUIT, Function Minimization and Error Analysis, Reference Manual. Unpublished. wwwasdoc.web.cern.ch/wwwasdoc/minuit/minmain.html.

[72] ROOT, An Object Oriented Data Analysis Framework. http://root.cern.ch/.

[73] Porter Frank. Interval Estimation using the Likelihood Function. *Nucl.Inst.Meth.*, A368:793–803, 1996.

[74] M. Pivk and F. R. Le Diberder. $_s\mathcal{P}lot$: A statistical tool to unfold data distributions. *Nucl. Instrum. Meth.*, A555:356–369, 2005.

[75] A. Garmash et al. *Phys. Rev.*, D71:092003, 2005.

[76] A. Garmash et al. Dalitz analysis of three-body charmless $B^0 \to K_S^0 \pi^+ \pi^-$ decay. *Phys. Rev.*, D75:012006, 2007.

[77] B. Aubert et al. Time-dependent Dalitz Plot Analysis of $B^0 \to K_S \pi^+ \pi^-$. Presented at 23rd International Symposium on Lepton-Photon Interactions at High Energy (LP07), Daegu, Korea, 13-18 Aug 2007.

[78] Owen Long, Max Baak, Robert N. Cahn, and David Kirkby. *Phys. Rev.*, D68:034010, 2003.

[79] V. Baru, J. Haidenbauer, C. Hanhart, A. Kudryavtsev, and Ulf-G. Meissner. Flatte-like distributions and the $a_0(980)/f_0(980)$ mesons. *Eur.Phys.J*, A23:523–533, 2005.

[80] M. Gronau, D. Pirjol, A. Soni, and J. Zupan. Constraint on $\bar{\eta}$, $\bar{\rho}$ from $B \to K^* \pi$. 2008. Unpublished. arXiv:0712.3751v2 [hep-ph].

[81] B.B. Brabson et al. *Nucl. Instrum. Meth.*, A332:419, 1993.

[82] A. V. Telnov. Private communication.